Development of functional nanoparticles for *in situ* tissue engineering

Matthew Joseph Walker

PhD

University of York

Biology

December 2018

Abstract

Mesenchymal stem/stromal cells (MSCs) are of significant clinical interest in regenerative medicine because of their trilineage potential to differentiate into cells integral for tissues such as bone and cartilage. Current therapies for tissue damage often require surgical intervention, which has drawbacks including invasiveness and susceptibility to infection. Stem cell-based therapies likely offer a more natural alternative to repair damaged tissue. Nanoparticles are a promising tool for biomedical applications, especially as a vehicle for biomolecule delivery when coated with temperature-responsive polymers to entrap and release biomolecules, such as proteins, in a triggered manner. Superparamagnetic iron oxide nanoparticles (SPIONs) can undergo a phenomenon termed magnetic heating in the presence of an alternating magnetic field. SPIONs surface-functionalised with temperature-responsive polymers present a potential combination for protein delivery and release.

In this study, I report the development of SPIONs coated with temperature-sensitive polymer poly(*N*-isopropylacrylamide) (PNIPAM). PNIPAM-coated SPIONs showed temperature-sensitive properties above the lower critical solution temperature (LCST) of PNIPAM (32^{o}C) when heated with or without magnetic heating. I could characterise the protein encapsulation and release of test protein apotransferrin from PNIPAM-coated nanoparticles in both a pH- and temperature-sensitive manner. Magnetic heating, though a constant or pulsed application, was sufficient to trigger the release of encapsulated apotransferrin from PNIPAM-coated nanoparticles, where switching off the magnetic field halted further protein release. Magnetically-triggered Wnt3a release from PNIPAM-coated nanoparticles elicited cellular activation through the enhanced green fluorescent protein (eGFP) response of an MSC Wnt reporter line, as well as increased proliferation of both immortalised and primary MSCs. I also developed temperature-responsive polymer, poly(*N*-isopropylmethacrylamide) (PNIPMAM), which exhibited a higher LCST than PNIPAM (42^{o}C) and could release apotransferrin above physiological temperature with/without magnetic heating.

The developed temperature and magnetically-responsive SPIONs could be a potential tool to promote MSC-driven tissue regeneration through biomolecule delivery and temperature-sensitive release.

Table of contents

List of tables

List of figures

List of schemes

List of equations

Preface

In tissue engineering there is a constant requirement for the development of better approaches to treat damaged and worn tissues. Current treatments for patients of joint disorders often involve surgical intervention through tissue grafting or implantation, which have drawbacks including improper joint function, infection and unfavourable immune response. The self-renewal and differentiation properties of MSCs offer an alternative as a natural cell-based therapy for the regeneration of tissue. However, direct administration of MSCs is difficult, often resulting in lack of desired targeting, which consequently diminishes their regenerative potential at sites of interest.

Towards improving current therapies, the development of effective biomaterials to stimulate MSCs *in situ* is an area of growing interest, particularly using nanomaterials. Nanoparticles are an appealing tool in this area as a vehicle for biomolecule delivery and release to activate MSCs. Properties of nanoparticles are highly favourable for such applications due to their small size and capacity for surface functionalisation. SPIONs are an attractive material for applications in nanomedicine due to their magnetic properties, particularly through their ability to undergo magnetic heating when exposed to an alternating magnetic field. SPIONs have largely been used in tissue engineering as contrast agents for MRI-based tracking of stem cells with their potential as drug delivery vehicles being relatively unexplored.

SPIONs can be coated with smart polymers that are responsive to temperature, where biomolecules can be entrapped and released in a triggered manner. PNIPAM is an extensively studied temperature-responsive polymer that can release entrapped drug molecules upon heating. Combining the magnetic heating properties of SPIONs and the temperature-sensitivity of PNIPAM could be an interesting tool for triggered biomolecule release to activate MSCs.

To investigate the potential of using temperature-sensitive nanomaterials for biomolecule release to activate MSCs, I chemically synthesised PNIPAM-coated SPIONs. These functionalised nanoparticles were assessed to establish their capabilities and extensively characterised in terms of their molecular, magnetic and temperature-responsive properties, using a variety of techniques (**Chapter 2.3**). Biochemical studies were conducted using the model test protein

apotransferrin to assess protein encapsulation and determine the required conditions for temperature-dependent release, largely focusing on release following magnetic heating of SPIONs (**Chapter 3.3**). I also treated MSCs with Wnt3a-loaded PNIPAM-coated SPIONs that were magnetically heated, to assess cellular activation following growth factor release. This was analysed by assessing the eGFP response of a Wnt-sensitive reporter line, as well as the proliferative response of both immortalised and primary MSCs (**Chapter 4.3**).

With a view to generate temperature-responsive SPIONs that could release proteins above physiological temperatures, I also began work using another temperature-responsive-polymer, PNIPMAM, which displays a higher LCST than PNIPAM. This was conducted by characterising the molecular and temperature-sensitive properties of PNIPMAM, as well as its protein encapsulation and release potential when coated onto SPIONs (**Chapters 2.3 and 3.3**).

This project shows a novel application of PNIPAM-coated SPIONs for the magnetically-triggered release of a growth factor to activate MSCs *in vitro*.

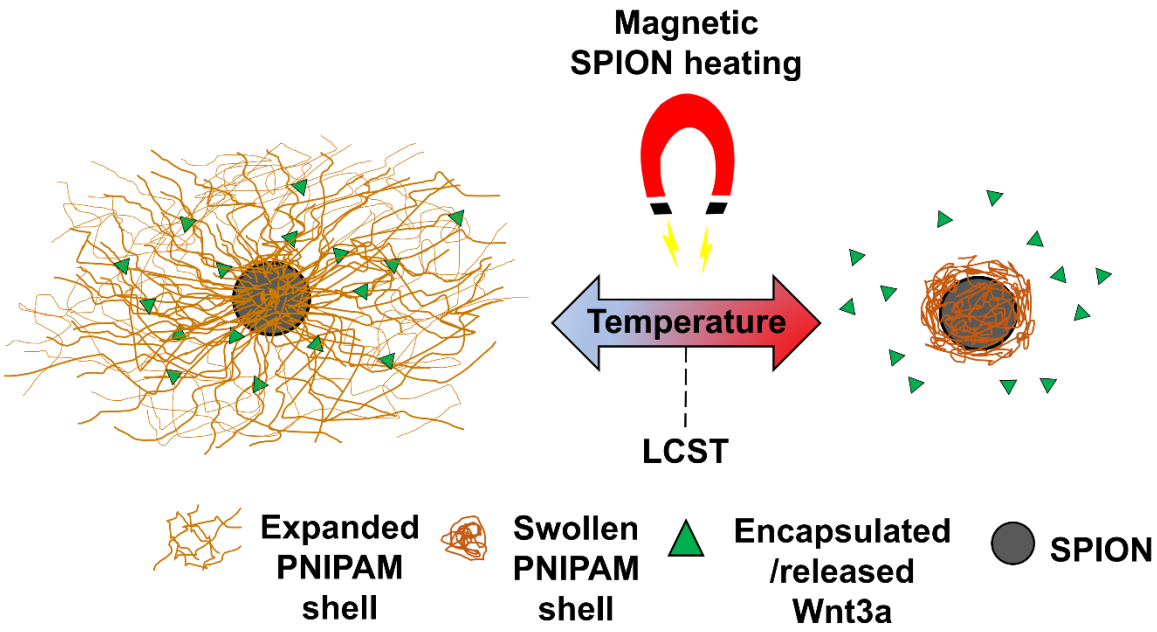

Schematic of magnetically-triggered Wnt3a release from PNIPAM-coated SPIONs: Schematic shows PNIPAM-coated SPIONs loaded with Wnt3a (left) where magnetic SPION heating with an alternating magnetic field (centre) triggers temperature-sensitive PNIPAM shell collapse and release of Wnt3a (right). Grey circle represents SPION core with a PNIPAM shell (orange lines). Wnt3a molecules (green triangles) are encapsulated within and released from PNIPAM shell.

Acknowledgements

I would like to thank my supervisors Dr. Dani Ungar, Prof. Paul Genver, Dr. Victor Chechik and Dr. Andrew Pratt for all their support and guidance throughout. Also, Dr. Iain Will (Department of Electronics, University of York, UK) for the kind donation of, and assistance using, the magnetic heating equipment for experimental work. I would like to thank Mark Bentley (Mechanical Workshop, University of York, UK) for the design of custom-made vessels for cell magnetic heating experiments. Also, I would like to acknowledge Andrew Stone (Department of Biology, University of York, UK) and Dr. Tom Dennison (Malvern Instruments Ltd, Worcestershire, UK) for processing and analysis of nanoparticle tracking analysis (NTA) samples. Also, I would like to thank Clifton Park Hospital (York, UK) for kind donation of patient femoral heads from which primary MSCs were isolated. I would also like to acknowledge the EPSRC for funding this work and members of the Cell Biology Lab and Chechik groups (University of York, UK) for any help and guidance provided.

Author’s declaration

I declare that this thesis is a presentation of original work and I am the sole author. Work was performed by the author between September 2015 and July 2018 in the Departments of Biology, Chemistry and Physics, University of York, in the laboratories of Dr. Dani Ungar, Prof, Paul Genever, Dr. Victor Chechik and Dr. Andrew Pratt. I declare that there are no conflicting interests regarding the content of this study and that this work has not previously been presented for an award at this, or any other, University. All sources are acknowledged as References.

Chapter 1: Introduction

1.1. Nanoparticles

Nanoparticles can be described as particles typically between 1-100 nm that have distinct properties compared to bulk samples of the same material (Auffan et al., 2009). The application of nanoparticles is often associated with cutting edge, modern day science, but has roots as far back as pottery surfacing in Roman history (Khan, 2012). Certainly, one of the pioneers to first describe nanoparticles in terms of their optical properties was Michael Faraday in the mid-1800's (Faraday, 1857). Purely metallic nanoparticles are of significant interest for many applications, including drug delivery, where their composition can range from being bimetallic, core-shell or coated with organic or inorganic molecules. The focus in this thesis is on inorganic nanoparticles, but nanoparticles can also be organic and exist in various forms such as polymeric nanoparticles, liposomes and viral capsids. Stability is often conferred to nanoparticles by coating with an organic layer of molecules known as stabilising or capping agents (Batista et al., 2015). Nanoparticles are defined by being within a size range larger than atomic dimensions, but small enough to exhibit random Brownian motion. Also, the size distribution of synthesised nanoparticles varies depending on the preparation method, where aqueous synthetic approaches typically produce polydisperse samples with Gaussian size distributions, whereas organic syntheses will generally produce highly monodisperse particles (Hayashi, 1997). Particles in the nanoscale size range have significantly higher surface area to volume ratios than those orders of magnitude larger. A high surface area to volume ratio is advantageous for the functionalisation of nanoparticles, allowing for extensive surface coating. Electron microscopy images of differently sized nanoparticles can be seen in **Figure 1.1**

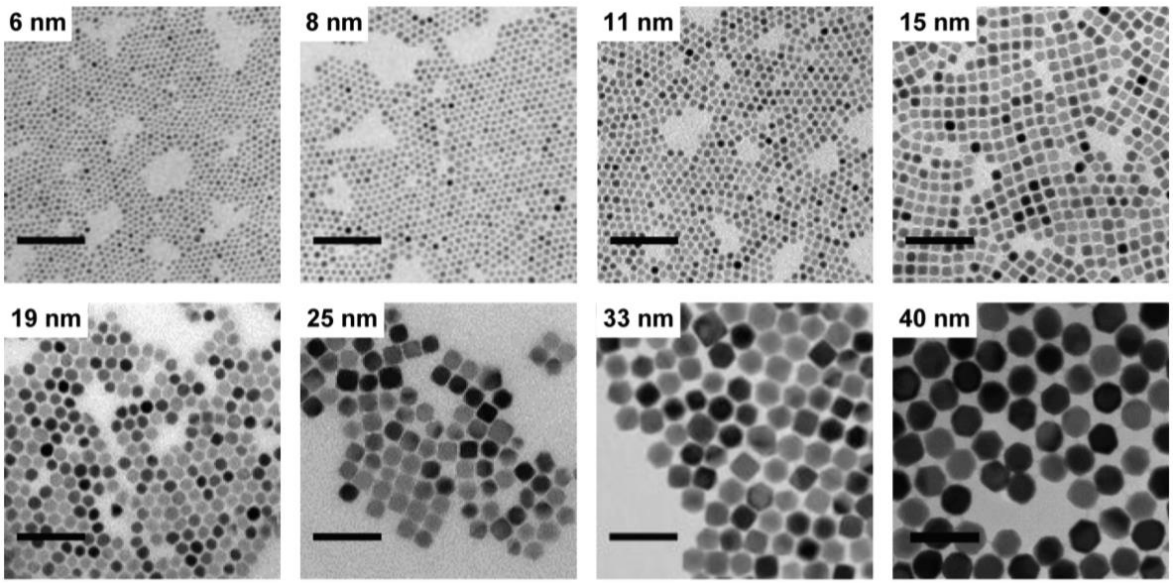

Figure 1.1. Electron microscopy images of iron oxide nanoparticles with sizes ranging between 6-40 nm: Iron oxide nanoparticles shown above were generated using an organic synthetic approach using thermal decomposition of iron carbonyls. Scale bars equal 100 nm. Figure was taken from a previous study (Tong et al., 2017).

1.1.1. Nanoparticle synthesis

Since nanoparticles can exist in various organic or inorganic forms across a range of sizes, it is important to regulate and optimise synthetic approaches to generate suitable particles for desired applications. There are a variety of approaches for generating nanoparticles either through the breakdown of bulk materials, usually on a macro- or micro-scale, or an atomic scale by nucleation and growth of nanoparticle seeds.

Bulk material breakdown can be achieved physically through ball mill grinding. However, this approach generally requires significant optimisation and yields larger particles on the nanometer-micrometer boundary that often aggregate (Rizlan and Mamat, 2014). Also, bulk material breakdown can be done hydrothermally through pyrolysis by forcing a vaporous precursor through an orifice at high pressure before burning and recovering particles from the soot produced. However, as with ball mill grinding, particles generated using this approach tend to be on the micrometer scale, again commonly with aggregation (Taniguchi et al., 2008). Using high energy methods such as thermal plasmas can vaporise micrometer-sized particles to form droplets which cool and form particles upon evaporation. This approach has been shown to generate nanoparticles of small size and high uniformity; however, drawbacks include lengthy optimisation and also elaborate, expensive setup (Shigeta and Murphy, 2011).

Most metal-based nanoparticles can be generated by nucleation and growth of seeds from the reduction or hydrolysis of chemical precursors. This approach is relatively simple and requires a minimum number of chemicals. For example, a synthesis could be carried out in an aqueous environment in the presence of a reducing agent using a soluble metallic salt, a radical scavenger and an organic surface-capping agent. During this process, radical-based reduction will lower metallic ions to a zero-valence state, which in turn, will cause metal atoms to coalesce into particles. A scavenger chemical will act to prevent re-oxidation of the metal by reacting with oxidising radicals. The organic surface-capping agent serves to regulate growth and prevent aggregation during particle formation. Generating nanoparticles using this method is advantageous due to its tunability through adjustment of precursor concentrations, relative to those of the other chemicals involved, to control and regulate particle size and shape (Belloni et al., 1998).

1.1.2. Nanoparticle characterisation

Nanoparticles have distinct physical properties which distinguish them from conventional materials, meaning that they have different analytical requirements for features such as size, shape and dispersity.

For size characterisation, optical microscopy is not appropriate since nanoparticles have a size below the diffraction limit of visible light. Electron microscopy is largely used for analysis of nanoparticles in the absence of solvent and often light scattering approaches are used for measuring their properties in solution. Additionally, the size heterogeneity of nanoparticles can be visualised by electron microscopy and also quantified using light scattering. Also, sub diffraction optical imaging techniques are available, such as super-resolution microscopy

1.2 Magnetism

One of the most interesting properties of metal nanoparticles, such as iron oxide, is their magnetic responsiveness. It is therefore important to understand the mechanisms by which magnetic nanoparticles are influenced by magnetic fields to be used in practical applications. Magnetism is a type of physical phenomenon mediated by magnetic fields which arise from electric currents and the magnetic moment of a particle. Magnetic moments represent the orientation and magnetic strength of a material that produces a magnetic field, such as electrons in magnetic particles. The magnetic moment of a material relates to its magnetic spin orientation, which will align with an external magnetic field in a temperature-dependent manner. The spin direction can exist in either an upwards or downwards state, where a full electron shell contains both an upward and downward magnetic moment spin. Materials containing atoms with filled electron shells have no magnetic moment since each is cancelled out by the opposing spin. By contrast, materials containing atoms with partially filled electron shells will have unpaired spin states and therefore exhibit a magnetic moment.

Above a defined temperature, known as the Curie temperature, magnetic materials will lose their permanent magnetic properties and revert to induced magnetism. The magnetic spins of materials operating as permanent magnets are ordered and aligned, whereas those that exist in an induced magnetic state are disordered and will forcibly align to an applied magnetic field.

1.2.1. Ferromagnetism and paramagnetism

There are various types of magnetism encountered in everyday life, the most familiar being ferromagnetism. Ferromagnetic materials are attracted to magnetic fields and can be magnetised to become permanent magnets that produce magnetic fields themselves. Ferromagnetism is shared across a few materials, the most common being iron, cobalt and nickel. These materials will remain magnetised even after removal of a magnetic field as their magnetic spin is ordered and aligned with the field orientation. This means that during the analysis of magnetic properties, ferromagnetic materials will display remanent magnetisation where they will retain magnetism after the action of the magnetising force has ceased.

By contrast to ferromagnets, paramagnetic materials, such as iron oxide, are weakly attracted to an external magnetic field and are not permanent magnets as they form internalised, induced magnetic fields in the direction of an applied field. Also, unlike ferromagnets, paramagnetic materials do not display any remanent magnetisation in the absence of an external magnetic field because thermal fluctuations randomly orient the spin direction to a disordered state. A comparison between ferromagnetic and paramagnetic electron spin states can be seen in **Figure 1.2.** During this magnetic phase transition, the time between magnetisation flips is known as the Néel relaxation time, first described by Néel in 1949 (Néel, 1949). The response of a material to the removal of an applied magnetic field is a characteristic feature that can distinguish ferromagnetic from paramagnetic materials (**Figure 1.3**).

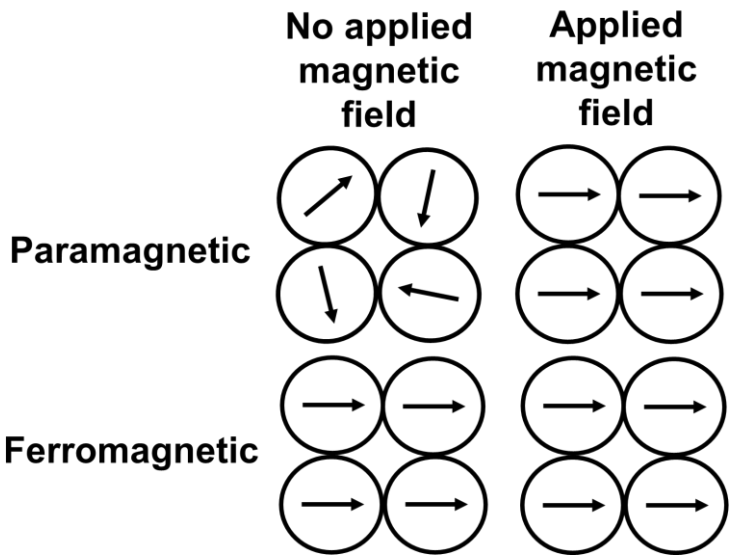

Figure 1.2. Paramagnetic vs. ferromagnetic electron spin states in the presence/absence of a magnetic field: Arrows denote electron spin orientation.

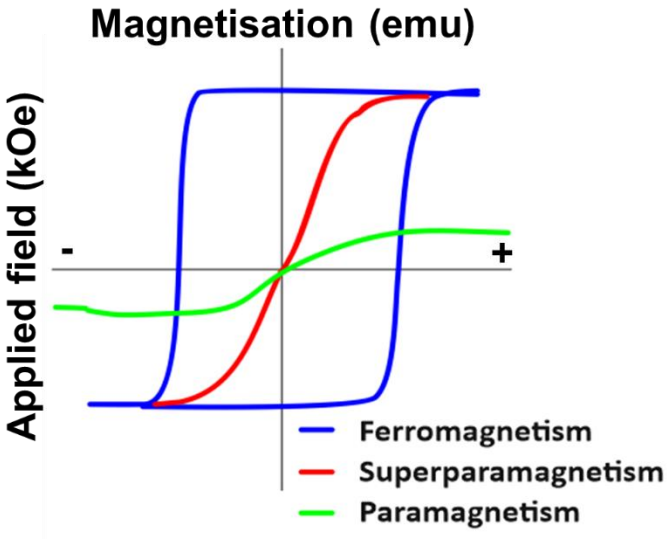

Figure 1.3. Magnetisation of magnetic materials in an applied field: Magnetisation of ferromagnetic (blue), superparamagnetic (red) and paramagnetic (green) materials in the presence of applied magnetic field sweeps.

The Curie temperature of a material is the temperature at which magnetic materials undergo significant changes in their magnetic properties. Below the corresponding Curie temperature of a material, ferromagnetic behaviour is observed where the atoms are spontaneously magnetised to an external magnetic field due to the parallel alignment of atoms. Above the Curie temperature, materials undergo a phase transition and enter a paramagnetic state as the atomic magnetic moments become disordered. Upon alignment of the magnetic moments, the response of paramagnetic materials is significantly weaker than that of ferromagnetic materials.

Despite their spin alignment and strong magnetic properties, ferromagnets can exist in an unmagnetized state. This occurs within bulk ferromagnetic materials which can be divided into regions knows as magnetic domains. Within each domain, the magnetic moment spin directions are aligned, however the spins of separate domains can orient in different directions when bulk materials are unmagnetized and in their lowest energy configuration, resulting in no net magnetic field.

1.2.1.1. Superparamagnetism

Superparamagnetism occurs in small ferromagnetic nanoparticles, where in the absence of an applied magnetic field, superparamagnetic materials appear to have zero net magnetisation, as the time taken to measure magnetisation extends that of the Néel relaxation time. Magnetisation of superparamagnetic nanoparticles can randomly flip under the influence of temperature (Teja and Koh, 2010). As with paramagnetic materials, an external magnetic field is able to magnetise superparamagnetic particles. However, the extent of magnetisation to an applied magnetic field, known as magnetic susceptibility, is significantly higher in superparamagnetic materials.

Ordinarily, a ferromagnetic material will undergo a phase transition to a paramagnetic state above its Curie temperature. However, this transition in a superparamagnetic material differs as it occurs below its Curie temperature. Superparamagnetic nanoparticles consist of a single magnetic domain, unlike larger ferromagnetic nanoparticles which have multiple domains. Because of their single domain properties, superparamagnetic nanoparticles behave through the sum of all their individual magnetic moments.

1.2.1.1.1. Superparamagnetic iron oxide nanoparticles (SPIONs)

SPIONs have a broad range of applications in nanotechnology due to their magnetic properties. The phases of iron oxide nanoparticles generally used in the field are magnetite (Fe_3O_4) and maghemite (γ-Fe_2O_3). SPIONs have a strong magnetic moment, particularly those composed of Fe_3O_4, where Fe^{3+} ions have 5 unpaired electrons. Because of their single domain properties, magnetic manipulation of SPIONs is more effective than that of larger, multiple-domain ferromagnetic particles. The transition from single domain SPIONs to single and multiple domain ferromagnetic nanoparticles occurs in a size-dependent manner, where the intensity of the applied magnetic field required to reduce the magnetization to zero (coercivity) also increases (**Figure 1.4**). The size at which SPIONs become ferromagnetic nanoparticles occurs above ~16 nm (Mohapatra et al., 2018), which will then become multiple domain above a size of ~76 nm (Li et al., 2017).

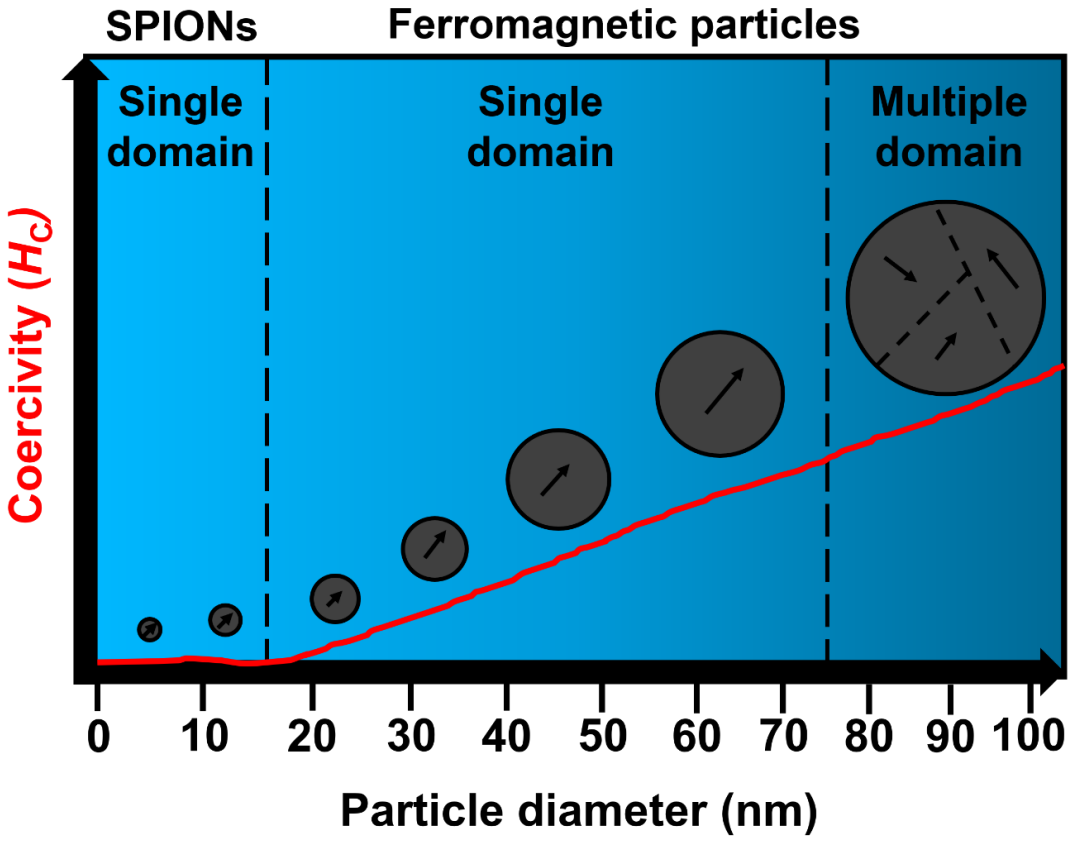

Figure 1.4. Schematic of the transition from single domain SPIONs to multiple domain ferromagnetic particles: Adapted figure (Sung Lee et al., 2015), where arrows represent electron flip orientation within nanoparticles of increasing size. Red line represents coercivity (H_C), where *Hc* represents oersted or ampere/meter, relative to increasing particle diameter (nm).

1.2.1.1.1.1. SPION synthesis

There are a variety of approaches reported for the preparation of SPIONs. The size, shape and surface chemistry properties of SPIONs differ depending on the method and conditions used, all of which affect magnetic behaviour. Therefore, it is important to consider the most suitable approach for generating SPIONs designed with specific applications in mind. A preference desired across all preparation techniques is to produce samples with high size and shape uniformity.

The most commonly employed approach is coprecipitation by nucleation to generate seeds that will subsequently grow to form SPIONs. This method can be further sub-divided into two main types, the first involving mixing iron salt precursors in the presence of a base (**Scheme 1.1**). For instance, it has previously been shown that nanoparticle samples can be generated within a size range containing SPIONs using different iron salts, including $FeSO_4$ and $FeCl_2$, and potassium hydroxide as a base (Sugimoto and Matijević., 1980). The other approach, involves ageing mixtures of ferrous and ferric hydroxides prepared stoichiometrically in aqueous solution. These approaches yield water-soluble SPIONs, making them ideal for biomedical applications through surface functionalisation with biocompatible molecules.

$$2Fe^{3+} + Fe^{2+} + 8OH^- \longrightarrow Fe_3O_4\downarrow + 4H_2O$$

Scheme 1.1. Example of a coprecipitation synthesis of SPIONs involving iron salt precursors in the presence of base.

Another approach for generating SPIONs is done using microemulsions which are stable isotropic dispersions of two immiscible liquids containing nano-sized droplet domains. Water-in oil systems are commonly employed for generating water droplets to serve as aqueous nanoreactor environments to synthesise SPIONs within. Amphiphilic surfactants are mixed into the system to lower the surface tension between water and oil which causes solution transparency. SPION size can therefore be tuned by modulating the size of the water droplets (Laughlin, 1976). SPIONs generated using this approach would likely require purification from the surfactant if they were being prepared with protein molecules for biological applications due to protein functional sensitivity to surfactants. The use

of anionic surfactant sodium dodecyl sulfate (SDS) for example, will bind to proteins, unfold them and give them a uniform negative charge. Consequently, this causes the protein to lose its 3-dimensional structure and consequently its functional properties.

SPIONs can also be generated through thermal decomposition of iron carbonyl complexes at high temperatures, followed by oxidation in air. Often this is carried out in the presence of hot organic surfactants to improve size distribution and dispersity. As with using microemulsion approaches, SPION preparation with proteins would need to be carried out after particle isolation since the extreme temperatures required during the synthesis would be detrimental to protein function. Additional ligand exchange steps would also be required to functionalise the organic surface with a layer to improve aqueous solubility for biological applications.

1.2.2. Induction heating

Magnetic nanoparticles are able to generate heat in the presence of an alternating/oscillating magnetic field which has potential in various biomedical applications. To utilise these magnetic properties effectively it is important to understand the process by which conductive materials generate heat as a consequence of electromagnetic induction. Induction heating is a process where under electromagnetic induction, electrically-conducting materials, such as metals, will generate heat through eddy currents in the material. Eddy currents represent loops of electrical current induced by an alternating magnetic field. Alternating magnetic fields are generated using an electromagnet and an electric oscillator passing a high frequency alternating current through the electromagnet. The eddy currents that arise by penetration of an alternating magnetic field, will flow through the resistance of the material and generate heat by Joule heating. Joule heating arises from interactions between charge carriers, such as electrons, and the body of the conductor, generally atomic ions. The charge carriers gain kinetic energy as a result of the voltage difference between the points of the conductor, which generates an electric field and accelerates the charge carriers towards the field. The charged particles scatter as a result of collisions with ions in the conductor, where their direction of motion then becomes scattered instead of aligned with the field. This scattering of particles constitutes thermal motion, brought about by a conversion of electrical energy into thermal energy.

1.2.2.1. SPION magnetic heating

Nanoparticle magnetic heating has largely been employed as a hyperthermia therapy in cancer research for localised heat-induced death of cancerous tissues. Specifically, the energy supplied by an alternating magnetic field displaces the magnetic moment from the preferred orientation and the subsequent relaxation to equilibrium releases thermal energy into the environment. The rate at which SPIONs undergo magnetic heating is relative to their specific absorption rate (SAR), which is the rate at which energy is absorbed by an electromagnetic field. SAR is an important property that influences heating and is affected by factors such as particle size and composition (Carrey et al., 2011). Typically for hyperthermia applications with SPIONs, an alternating magnetic field strength up to 200 Oe is operated at a frequency of around 100 kHz (Atkinson et al., 1984).

There are various mechanisms by which SPIONs undergo magnetic heating; susceptibility loss, hysteresis heating and stirring, where the dominating mechanism has been shown to be influenced significantly by particle size (**Figure 1.5**) (Vallejo-Fernandez et al., 2013). These mechanisms are described for particles within a size limit that defines them as single domain SPIONs that transition to single domain ferromagnetic particles (**Figure 1.4**)**.** The susceptibility loss mechanism occurs with SPIONS up to ~13 nm in size (Vallejo-Fernandez et al., 2013), based on two relaxation times associated with Néel relaxation and Brownian/random rotation of the particles as they are in a liquid environment (Pankhurst et al., 2003). This is brought about through rapid switching of the magnetic moment orientation within the alternating magnetic field, (Vallejo-Fernandez et al., 2013). Particles between 13-20 nm exhibit hysteresis heating, which is the most efficient heating mechanism of the three described. This arises due to magnetic hysteresis where remanent magnetisation occurs that is characteristic of ferromagnetic particles as the size transitions across the superparamagnetic-ferromagnetic boundary. Over 20 nm, particles are unable to switch in the field where the majority of particles are not aligned with field and viscous heating as a function of stirring will occur (Vallejo-Fernandez et al., 2013). This mechanism is more pronounced for aggregated particles and likely accounts for anonymously large heating effects previously reported (Hergt et al., 2008). Heating measurements were recorded in **Figure 1.5** where K represents units of energy per cm cubed.

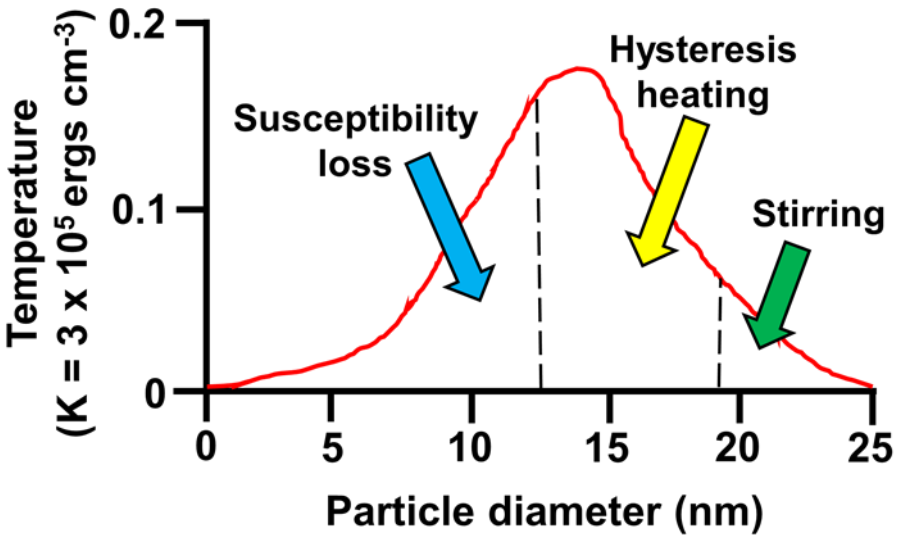

Figure 1.5. Mechanisms of nanoparticle magnetic heating: Adapted figure (Vallejo-Fernandez et al., 2013) where arrows (blue = susceptibility loss, yellow = hysteresis heating, green = stirring) denote magnetic heating mechanisms for particle size ranges (nm) between black dotted lines. Temperature is represented as K, where K = 3 x 10^5 ergs cm^{-3}.

1.3 Nanomedicine

Using the various properties of nanoparticles for biomedical applications falls into the bracket of nanomedicine, which can be described as the medicinal application of nanotechnology. Nanomaterials are useful tools for both *in vivo* and *in vitro* biomedical studies as they can be functionalised with biocompatible molecules and are suitably sized to interface with biological structures and molecules. These features allow for a broad range of biomedical applications including drug delivery, imaging and sensing. Current challenges in nanomedicine are largely related to safety, in terms of toxicity and environmental concerns, as well as efficacy with regards to specific, localised applications. Selecting the most appropriate materials to use biomedically is therefore of the upmost importance.

1.3.1. SPIONs in nanomedicine

The use of magnetite and maghemite SPIONs in nanomedicine are highly preferential as they have shown good biocompatibility in previous work (Soenen et al., 2012). It has been highlighted previously that surface coating is important for solubility and biocompatibility using human mesothelium and murine fibroblast cell lines with SPIONs (Brunner et al., 2006). Also, using the contrast properties of SPIONs has been an effective tool to monitor both stem and dendritic cells in real-time by magnetic resonance tomography (Bulte and Kraitchman, 2004).

One of the most prominent areas of research for SPION applications in nanomedicine is magnetic heating treatments of cancer. This treatment is referred to as magnetic hyperthermia, where SPIONs in a ferrofluid are injected into a tumour site before exposure to an alternating magnetic field to cause heating (**Figure 1.6**). The temperature distribution as a consequence of magnetic heating has been shown to help destroy cancerous cells within tumours (Javidi et al., 2014, Heydari et al., 2015). The extent of magnetic heating can be modulated based on the SPION concentration and parameters of the alternating magnetic field, providing control over the application.

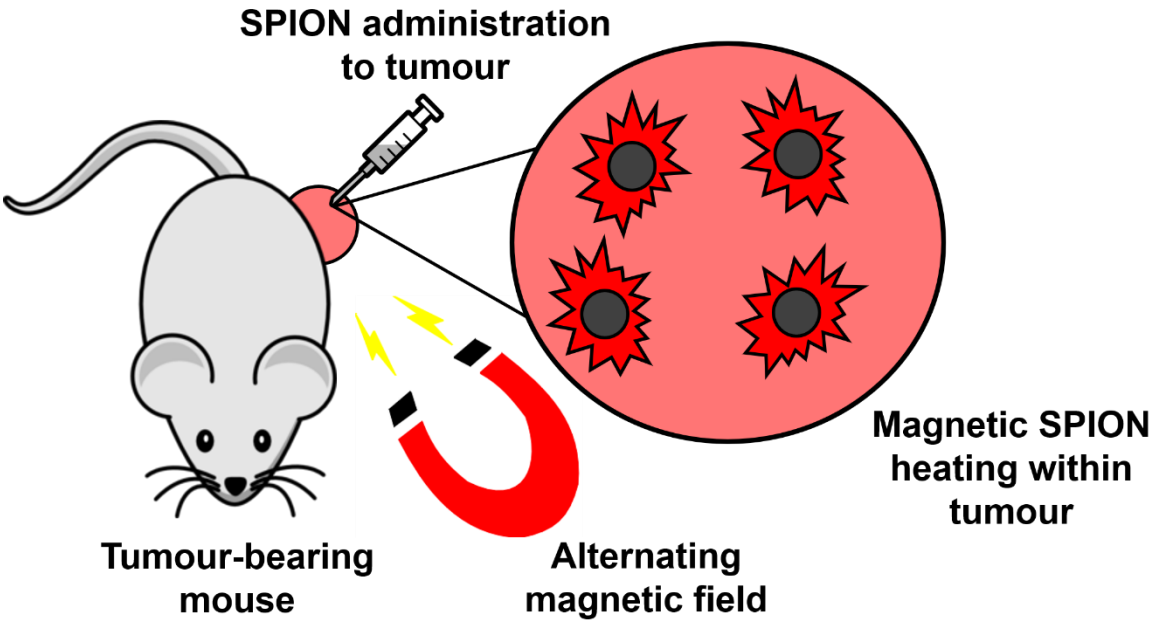

Figure 1.6. Magnetic hyperthermia treatment of a tumour-bearing mouse using SPIONs exposed to an alternating magnetic field

1.3.2. Drug delivery

One of the largest applications in nanomedicine is using nanoparticles for the delivery of molecules to specific cells and tissues. Nanoparticles offer a promising vehicle to carry biomolecules to niches of interest due to their small size which makes them evasive from immune responses and allows for effective biodistribution. Indeed, it has been shown previously that nanoparticles below 200 nm in size can evade clearance by phagocytosis (van Rijt et al., 2014) and that nanocarrier size below 150 nm is essential for entry and exit from capillary circulation (Blasi et al., 2007). The rate at which cellular uptake of nanoparticles occurs depends which mechanism is employed and relates to the specific properties of the particles. For example, particles between sizes of 0.5 – 5 µm are taken up commonly through macropinocytosis or circular dorsal ruffles where cells simply envelop materials into the cytoplasm. By contrast, a slower, more regulated mechanism for the uptake of smaller particles between 20 – 500 nm is Clathrin-mediated endocytosis. Scavenger, mannose and Toll-like receptors are known recognition and induction mechanisms for the process, involving formation of clathrin pits in the cell membrane that wrap and pull their cargo into the cell (Gustafson et al., 2015).

The surface of nanoparticles is often functionalised with polymers to improve bio-suitability and act as a layer for biomolecule entrapment and release. Further surface functionalisation can confer nanoparticle targeting to desired sites by the conjugation of molecules, such as antibodies, that will recognise cell- and tissue-specific markers. Functionalised nanoparticles are designed to deliver biomolecules specifically with minimal off-target effects by depositing an appropriate dose of the active agent at morbid regions only. Ongoing research in this field is continuously attempting to better understand and optimise the design of nanomaterials for the most effective biodistribution, targeting and biomolecule release whilst reducing any adverse nanoparticle toxicity. Many studies have highlighted the rationale behind nanoparticle design for specific applications, for example generating ultra-small 10.5 nm polyethylene glycol (PEG)-coated gold nanoparticles to bypass the extracellular matrix and deliver drug molecules to endothelial cells (Cheng et al., 2018). PEG was selected as a suitable material for nanoparticle coating as it increases biocompatibility and reduces systemic clearance (Kumar et al., 2013). Polymer shells coated onto the surface of

nanoparticles can be significantly larger than the particles themselves, but this is ultimately dependent on the structural properties of the polymer, particularly the chain length. A schematic of a functionalised nanoparticle for targeted biomolecule delivery that has a polymer shell significantly larger than the nanoparticle core can be seen in **Figure 1.7**.

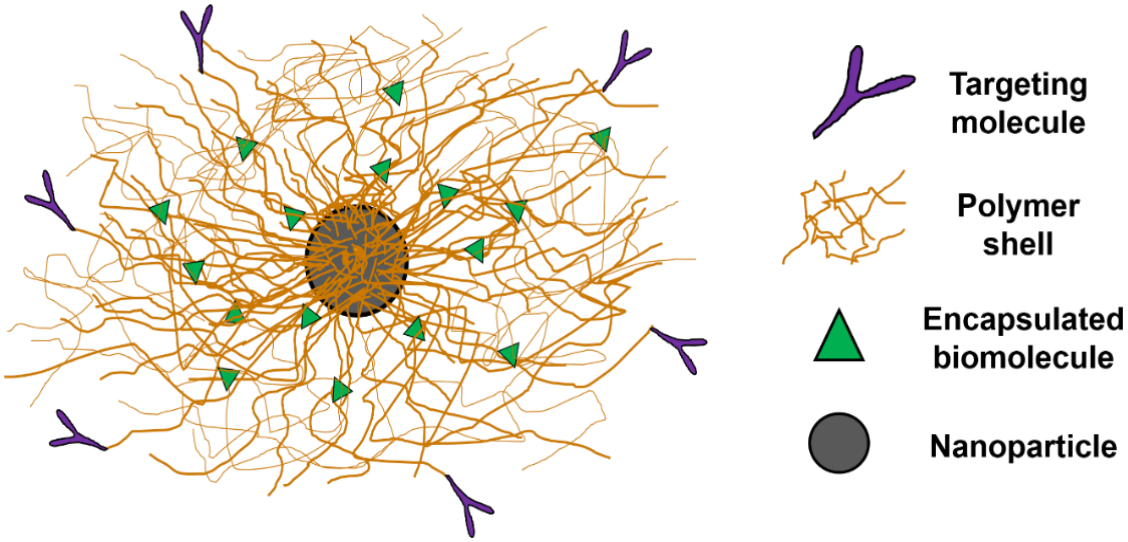

Figure 1.7. Schematic of functionalised nanoparticle for targeted biomolecule delivery: Grey circle in centre represents nanoparticle core with a polymer shell (orange lines). Within polymer shell are encapsulated biomolecules (green triangles) and on the polymer shell surface is a conjugated targeting molecule (purple shape).

1.3.2.1. SPIONs in drug delivery

SPIONs have been used extensively in the field of drug delivery because of their biocompatibility and potential for surface functionalisation with polymer layers for biomolecule encapsulation. Various studies have been conducted investigating surface coating with different types of natural and synthetic polymers, such as chitosan and PEG respectively, which have been shown to significantly reduce SPION oxidation, agglomeration and toxicity (Guo et al., 2017, Huang et al., 2017). For drug delivery applications, such studies highlight the importance of SPION polymer coating to improve stability and biocompatibility.

Some studies have shown progressive biomolecule release from SPION-polymer networks. This has been shown using composites of SPIONs and starch copolymers that could release the small molecule $H_3PW_{12}O_{40}$ (HPA) over time upon gradual hydrolysis of the polymer (Hamidian and Tavakoli, 2016). However, the disadvantage of this approach is the lack of control over drug release which, in a biomedical application, would likely result in drug loss during delivery to a target site. This highlights the attractiveness of using stimuli-responsive polymers with SPIONs as a tool for triggered biomolecule release. Also, the disadvantage of using larger composite nanomaterials is that there is a significantly reduced surface area compared with nanoparticles, which lowers the efficiency of biomolecule encapsulation and release. This can be improved markedly by designing functionalised SPIONs that have a polymer shell grafted onto the surface.

Focus has largely been directed towards using SPIONs for the delivery and release of simple molecules such as drugs or short peptides over those that are more complex, like proteins. This is perhaps due to the inherent functional sensitivity of proteins to factors such as temperature and pH, which are common triggers to release biomolecules from SPIONs coated with stimuli-responsive polymers. Stimuli-responsive polymers are very appealing for releasing encapsulated biomolecules from functionalised SPIONs in a triggered manner. Their use in nanomedicine has gained significant interest. For example, a study showed that using SPIONs encapsulated into photo-sensitive polymer polydopamine (PDA) could load a heat shock protein 70 (HSP70) inhibitor and release it under near infrared (NIR) radiation through weakening of the polymer π-π and hydrogen bonds (Guo et al., 2017).

Additionally, many studies have utilised the magnetic properties of SPIONs for targeting to sites of biomedical interest. For example, a study generated SPIONs coated with graphene oxide and a surface-grafted polymer shell consisting of chitosan and PEG. These particles could release the encapsulated anti-cancer drug Doxorubicin (DOX) in a pH-triggered manner which showed enhanced cytotoxicity to U87 cancer cells that was enhanced following magnetic targeting (Huang et al., 2017). Using pH as a trigger for biomolecule release is useful for applications where the environmental pH at the delivery site permits this approach. However, in a physiological context, this may not be the case for all applications where alternative triggers for biomolecule release may be more appropriate.

1.4. Temperature-responsive polymers

For nanoparticle applications, particularly involving drug delivery, it is often desirable to have polymer shell coatings to improve biological suitability. The use of a stimuli-responsive polymer is attractive for drug delivery applications as a triggered mechanism to release molecules trapped within a polymer shell. Temperature-responsive polymers are a specific group of stimuli-responsive polymers that exhibit a drastic change of their physical properties in response to temperature. Generally, the significant property that is affected in response to temperature is the polymer solubility in a given solvent. There are two sub-classes of temperature-responsive polymer which are distinguished based on whether their miscibility gap is found at high or low temperatures. The most common temperature-responsive polymers are those that show a reduced solubility following an increase in temperature, known as a lower critical solution temperature (LCST). The phase transition that occurs as a result of the temperature exceeding the LCST can cause significant conformational changes in polymer structure following dissociation with solvent molecules. The other, less common sub-class of temperature-responsive polymers are those that show increased solubility following a temperature increase, known as an upper critical solution temperature (UCST). The temperature-responsive properties of these polymers have gained significant interest in nanomedicine, particularly for temperature-triggered release of biomolecules in drug delivery applications.

1.4.1. Coil-globule transition

Upon a phase transition, many temperature-responsive polymers exhibit a coil-globular transition following macromolecular collapse from an expanded coil state, to a collapsed globule state, or vice versa. During this transition, a significant proportion of solvent is either expelled, or associated with the polymer for transition to a globule or coil, respectively. Specifically, polymers that morphologically behave as chains can be regarded as exhibiting theta solvent behaviour. For LCST polymers, above the LCST or theta point, a temperature-induced collapse occurs which is associated with an unfavourable entropy/randomness of mixing (Simmons and Sanchez, 2008). The enthalpy/energy in the system is high below the LSCT due to hydrogen bonding between solvent and polymer molecules. This also results in a loss of entropy where random mixing of solvent molecules is prevented as a consequence of hydrogen bonding to the polymer. However, upon an increase in temperature above the polymer LCST, loss of hydrogen bonding between solvent and polymer molecules causes an increase in entropy as water molecules are expelled from the polymer and revert to a disordered/randomised state. Previous studies have modulated pH and solution ionic strength to show that polyelectrolytes can drive charge effects which impact upon the transition point through electrostatic disruption between solvent and polymer molecules (Ulrich et al., 2005). The polymer structural change following a phase transition has great potential as a mechanism to release entrapped biomolecules for delivery applications, particularly when heated using the heating properties of magnetic nanoparticles. A schematic of the coil-globule transition following a temperature increase above polymer LCST can be seen in **Figure 1.8**.

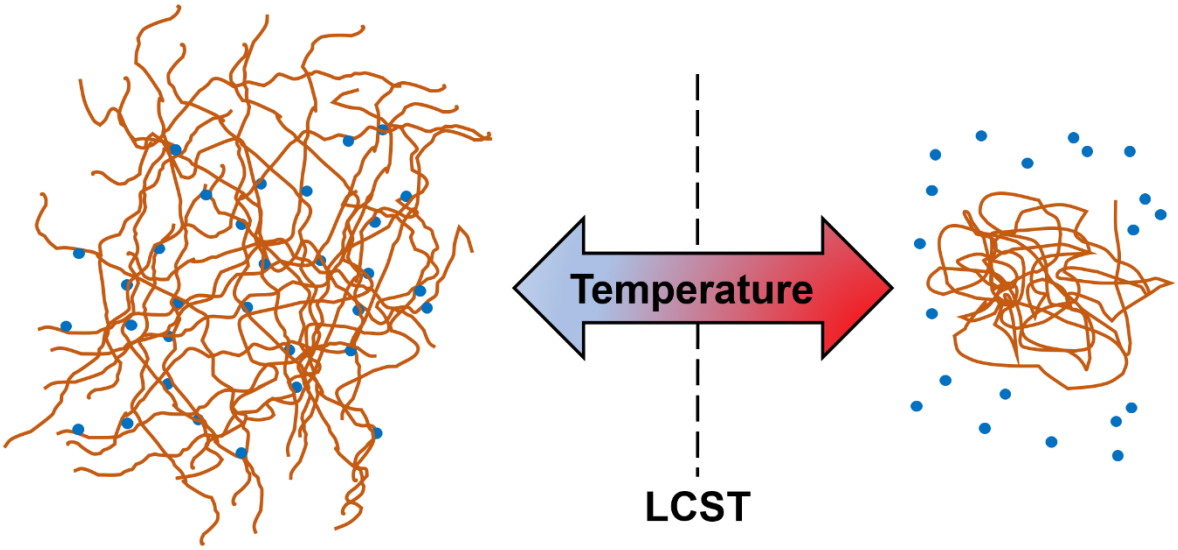

Figure 1.8. Schematic of coil-globule transition of an LCST-sensitive polymer: Polymer (orange lines) with coil morphology (left) interacting with solvent molecules (blue dots) below the LCST. Polymer with globule morphology (right) dissociated with solvent molecules above the LCST.

1.4.2. Polymer synthesis

To generate polymers suitable for desired applications, it is important to consider the most appropriate synthetic methods available. Polymers are synthesised using a broad range of approaches, including anionic, cationic and radical polymerisation. Radical polymerisation approaches involve three common steps; initiation, propagation and termination. Initiation involves the initial double bond break of monomer units by radicals to generate a radicalised product. This is commonly facilitated by an initiator molecule to generate an active centre from where a polymer chain is produced. Propagation of the polymer chain will subsequently occur where the radicalised monomer units will react with new monomers by transferring the reactive unit to form polymer chains by the successive addition of monomers. Polymerisation then ends with termination, where the formation of reactive monomers ceases thereby ending further polymer chain growth. A reaction scheme of radical polymerisation can be seen in **Scheme 1.2.**

Some of the main types of radical polymerisation are free radical polymerisation (FRP) and reversible-deactivation radical polymerisation (RDRP). Both these approaches are types of chain-growth polymerisation. This involves a chain reaction in which the growth of a polymer chain proceeds exclusively by reaction(s) between monomer(s) and active site(s) on the polymer chain with regeneration of the active site(s) at the end of each growth step (Penczek & Moad, 2008). These approaches differ since during propagation in RDRP radicals are deactivated reversibly, bringing them into active/dormant equilibria, whereas during propagation in FRP the polymer chains are constantly active (Jenkins et al., 2009). Polymer properties differ greatly depending on the synthetic approach used and therefore understanding each mechanism is important for generating desired polymers.

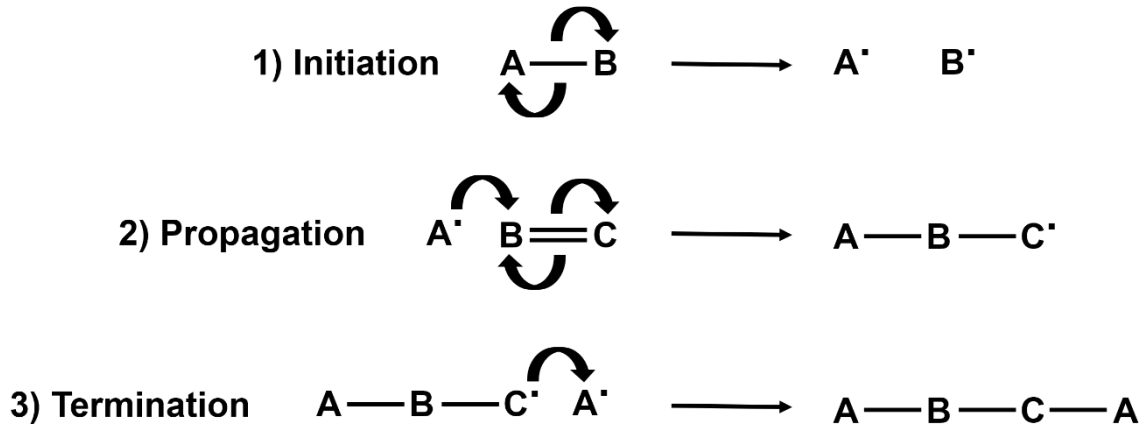

Scheme 1.2. Mechanisms of initiation, propagation and termination steps of radical polymerisation: Where A-B represents initiator molecule, A·/B·/C· represents radicals, B=C represents double bond of monomer molecule, A-B-C· represents active growing polymer chain, A-B-C-A represents terminated polymer chain.

1.4.2.1. Free radical polymerisation (FRP)

FRP is a very commonly employed approach that is used to generate a variety of different polymers and composites. This approach was first described in 1920 by Staudinger, where he proposed that trivalent carbon atoms, now known as radicals, participated with monomers to generate long chain molecules (Staudinger, 1920). Staudinger later postulated that the chain ends contain “free valences” which are unstable and will grow until inactivation (Staudinger, 1926). The activation of monomers by “catalysts” for propagation to form polymers was suggested by Schulz (Schulz, 1935). The kinetics of the vinyl polymerization as a chain reaction with participation of free radicals was first described by Flory, where he proposed that two active chains can be terminated only by bimolecular combination or disproportionation reactions (Flory, 1937). These early postulations laid the foundations for the understanding and development of FRP, a highly non-specific and facile procedure, making it one of the more versatile forms of polymerisation.

Despite its versatility, FRP has drawbacks, particularly regarding premature chain termination due to the highly non-specific nature of the polymerisation. There are several ways in which polymer chains can prematurely terminate, one of which being the combination of two active, propagating chains to form a non-active polymer. Also, this combination can occur between an active propagating chain and an initiator radical. Slower propagation can occur through interaction with impurities, notably oxygen, where active chains will react with molecular oxygen to form an oxygen radical that is significantly less reactive. Due to the nature of termination with FRP, this restricts control somewhat over polymer molecular weight distributions, chain architecture and composition, which may generate undesirable polymers for certain applications.

1.4.2.2. Reversible-deactivation radical polymerisation (RDRP)

RDRP is an approach that is often described as more of a “living” polymerisation than FRP, in that premature chain termination is far less common, although it is still a possibility (Jenkins et al., 1996). RDRP can be described as chain polymerisation propagated by radicals that are deactivated reversibly, bringing them into active/dormant equilibria (Jenkins et al., 2009). This procedure originated in the late 20th century, where it was observed that the addition of specific components during polymer chain propagation could reversibly react with the radicalised chains and place them temporarily in a dormant state (Moad and Rizzardo, 1995). This prolongs the lifetime of growing polymer chains since at any given instance, where the majority of radicalised polymer species are in an inactive, dormant state but are not irreversibly terminated. Only a small proportion of chains are active and propagating at a rapid rate of interconversion between dormant and active forms. This approach provides significantly improved control compared to FRP over polymer molecular weight and distribution since theoretically all chains are growing at a similar rate. Undesired chain termination through combinations is still possible, but the more likely cause of chain termination is an absence of monomer which is suitable for generating polymers with a desired molecular weight and narrow distribution. Also, an advantage of this approach is the ability to selectively end-functionalise polymer chains, which allows for their use in certain applications, such as grafting to nanoparticle surfaces.

Some of the most commonly employed RDRP approaches are nitroxide-mediated polymerisation (NMP), reversible addition-fragmentation chain transfer (RAFT) and atom transfer radical polymerisation (ATRP). NMP involves the use of an alkoxyamine initiator to generate polymers with well controlled stereochemistry and a low polydispersity index (PDI). One of the early studies using this method showed that NMP of styrene could yield a polymer with a low PDI and predictable molecular weights based on the ratio of nitroxide and monomer (Georges et al., 1993). The development of NMP sparked widespread interest due to its simplicity and capability to generate a broad range of materials, including block copolymers and surface-grafted polymer brushes. RAFT polymerisation was first described in 1998 and has since been widely used in research as a process without requirement for metal catalysts and with the capabilities to mediate the

polymerization of a wide range of monomers (Chiefari et al., 1998). ATRP is widely used due to its flexibility regarding choice of end groups and catalytic species, which has led to the synthesis of polymers with a range of architectures and compositions. The fundamental mechanisms of NMP, ATRP and RAFT polymerisation approaches can be seen in **Scheme 1.3**.

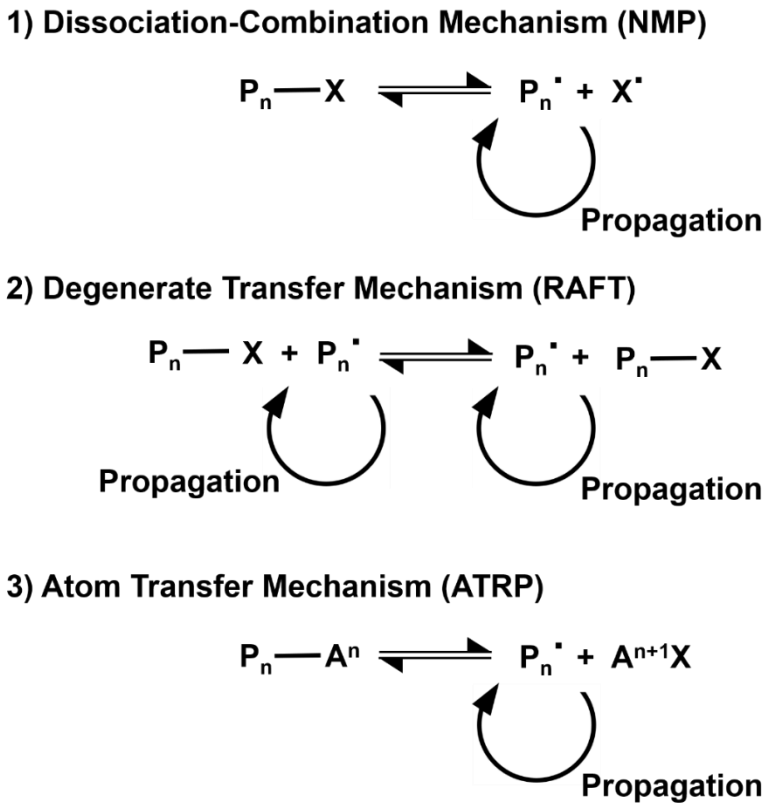

Scheme 1.3. The fundamental mechanisms of commonly used RDRP approaches: 1) Dissociation-Combination (NMP) **2)** Degenerate Transfer (RAFT) **3)** Atom transfer. Where P_n represents dormant polymer, X represents initiator molecule, $X^{\cdot}$ represents radicalised initiator, $P_{n^{\cdot}}$ represents active, propagating polymer and A represents atomic transfer, Adapted from Shipp (2011).

1.4.2.2.1. ATRP

ATRP is a type of RDRP that involves the formation of a carbon-carbon bond, in which the deactivation of radicals involved occurs through reversible atom transfer (Jenkins et al., 2009). This approach was independently reported on by different research groups in 1995 (Kato et al., 1995, Wang and Matyjaszewski, 1995).

ATRP generally involves a transition metal catalyst, such as copper, and an alkyl halide initiator. During the process, activation of the dormant species occurs through the transition metal complex which generates radicals by one electron transfer process. The transition metal complex is simultaneously oxidised to a higher oxidation state which causes a reversible process in which equilibrium is rapidly achieved that largely favours the side with low radical concentrations. The number of initiators present determines the number of polymer chains, where each propagating chain has an equal chance of reacting with monomer units to elongate living/dormant chains. This results in generating polymers with similar molecular weights that are narrowly distributed. A typical depiction of an ATRP reaction can be seen in **Scheme 1.4**.

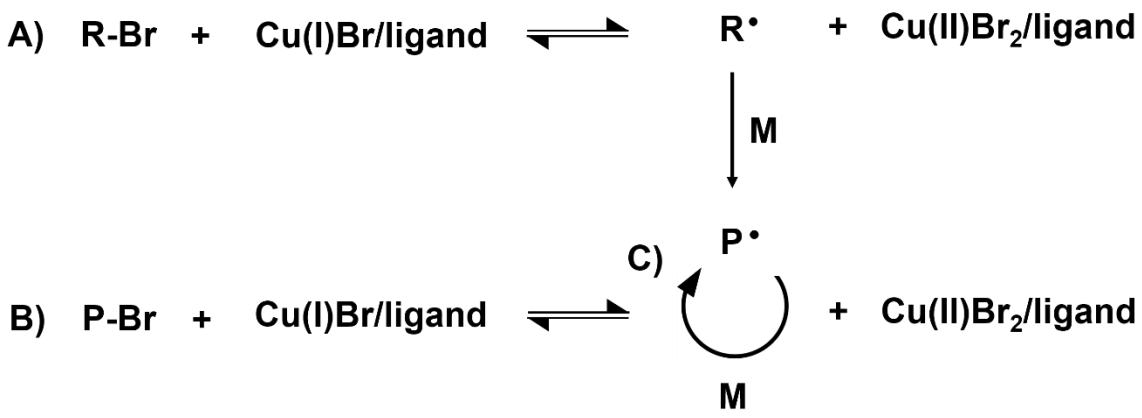

Scheme 1.4. Example of an ATRP reaction using a bromine-based halide alkyl initiator and copper bromide-based transition metal catalysts: Where R-Br is bromide-based halide alkyl initiator, Cu(I/II)Br/ligands are copper bromide-based transition metal/ligand complexes, R· is a generated radical, M is the monomer, P-Br is the dormant polymer species and P· is the active, propagating polymer species. **A)** Initiation step **B)** Equilibrium with dormant species **C)** Propagation.

As with any radical polymerisation reaction, the crucial constituents are monomer, initiator, catalyst, ligand and solvent. Firstly, monomers used in ATRP reactions generally have substituents that are able to stabilise propagating radicals, such as styrenes (Patten and Matyjaszewski, 1998). The rate of polymer propagation is relative to the unique properties of specific monomers. It is therefore essential to optimise reaction conditions along with the other components to ensure that the concentration of dormant species is greater than the propagating radical without being insufficient and leading to the reaction slowing or halting.

The equilibrium constant between the dormant and active species is determined by the catalyst, which makes it the most important component of ATRP. Catalyst concentration determines the fine balance between inhibiting or slow polymerisation through a low equilibrium constant, and a wide molecular weight distribution due to a high equilibrium constant (Matyjaszewski and Tsarevsky, 2009). Important criteria for selecting catalysts include high affinity for halogens by the metal centre, as well as no significant side reactions such as irreversible coupling with propagating radicals. Copper is a widely selected catalyst as it has shown high versatility in mediating polymerisation with a range of monomers. Pyridine-based ligands are often selected which generally form a complex with the transition metal catalyst to improve its solubility, such as a tris[2-(dimethylamino)ethyl]amine (Me_6TREN) and CuBr (copper bromide) transition metal/ligand complex (Lu et al., 1996).

The amount of initiator determines the number of polymer chains, where rapid initiation leads to narrow molecular weight distributions as a result of consistent propagating chains. Alkyl halides are commonly used initiators, particularly alkyl bromides, as they are more reactive than alkyl chlorides, where both offer good molecular weight control (Matyjaszewski and Tsarevsky, 2009).

Finally, since multiple components are required for ATRP that will exhibit different solubilities, selecting an appropriate solvent is essential for efficient polymerisation. Various polar solvents have been commonly used, such as water and methanol, as well as non-polar solvents like toluene and anisole.

1.4.3. Characterisation of LCST properties

Following the synthesis of temperature-responsive polymers it is important to characterise their phase transition properties to ascertain the extent of phase separation and specific temperature this occurs at. There are numerous methods by which the properties of temperature-responsive polymers are characterised. One approach is a measurement of the cloud point, which is the temperature at the onset of cloudiness or inflection of a transmittance curve (**Figure 1.9**). There is no definitive approach for determining the cloud point across all systems and is often either determined visually, or quantitatively using turbidimetry by measuring the loss of light transmittance at the cloud point temperature. Previous studies have shown that different structural parameters of polymers can influence the cloud point, such as hydrophobic content, architecture and molar mass (Ward and Georgiou, 2010, Georgiou et al., 2004).

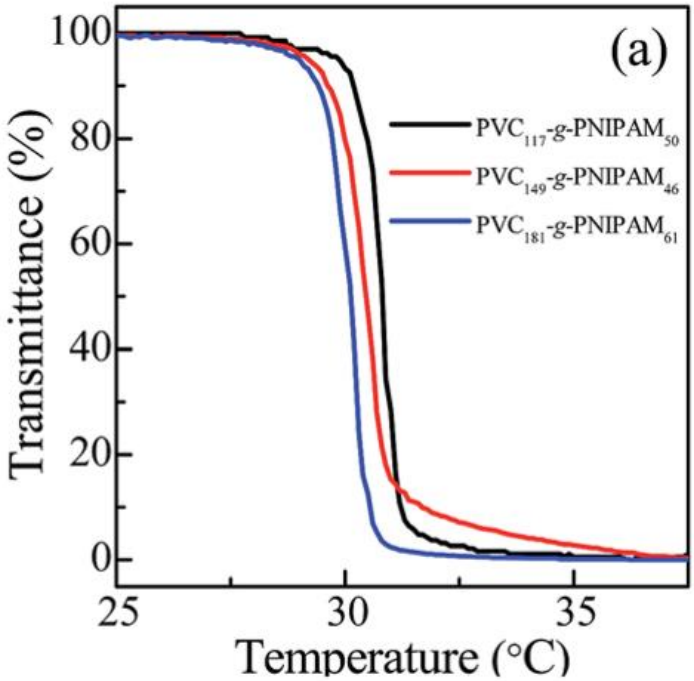

Figure 1.9. Example of a temperature-transmittance curve for temperature-responsive polymers (Liu et al., 2015).

Also, an important consideration for possible applications is the extent of phase transition, which is represented by the polymer content in each phase after temperature-responsive separation. For most applications, a sharp phase transition is desirable with a phase separation of pure solvent and pure polymer. This however is often not the case, for example it has previously been shown that polystyrene dispersed in solvent cyclohexanol has a partial phase separation upon cooling from 25^{o}C - 20^{o}C with a polymer-poor and polymer-rich phase (Schultz and Flory, 1952). Phase transition sharpness is related to the extent of phase separation and is influenced by molecular properties of the polymer such as dispersity and also composition, particularly regarding copolymers, which may exhibit a range of cloud points (Seuring and Agarwal, 2012).

1.4.4. Applications of temperature-responsive polymers

The properties of temperature-responsive polymers make them very attractive for a variety of applications in cell biology and biochemistry. One useful property is their capacity to be functionalised, which has been utilised in bioseparation techniques by covalently attaching moieties that bind specific molecules. Subsequently, the polymer-biomolecule conjugate can be separated through temperature-induced precipitation and purified by filtration or centrifugation. This has previously been shown in a study where human immunogammaglobulin was purified using a protein A-polymer conjugate (Chen, 1990).

Another biochemical application of temperature-responsive polymers is their use in the stationary phase of liquid chromatography. It has been shown that the extent of separation can be enhanced using not only the temperature-sensitive polymer properties, but also by adding moieties that affect hydrophobic or electrostatic interactions (Ayano and Kanazawa, 2006).

Additionally, the swelling properties of temperature-responsive polymers that exhibit a coil-globule transition (**Figure 1.8**) have been utilised for molecular “catch and release” techniques. This has been utilised particularly for temperature-triggered drug delivery applications where polymers in the swollen state have been shown to readily release incorporated drugs by diffusion (Dinarvand and D'Emanuele, 1995). This mechanism has also been employed in a more sophisticated manner for other approaches such as molecular imprinting by creating template-shaped cavities in polymer matrices for molecular recognition (Suedee et al., 2006). A schematic of drug release using nanoparticles functionalised with temperature-responsive polymers for drug delivery applications can be seen in **Figure 1.10**.

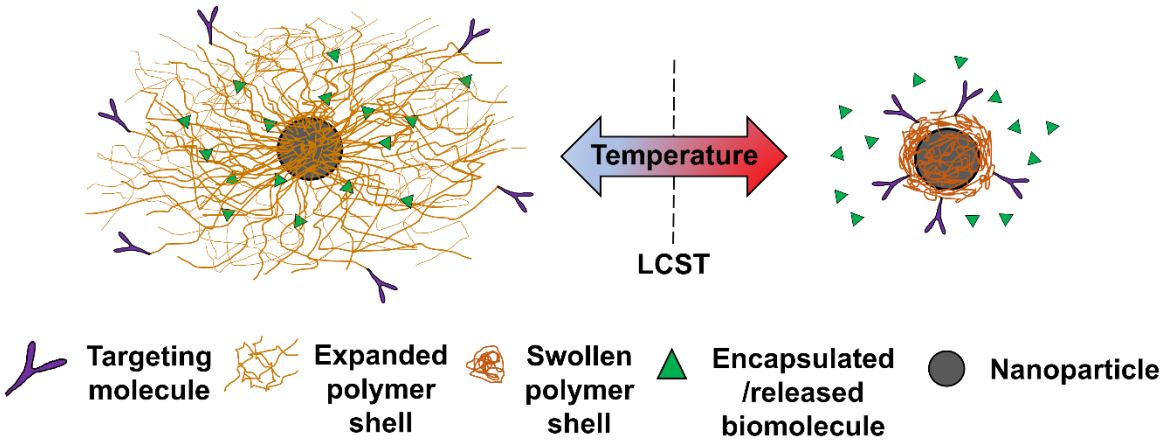

Figure 1.10. Temperature-responsive polymer "catch and release" of drug molecules from functionalised drug delivery nanoparticles: Schematic shows temperature-responsive polymer shell in the expanded form below phase transition temperature that can catch biomolecules (left) and in the collapsed form above the transition temperature that will release biomolecules (right). Grey circle in centre represents nanoparticle core with a polymer shell (orange lines). Within polymer shell are encapsulated biomolecules (green triangles) and on the polymer shell surface is a conjugated targeting molecule (purple shape).

Also, temperature-responsive polymers have been used in cell biology for tissue regeneration and engineering purposes. One application has been to transfer the polymer temperature-sensitive properties to surfaces for cell culture by generating films or covalent attachment. It has been shown that cells can be detached from surfaces functionalised with temperature-responsive polymers in a temperature-triggered manner (Lee and von Recum, 2010). Because cell adhesion to surfaces is highly dependent on the hydrophilic/hydrophobic interactions, utilising the temperature-responsive polymer properties allows modulation of this environment which causes detachment. This has been shown to be non-destructive to cells and provides an alternative to conventional enzymatic detachment.

Also, in tissue engineering, temperature-responsive polymers have been used as physical gels, rather than covalently linked, to produce thermoresponsive injectable gels. This approach has been used to effectively prepare injectable cell solutions at room temperature, for example by delivering stem cells to rats *in vivo* (Borden et al., 2010). One of the challenges when generating injectable solutions is tuning the polymer properties to allow for gel formation which is significantly affected by the molecular composition, architecture and molar mass (Ward and Georgiou, 2010).

1.4.5. Poly(*N*-isopropylacrylamide) (PNIPAM)

One of the most extensively studied and characterised temperature-responsive polymers is PNIPAM (**Figure 1.11**). PNIPAM was first characterised in terms of its temperature-responsive properties in 1968 by Heskins and Guillet, where they established its unique behaviour in aqueous solutions at an LCST of 32^{o}C (Heskins and Guillet, 1968). From the 1980's onwards, PNIPAM has gained a significant amount of research interest after realisation of its potential for a variety of applications (Schild, 1992).

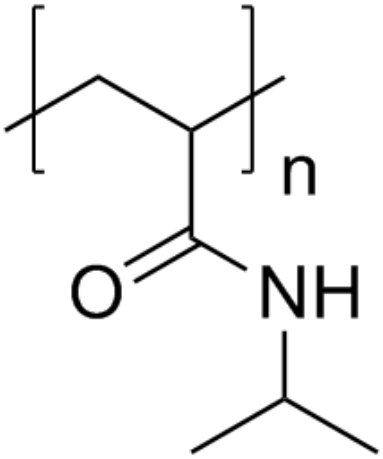

Figure 1.11. Chemical structure of PNIPAM

In aqueous solution, PNIPAM exhibits a coil-globule transition above its LCST, where it loses around 90% of its hydrated volume after going from a swollen, hydrated to shrunken, dehydrated state (**Figure 1.8**) (Wu and Wang, 1998). The phase transition of PNIPAM is extremely sharp, with an abrupt hydrophilic-hydrophobic shift at its LCST that is reversible, making it highly attractive for many applications. Specifically, at temperatures below the LCST in aqueous solution, PNIPAM orders itself in solution to hydrogen bond with water molecules. Water molecules will reorient around nonpolar regions of PNIPAM, resulting in decreased entropy. PNIPAM is stably soluble in aqueous solution as the negative enthalpy of hydrogen bonding is dominant. However, after heating above the PNIPAM LCST, the negative entropy of mixing then dominates causing PNIPAM to expel its water content and phase separate. Also, by contrast to many other temperature-responsive polymers, the LCST properties of PNIPAM are not influenced by its molecular mass (Šolc et al., 1995, Afroze et al., 2000). In dilute PNIPAM solutions

at its LCST, the phase transition can be visualised as a shift from clear to cloudiness and in more concentrated PNIPAM solutions precipitation is observed. A pictorial depiction of the PNIPAM phase transition can be seen in **Figure 1.12**.

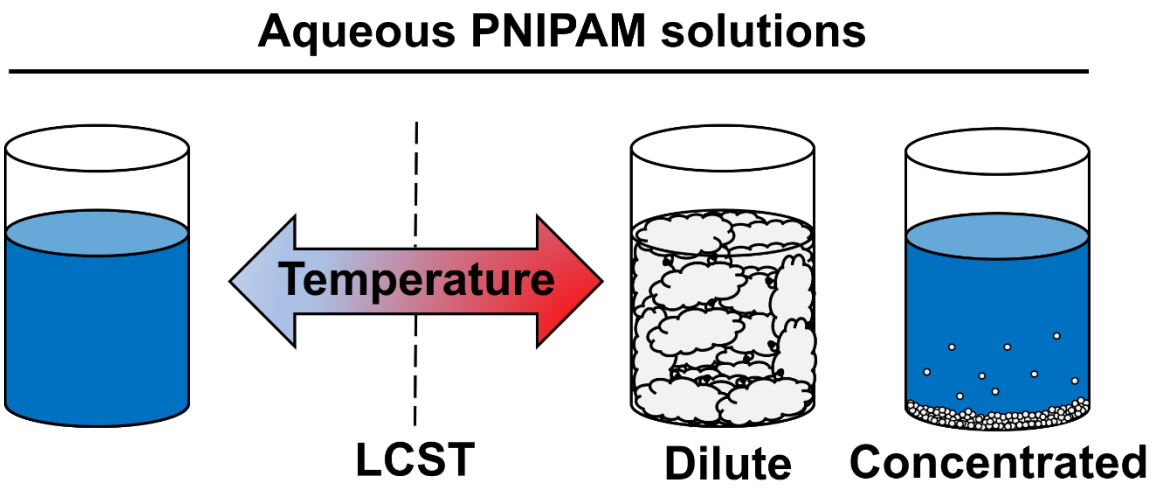

Figure 1.12. PNIPAM temperature-responsive properties above and below its LCST: Schematic of aqueous solutions of PNIPAM below (left) and above (right) the LCST at both concentrated and dilute concentrations. Dilute PNIPAM concentrations above the LCST shows cloudiness and when concentrated shows precipitation. The temperature-responsive properties of PNIPAM occur independently of its molecular weight and concentration at approximately 32^{o}C (Fujishige et al., 1989).

PNIPAM is also favourable for applications due to its ease of synthesis and range of possible modifications. Homopolymers and copolymers of PNIPAM can be readily produced by radical polymerisation approaches. An advantage of copolymerisation with additional monomers is tunability of the polymer LCST, which could improve its suitability for certain applications, such as release of biomolecules above physiological temperatures in drug delivery. Additionally, it is possible to form cross-linked hydrogels with PNIPAM which can be composed of copolymers and even versions with three types of monomer, formed in a process known as terpolymerisation. Also, from a synthetic perspective, PNIPAM can be terminally-functionalised with interesting moieties, such as catechol groups, that can allow for surface coating of nanoparticles.

PNIPAM is an excellent candidate for drug delivery purposes as a tool for temperature-triggered biomolecule release. Solutions of PNIPAM can be loaded

with biomolecules and then subsequently administered *in vivo* before polymer collapse above the LCST to eject the entrapped cargo (**Figure 1.10**) (Huffman et al., 1986). PNIPAM has also been shown to be sensitive to pH as well as temperature in various studies investigating release of different biomolecules, such as ibuprofen (Zhou et al., 2007).

Additionally, PNIPAM hydrogels have been utilised for various tissue engineering applications, most notably as gel actuators on cell culture surfaces. During the PNIPAM hydrophilic-hydrophobic phase transition at its LCST, the expulsion of water molecules causes a physical conformational change and mechanical hinge movement (Zhang et al., 2011). This temperature-sensitive mechanical property of PNIPAM has been employed as a tool for non-destructive cell detachment from modified culture surfaces.

1.4.5.1. PNIPAM drug delivery applications with SPIONs

The use of PNIPAM-based materials with SPIONs, either by polymer grafting directly onto nanoparticle surfaces or generating nanoparticle-polymer composites, has great potential as a drug delivery application. The magnetic heating properties of SPIONs are particularly appealing for use with temperature-sensitive polymers as a mechanism to trigger a phase transition. Using this approach with PNIPAM-based materials loaded with biomolecules is a possible tool for thermally-triggered release of drug molecules. This mechanism theoretically works in the same fashion highlighted in **Figure 1.10**, using magnetic heating to induce a PNIPAM coil-globule transition. Indeed, previous work has shown effective DOX release upon magnetic heating of SPION-PNIPAM composites above the polymer LCST (Purushotham et al., 2009) which has also been reported for anti-cancer drug mitoxantrone (Regmi et al., 2010). Also, it has been shown that SPIONs encapsulated within a PNIPAM network could release the dye molecule rhodamine 6G (R6G) through mesoporous silicon oxide channels in a temperature-sensitive manner (Shen et al., 2016).

Additionally, PNIPAM has also been shown to be sensitive to pH as well as to temperature. For example, previously generated SPION-PNIPAM composites could release DOX more rapidly by lowering the pH from 7.4 to 5.8 (Kaamyabi et al., 2016).

There are numerous studies that report temperature-sensitive drug release from PNIPAM-based materials, however studies investigating release of complex biomolecules, such as proteins, are less common. This is perhaps due to the inherent sensitivity of proteins to temperature which could have a detrimental effect on function and activity. However, there are some reports of protein activity following magnetically-heated release from SPION-PNIPAM materials, for example, vascular endothelial growth factor (VEGF) release from composites upon magnetic heating could activate human umbilical vein endothelial cells (HUVECs) (Dionigi et al., 2014). Therefore, there is probable scope for magnetically- and temperature-responsive nanomaterials as a tool for triggered protein release in other biomolecule delivery applications.

1.4.6. Poly(*N*-isopropylmethacrylamide) (PNIPMAM)

A far less studied temperature-responsive polymer than PNIPAM is PNIPMAM, which is almost identical in structure aside from the presence of an additional α-methyl group on the monomer (**Figure 1.13**). This structural difference has been found to have a marked effect on the polymer temperature-responsive properties, leading to an increased LCST as compared to PNIPAM (Kubota et al., 1990). However, by contrast to PNIPAM, the LCST properties of PNIPMAM have been found to be influenced by the polymer molecular weight and concentration (Djokpé and Vogt, 2001; Rathfon and Tew, 2008). PNIPMAM is readily synthesised through radical polymerisation approaches and its tuneable LCST properties are potentially interesting for thermally-triggered release above physiological temperatures in drug delivery applications. Indeed, some work has been conducted in this area, where PNIPMAM nanogels could encapsulate and release DOX in a temperature-sensitive manner (Peters et al., 2018). Since the field is dominated by PNIPAM-based materials, PNIPMAM is still an emerging presence for drug delivery applications. However, the facile nature of PNIPMAM synthesis and tunability of its LCST make it a promising candidate for developing a temperature-responsive polymer capable of biomolecule release above physiological temperature.

The use of SPIONs coated with polymers like PNIPAM or PNIPMAM, could be an interesting tool for temperature-triggered biomolecule release using magnetic SPION heating. This is a novel approach in the field of tissue engineering where PNIPAM-based materials are largely used as hydrogel surfaces to promote cellular attachment and differentiation. The development of temperature-responsive SPIONs could be potentially useful for the activation of stem cells *in situ* through the delivery and release of growth factors to promote stem cell-driven tissue regeneration.

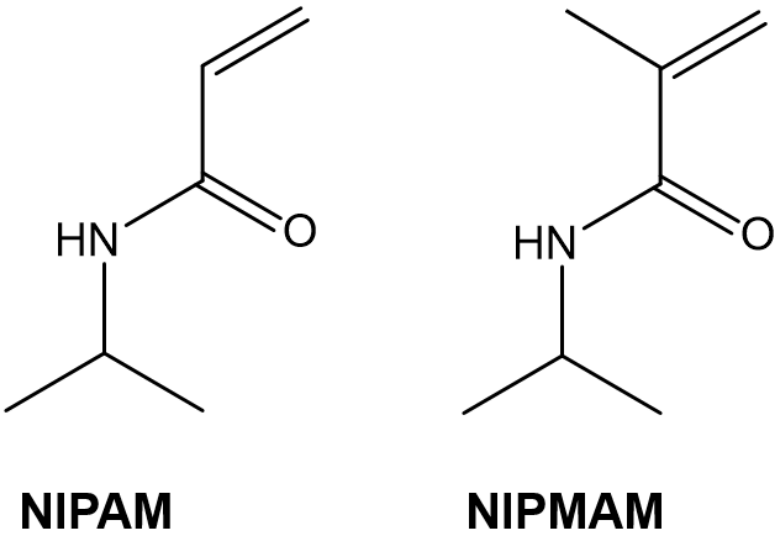

Figure 1.13. Monomer structures of PNIPAM and PNIPMAM: Monomer structure for PNIPAM (left) and PNIPMAM (right).

1.5. Stem cells

The use of nanomaterials for drug delivery applications has great potential as a therapy in numerous disease fields. One of these is in tissue engineering as a tool to deliver biomolecules that can activate stem cells to help regenerate damaged tissue. A stem cell is a type of cell capable of differentiating into multiple, specific cell types that are responsible for particular functional roles. Human embryonic stem cells (hESCs) have the most diverse differentiation capacity and are classified as being pluripotent as they can form all cell types in the human body, except specific supporting tissues required during embryonic development like the placenta. These cells are derived from the embryonic inner cell mass and are capable of self-renewal and differentiation to form more mature adult stem cells during development. Adult stem cells have a more limited differentiation potential than hESCs and are known as being multipotent. In response to tissue damage through injury- or age-related events, adult stem cells can differentiate into specific cells required to regenerate the damaged tissue.

1.5.1. Mesenchymal stem/stromal cells (MSCs)

MSCs are a highly heterogeneous population of adult stem cells capable of differentiating, via specific lineages, into osteoblasts, adipocytes and chondrocytes, which *in vivo* form bone, fat and cartilage tissue, respectively (**Figure 1.14**). Generally, MSCs are isolated from bone marrow but are not limited to this niche environment and have been found to reside in most bodily tissues (da Silva Meirelles, 2006). Over many passages, MSCs display the ability to retain their capacity to differentiate upon stimulation with specific biochemical cues (Pittenger, 1999). The heterogeneity of MSCs is evident, where within a given population, it has been shown that some cells displayed a more limited differentiation potential than others and some do not differentiate at all, but have immunomodulatory functions (James et al., 2015).

MSCs used in research are isolated from different sources using various procedures, which makes it difficult to define an already highly heterogeneous cell type. To allow for better comparisons between studies and ensure that MSCs used are derived from the same population, the International Society for Cellular Therapy developed criteria for defining MSCs. The established criteria were that MSCs must be plastic adherent, capable of tri-lineage differentiation, to express specific cell surface markers CD105, CD73, CD90, and be negative for the haematopoietic stem cell (HSC) surface markers CD45, CD43, CD14 or CD11b, CD79a or CD19 and HLA-DR (Dominici et al., 2006).

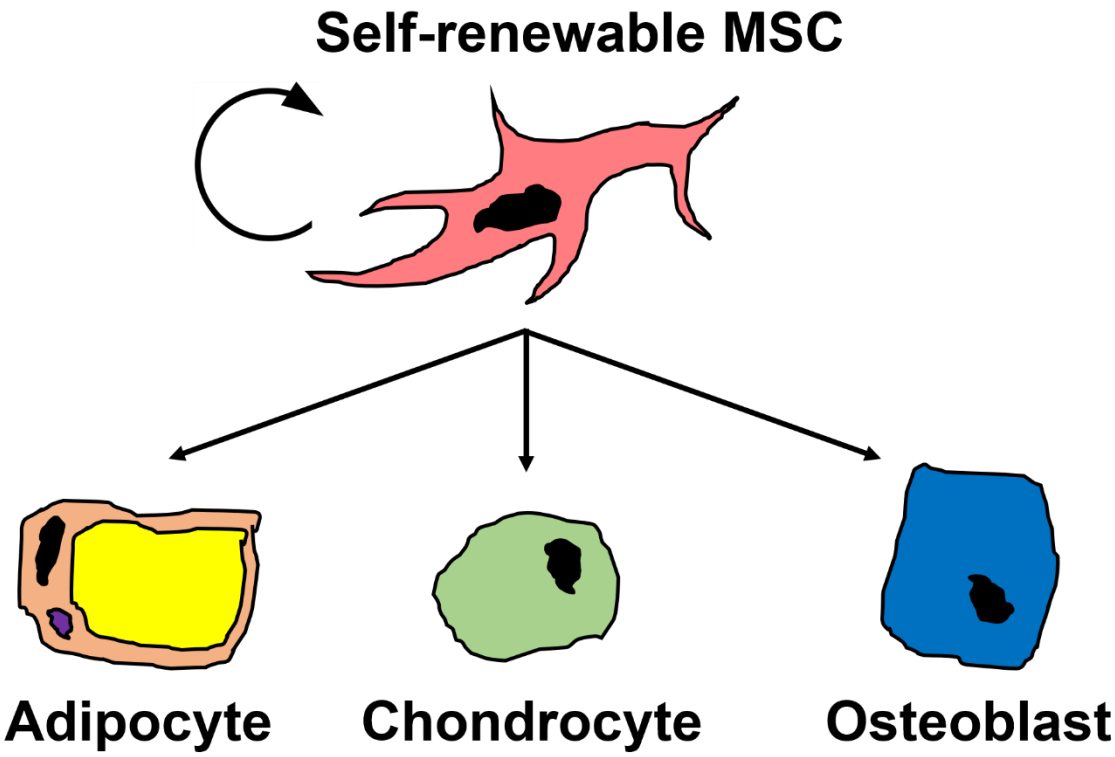

Figure 1.14. Differentiation potential of MSCs: Upon stimulation with specific biological components, MSCs can differentiate both *in vitro* and *in vivo* to form adipocytes (fat), chondrocytes (cartilage) and osteoblasts (bone).

1.5.1.1. Functional roles of MSCs

MSCs are integral for tissue regeneration through their differentiation capacity to form cells important for tissues such as bone and cartilage. Using patient-derived MSCs, it is possible to generate autologous tissue that is biocompatible with the individual to replace damaged or diseased areas. Early experiments using MSCs as a tool for regenerative medicine, began with treatments of bone defects or disorders. Promising results were initially found in sheep experiments after using MSC-loaded scaffolds to repair tibia bone defects (Kon et al., 2000). These results were subsequently recapitulated in human clinical trials using patients with various bone defects (Marcacci et al., 2000).

MSCs are not just limited to applications in tissue regeneration and have been shown to also have immune-regulatory functions. In the bone marrow environment where MSCs reside, HSCs also populate this biological niche. HSCs are capable of differentiating into all types of blood cell, as well as immune cells. Because MSCs and HSCs co-exist in the same region, it was tested whether MSCs could regulate lymphocyte proliferation. MSCs were found to reduce lymphocyte proliferation *in vitro* and also displayed immune-regulatory properties *in vivo* based on skin graft analysis (Bartholomew et al., 2002). Following this discovery, MSCs have been used in clinical trials for the treatment of graft vs. host disease. Graft versus host disease is an immune disorder that generally arises following transplantation when immune cells from the donor attack the recipient patient's tissues. This disease is often a side effect following allogeneic bone marrow transplantation involving stem cells. There is evidence to suggest some success with this treatment, however avoiding complications and optimisation of the appropriate MSC dose still requires further investigation (Ringden and Keating, 2011). The potential for using MSCs to treat a variety of diseases is highlighted by ongoing research towards their therapeutic use in multiple fields, such as muscle regeneration following heart attacks, diabetes and strokes (Gersh, 2010, Jiang et al., 2011, Jang et al., 2010).

1.5.1.1.1. Osteogenesis

MSCs have been used extensively in research as a precursor cell type to form cells integral for joint tissue. One of the major constituents of joint tissue is bone and it is therefore crucial to highlight the biochemical pathways that oversee this process in order to effectively develop therapies. The process by which cells differentiate to form osteoblasts is known as osteogenesis, which is essential for the development of bone tissue. A multitude of transcription factors have been implicated in osteogenesis, most notably Runt-related transcription factor 2 (Runx2). Runx2 binds to the promotor region of osteogenic genes, including osteocalcin and osteopontin (Ducy et al., 1997). The role of Runx2 in osteogenesis has been confirmed in previous work by showing that loss of Runx2 is lethal to mice, causing complete lack of bone ossification (Komori et al., 1997). Also, it has been shown that overexpression of Runx2 in mouse-derived MSCs enhances the expression of bone-related genes *in vitro* and shows increased bone mineralisation capacity *in vivo* (Zheng et al., 2004). Another transcription factor, Osterix, acts downstream of Runx2 and has been found to be essential for bone formation (Nakashima et al., 2002).

Osteogenesis is a complex process, overseen by a plethora of signalling pathways that require tight regulation and control. The expression of transcription factors is modulated by these pathways, following activation by growth factors and signalling molecules from the cellular environment. Some of the key signalling pathways implicated in osteogenesis include bone morphogenetic protein (BMP) and Hedgehog (Hh) signalling. BMPs belong to the transforming growth factor β (TGF-β) superfamily and act at different stages of development. Downstream events of BMP signalling involve binding to specific receptors to bring about phosphorylation of receptor SMAD proteins. Phosphorylated receptor SMAD proteins form complexes with other SMAD proteins before translocation to the nucleus where they influence transcription factor activity. BMP-2 has been directly implicated in osteogenesis that has been shown to activate Runx2 (Lee et al., 2000) and Osterix activity (Lee et al., 2003). Hh signalling activates Gli family transcription factors after a Hh factor-receptor interaction suppresses a downstream protein called Smoothened. *In vitro*, it has been shown that mouse MSCs treated with the Hh signalling factor Indian Hedgehog (IHh), showed positive induction of osteogenesis following a 2-day treatment (Hu et al., 2005).

One of the other major signalling pathways implicated in osteogenesis is the canonical Wnt pathway. This pathway operates in a similar fashion to the Hh signalling pathway, through the suppression of a downstream protein to allow transcriptional activation. Specifically, the prevention of β-catenin phosphorylation allows for its translocation into the nucleus to regulate gene transcription via the T-cell factor (TCF)/lymphoid enhancer factor (LEF) transcription factor family. It has been shown in a study with mice that prevention of β-catenin phosphorylation using an inhibitor resulted in increased osteogenesis *in vitro* and *in vivo* (Kulkarni et al., 2006). Another study identified a TCF binding site in the promotor region of Runx2, suggesting a role for Wnt signalling in promoting osteogenesis (Gaur et al., 2005). It has also been shown that specific Wnt signalling ligands impact osteogenesis differently, where Wnt3a could inhibit the process and Wnt5a promoted it (Boland et al., 2004). It was found in a subsequent study that Wnt3a affected osteogenesis differently at specific stages by inhibiting early osteogenesis of MSCs, but promoting later osteogenic events in mature osteoblasts (Quarto et al., 2010).

Since osteogenesis is crucial for effective bone formation, control of this process by activation of signalling pathways is an area of great therapeutic potential in tissue engineering.

1.5.1.1.2. Chondrogenesis

As with bone, MSCs have been used for the development of cartilage, another major component of joint tissue. It is therefore important to understand the major pathways that govern this process to effectively develop therapies in this area. Chondrogenesis involves the differentiation of cells into chondrocytes, an integral component of cartilage tissue. As with osteogenesis, chondrogenesis is a process heavily regulated by signalling pathways that control transcriptional activation of target genes. The major transcription factor involved in chondrogenesis is SRY-related high mobility group-box gene 9 (Sox9) (Augello and De Bari, 2010). Sox9 controls the expression of collagen type 9 by binding to its promotor region and forming trans-activating complexes with other proteins (Bridgewater et al., 1998, Wang et al., 2014). Overexpression of Sox9 was found to increase, whilst Sox9 inhibition decreased, mRNA levels of chondrogenic marker genes like collagen (type 2, type 9 and type 11) and aggrecan (Yang et al., 2011). Cross-talk between differentiation pathways has been shown where the potent transcriptional enhancer of osteogeneic differentiation BMP-2 could also enhance chondrogenic differentiation, an effect which was potentiated by the co-expression of Sox9 (Liao et al., 2014). Other important transcription factors for chondrogenic differentiation include Forkhead box O3A (FOXO3A) and Zinc-finger protein 145 (ZNF145). It has been shown that FOXO3A down-regulation causes a decrease in the expression of chondrocyte-specific markers (Guérit et al., 2014). ZNF145 inhibition has been found to decrease chondrogenic differentiation of MSCs, whereas its overexpression enhanced Sox9 expression and chondrogenesis (Liu et al., 2011).

Key pathways involved in osteogenesis, such as BMP and Hh signalling, have also been heavily implicated in chondrogenesis. BMP signalling has been shown to positively regulate chondrogenesis, where overexpression of BMP-2 and BMP-4 could enhance chick limb cartilage development (Duprez et al., 1996). Also, knockout of key SMAD receptors involved in BMP signalling, caused lack of Sox5, Sox6 and Sox9 expression which inhibited chondrocyte formation and maturation (Yoon et al., 2005, Yoon et al., 2006). Hh signalling also impacts upon chondrogenesis, where IHh-deficient mice displayed a markedly reduced chondrocyte proliferation and premature chondrocyte hypertrophy (St-Jacques et al., 1999).

As with osteogenesis, Wnt signalling is also an essential pathway for the regulation of chondrogenesis. The canonical Wnt/β-catenin pathway has been shown to act upon chondrogenesis differently to the non-canonical Wnt pathway that operates independently of β-catenin. For example, the canonical Wnt signalling ligand Wnt3a has been reported to repress chondrogenesis and chondrocyte gene expression (Reinhold et al., 2005). Cross-talk has been shown between chondrogenic and osteogenic differentiation, where inactivation of β-catenin could increase Sox9 expression and induce chondrocyte differentiation at the expense of osteogenic differentiation during the process of intramembranous and endochondral ossification (Day et al., 2005, Guo et al., 2009). By contrast, it has been shown that the non-canonical Wnt signalling ligand Wnt11 could stimulate the gene expression of chondrogenic regulators and promote chondrogenic differentiation of MSCs synergistically with TGF-β (Liu et al., 2014). Also, it was shown that non-canonical Wnt signalling ligands Wnt5a and Wnt5a could function in coordination to enhance chondrocyte proliferation and differentiation through regulation of chondrocyte-specific collagen type 2 alpha 1 (Col2a1) expression (Yang, 2003).

As with osteogenesis, chondrogenesis relies on signalling pathways, such as Wnt signalling, to regulate the expression of specific transcription factors that are key to the process. Using biomolecules like growth factors that are integral to chondrogenesis as tools for tissue regeneration of cartilage, is an area of significant clinical interest.

1.6. Wnt signalling

It is well understood that specific biomolecules can greatly influence the differentiation of MSCs down certain lineages, such as osteogenesis and chondrogenesis. MSC fate is largely overseen by a plethora of signalling pathways, which makes biomolecules important for signalling regulation, such as growth factors, crucial for therapeutic applications (Frith and Genever, 2008). Wnt signalling is one of the most important pathways in development and has been implicated in a variety of processes such as tissue regeneration of adult bone marrow (Goessling et al., 2009). The discovery of Wnt signalling began with the identification of a novel proto-oncogene in mice named integration 1 (int1) in 1982 by Roel Nusse and Harold Varmus (Nusse et al., 1984). It was later realised that the int1 gene in *Drosophila* had already been characterised as the Wingless (Wg) gene that functioned in segment polarity during formation of body axis during embryonic development. This led to subsequent research where it was discovered that mammalian int1 was also involved in mouse embryonic development (Wilkinson et al., 1987). The Wnt gene family began to develop following further discoveries of int1-related genes, where the Wnt nomenclature was derived from int/Wingless that stands for “Wg-related integration site”.

A variety of proteins are involved in the Wnt signalling cascade that are heavily modified post-translationally through palmitoylation and glycosylation. These modifications have been shown to be essential for Wnt protein targeting to the plasma membrane for secretion and also receptor binding, for example with the ligand Wnt5a (Kurayoshi et al., 2007).

There are three Wnt signalling pathways that have been characterised, which are a canonical pathway involved in regulation of gene transcription, and two noncanonical pathways involved in either cytoskeletal or calcium regulation. All pathways share common features, where pathway activation arises following Wnt protein ligand binding to a Frizzled (Fz) family receptor that transduces a signal to the intracellular Dishevelled (Dsh) protein.

1.6.1. Canonical Wnt signalling

Since the canonical Wnt signalling pathway is heavily involved in gene transcription, it has a significant impact on crucial biological processes, such as MSC fate. Our understanding of this pathway has allowed for the development of useful tools to study signalling activation, such as a reporter MSC line (Saleh et al., 2016). The canonical Wnt or Wnt/β-catenin pathway involves β-catenin translocation from the cytoplasm to the nucleus where it functions as a transcriptional coactivator of factors belonging to the TCF/LEF family. Wnt ligand binding to a Fz family receptor and co-receptor low-density lipoprotein receptor-related protein 5/6 (LRP5/6) causes the translocation of the protein axin to the plasma membrane. The Wnt-Fz-LRP5/6 complex was first characterised where extracellular domains of LRP6 and Fz8 were shown to form a complex *in vitro* in the presence of Wnt1 (Tamai et al., 2000). Axin is associated with a destruction complex that ordinarily degrades β-catenin by proteasomal degradation through ubiquitination in the absence of Wnt activation (Nakamura et al., 1998). The destruction complex consists of proteins adenomatosis polyposis coil (APC), protein phosphatase 2A (PP2A), glycogen synthase kinase 3 (GSK3), and casein kinase 1α (CK1α) (Nakamura et al., 1998). Once the destruction complex is moved to the plasma membrane, it becomes associated with the cytoplasmic tail of LRP5/6 through axin phosphorylation and binding. Then, axin becomes de-phosphorylated which lowers its stability and levels to allow for the activation of Dsh by phosphorylation (Willert et al., 1999). Through its DIX and PDZ domains, Dsh then inhibits the kinase activity of GSK3 within the destruction complex (Fiedler et al., 2011). Inhibition of destruction complex activity allows β-catenin to accumulate and translocate to the nucleus for transcriptional activation alongside TCF/LEF transcription factors. The connection between TCF/LEFs and Wnt signalling originated from yeast-two-hybrid screens that revealed β-catenin could tightly bind to LEF1 and TCF1, an interaction subsequently found to involve a conserved motif in the amino terminus of TCF/LEFs (Behrens et al., 1996, Huber et al., 1996). β-catenin also recruits other transcriptional co-activators, including B-cell CLL/lymphoma 9 protein (BCL9), Pygopus (Kramps et al., 2002) and Parafibromin/Hyrax (Mosimann et al., 2006). A schematic of Wnt/β-catenin signalling can be seen in **Figure 1.15**.

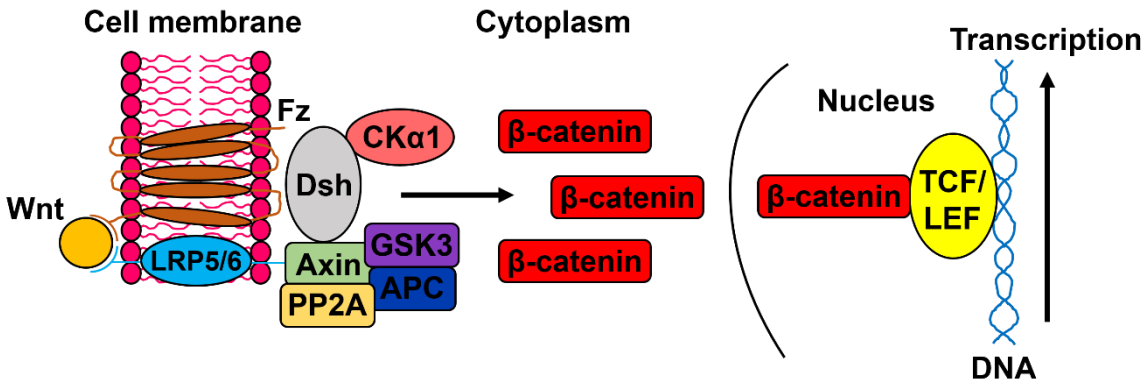

Figure 1.15. Schematic of canonical Wnt/β-catenin signalling: Wnt ligand-mediated activation inhibits destruction complex allowing β-catenin-dependent transcriptional activation of target genes.

1.6.2. Wnt3a

Wnt3a is a growth factor encoded for by the *WNT3A* gene (Saitoh et al., 2001) and is a key ligand in Wnt signalling activation that has been implicated in various biological processes. It has been shown that Wnt3a-mediated signalling promotes proliferation, myogenic differentiation and migration of rat bone barrow-derived MSCs (Shang et al., 2007), as well as suppression of osteogenic differentiation in human MSCs (Boland et al., 2004). The functional stimulation of MSCs by Wnt3a, coupled with availability of Wnt-sensitive MSC lines (Saleh et al., 2016), make this growth factor a useful candidate for studies of Wnt signalling activation and enhancement of cellular events, such as proliferation.

1.7. Tissue engineering

The differentiation properties of stem cells, like MSCs, make them an attractive cell-based therapeutic for the repair of damaged tissues. This can be achieved using cell-based approaches alone, or in conjunction with materials, such as nanoparticles, which is known as tissue engineering. Tissue engineering generally involves the use of cell- and material-based approaches, often in combination with biomolecules and biochemical factors, to improve or replace biological tissues. The requirement for tissue engineering often arises due to tissue damage through injury, or disorders as a consequence of genetic predisposition, such as osteoarthritis.

1.7.1. Cell-based therapies in tissue engineering

Often the term regenerative medicine is used synonymously with tissue engineering, but with regenerative medicine research on self-healing is included alongside tissue engineering to encourage the body to use its own systems, sometimes with the help of foreign biological material like bioactive drugs/proteins, to regenerate cells and rebuild tissues.

The main stem cell-based therapy that is widely practised, involves the application of bone marrow-derived HSCs for cancer treatments of conditions such as leukaemia and lymphoma (Karanes et al., 2008). As a consequence of non-specific chemotherapy treatments, many off-target cells are killed which require regeneration by donor-derived stem cells that must be administered in a controlled manner to prevent unwanted graft vs. host immune responses (Malard and Mohty, 2014). In 2012, an allogenic stem cell-based therapy called Prochymal was approved in Canada for the management of acute graft vs. host disease in children unresponsive to steroids. This treatment involves the application of bone marrow-derived MSCs purified from adult donors and has shown promising clinical results (Kebriaei et al., 2009).

Outside of clinically approved therapies, there is an ongoing body of research dedicated to further the advancement of regenerative medicine. The differentiation capacity of cells like MSCs, have great potential for regenerating tissues, such as bone and cartridge. For instance, it has been shown that healthy MSCs transplanted from a young donor mouse into an osteopenic recipient mouse could enhance osseointegration of a femoral implant (Gao et al., 2012). Another study showed that injected MSCs could effectively regenerate the cartilage tissue of an adult minipig following a cartilage defect medial femoral condyle (Lee et al., 2007).

Despite the clinical approval of some cell-based therapies, there are still several underlying issues, meaning alternatives are desired. One of the problems researchers face is specific targeting of cells to the desired site, for example MSCs have been found to accumulate in the lungs following intravenous injection (Nenasheva et al., 2017). Studies have also reported side effects of fever, chills, infection and liver damage following systemic infusion of MSCs (von Bahr et al., 2012, Ren et al., 2011) Also, there have been many discrepancies documented following reports of clinical trials. For example, results of an autologous bone marrow stem cell trial towards improving ventricular function were presented in two

separate publications and found to be largely contradictory (Francis et al., 2013). Additionally, inconsistencies were shown where meta-analysis on therapies using bone marrow-derived stem cells for heart disease showed discrepancies regarding increased effect sizes (Nowbar et al., 2014), as well as lack of significant therapy benefits (Gyöngyösi et al., 2015). Therefore, there is a clear requirement for effective tissue engineering alternatives that show clinical consistency.

1.7.1.1. Immortalised MSC lines

It is important to conduct basic scientific research in order to realise the true potential of MSCs as a cell-based therapy. Since MSCs are highly heterogeneous, the behaviour of primary cells isolated from donors is highly variable. In an effort to prevent variability between cells derived from different donors, immortalised MSC lines have previously been generated and characterised by the Genever research group in York (James et al., 2015). Specifically, the cell lines were generated using a lentiviral expression system to overexpress human telomerase reverse transcriptase (hTERT) where four candidate clones were selected for further characterisation based on their growth stability (James et al., 2015). Because these MSCs can stably grow in culture and retain consistent properties throughout, they are a useful tool for experimental work and are more likely to be reproducible compared to donor-derived primary cells. Also, since each cell line is derived from a single cell, the variability due to a mixed population is circumvented.

The cell lines derived from this study were termed Y101, Y102, Y201 and Y202 cells, which each had distinct properties despite all displaying characteristic markers of bone marrow-derived MSCs. When plated at clonal density, Y101 and Y201 cells formed dispersed colonies, characteristic of a migratory phenotype, whereas Y102 and Y202 cells formed dense, highly compact colonies (James et al., 2015). Additionally, differences could be observed in the differentiation potential of the lines, where Y101 and Y201 cells showed significant adipogenic potential, particularly Y201s, whereas Y102 and Y202 cells showed severely limited adipogenic potential by comparison (James et al., 2015). In terms of osteogenesis, Y101 and Y201 MSCs showed significant osteogenic potential (notably Y101s showed the greatest increase in alkaline phosphatase (ALP) gene expression) compared to minimal osteogenic potential observed for Y102 and Y202 cells (James et al., 2015). Y102 and Y202 cells also showed no signs of chondrogenic differentiation potential, whereas both Y101 and Y201 cells displayed clear chondrogenesis (James et al., 2015). Despite their limited differentiation capacity, Y102 and Y202 cells showed significantly over-represented expression of genes responsible for immunomodulatory and inflammatory roles compared with Y101 and Y201 cells (James et al., 2015). This study highlights the heterogeneity of MSC populations by providing evidence showing significantly different roles for cells from distinct subpopulations.

Additionally, using Y201 MSCs, the Genever lab were able to generate and characterise a Wnt reporter line by stably transfecting the cells with a TCF/LEF plasmid reporter construct driving the expression of eGFP (Saleh et al., 2016). Since members of the TCF/LEF transcription factor family interact with nuclear β-catenin during Wnt signalling to activate target genes, the design of a TCF/LEF-based eGFP reporter construct is useful as a functional readout of canonical Wnt signalling and therefore could be used as a tool to study the activity of Wnt-activating ligands.

The generation of MSC cell lines for basic research into MSC biology is extremely useful for future developments in regenerative medicine.

1.7.2. Biomaterials in tissue engineering

In tissue engineering, materials used in combination with cells are known as biomaterials. It is worth noting the limitations of current therapies in tissue repair to highlight the motivation during the development of alternative material-based approaches. Conventional tissue reconstruction approaches have several drawbacks, such as immunogenic reactions to grafts and infections of implants. Also, despite cell-based therapies being a desirable alternative, this application also has issues, such as specific targeting to desired tissue sites. Towards the improvement of current therapies for tissue regeneration, the development of effective biomaterials is an area of growing interest. This has been explored in various ways, either by using materials to mimic and replace damaged tissues, provide surfaces for cell attachment that can promote tissue regeneration by differentiation, or trigger repair *in situ* by the delivery and release of specific growth factors to activate signalling pathways and drive cellular tissue regeneration. It is important to evaluate the potential of these applications for tissue engineering, as well as any drawbacks associated with each.

1.7.2.1. Scaffolds in tissue engineering

Biomaterials research in this field has focused on engineering scaffolds to serve multiple roles, including supportive applications through mechanical joint reinforcement. Often when used in this context, scaffolds are designed to mimic the mechanical properties of the specific tissue of interest. An example of this is in cartilage replacement therapy where it was shown that anisotropic 3D poly(lactic acid) (PLA) structures with incorporated hydrogels displayed similar mechanical properties to native cartilage and could provide good permeability for chondrocytes to attach and proliferate (Li et al., 2012). Also, this has been shown in bone engineering where synthetically produced 3D tissues composed of various naturally-occurring materials, including fibrin, thrombin, collagen and hydroxyapatite, could be used as biocompatible grafts that mimic bone tissue (Lechner and Huss, 2006).

Scaffolds can provide surfaces for cellular attachment and be engineered to actively stimulate biological events. For example, previous work can show that stem cell osteogenic differentiation is modulated by functionalising scaffold surfaces with specific adhesion peptides that interact with stem cell integrins (Nuttelman et al., 2005). Additionally, structural modifications of biomaterial surfaces have been shown to directly influence stem cell fate. This could be seen using PEG hydrogel microwells that were designed to allow for cultures of cells to form embryonic bodies (EBs) within different size ranges (Hwang et al., 2009). It was shown that EBs formed at different sizes determined the extent of hESC differentiation (Hwang et al., 2009). This size-dependent effect on differentiation could be correlated with differential expression of Wnt5a and Wnt11, both involved in the non-canonical Wnt pathway (Hwang et al., 2009).

Biomaterial scaffolds have shown great promise as tools for tissue regeneration by mechanically improving joint function directly, as well as indirectly by influencing stem cell fate. However, drawbacks of using scaffolds include the optimisation requirements to architecturally develop suitable materials to mimic appropriate tissues. Additionally, most available 3D scaffolds fail to mimic an *in vivo* situation and only represent a static environment (Rimann and Graf-Hausner, 2012). There is also the risk of disease transmission when using scaffold biomaterials that are animal- or human-derived (Rimann and Graf-Hausner, 2012). Batch-to-batch reproducibility is an area of limitation where variability is often shown, particularly

when using animal-based materials (Rimann and Graf-Hausner, 2012). Additionally, specificity can be a problematic area, where often a variety of compounds can interact with scaffolds, which can be an issue for certain applications, particularly imaging (Nugraha et al., 2011). Scaffold size and capacity for degradation is also an important consideration so long-term accumulation does not occur. Therefore, alternatives to biomaterial scaffolds could be useful for tissue engineering applications.

1.7.2.2. Drug delivery and nanoparticles in tissue engineering

The delivery of biomolecules to functionally activate stem cells is an area of significant interest for biomaterial applications in tissue engineering. There have been strategies to develop scaffolds for the biomaterial presentation of biomolecules, such as growth factors, to functionally activate cells. This has been demonstrated through chemical conjugation of biomolecules to scaffold materials, or physical encapsulation into a layer for programmed or diffusion-based release into immediate tissues. Diffusion-based release has been shown previously with arginine-glycine-aspartic acid (RGD) peptide release from scaffolds composed of PEG hydrogels with incorporated degradable lactic acid units (Han and Hubbell, 1996). For programmed biomolecule release, the use of smart, polymeric materials is appealing for applications in a controlled, triggered manner using specific stimuli. Triggered release has been previously shown using a dual-responsive scaffold composed of two smart polymers, pH-sensitive chitosan and temperature-sensitive PNIPAM. It was found that after incorporating the protein bovine serum albumin (BSA) and the drug ibuprofen that PNIPAM temperature responsiveness could control release of BSA, and ibuprofen was released in a pH-sensitive manner (Temtem et al., 2012). However, triggering pH-sensitive biomolecule release under physiological conditions is challenging and would require the scaffold to be in an environment that could permit such release following a shift in pH, such as within the endocytic pathway. The main drawback of using scaffolds for applications involving biomolecule release is a lack of specific targeting, which may hamper the efficiency of cellular activation.

The use of nanoparticles is highly appealing as a vehicle for biomolecule delivery in regenerative medicine. Due to their small size and capacity for surface modification, nanoparticles have great potential to deliver and release biomolecules at specific target sites. It has previously been shown that retinoic acid (RA)-loaded polymeric nanoparticles could enhance vascular regulation of neural stem cell survival and differentiation post-ischemia (Ferreira et al., 2016). Additionally, chitosan-based polymeric nanoparticles loaded with stromal-derived factor 1α (SDF-1α) could induce bone marrow MSC migration *in vitro* (Huang and Liu, 2012).

For some cancer-specific applications, stem cells have been used as a vehicle to transport nanoparticles to tumour sites. This has been investigated since there are

some drawbacks of nanoparticle-based delivery systems, such as phagocytosis in a size-dependent manner and inefficient infiltration into the target area. It has been shown previously that MSCs could act as vehicles of PLA nanoparticle and lipid nanocapsule delivery in glioblastoma research (Roger et al., 2010). MSCs have also been used as a nanoparticle delivery vehicle in breast and lung cancer studies using DOX-loaded mesoporous silica nanoparticles (Paris et al., 2016) or poly(lactic-co-glycolic acid) (PLGA) nanoparticles (Zhao et al., 2017), respectively.

Triggered activation of nanoparticles has been used to release molecules in response to a specific stimulus. Light can be an effective trigger for release of molecules from nanoparticles. For example, it has been shown that upconversion nanoparticles coated with a NIR light-sensitive diblock copolymer consisting of poly(4,5-dimethoxy-2-nitrobenzyl methacrylate) (PNB), where the outer block is hydrophilic poly(methoxy polyethylene glycol monomethacrylate) (POEG), could encapsulate and release DOX under NIR light (Xiang et al., 2018). Also, it has been shown that core-shell upconversion nanoparticles composed of lanthanide-doped nanocrystals could release the chemotherapeutic 5-fluorouracil (5-FU) following photocleavage at the particle surface (Fedoryshin et al., 2014).

It has been shown that temperature-sensitive liposomes can also be used as a stimuli-triggered system to release molecules. For example, it has been shown that intravenous administration of temperature-sensitive vesicles designed by inclusion of leucine zipper peptides within a lipid bilayer encapsulating DOX could prolong blood circulation kinetics and maximised drug release and accumulation at tumours *in vivo* with local mild hyperthermia (Al-Ahmady et al., 2015). Additionally, it has been shown that high intensity focused ultrasound can be used as a mechanism to induce the required temperature elevation for the release of DOX from temperature-sensitive liposomes (Mannaris et al., 2011).

Moreover, pH-sensitive polymersomes have been shown to be effective for pH-triggered release of molecules. For example, it has been shown that pH-sensitive amphiphilic block-copolymers could release the anti-cancer drug paclitaxel in acidic pH conditions, typical of tumour tissue, and show increased cytoxicity for cancer cells following drug release (Villani et al., 2017).

1.7.2.2.1 SPIONs in tissue engineering

The properties of SPIONs make them highly attractive as a tool for tissue engineering, particularly when used in cell-based therapies. The regenerative capacity of MSCs make them a favourable candidate for studies with SPIONs as an approach to regenerate tissue. There are various ways in which SPIONs have been used with MSCs for applications such as cell homing (Yun et al., 2018, Naseroleslami et al., 2018), imaging/tracking (Moraes et al., 2012, Novotna et al., 2017) and drug delivery (Chung et al., 2018, Corradetti et al., 2017).

As is the case with various nanomaterials, SPIONs have been internalised by stem cells as a vehicle for their delivery to tissue-specific sites. The significant advantage of using SPIONs over other materials is their strong magnetic properties, which allows for magnetically-directed homing to sites of interest. This has previously been shown to be an effective strategy to promote tissue regeneration through magnetically targeting MSCs with internalised SPIONs to both olfactory (Yun et al., 2018) and cardiac (Naseroleslami et al., 2018) tissues.

Additionally, the magnetic properties of SPIONs make them useful for imaging techniques, particularly as contrast agents for magnetic resonance imaging (MRI). MRI is a non-invasive imaging approach where finding suitable, safe materials to use as MRI contrast agents is an area of active research. This is particularly prevalent in stem cell research as a tool for tracking cells that have been implanted in living organisms. SPIONs have previously been shown to function effectively as safe contrast agents to visualise implanted MSCs in brain tissue (Moraes et al., 2012, Novotna et al., 2017).

Because SPIONs have the capacity for chemical surface functionalisation, they have also been used as vehicles for MSC-targeted drug delivery applications. MSC-specific markers have been investigated in previous studies as potential drug delivery targets, where CD44 has been highlighted as a likely candidate for bone marrow therapies that can be markedly upregulated through MSC culture on hyaluronic acid (HA)-treated plates (Corradetti et al., 2017). Additionally, it has been shown that dextran-coated SPIONs can promote migration towards damaged neurons and enhance their neuronal differentiation in a mouse model of Parkinson’s disease (Chung et al., 2018).

With the field largely focused on MRI-based imaging methods, using functionalised SPIONs as a delivery and release system of biomolecules, such as growth factors, to stimulate MSC activation, is still relatively unexplored.

1.7.2.3. PNIPAM in tissue engineering

The application of stimuli-responsive polymers has gained significant research interest over recent years, particularly in tissue engineering. PNIPAM is one of the most prevalent materials in the field, largely because of its temperature-responsive properties and tunability to suit physiological conditions. There are reports of PNIPAM applications as a hydrogel surface for culturing MSCs on, as well as assessment of the polymer effects on cellular events such as growth and differentiation. For example, it has been shown that culturing MSCs on PNIPAM-based surfaces can positively impact upon their osteogenic differentiation potential (Dai et al., 2016).

PNIPAM has been used as a hydrogel layer to encapsulate nanoparticles or cells for *in vivo* administration. Often in tissue engineering applications, naturally occurring materials such as hydroxyapatite, which comprises bone and teeth, are used to improve biocompatibility when mimicking a tissue environment or inducing cell-based tissue regeneration. A study showed that PNIPAM-based hydrogels could be mixed with hydroxyapatite nanoparticles in a liquid state *ex-vivo*, before rat-based injection which induced nanoparticle encapsulation through gelation (Abbey et al., 2016). This study also showed that bone regeneration was markedly improved at sites where the PNIPAM-hydroxyapatite composite gels were applied, indicating the regenerative properties of functionalised PNIPAM-based materials (Abbey et al., 2016). Another study shows that bone marrow-derived MSCs could be packaged into PNIPAM-based hydrogels for transplantation into wound sites of diabetic ulcers (Chen et al., 2015). They could further show that the cell-based hydrogel treatment contributed to rapid wound healing, brought about through enhanced MSC secretion of TGF-β1 and basic fibroblast growth factor (bFGF), leading to a series of biological events including angiogenesis and granulation tissue formation (Chen et al., 2015).

PNIPAM nanoparticles have also been used as a biomolecule delivery and release system for regenerative medicine applications. For example, a previous study generated 100 nm PNIPAM nanoparticles by FRP that could be loaded with VEGF and released upon heating. This triggered a PNIPAM transition to a hydrophobic state which could activate human bone marrow-derived MSCs *in vitro* by promoting osteogenic differentiation (Adibfar et al., 2018). Temperature-sensitive growth factor release from PNIPAM using SPION magnetic heating is an

unexplored approach in tissue engineering and could be useful for triggered biomolecule release.

Chapter 2: Synthesis and characterisation of temperature-sensitive, magnetically-responsive nanoparticles

2.1. Rationale, aims and summary

There is a broad range of previous work on the synthesis and characterisation of nanoparticles for use in biomedical applications. Nanoparticles can be modified by surface functionalisation with polymers that can be loaded with biomolecules such as proteins. The small size of nanoparticles adds to their therapeutic potential as a system capable of delivering molecules to biological niches of interest.

Iron oxide nanoparticles have been extensively studied in biomedicine due to their magnetic properties and have shown promise in numerous applications such as a contrast agent in MRI (Wei et al., 2017). Moreover, iron oxide nanoparticles of a sufficiently small size (<76 nm) are single domain with one magnetic moment, exhibiting superparamagnetism below 16 nm, meaning they have zero magnetisation until an external magnetic field is applied (Li et al., 2017). Of particular biomedical interest is the fact that SPIONs can undergo a phenomenon termed magnetic heating. This occurs in the presence of an alternating/oscillating magnetic field, in which energy is supplied that excites the magnetic moment fluctuations to convert the magnetic energy into thermal energy (Fortin et al., 2007). Studies have shown these properties can be utilised in a medicinal context, particularly in research targeting cancerous cells, where magnetic heating has induced elevated temperatures, known as magnetic hyperthermia, to induce tumour cell death *in vitro* and *in vivo* (Shinkai et al., 1999, Shinkai et al., 2002). The size of SPIONs is a crucial property to ensure effective use for magnetic heating applications. Previous studies have highlighted the correlation between increasing SPION size and the improved rate of energy absorption/SAR, in response to an electromagnetic field (Tong et al., 2017). SPIONs with a higher SAR will undergo magnetic heating more effectively. Fine tunability of SPION size can be achieved through organic synthetic approaches involving thermal decomposition of iron carbonyl complexes (Tong et al., 2017). However, due to their insolubility in an aqueous environment, they are unsuitable for biological applications and require further functionalisation steps by ligand exchange to improve their solubility. Therefore, an aqueous synthetic approach would be much

more favourable for generating SPIONs for biological applications. Moreover, an important factor when determining appropriate SPION size is whether they are suitable for biological applications. Previous studies have investigated the relationship between nanoparticle size and ability to cross biological barriers, for example gold nanoparticle crossing of the blood-brain barrier is very size dependent, with 20 nm being optimal over 50 nm and 70 nm (Betzer et al., 2017). Nanoparticle surface functionalisation with polymer shells will also influence the hydrodynamic diameter. Size properties of SPIONs are therefore crucial for both magnetic heating and suitability as a tool for biomolecule delivery.

Nanoparticle surface functionalisation is an important process which adds to their bio-suitability. In particular biocompatible polymer shells on the surface of nanoparticles are favourable as they can act as a matrix to entrap biomolecules such as drugs or proteins. Generating such functionalised nanoparticles has great potential as a biomolecule delivery system. Temperature-sensitive polymers are of particular interest in this field through their capacity to undergo phase transitions at defined temperatures. Indeed, it has been shown that hydrogels of the temperature-sensitive polymer PNIPAM were able to release the therapeutic polysaccharide dextran in a controlled, temperature-sensitive fashion (Huang et al., 2004). Moreover, polymer phase transition (LCST) temperatures can be modulated through block co-polymerisation approaches, or polymerisation of different monomers to either increase or decrease the LCST. For example, block co-polymers of PNIPAM with increasing acrylic acid content have been shown to correlate with increasing polymer LCST (Burmistrova et al., 2011), as well as showing LCST modulations in a mass average molar mass (M_w) dependent manner with PNIPMAM (Rathfon and Tew, 2008).

Studies investigating temperature-dependent protein release using the magnetic heating properties of SPIONs are more limited. The majority of studies investigating magnetically-triggered protein release have been carried out using small biomolecules such as drugs. This perhaps is due to the inherent sensitivity of protein function to changes in temperature. Utilising the properties of temperature-sensitive polymers coated on the surface of SPIONs could be a potentially interesting combination for protein delivery and temperature-sensitive release.

The aims of the work in this chapter were to generate stable, water-soluble iron oxide nanoparticles at a suitable size for biological applications. I wanted to generate nanoparticles that exhibited superparamagnetic properties and would undergo magnetic heating when exposed to an alternating magnetic field. This was achieved using an aqueous synthetic approach which produced water soluble nanoparticles at a size of 6.3 ± 0.9 nm (n=84). Superparamagnetism could be observed and the nanoparticles were able to undergo magnetic heating when exposed to an alternating magnetic field. Moreover, I have shown SPION stability over a 3-month period using magnetic susceptibility measurements.

Additionally, I aimed to synthesise a functionalised form of temperature-sensitive polymer PNIPAM that could coat the surface of the synthesised SPIONs. I then wanted to observe whether the PNIPAM-coated SPIONs were temperature-sensitive as a consequence of PNIPAM coating. I was able to synthesise acid-terminated PNIPAM and confirm an LCST at 32^{o}C. This was then functionalised with catechol molecule nitrodopamine (NDA) to permit binding to the SPION surface. PNIPAM coating was confirmed and quantified which conferred temperature-sensitive properties on the SPIONs when heated above the PNIPAM LCST.

Finally, I was able to synthesise an alternative polymer PNIPMAM, which displayed a more gradual, but higher LCST at 42^{o}C. I could also functionalise this polymer with NDA to permit coating of the SPION surface.

2.2. Materials and Methods

2.2.1. Chemicals

All chemicals were purchased from Sigma-Aldrich unless otherwise stated.

2.2.2. Characterisation

2.2.2.1. Nuclear magnetic resonance (NMR)

NMR characterisation was carried out on a JEOL ECS-400 spectrometer using 10 mg/mL and 50 mg/mL samples for ^{1}H and ^{13}C NMR, respectively. Samples were dissolved in either deuterated chloroform ($CDCl_3$) or deuterated dimethyl sulfoxide (DMSO-D_6) for analysis. A 400 MHz field strength was used with 8 scans across a scan range of -2 to 12 ppm and scan acquisition time of 2 s for ^{1}H NMR. A 100 MHz field strength was used with 256 scans across a scan range of -60 to 240 ppm and scan acquisition time of 1 s for ^{13}C NMR. Peak assignment was carried out using Structure-based Predictions in Nuclear Magnetic Resonance Spectroscopy (SPINUS) software online to simulate spectra for comparison with experimental data. A table highlighting the abbreviations used to describe features in simulated NMR spectra generated using SPINUS software can be seen in **Table 2.1**.

NMR abbreviation	Meaning
s	Singlet
d	Doublet
t	Triplet
m	Multiplet

Table 2.1. NMR abbreviations and definitions used in SPINUS software simulations of NMR spectra.

2.2.2.2. Matrix-assisted laser desorption/ionisation-time of flight (MALDI-TOF) mass spectrometry

Molecular weight characterisation was conducted using MALDI-TOF mass spectrometry (Ultraflex, Bruker) in positive, linear ion mode. 3000 shots were fired in sequences of 1000 with the Smartbeam laser power at 60-80% and summed to generate each spectrum. Mass spectra were recorded over a range of 7000-17000 mass-to-charge ratio (m/z). 2 µL samples were spotted out for measurements using polymer solutions diluted from a 1 mg/mL stock at 1/10, 1/100 and 1/1000 in a 20 mg/mL matrix solution of 2-(4-hydroxyphenylazo)benzoic acid (HABA) in tetrahydrofuran (THF). No data transformation was carried out since the charge for the analytes measured was always 1 giving m/z measurements equivalent to the polymer molecular weight.

2.2.2.2.1. Number average molar mass (M_n), mass average molar mass (M_w) and PDI calculations

All calculations were carried out using data acquired by MALDI-TOF mass spectrometry where Ni is the intensity, and Mi the mass of peak

$$M_n = \frac{\mathbf{Ni} * \mathbf{Mi}}{\mathbf{\Sigma(Ni)}}$$

$$M_w = \mathbf{\Sigma} \frac{(\mathbf{Ni} * \mathbf{Mi} * \mathbf{Mi}}{\mathbf{\Sigma(Ni} * \mathbf{Mi)}}$$

PDI was determined by dividing the M_w by the M_n.

2.2.2.3. LCST measurements

Polymer LCST was measured with a thermocouple probe on 10 mg/mL polymer solutions in 50 mL deionised water (dH_2O) (typical resistivity of 18.2 M Ohm cm) under magnetic stirring and determined upon visual insolubility during heating.

2.2.2.4. UV-vis spectroscopy

UV-vis spectroscopy was conducted across a wavelength range of 300-800 nm, recorded on a Shimadzu UV-1800 UV-vis spectrophotometer. Disposable plastic cuvettes were used with a 1 cm pathlength and samples were dissolved in 1 mL sodium citrate (1 mM, pH 5.5) made up in dH_2O for analysis.

2.2.2.5. Thermal gravimetric analysis (TGA)

TGA was carried out using 10 mg dry samples on a PL Thermal Sciences STA 625 instrument under nitrogen gas at a ramp rate of 10^{o}C min^{-1} between 0-600^{o}C.

2.2.2.5.1. Grafting density calculation

Polymer grafting density on the SPION surface was determined using an adapted calculation for TGA-derived grafting density (σ_{TGA}) (**Equation 2.1**) (Benoit et al., 2012). First, the nanoparticle volume was calculated using $4/3\pi r^3$ (where r is particle radius, shown by electron microscopy). From this, the mass of a single nanoparticle could be determined by multiplying the nanoparticle volume by the density of bulk iron oxide (5.18 g/cm) (Kurzhals et al., 2015). The mass of a single PNIPAM-coated SPION was derived by dividing single nanoparticle mass by the inorganic fraction percentage. The inorganic fraction percentage was calculated using TGA data by dividing the mass percentage between 450 – 600^{o}C by the mass percentage between 350 – 600^{o}C. The polymer shell mass proportion of a PNIPAM-coated SPION was determined by dividing the nanoparticle mass proportion of a PNIPAM-coated SPION by the organic fraction percentage shown by TGA (between 350 – 450^{o}C). To calculate how many polymer chains were present per PNIPAM-coated SPION, the polymer shell mass proportion of a PNIPAM-coated SPION was divided by the mass of a single PNIPAM chain (polymer M_w/Avagado's number) (polymer M_w was determined by MALDI-TOF mass spectrometry). The grafting density for polymer chains per nm^2 was calculated by dividing the number of polymer chains per PNIPAM-coated SPION by the nanoparticle surface area ($4\pi r^2$).

$$\sigma TGA = \frac{\textbf{Total number polymer chains}}{\textbf{Total nanoparticle surface}}$$

Equation 2.1. Grafting density equation using data derived from TGA analysis of PNIPAM-coated SPIONs (Benoit et al., 2012).

2.2.2.6. X-ray photoelectron spectroscopy (XPS)

XPS was conducted by drop casting particle samples (10 mg/mL) in aqueous solution onto silicon substrates. After solvent evaporation, dense layers of deposited particles were probed using a monochromated Al anode source (1486.6 eV, Omicron XM 1000) with a power of 220 W. Photoelectrons were detected using an Omicron EA 125 hemispherical energy analyser with a 2 nm entrance aperture and the sample normal oriented at 22.5 ^{o} to both the X-ray source and entrance optics of the analyser. Experiments took place in an ultrahigh vacuum system with a base pressure of $<2 \times 10^{-10}$ mbar.

2.2.2.7. Transmission electron microscopy (TEM)

TEM images were obtained using a JEOL 2011 transmission electron microscope operated at 200 kV accelerating voltage. CCD images were extracted using Gatan Digital Micrograph software. Prior to analysis, 10 mg/mL samples were prepared in dH_2O by sonication for 15 min. One drop of the dispersion was deposited onto 3 mm holey carbon coated copper grids and allowed to dry in air prior to analysis.

2.2.2.7.1. TEM size distribution quantification

A histogram of nanoparticle size (nm) vs frequency (%) was generated and a normal/Gaussian distribution was plotted in Origin 2017 software. This is a function that represents the distribution of random variables as a symmetrical, bell-shaped graph.

2.2.2.8. Dynamic light scattering (DLS)

DLS and zeta potential measurements were recorded using a Zetasizer instrument and analysed using the DTS v. 5.1 supplied by Malvern. 10 mg/mL samples were prepared by sonication in dH_2O for 15 min before placing sample (1 mL) into a quartz, U-bend cell. Measurements were made at 25^oC and carried out in triplicate at 10 runs per measurement.

2.2.2.9. Nanoparticle tracking analysis (NTA)

PNIPAM-coated SPIONs were diluted in dH_2O to an appropriate concentration (10 µg/mL) to visualise on the NS300 (Malvern). The NS300 chamber was left at room temperature or preheated to 37^{o}C and samples were injected using solutions at room temperature. Particles were visualised using a 405 nm laser and were tracked for a series of 10, 1 min videos.

2.2.2.10. Vibrating sample magnometry (VSM)

A Microsense (ADE Model 10) vibrating sample magnetometer equipped with an Oxford Instruments CF-1200 cryostat was used to characterise the nanoparticle magnetic properties at temperatures between 5^{o}C - 40 °C. Nanoparticles in an aqueous suspension (10 mg/mL) were loaded into a vial of dimensions 10 mm x 8 mm x 5 mm (length x depth x width) which was then placed at the measurement position of the cryostat. Magnetisation curves at each temperature were obtained by sweeping the field from -10 kOe to +10 kOe.

2.2.2.11. Magnetic susceptibility measurements and calculations

Magnetic susceptibility measurements were recorded on a Guoy balance (Sherwood Scientific, MK1 Magnetic Susceptibility Balance) using nanoparticle samples (10 mg/mL) immobilised in an agarose gel. 10 mg/mL samples were prepared by dissolving nanoparticles in dH_2O by brief bath sonication at room temperature (1 min). A 3% (w/v) agarose solution was made in a sample vial by heating in a microwave until the agarose dissolved. Immediately after the agarose was dissolved, hot agarose solution (250 µL) was mixed with the nanoparticle solution (250 µL) by brief bath sonication (1 min). Once homogenous, the nanoparticle-agarose solution was added to the Guoy balance tube and allowed to cool until the gel-nanoparticle composite solidified before measurements were taken.

Calculations for magnetic susceptibility were conducted using the **Equation 2.2** for determination of mass susceptibility (cgs) of samples from Guoy balance readings and **Equation 2.3** for the conversion from cgs into SI units (m^3kg^{-1}):

$$\textbf{2.2)} \qquad \chi_g = \frac{\mathbf{l}}{\mathbf{m}}\, c\,(R - R_o)$$

$$\textbf{2.3)} \qquad \chi_g\,(m^3 kg^{-1}) = (cgs) * \frac{4\pi}{1000}$$

Where χ_g is mass susceptibility, l is the sample length in the tube (cm), m is sample mass (g), c is the balance constant, R is the sample balance reading and R_o is the empty balance reading.

Equations 2.2 and 2.3. Magnetic susceptibility equations: 2.2) Determination of mass susceptibility (cgs) of samples from Guoy balance readings **2.3)** Conversion from cgs into SI units (m^3kg^{-1}).

2.2.3. Synthesis

2.2.3.1. Iron oxide nanoparticles

1,2-propanediol was acquired from VWR International.

Synthesis was adapted from a previous study (Carroll et al., 2010). For a 5 g scale reaction, two solutions were prepared separately, solution A and solution B. Solution A was prepared by mixing iron (II) chloride tetrahydrate (5 g, 0.25 mol) and 1,2-propanediol (100 mL) in a 500 mL round-bottomed flask containing a magnetic stir bar, condenser and side-arm blocked with stopper. Solution B was prepared by mixing 5 M sodium hydroxide (NaOH) (50 mL) and 1,2-propanediol (50 mL) in a 250 mL round-bottomed flask containing a magnetic stir bar. With magnetic stirring, solution A was heated to 180^{o}C under reflux using a graphite bath, while solution B was heated to 100^{o}C in an oil bath simultaneously for 30 min. Subsequently, hot solution B was rapidly added to solution A via the side-arm before re-sealing with the stopper and leaving under reflux for 1 h. The solution underwent a colour change from dark orange to grey in the initial 10 min, before turning jet black 30 min post-addition. The reaction was then allowed to cool to room temperature under stirring before quenching with methanol (MeOH) (200 mL). Particles were collected and purified via centrifugation (4000 rpm/2580 x g, 10 min) using a benchtop centrifuge with swinging bucket rotor to accommodate 50 mL Falcon tubes after separating the crude reaction mixture into Falcon tubes of equal volumes (50 mL). Supernatants were removed and nanoparticle pellets were redispersed in MeOH (50 mL) by sonication. The purification step was repeated 3 times. Dry nanoparticles were collected by redispersing pellets in a minimal volume of MeOH (~20 mL) by sonication, before drying on a rotary evaporator. Yield: 4.7 g (94%).

2.2.3.2. Acid-terminated PNIPAM/PNIPMAM

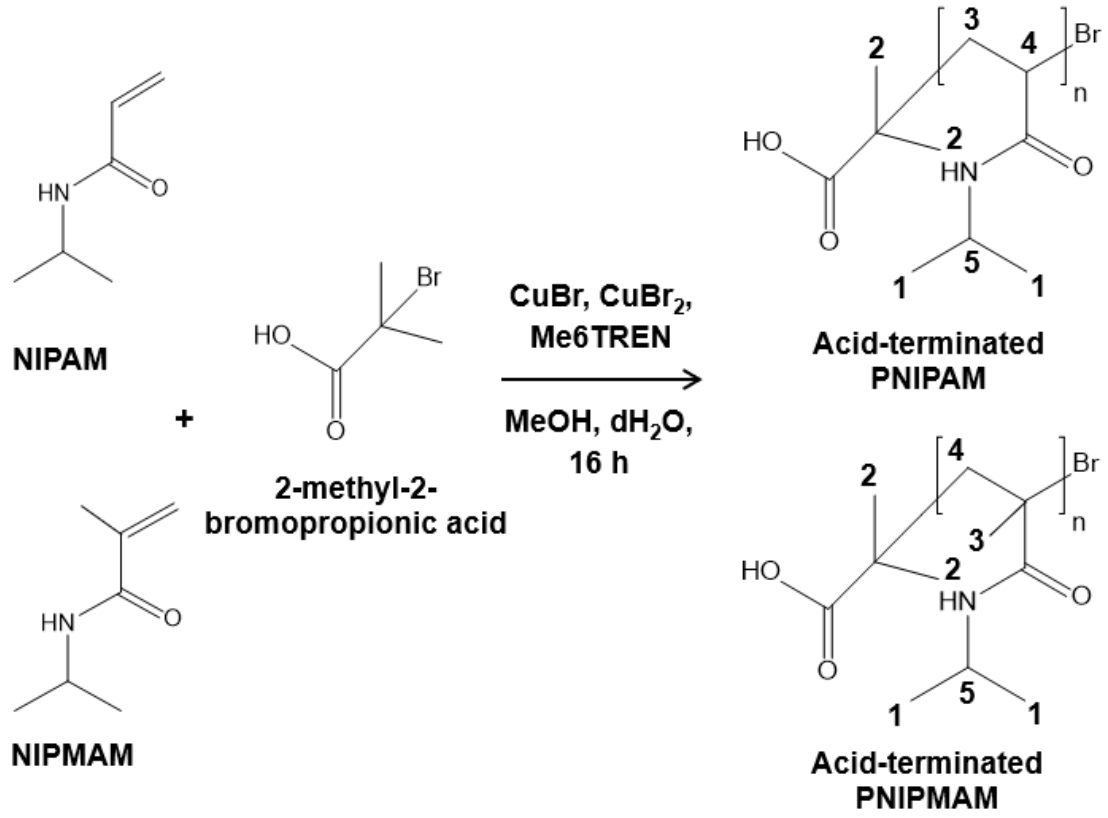

Scheme 2.1. Reaction scheme for ATRP synthesis of acid-terminated PNIPAM/PNIPMAM, simulated PNIPAM ^{1}H NMR: δ = 1.17 ppm (d, 3H, **1**) 1.26 ppm (s, 3H, **2**) 2.05 ppm (d, 2H, **3**) 4.22 ppm (m, 1H, **4**) 4.27 ppm (m, 1H, **5**), simulated PNIPMAM ^{1}H NMR: δ = 1.17 ppm (d, 3H, **1**) 1.26 ppm (s, 3H, **2**) 1.36 ppm (s, 3H, **3**) 1.78 ppm (s, 2H, **4**) 4.28 ppm (m, 1H, **5**).

Copper bromide (CuBr), copper(II) bromide ($CuBr_2$) and 2-methyl-2-bromopropionic acid was from acquired Fisher Scientific and Me_6TREN was acquired from Tokyo Chemical Industry (TCI).

Synthesis was adapted from previous study (Kurzhals et al., 2015). For a 1 g scale reaction, *N*-isopropylacrylamide/*N*-isopropylmethacrylamide (NIPAM/NIPMAM) (1 g, 8.8 mmol), CuBr (13 mg, 0.09 mmol), $CuBr_2$ (2 mg, 0.009 mmol), and 2-methyl-2-bromopropionic acid (16.7 mg, 0.1 mmol) were added to a 50 mL round-bottomed flask containing a magnetic stir bar. dH_2O (9 mL) and MeOH (1 mL) were added before sealing with a septum and purging the vessel with nitrogen for 20 min whilst dissolving the reagents with stirring. The reaction vessel was then cooled in an ice-water bath. In parallel, Me_6TREN (40 µL, 0.15 mmol) was

dissolved in dH_2O (1 mL) by mild manual agitation in a sample vial and the vessel was sealed with a septum and purged with nitrogen for 20 min. The ligand solution (Me_6TREN) was subsequently injected rapidly under inert conditions (using a nitrogen purged syringe) into the NIPAM-containing flask and left stirring for 16 h. After polymerisation the reaction vessel was opened to air and heated to 50^oC in an oil bath with magnetic stirring to precipitate out the polymer. The supernatant volume was removed and the polymer was dried on a rotary evaporator. Once dried, the crude product was dissolved in THF (10 mL) and precipitated by pouring into ice-cold diethyl ether (40 mL). The mixture was subsequently added to a 50 mL Falcon tube for centrifugation (4000 rpm/2580 x g, 10 min) using a benchtop centrifuge with swinging bucket rotor to accommodate 50 mL Falcon tubes. Afterwards the supernatant was removed and the purified polymer pellet was dissolved in a minimal amount of dH_2O (~10 mL) before drying on a rotary evaporator at 40^oC. PNIPAM: Yield: 930 mg (93%), M_n: 13 kDa, M_w: 13.26 kDa, PDI: 1.02, LCST: 32^oC, PNIPAM experimental ^{1}H NMR: ($CDCl_3$, 400MHz) δ = 1 - 1.2 ppm (**1, 2**) 2.14 ppm (**3**), 3.8 – 4.2 ppm (**4, 5**), PNIPMAM: Yield: 880 mg (88%), 3 day polymerisation: M_n: 10.8 kDa, M_w: 9.5 kDa, PDI: 0.88, 7 day polymerisation: M_n: 12.8 kDa, M_w: 12.2 kDa, PDI: 0.94, 3 and 7 day polymerisation experimental ^{1}H NMR: ($CDCl_3$, 400MHz) δ = 1 – 1.3 ppm (**1** – **3**) 1.5 ppm (**4**) 4 ppm (**5**).

2.2.3.3. Poly(*N*-succinimidyl methacrylate) (PMASI) synthesis

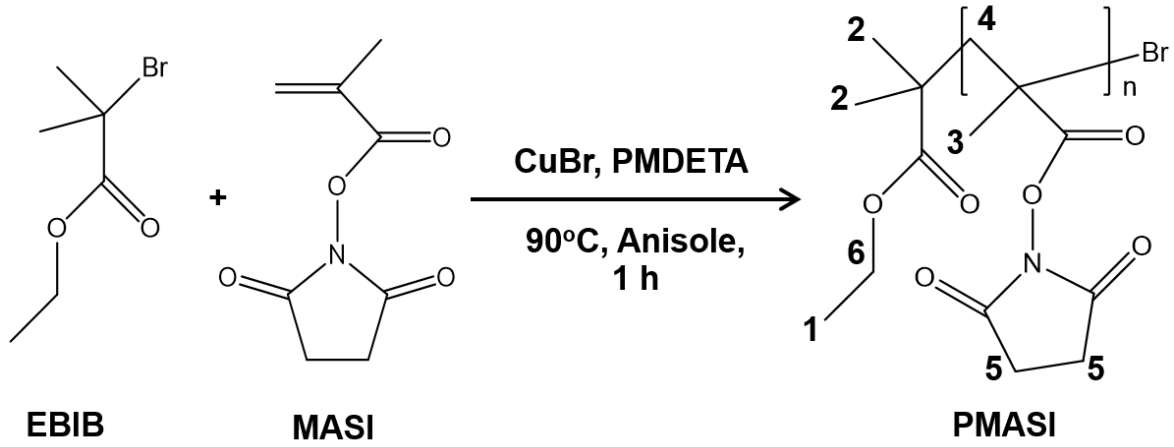

Scheme 2.2. Reaction scheme for synthesis of PMASI precursor, simulated ^{1}H NMR: δ = 1.19 ppm (t, 3H, **1**) 1.25 ppm (s, 3H, **2**) 1.44 ppm (s, 3H, **3**) 1.77 ppm (s, 2H, **4**) 2.83 ppm (m, 2H, **5**) 4.12 ppm (m, 2H, **6**).

N-succinimidyl methacrylate (MASI), *N, N, N', N", N"*-pentamethyldiethylenetriamine (PMDETA) and ethyl 2-bromoisobutyrate (EBIB) were purchased from TCI and dry anisole from Acros Organics.

Synthesis was adapted from a previous study (Rathfon and Tew, 2008). For a 1 g scale reaction MASI, (1 g, 5.46 mol) and CuBr (17.8 mg, 0.12 mmol) were added to a 25 mL round-bottomed flask containing a magnetic stir bar, sealed with a septum and purged with nitrogen for 15 min. Simultaneously, dry anisole was purged with nitrogen for 15 min. Dry anisole (8 mL) was then added under inert conditions (using a nitrogen purged syringe) to the round-bottomed flask and the solution was allowed to dissolve with stirring for 15 min. In parallel, a sample vial and the PMDETA-containing vial were sealed with a septum and purged with nitrogen for 5 min. PMDETA (26 µL, 0.12 mmol) and 400 µL dry anisole were added to the purged sample vial under inert conditions (using a nitrogen purged syringe), mildly agitated to mix and left for a further 10 min. The PMEDTA solution was then added to the round-bottomed flask under inert conditions (using a nitrogen purged syringe) and left to stir at room temperature for 20 min to form the catalyst causing a blue colour change. In parallel, a sample vial and the EBIB-containing vial were sealed with a septum and purged with nitrogen for 5 min. EBIB (20 µL, 0.12 mmol) and 400 µL dry anisole were added to the purged sample vial under inert conditions (using a nitrogen purged syringe), mildly agitated to mix

and left for a further 15 min. The EBIB solution was then injected into the round-bottomed flask under inert conditions (using a nitrogen purged syringe) and left to stir at 90^{o}C for 1 h. Crude product was then dried on a rotary evaporator at 40^{o}C. Crude dry product was dissolved in a minimal amount of DMSO (~10 mL) and precipitated by pouring in ice-cold acetone (40 mL). The mixture was subsequently added to a 50 mL Falcon tube for centrifugation (4000 rpm/2580 x g, 10 min) using a benchtop centrifuge with swinging bucket rotor to accommodate 50 mL Falcon tubes. The supernatant was then removed and the polymer pellet was dissolved in a minimal amount of DMSO (~10 mL) before drying on a rotary evaporator at 40^{o}C. Yield: 900 mg (90%), experimental ^{1}H NMR: (DMSO-d_6, 400MHz), δ = 1 – 1.8 ppm (**1** – **4**) 2.8 ppm (**5**) 3.6 ppm (**6**).

2.2.3.4. Acid-terminated PNIPMAM

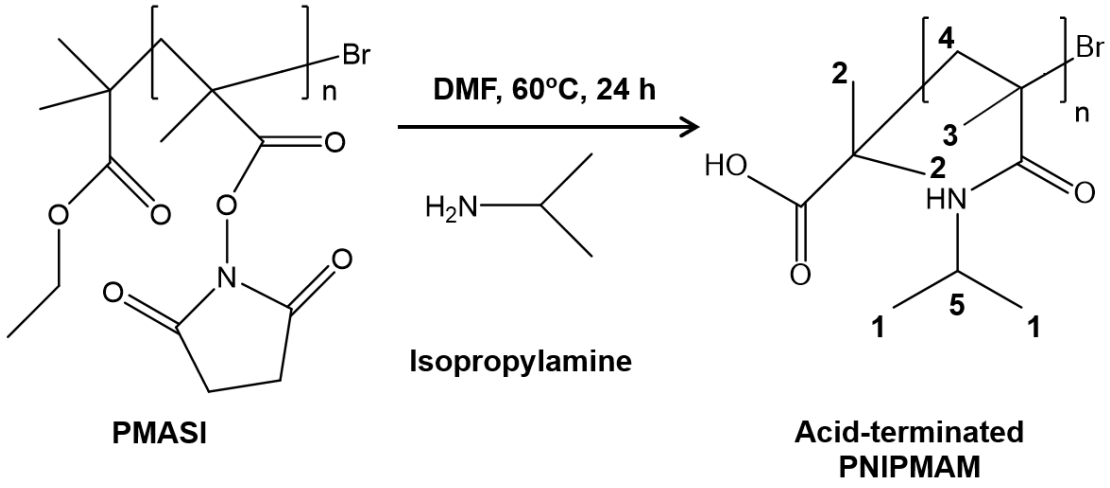

Scheme 2.3. Reaction scheme for synthesis of acid-terminated PNIPMAM, simulated ^{1}H NMR: δ = 1.17 ppm (d, 3H, **1**) 1.26 ppm (s, 3H, **2**) 1.36 ppm (s, 3H, **3**) 1.78 ppm (s, 2H, **4**) 4.28 ppm (m, 1H, **5**).

Isopropylamine was purchased from Alfa Aesar and PMASI was synthesised in-house.

Synthesis was adapted from a previous study (Rathfon and Tew, 2008). For a 900 mg scale reaction, PMASI (900 mg, 0.09 mmol) was added to a 25 mL round-bottomed flask in an oil bath at 60°C containing a magnetic stir bar and dissolved in dry dimethylformamide (DMF) (10 mL). The vessel was sealed with a septum and purged with nitrogen for 15 min. Simultaneously the isopropylamine-containing vial was purged with a nitrogen balloon for 15 min. Four equivalents of isopropylamine (1.25 mL, 0.36 mmol) were then added under inert conditions (using a nitrogen purged syringe) to the round-bottomed flask and left stirring for 24 h at 60°C. Subsequently, the polymer was precipitated by pouring the reaction volume in ice-cold diethyl ether (40 mL). The mixture was then added to a 50 mL Falcon tube for centrifugation (4000 rpm/2580 x g, 10 min) using a benchtop centrifuge with swinging bucket rotor to accommodate 50 mL Falcon tubes. The supernatant was removed and the polymer pellet dissolved in a minimal amount of dH_2O (~10 mL) before drying on a rotary evaporator at 40°C. The product was then added to a 25 mL round-bottomed flask containing a stir bar and dissolved in 1 M aqueous NaOH (10 mL). This solution was left stirring at room temperature for

6 h before neutralising with hydrochloric acid (HCl). The polymer was precipitated by heating to 50^{o}C and then the mixture was transferred into a 50 mL Falcon tube and centrifuged (4000 rpm/2580 x g, 10 min) using a benchtop centrifuge with swinging bucket rotor to accommodate 50 mL Falcon tubes before removal of the supernatant and dissolving the pellet in 25 mL dH_2O, this purification step was repeated 3 times. The polymer was then dissolved in a minimal amount of dH_2O (10 mL) and dried on a rotary evaporator at 40^{o}C. Yield: 756 mg (84%), M_n: 11,245 Da, M_w: 10,378 Da, PDI: 0.92, LCST: 42^{o}C, experimental ^{1}H NMR: (DMSO-d_6, 400MHz), δ = 1-1.4 ppm (**1** – **3**) 1.7 ppm (**4**) 3.8 – 4 ppm (**5**).

2.2.3.5. NDA

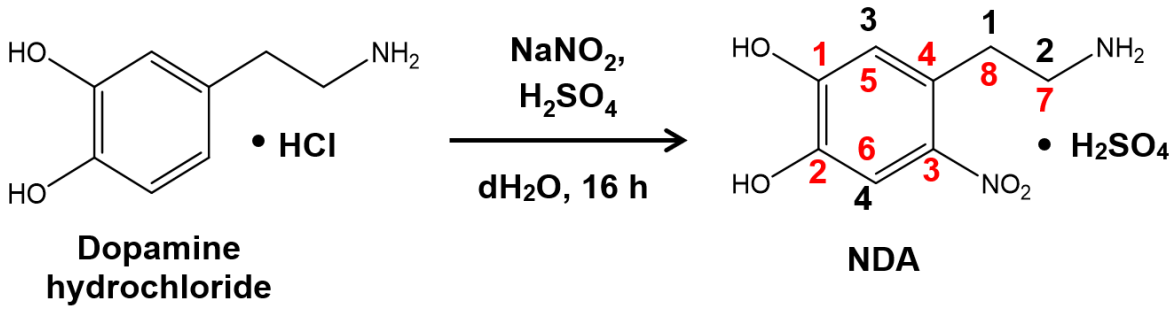

Dopamine hydrochloride

NDA

Scheme 2.4. Reaction scheme for synthesis of NDA, black numbers denote ^{1}H NMR assignment, red numbers denote ^{13}C NMR assignment, simulated ^{1}H NMR: δ = 2.26 ppm (t, 2H, **1**) 2.76 ppm (t, 2H, **2**) 6.36 ppm (s, 1H, **3**) 6.67 ppm (s, 1H, **4**), simulated ^{13}C NMR: δ = 145.4 ppm (**1**) 143.1 ppm (**2**) 140.5 ppm (**3**) 129.9 ppm (**4**) 111.0 ppm (**5**) 100.9 ppm (**6**) 42.2 ppm (**7**) 31.1 ppm (**8**).

Synthesis was adapted from a previous study (Napolitano et al., 1992). For a 2 g scale reaction, dopamine hydrochloride (2 g, 10 mmol) and sodium nitrite (1.52 g, 22 mmol) were dissolved in dH_2O (25 mL) in a 100 mL round-bottomed flask containing a magnetic stir bar resulting in a pale, yellow solution. The vessel was subsequently cooled in an ice-water bath while stirring. In parallel, concentrated sulfuric acid (H_2SO_4) (960 µL, 17 mmol) was added slowly to dH_2O (6 mL) before making the solution up to 10 mL. The H_2SO_4 solution was then added dropwise, slowly (over ~30 min) to the ice-cooled dopamine solution while stirring. A yellow precipitate formed and the reaction vessel was left stirring overnight at room temperature. Subsequently the solution was filtered using a Büchner funnel. The precipitate was recrystallised from hot (70°C) dH_2O (50 mL) to yield small, yellow crystals which were dried on a rotary evaporator at 40°C. Yield: 1.3 g (65%), experimental ^{1}H NMR: (DMSO-D_6, 400MHz) δ = 2.9 – 3.1 ppm (**1**, **2**), 6.87 ppm (**3**), 7.48 ppm (**4**), experimental ^{13}C NMR: (DMSO-d_6, 100 MHz), δ = 154.1 ppm (**1**) 145.2 ppm (**2**) 139.3 ppm (**3**) 127.1 ppm (**4**) 119.2 ppm (**5**) 112.6 ppm (**6**) 40.1 ppm (**7**) 31.3 ppm (**8**).

2.2.3.6. NDA-terminated PNIPAM/PNIPMAM (NDA-PNIPAM/PNIPMAM)

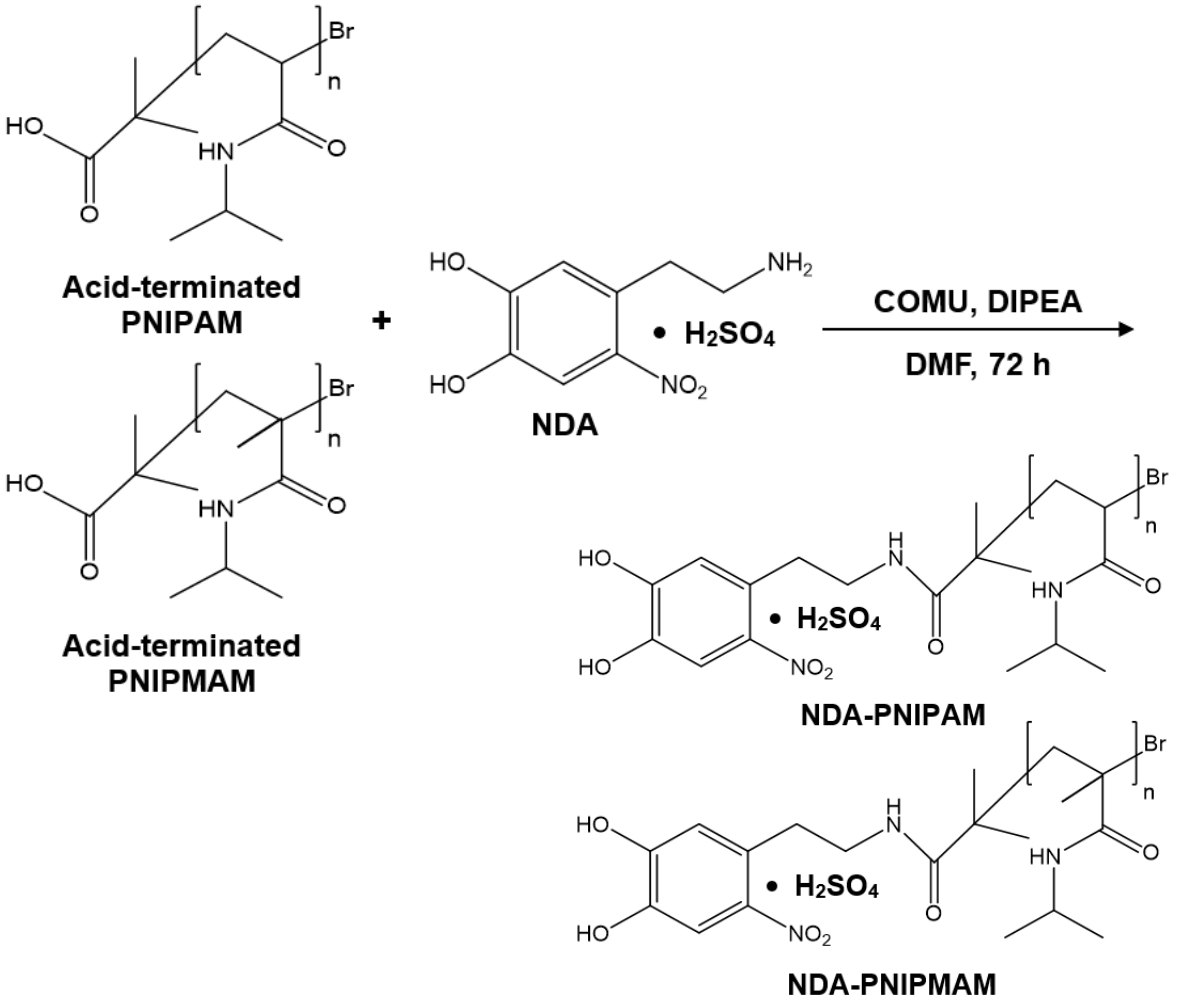

Scheme 2.5. Reaction scheme for amide coupling reaction to form NDA-PNIPAM/PNIPMAM.

Acid-terminated PNIPAM, PNIPMAM and NDA were synthesised in-house.

Synthesis was adapted from a previous study (Kurzhals et al., 2015). For a 1 g scale reaction acid-terminated PNIPAM/PNIPMAM (1 g, 0.1 mmol), 1-cyano-2-ethoxy-2-oxoethylidenaminooxy)dimethylamino-morpholino-carbenium hexafluorophosphate (COMU) (51 mg, 0.12 mmol) and *N*, *N*-diisopropylethylamine (DIPEA) (17 µL, 0.1 mmol) were added to a 50 mL round-bottomed flask containing a magnetic stir bar. Dry DMF (20 mL) was added before sealing the flask with a septum and purging with nitrogen for 5 min whilst dissolving the reagents by stirring. The solution was left stirring under nitrogen for 1 h at room temperature resulting in a yellow colour change. Subsequently NDA (89 mg, 0.3

mmol) and DIPEA (34 µL, 0.2 mmol) were added to DMF (1 mL) in a sample vial before sealing with a septum and purging with nitrogen for 5 min. The NDA solution was then injected under inert conditions (using a nitrogen purged syringe) into the polymer-containing round-bottomed flask and left stirring under nitrogen at room temperature for 3 days. Acidification of the solution was then carried out by the addition of a few drops (5-6) of 2 M HCl before precipitating the polymer by pouring into ice-cold diethyl ether (80 mL). The mixture was subsequently added to 50 mL Falcon tubes for centrifugation (4000 rpm/2580 x g, 10 min) using a benchtop centrifuge with swinging bucket rotor to accommodate 50 mL Falcon tubes. Then the supernatant was removed and the polymer pellet dissolved in a minimal amount of dH_2O (~10 mL) before dialysis (M_w cut-off: 3.5 kDa) against dH_2O. The product was dried on a rotary evaporator at 40^oC. NDA-PNIPAM: Yield: 750 mg, (75%), UV-vis NDA-functionality: 67%. NDA-PNIPMAM: Yield: 785 mg, (78.5%), UV-vis functionality: 60%.

2.2.3.7. Polymer-coated nanoparticle preparation

All reagents used were synthesised in-house.

Preparation was adapted from a previous study (Kurzhals et al., 2015). For a 1 g scale coating, iron oxide nanoparticles (1 g) were dissolved in 100 mL sodium citrate (1 mM, pH 7.4) in a 500 mL round-bottomed flask. The solution was briefly sonicated (1 min) before nanoparticle magnetic separation and 3 wash steps with dH_2O (100 mL). NDA-terminated polymer (5 g) was then dissolved into the flask by sonication. Then, in an ice-cold sonicator bath, the mixture was sonicated for 5 h ensuring that throughout the water temperature did not exceed that of the polymer phase transition (32^oC for PNIPAM, 42^oC for PNIPMAM). The mixture was then left in a room temperature shaker overnight before subsequently collecting the polymer-coated nanoparticles by ultracentrifugation (50,000 rpm/135,800 x g, 30 min) using a Beckman Optima series benchtop ultracentrifuge and a TLA-110 rotor. The supernatant was removed and the particles were re-dissolved in dH_2O (~200 µL) before repeating the centrifugation step a further 3 times. Dry polymer-coated nanoparticles were then collected by re-dissolving the particles in minimal dH_2O (~10 mL) prior to rotary evaporation under high vacuum at 40^oC. PNIPAM-coated nanoparticles: Yield: 1.45 g (72.5%), LCST: 32.8^oC, TGA: ~50% mass loss >400^oC, grafting density: 0.275 chains/nm^2, XPS: 714.5 eV (Fe), 532.6 eV (O), 400.5 eV (N), 285.5 eV (C). PNIPMAM-coated nanoparticles: Yield: 1.25 g (62.5%), LCST: 42^oC.

2.2.4. Magnetic heating

2.2.4.1. Magnetic heating equipment specifications

All equipment for magnetic heating work was kindly provided by Dr. Iain Will, (Department of Electronics, University of York).

The electromagnet used comprised a capacitor and inductor coil (wrapped around a ferrite core) for improved efficiency. The operating frequency was determined using **Equation 2.4**:

$$f_o = \frac{\omega 0}{2\pi} = \frac{1}{2\pi\sqrt{LC}}$$

Where *fo* is frequency (Hz), L is inductance (H) and C is the capacitance (F). The angular frequency (ω_0) has units of radians per second.

Equation 2.4. Operating frequency determination from electromagnet.

The inductor coil of the electromagnet formed part of a tuned oscillating tank circuit, providing the alternating magnetic *B*-field. The coil is shown here below in **Figure 2.1,** where the inductance (L) of the coil around the magnet is linked to the frequency, *fo* (Hz) of the circuit in **Equation 2.4**. The magnetic field direction changes by 180º at a frequency of 80 kHz.

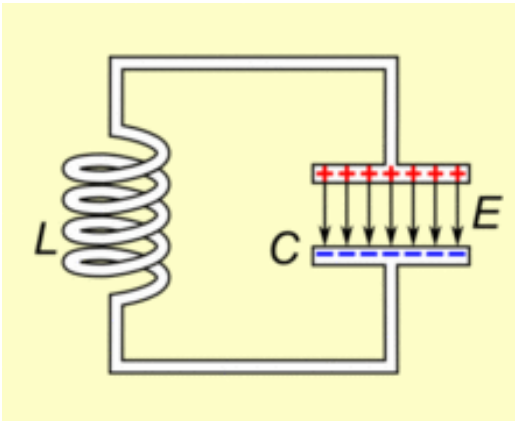

Figure 2.1. Schematic of electromagnetic inductor coil and oscillating tank circuit to establish alternating magnetic *B*-field, where L (Henry) is the inductor, E (volts/meter) is the electric field and C (farads) is the capacitance. Diagram was provided by Dr. Iain Will (Department of Electronics, University of York) (personal communication).

The field strength was set by the current supplied to a centre tap (**Figure 2.3(a)**) on the coils of the magnet. Field strength was measured using a standard search coil approach from **Equations 2.5 – 2.10:**

2.5) $V_{pp} = \omega NAB_{pp}$

2.6) $V_{pp} = 2\pi f\, NAB_{pp}$

2.7) $B = \mu H$

2.8) $V_{pp} = 2\pi f\, NA\, \mu H_{pp}$

2.9) $V_{pp} / \mu\, 2\pi f\, NA = H_{pp}$

2.10) $H_{pp}/2 = H$

Where $2\pi f$ is the angular frequency (ω, radians/s), N is number of turns in the search coil, f is frequency, A is area, V_{pp} is voltage in the search coil, B_{pp} (T) is peak to peak induction from the field coils and H_{pp} (H) from the search coil. Frequency is measured using an oscilloscope.

Equations 2.5 – 2.10: Field strength measurement equations using a standard search coil technique.

The sinusoidal wave form of the magnetic field across the sample can be seen below in **Figure 2.2**.

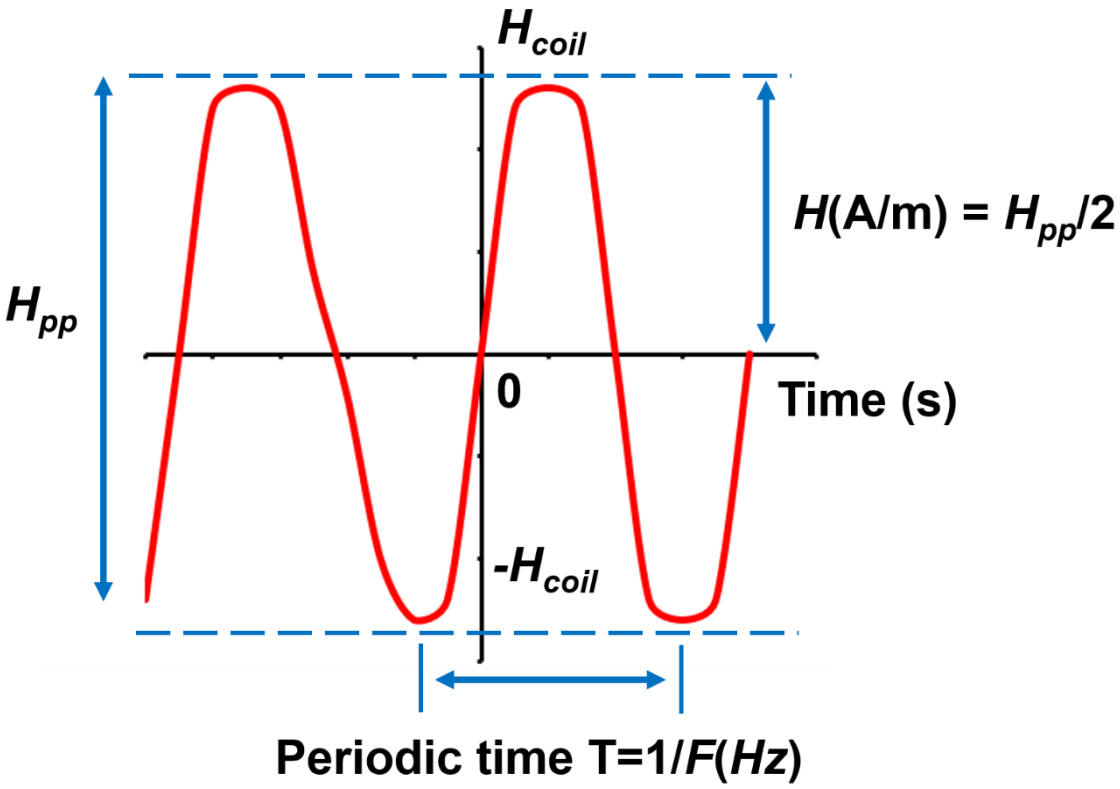

Figure 2.2. Sinusoidal wave form of the magnetic field across the sample.

The setup used for magnetic heating experiments can be seen below in **Figure 2.3**. **Figure 2.3(a)** shows the internal components of the setup which are contained within a sealed box with a circulating fan, including the ferrite core which has high magnetic permeability and low electrical conductivity (inhibits eddy current formation). The windings of the inductors are formed on this magnetic, ferrite core. For this application (< 5 MHz), a MnZn ferrite was used which concentrates the magnetic field (H) across a narrow 10 mm gap where the sample is placed. This allows for larger field strength production. Also, in **Figure 2.3(a)** the sample tube gap where the field is concentrated can be seen highlighted in red**.** Around the ferrite core is a water-cooled copper coil which forms the magnetic field (inductor in **Figure 2.1**). **Figure 2.3(a)** shows the choke used to prevent AC power being reflected back into a power supply, providing an energizing current to the centre tap of the inductor coil. Moreover, the transistor circuit can be seen in **Figure 2.3(a)** which is coupled with the capacitor and feeds the inductor coil with additional electrical energy, allowing the LC circuit to keep resonating. **Figure 2.3(b)** shows the entire setup as arranged for experimental work where the gallium

arsenide thermocouple probe and temperature sensor display are highlighted in red. The operating parameters of the magnetic field used were a 0.67 T field strength and a 108 kHz alternating frequency.

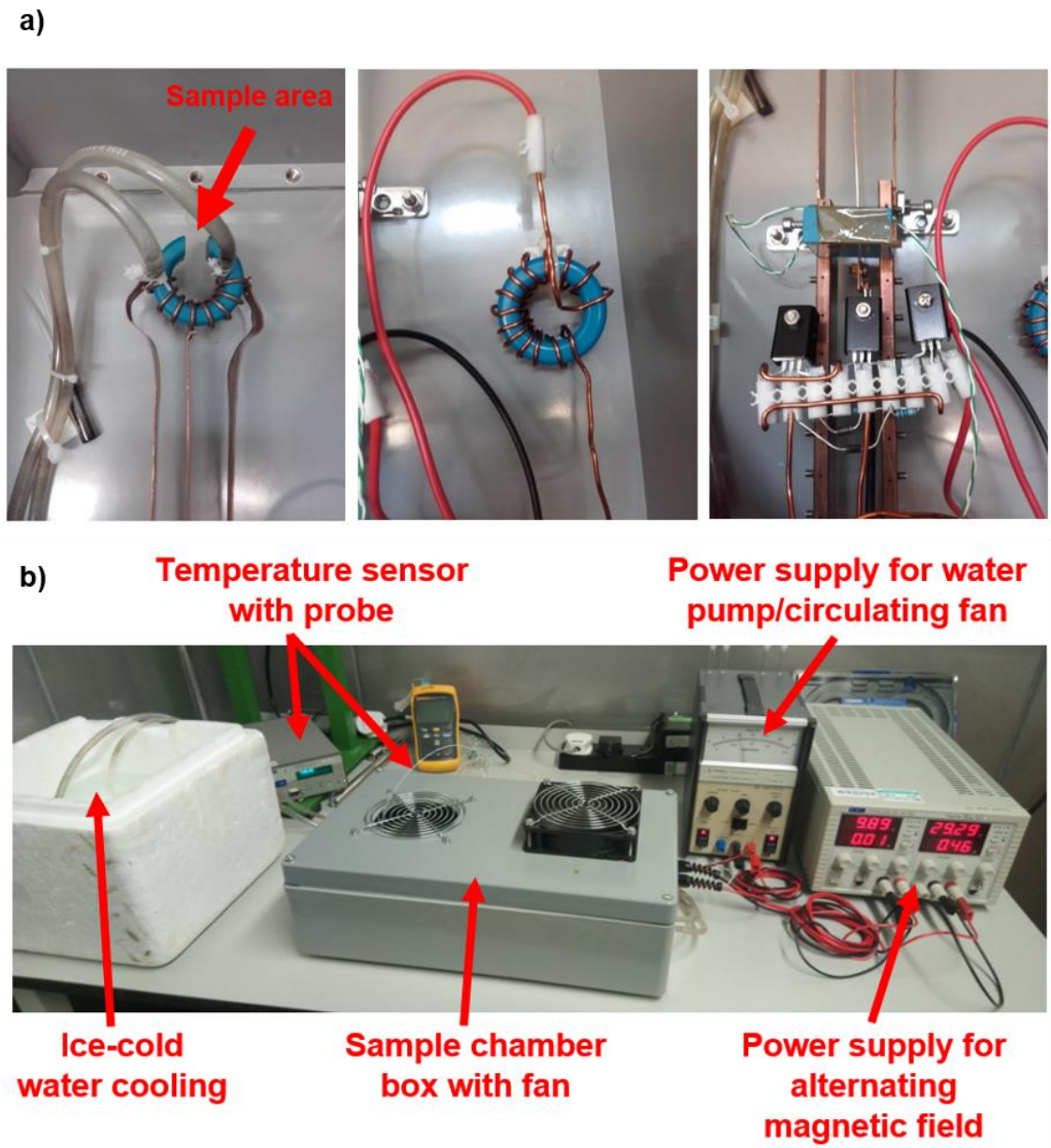

Figure 2.3. Magnetic heating setup: a) Internal components of sealed box with sample area for magnetic heating (red), ferrite core, induction coil and electrical connections with centre tap power conductor in the centre (left), choke (centre) and transistor circuit (right). **b)** Entire setup for experimental work from left to right; ice-water box for coil cooling, infrared thermocouple with probe, sample chamber box with circulating fan, power box for circulating fan/ice-water coil cooling, and power box for alternating magnetic field.

2.2.4.2. Magnetic heating measurements

Assays for magnetic heating were conducted in a sample chamber, contained within a sealed box equipped with a circulating fan (**Figure 2.3(b)**), allowing for a constant temperature to flow over the sample area (**Figure 2.3(a)**). The sample area setup within the sealed box, where the alternating magnetic field was concentrated, can be seen in **Figure 2.5**. This shows a sample tube (used for biochemical, apotransferrin experiments) of dimensions 50 mm x 45 mm x 8 mm (length x depth x width) held in a fixed position by a plastic holder. The lid was adapted to allow for insertion of thin plastic tubing for gallium arsenide thermocouple probe to go through and measure sample temperature.

Prior to magnetic heating experiments, a calibration was conducted using a sample tube filled with 100 µL dH_2O and the magnetic field was switched on with ice-cold water circulating through the copper coils, pumped from an external ice-water reservoir by an external pump (**Figure 2.3(b)**). The temperature was monitored until a stable baseline was achieved, at which point the water calibration sample was removed and experimental samples were placed in the setup.

During magnetic heating experiments, with the magnetic field switched on, the lid for the sample chamber was sealed on top of the box. When a sample was withdrawn from the tube during assays, the box lid was lifted to allow access to the sample. The sample tube was removed briefly from the field, the lid was loosened and a thin, long pipette tip, affixed to a pipette, was used to withdraw an aliquot from the tube whilst separating the nanoparticles with a magnet. After removal of sample, the nanoparticles were agitated by pipetting to restore homogeneity before returning to the holder, re-attaching the sample tube lid and securing the box lid on the sample chamber. Sample extraction was done rapidly to ensure the sample environment was not perturbed significantly. It was essential to remove the aliquots away from the alternating magnetic field to prevent interference from the magnet used for particle separation through attraction or heating of the magnet itself. Tubes for cell magnetic heating assays did not have an adapted lid for thermocouple probe, so thermocouple attachment was secured using Parafilm. A diagrammatical representation to show how magnetic heating experiments were conducted can be seen in **Figure 2.4**.

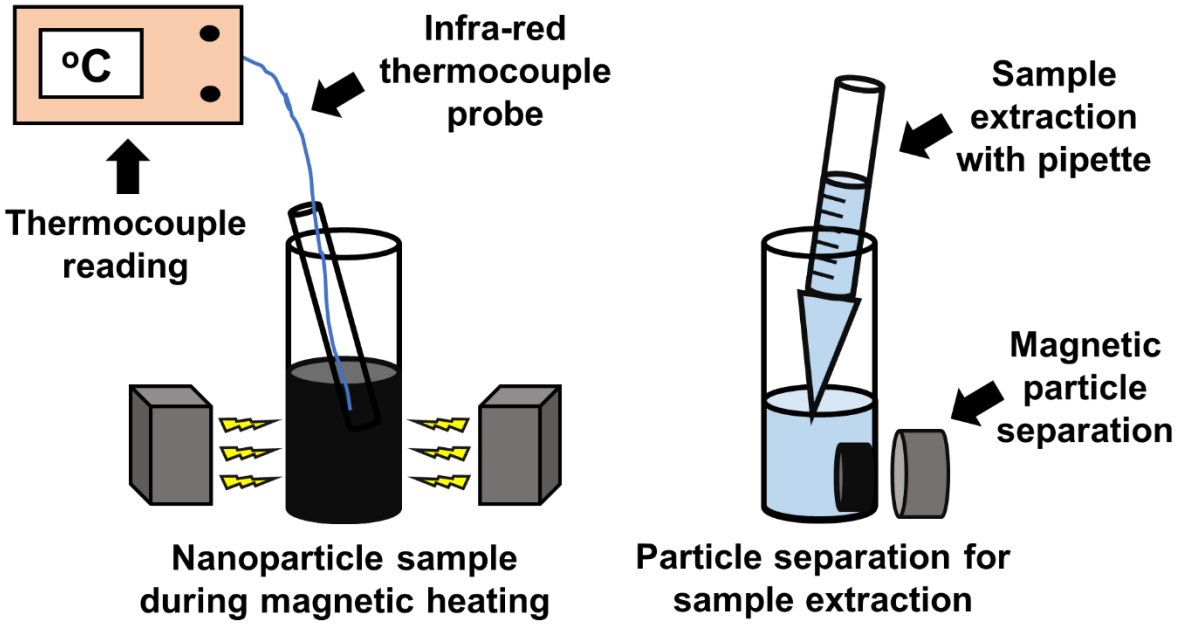

Figure 2.4. Diagrammatical representation of magnetic heating experimental procedure: Magnetic heating of nanoparticle samples with thermocouple inserted to measure temperature (left) and magnetic separation of nanoparticles to allow for removal of sample volume for analysis (right).

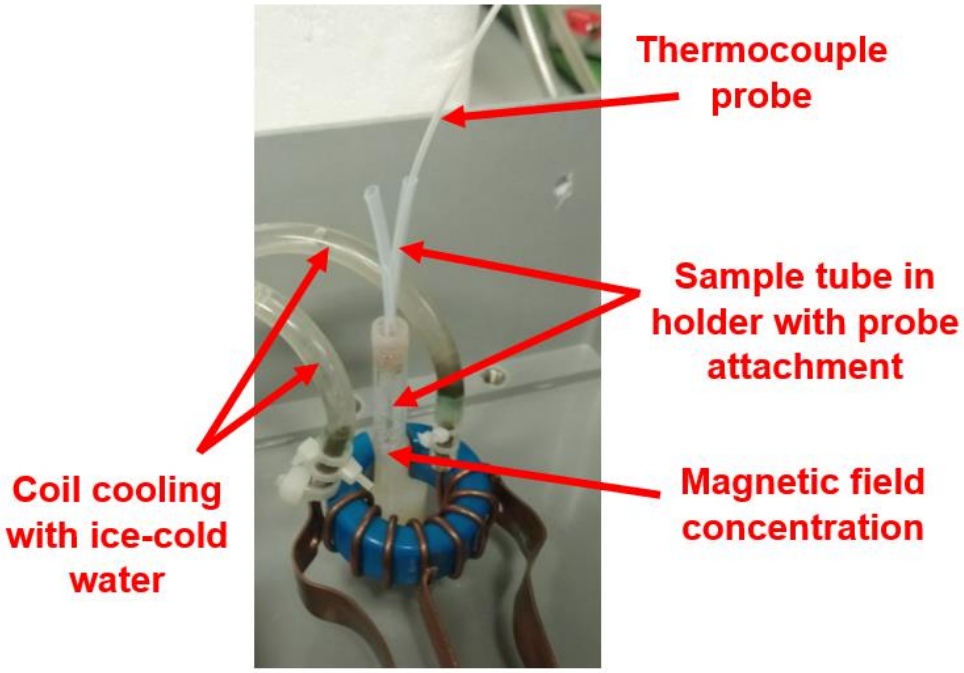

Figure 2.5. Sample setup for magnetic heating experiments: Sample-specific area for magnetic heating assays contained within sealed box. Samples were positioned in an area where the alternating magnetic field was focused. Annotations highlight specific components in this area; thermocouple probe was inserted though adapted inlet for temperature readings and tubing for ice-cold water pumping through surrounding coils was connected.

2.2.4.3. SAR calculation

SAR was calculated using the following equation (Tong et al., 2017):

$$\mathbf{SAR} = \frac{\mathbf{1}}{\mathrm{m}_{\boldsymbol{Fe}}} \boldsymbol{C}_{\mathbf{sol}} \boldsymbol{m}_{\mathbf{sol}} \left(\frac{\mathbf{d}\boldsymbol{T}}{\mathbf{d}\boldsymbol{t}}\right)$$

Where m_{Fe} is the mass of iron in the sample (g), C_{sol} is the specific heat capacity of the solvent (C_{H2O}= 4.184 J K^{-1} g^{-1}), m_{sol} is the mass of solvent (g) and d*T*(K) / d*t* (s) is the temperature gradient vs time.

Equation 2.11. Equation for determining nanoparticle SAR value.

2.3. Results

2.3.1. Synthesis and characterisation of iron oxide nanoparticles

In order to generate iron oxide nanoparticles at a size suitable for biological applications and to confer superparamagnetic properties, a synthetic approach was selected to produce stable, water-soluble particles (Carroll et al., 2010). The synthesis employs a modified polyol process enabling the liquid polyol used to serve as a solvent and reducing agent. Reduction in metal salt precursors can occur in the presence of a base with the polyol functioning as an ideal medium for this, whilst additionally capping the nanoparticle surface for improved stability (Samiee et al., 2012). The synthesis was carried out in a 1,2-propanediol/water solvent mixture as a liquid polyol/reducing agent, using iron (II) chloride tetrahydrate as the metal salt precursor in the presence of NaOH as a base. Nanoparticles were purified using MeOH wash steps and isolated by centrifugation. High yields (94%) of nanoparticles could be generated following this approach, which showed good solubility in water.

For an accurate representation of nanoparticle size and dispersity, analysis was carried out by TEM. The synthesised nanoparticles displayed an average size of 6.3 ± 0.9 nm (**Figure 2.6**). In the literature procedure I followed, the group measured a nanoparticle diameter of 15 ± 2.5 nm, which are larger and less uniform than the nanoparticles generated in previously published work using this synthetic procedure (Carroll et al., 2010). The observed differences could be attributed to variations in how the synthetic procedures were carried out. Factors such as the rate of nanoparticle seed nucleation, growth and termination are all influenced by multiple factors during the synthetic procedure. Nanoparticle size and uniformity can vary based on variables such as rate of stirring, which maintains sample homogeneity during seed nucleation by metal salt reduction, or rate of solution cooling to terminate nanoparticle growth. This means exactly replicating nanoparticle synthesis conditions can be challenging. Additionally, the TEM micrographs below show a uniform contrast throughout the entirety of the nanoparticle unlike previously published images where they show some core-shell contrast (Carroll et al., 2010). This likely indicates full oxidation of the nanoparticles to iron oxide compared to an iron-iron oxide core-shell structure. The dispersity of the nanoparticles could be markedly improved by briefly pre-dispersing in sodium citrate before washing and polymer coating. Nanoparticles

without citrate treatment appeared to aggregate more significantly which has been observed previously for these particles (Carroll et al., 2010). These results indicate that I have produced stable, disperse solutions of nanoparticles at a size suitable for biological studies.

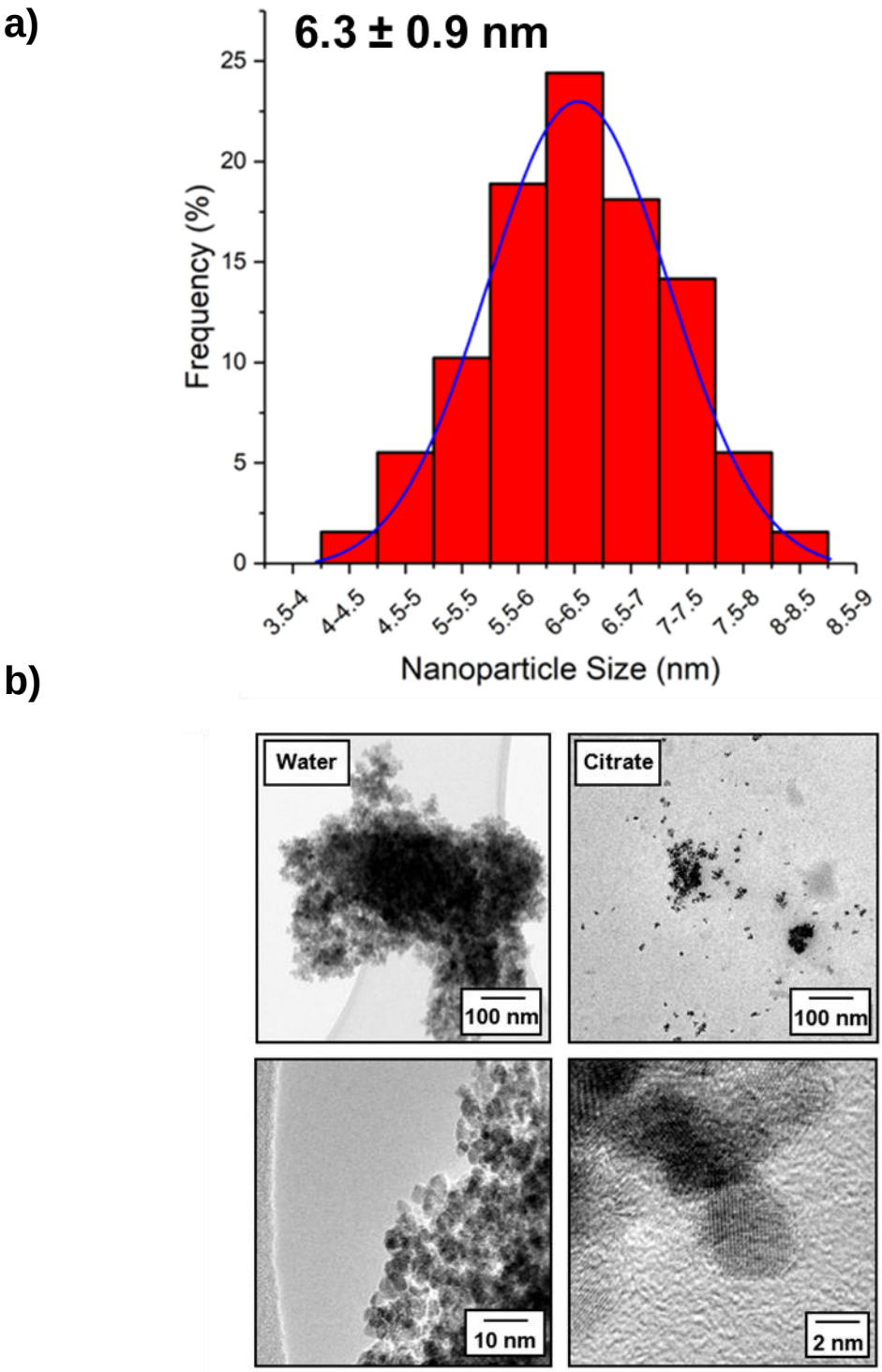

Figure 2.6. TEM analysis of iron oxide nanoparticles: a) Size distribution histogram of nanoparticles analysed by TEM with an average diameter of 6.3 ± 0.9 nm (± error denotes standard deviation, n = 84). Nanoparticle size measured using ImageJ software with line drawing tool relative to scale bar. Graph was generated using Origin software and plotted with a Gaussian distribution trendline. **b)** TEM micrographs at low magnification of nanoparticles without (water) (top left) and with (top right) citrate coating. Higher magnification images (bottom left, right) were used for measuring size distribution as shown for citrate coated particles in panel **(a)**.

2.3.2. Magnetic characterisation of iron oxide nanoparticles

In order to ascertain suitability of the nanoparticles for magnetic heating assays, their magnetic properties were assessed. Measurements were conducted to characterise the type of magnetism exhibited, magnetic stability and magnetic heating efficiency.

To determine the magnetisation properties of the nanoparticles, vibrating sample magnometry (VSM) was conducted at a range of temperatures from 10 – 40^{o}C. During VSM measurements, the sample is magnetised in a uniform magnetic field before being sinusoidally vibrated using a piezoelectric material. The induced voltage is measured with a lock-in amplifier using the piezoelectric material as a frequency reference, where the induced voltage of pickup coils is proportional to the magnetic moment of the material and independent of the strength of the applied magnetic field. Magnetisation of the material is measured as electromagnetic units/magnetic moment (emu) and is a measure of the density of magnetism derived from the number of magnetic moments in a given volume. A robust method to measure whether nanoparticles display superparamagnetic properties is to correlate increasing temperature with reduced magnetisation in response to an applied field. This is because magnetisation will be affected even by thermal fluctuations in superparamagnetic particles (Teja and Koh, 2010). Based on my observations of nanoparticle size at 6.3 ± 0.9 nm nm by TEM, I would expect to see superparamagnetic features as their size falls within the appropriate region for exhibiting this type of magnetism with single domain properties (Li et al., 2017). VSM analysis showed a trend corresponding to nanoparticles of a superparamagnetic nature as they displayed no remanent magnetisation throughout (**Figure 2.7**). Remanent magnetisation is characteristic of ferromagnetic materials (**Figure 1.3**) where hysteresis loops are observed due to a magnetic response even in the absence of a magnetic field (Somasundaran, 2006).

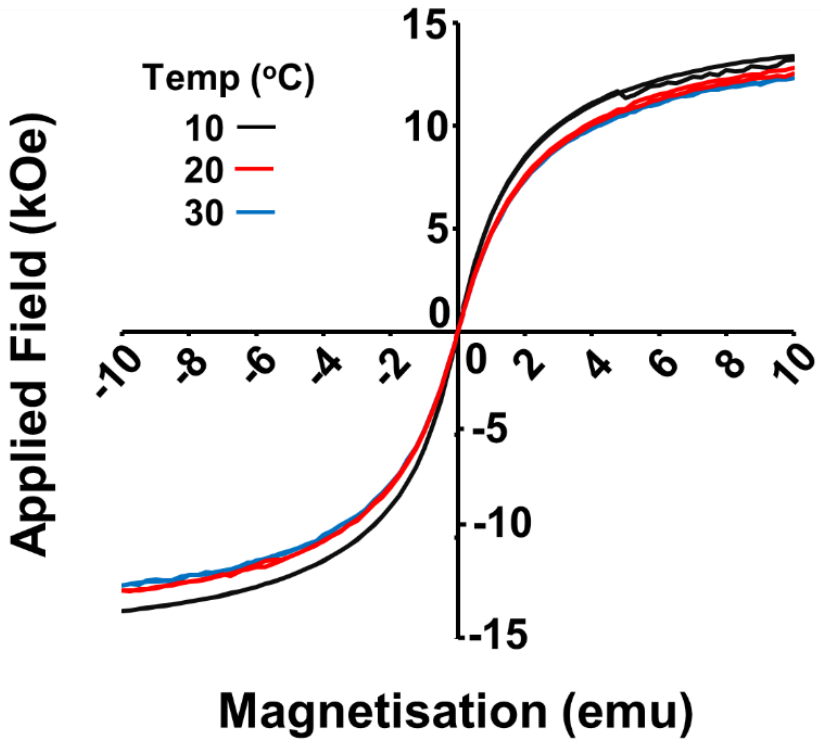

Figure 2.7. VSM of iron oxide nanoparticles: Analysis of 10 mg/mL samples recorded across an applied field of -10 to 10 kOe with forward and reverse field sweeps taken at temperatures from 10 – 30°C with 10°C intervals, (black = 10°C, red = 20°C, blue = 30°C). The graph was generated by plotting the raw signal (magnetisation) relative to the magnetic field strength (applied field).

I also wanted to assess long-term stability of the nanoparticles and monitor their magnetic properties over time. This was conducted using magnetic susceptibility as a quantitative readout of the nanoparticle responsiveness to an external magnetic field. Nanoparticles were stored by refrigeration at 10 mg/mL in dH_2O and measured immediately following synthesis and also 3 months post-synthesis. Nanoparticles were prepared for susceptibility measurements by immobilisation in an agarose gel prior to analysis. This was done because nanoparticle samples suspended in water were attracted to the magnet within the Guoy balance which gave overestimated readings, meaning accurate measurements could not be made. Over a 3-month period, I could calculate a susceptibility loss of 0.3 $\chi_g/m^3kg^{-2}(x10^{-4}$ (**Table 2.2**). This indicates that over long time periods, the nanoparticles largely retain their magnetic properties indicating good stability. This allows for batch production on a large scale removing the need to synthesise particles on a

frequent basis to retain high levels of magnetic stability. Previous work from a project student (Daniel Wrigley, personal communication) also observed very little decrease in nanoparticle susceptibility over a 3-month period. The literature followed for the particle synthesis reports long term stability over a 1-year period (Carroll et al., 2010). Since the susceptibility measurements were conducted on samples from a single nanoparticle batch, it would be beneficial to conduct further measurements on separate batches/samples in the future to more reliably ascertain the particle stability.

Time (weeks)	**Magnetic susceptibility ($\chi_g/m^3kg^{-2}(x10^{-4})$**	**Susceptibility loss ($\chi_g/m^3kg^{-2}(x10^{-4})$**
1	2.9	0.3
12	2.57	

Table 2.2. Magnetic susceptibility analysis for iron oxide nanoparticles: Magnetic susceptibility measurements recorded on 10 mg/mL iron oxide nanoparticles after synthesis (1 week) and 3 months (12 weeks).

Having observed that the nanoparticles displayed superparamagnetic properties, I investigated their magnetic heating capacity. These, and all subsequent magnetic heating assays, were conducted using an in-house engineered setup (Iain Will, Department of Electronics) which can be seen in **Figure 2.3**. Real-time temperature measurements of the sample volume could be recorded through the use of a gallium arsenide infrared thermocouple probe. As this contained no trace paramagnetic material, any heating observations could be attributed to those generated by the sample. Additionally, as a further control, ice-cold cooling of the coils prevented any background heating generated from components of the setup during the measurements. A magnetic heating rate of $0.3^oC\ min^{-1}$ was observed from 5 mg/mL nanoparticles after measuring over a 30 min period. As a control, a sample containing no nanoparticles (water) was exposed to the field for 30 min

also with no significant temperature change observed. Moreover, when exposing nanoparticles to an alternating magnetic field, by correlating the temperature readings over time with the mass and specific heat capacities of both the solvent and particles, the SAR can be determined as a readout of total energy input in the solution and thereby acts as a value for optimisation of magnetic nanoparticles for magnetic heating applications (Tong et al., 2017). By applying the magnetic heating data to **Equation 2.11**, I could determine a nanoparticle SAR value of 65.27 W/g Fe (watts/gram iron). Generating larger nanoparticles that still exhibit superparamagnetic properties, ideally using aqueous synthetic approaches to improve bio-suitability, would certainly be more suitable for higher SAR values and more efficient magnetic heating rates.

Here I have been able to generate SPIONs that are stable over long periods of time and are able to undergo magnetic heating in the presence of an alternating magnetic field.

2.3.3. Synthesis and characterisation of acid-terminated PNIPAM

Coating of nanoparticles with a suitable polymer is essential for targeted delivery and release of biomolecules. I considered using a temperature-sensitive polymer capable of undergoing a specific phase transition that could be used as a mechanism to encapsulate and release proteins upon heating. Also, having observed magnetic heating of the nanoparticles, utilising this mechanism as a means of inducing a coil-to-globule transition in a temperature-sensitive polymer would be a potentially interesting approach to trigger release of entrapped proteins. PNIPAM is an extensively studied, temperature-sensitive polymer and has great potential particularly in the field of biomolecule delivery. It has a well-defined LCST of ~32^{o}C, which is an appropriate temperature for heating assays involving proteins in that their functionality is likely to be unaffected under such conditions. Moreover PNIPAM-based materials have been used in various biological studies, such as for hydrogel scaffolds, highlighting its biocompatibility (Zhernenkov et al., 2015). The broad array of synthetic approaches available to generate PNIPAM made it an ideal candidate for functionalising the surface of nanoparticles.

I proceeded to generate an acid-terminated variant of PNIPAM to allow for the terminating OH^- moiety to be functionalised with a catechol molecule suitable for anchoring the polymer to the particle surface. This was conducted following a literature procedure (Kurzhals et al., 2015) using an ATRP approach (**Scheme 2.6**), a successful method for generating polymers in a controlled fashion with narrow M_w distributions and defined terminal groups (Queffelec et al., 2000). The procedure involves formation of a transition metal/ligand complex (CuBr/Me_6TREN) which reacts with an alkyl halide initiator (2-methyl-2-bromopropionic acid) generating a radical to activate/propagate dormant polymer

chains by halogen atom transfer (Queffelec et al., 2000). After synthesis, the polymer molecular and phase transition properties were characterised.

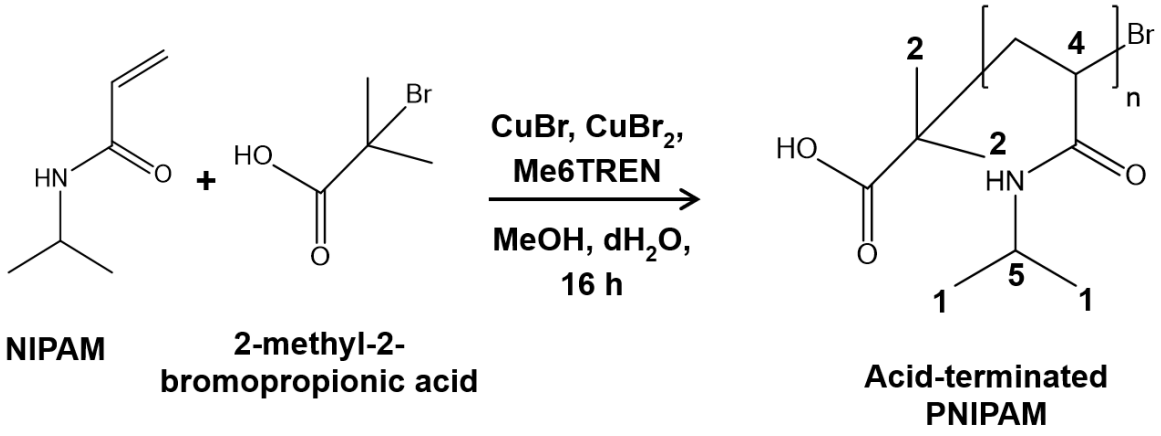

Scheme 2.6. Reaction scheme for ATRP synthesis of acid-terminated PNIPAM, simulated ^{1}H NMR: δ = 1.17 ppm (d, 3H, **1**) 1.26 ppm (s, 3H, **2**) 2.05 ppm (d, 2H, **3**) 4.22 ppm (m, 1H, **4**) 4.27 ppm (m, 1H, **5**).

During polymer collection post-synthesis, separation of PNIPAM from the dH_2O/MeOH solvent system is carried out by temperature-induced precipitation. There was a clear phase transition which occurred upon heating the reaction mixture to 50^{o}C resulting in rapid precipitate formation. Once isolated and purified, a controlled LCST assay was conducted monitoring the turbidity of a 10 mg/mL polymer sample while stirring and monitoring the temperature from ambient to 50^{o}C. I could observe that there was a defined temperature (32^{o}C) where evident precipitation occurred (**Figure 2.8**). This agrees with observations made in the literature procedure (Kurzhals et al., 2015). The polymer has a distinct blue colouration which is explained by the presence of CuBr during the synthesis, however this is not crucial as it is removed post-functionalisation.

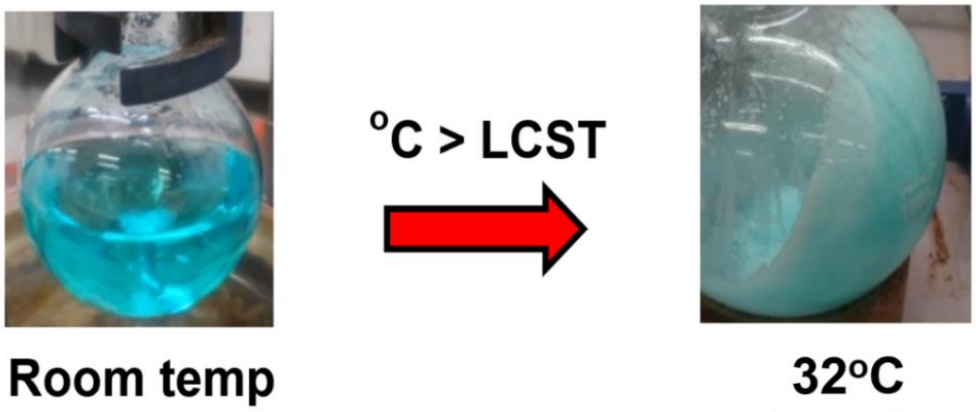

Figure 2.8. LCST measurements of acid-terminated PNIPAM: Phase transition analysis on 10 mg/mL acid-terminated PNIPAM following heating from room temperature to 50°C, polymer solution at room temperature (20.4°C) (left) and at 32°C (right).

The polymer M_w was determined by MALDI-TOF mass spectrometry and can be seen below in **Figure 2.9**. The m/z distribution was consistent with masses between 10-15.5 kDa in regions where peaks are distinguishable from noise. I could calculate an M_n value of 13 kDa and an M_w of 13.26 kDa, from which a PDI of 1.02 was determined. Additionally, spacings between polymer peaks denote monomer units at ~113 Da. The M_w observed correlates well with the literature procedure characterisation, which showed a 10 kDa polymer using the same synthetic approach (Kurzhals et al., 2015).

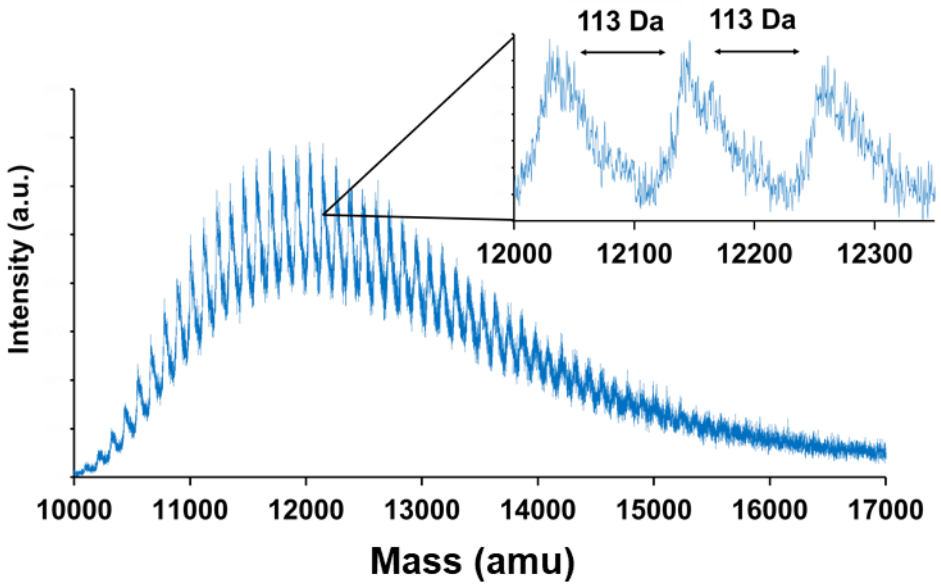

Figure 2.9. MALDI-TOF mass spectrometry of acid-terminated PNIPAM: Spectra from 1 mg/mL acid-terminated PNIPAM acquired between mass range 10-17 kDa, inset (top right) shows spacings between polymer peaks of 113 Da. M_n = 13 kDa, M_w = 13.26 kDa, PDI = 1.02.

Additionally, molecular characterisation of acid-terminated PNIPAM was carried out using ^{1}H NMR, showing broad NMR peaks indicative of polymerisation (**Figure 2.10**). Characteristic peaks representing PNIPAM can be seen for hydrogens present on repeat NIPAM monomer units between 3.8 – 4.2 ppm (**4**, **5**) for the CH bonds and 2.14 ppm (**3**) for CH_2, while 1-1.2 ppm (**1**, **2**) represents CH_3 present on the polymer and on methyl groups of the terminating carboxylic acid molecule.

Here I have generated acid-terminated PNIPAM which displays a phase transition at 32^{o}C and has an average M_w of 13.26 kDa.

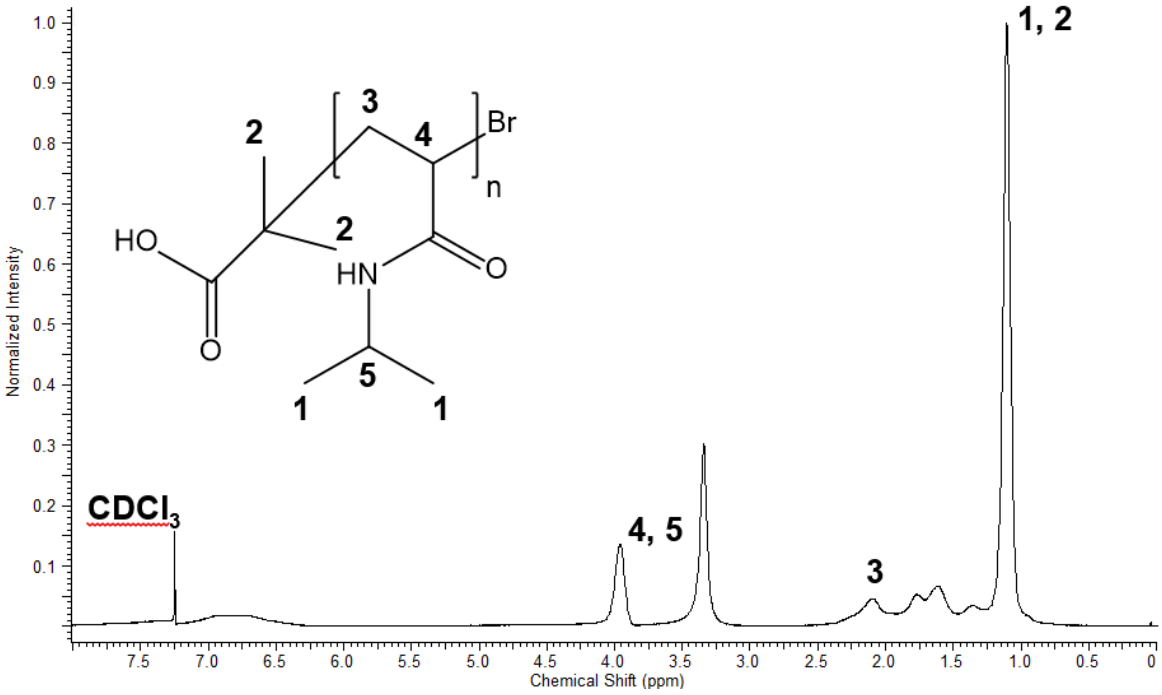

Figure 2.10. ^{1}H NMR of acid-terminated PNIPAM: 10 mg/mL sample dissolved in $CDCl_3$ for analysis, characteristic PNIPAM peaks detected at: δ = 1-1.2 ppm (**1**, **2**) 2.14 ppm (**3**) 3.8 – 4.2 ppm (**4, 5**).

2.3.4. Synthesis and characterisation of NDA

NDA has been shown to be a more effective molecule than dopamine for polymer anchorage onto iron oxide nanoparticle surfaces, producing stable dispersions of particles (Amstad et al., 2009). Also, dopamine is prone to oxidation by ferric cations such as Fe^{3+}, introduction of the nitro group makes oxidation more difficult. For these reasons, NDA was selected as a suitable molecule and synthesised before molecular characterisation was carried out by ^{1}H NMR. NDA was synthesised by nitration of dopamine via a radical cation mechanism using sodium nitrite (**Scheme 2.7**). This approach is more effective than using liquid phase counterparts like nitric acid, because it uses simpler, milder conditions with shorter reaction times.

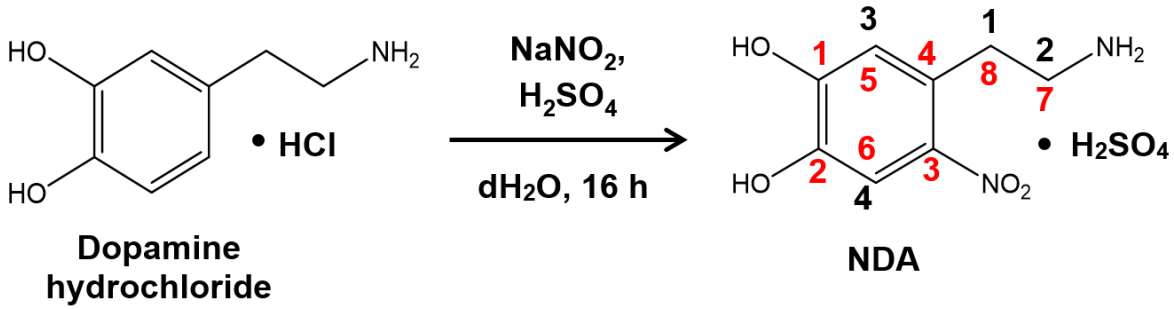

Scheme 2.7. Reaction scheme for synthesis of NDA, black numbers denote ^{1}H NMR assignment, red numbers denote ^{13}C NMR assignment, simulated ^{1}H NMR: δ = 2.26 ppm (t, 2H, **1**) 2.76 ppm (t, 2H, **2**) 6.36 ppm (s, 1H, **3**) 6.67 ppm (s, 1H, **4**), simulated ^{13}C NMR: δ = 145.4 ppm (**1**) 143.1 ppm (**2**) 140.5 ppm (**3**) 129.9 ppm (**4**) 111.0 ppm (**5**) 100.9 ppm (**6**) 42.2 ppm (**7**) 31.1 ppm (**8**).

NDA characterisation by ^{1}H NMR showed representative peaks between 2.9 – 3.1 ppm (**1**, **2**) for the CH_2 groups alongside the NH_2 moiety and also at 6.87 (**3**) and 7.48 ppm (**4**) for CH groups of the aromatic ring (**Figure 2.11**).

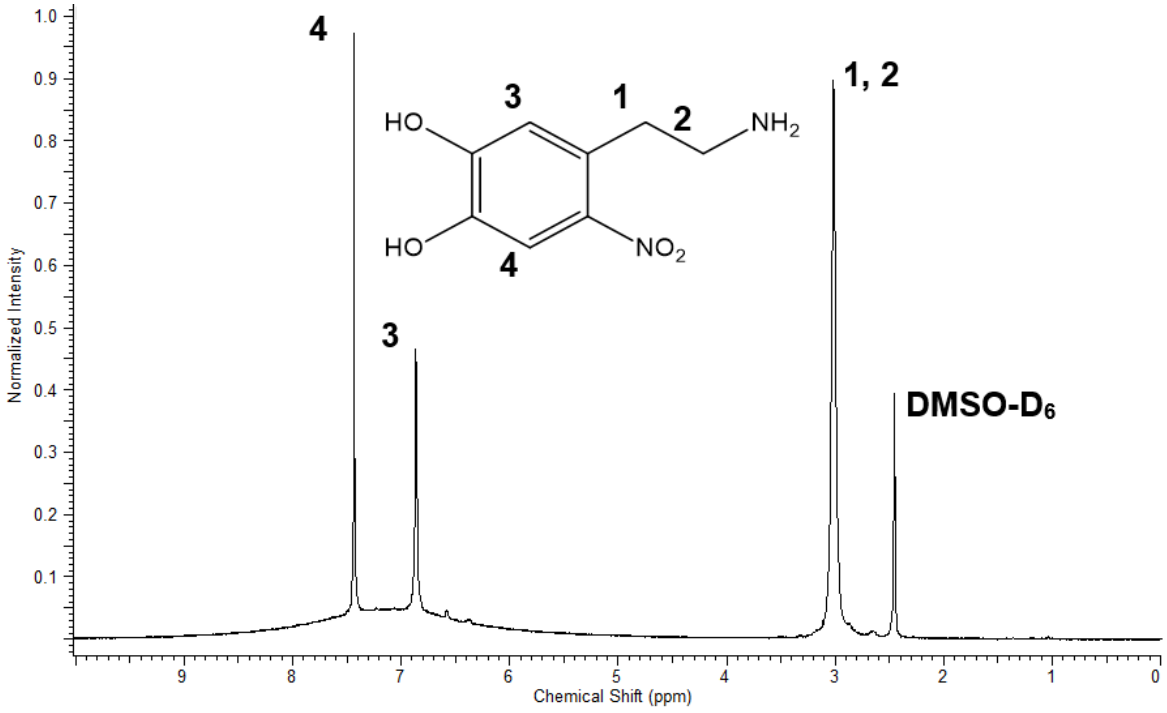

Figure 2.11. ^{1}H NMR of NDA: 10 mg/mL sample dissolved in DMSO-D_6 for analysis, characteristic NDA peaks detected at: δ = 2.9 – 3.1 ppm (**1**, **2**) 6.87 ppm (**3**) 7.48 ppm (**4**).

2.3.5. Synthesis and characterisation of NDA-PNIPAM

Acid-terminated PNIPAM was then functionalised to terminate with NDA through an amide coupling reaction (**Scheme 2.8**). Synthesis was conducted using coupling agent COMU which has been shown to be highly efficient with good solubility (Hjørringgaard et al., 2012). Purification was done using dialysis with a 3.5 kDa membrane cut off which is appropriate to remove excess NDA (M_w: 198.1 Da) and retain the functionalised polymer (M_w: 13.26 kDa).

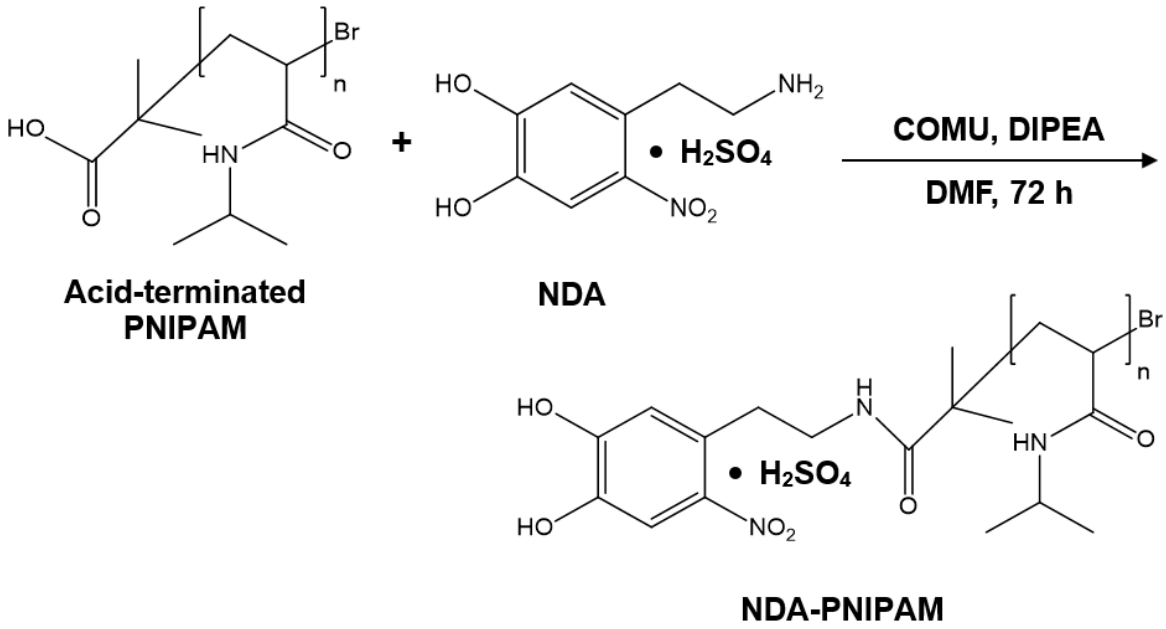

Scheme 2.8. Reaction scheme for amide coupling reaction of NDA with acid-terminated PNIPAM to form NDA-PNIPAM.

NMR was carried out on NDA-PNIPAM; however, I was unable to detect peaks corresponding to NDA. This is likely due to the significant abundance of monomer units compared to single terminating NDA molecules per polymer chain, meaning the detection of polymer largely outweighed that of NDA. UV-vis spectroscopy was carried out as an alternative to characterise the efficiency of NDA coupling to PNIPAM as NDA displays a λ_{max} of ~350 nm in its reduced form at mildly acidic pH (Cencer et al., 2014). This arises as a function of the nitro-functionality of NDA which lowers the pK_a values of the catechol hydroxyl groups to 6.6 and 11 from 9.2 and 14 without the nitro group (Nurchi et al., 2009). The relationship between concentration and absorbance could be plotted at a λ_{max} of ~350 nm for NDA-

PNIPAM as compared with NDA standards (**Figure 2.12**). Using equimolar amounts of NDA and NDA-PNIPAM at 300 µM, the concentration of NDA that had been functionalised to terminate the PNIPAM chains could be determined. The percentage of PNIPAM chains functionalised with NDA could be calculated using the absorbance readings from 300 µM NDA-PNIPAM to determine its NDA concentration, compared against a calibration curve of NDA standards. The concentration of NDA determined in 300 µM NDA-PNIPAM was then calculated as a percentage of 300 µM NDA which showed a 67% functionalisation of PNIPAM with NDA.

Here I have been able to successfully synthesise the catechol molecule NDA and terminally functionalise this onto PNIPAM chains.

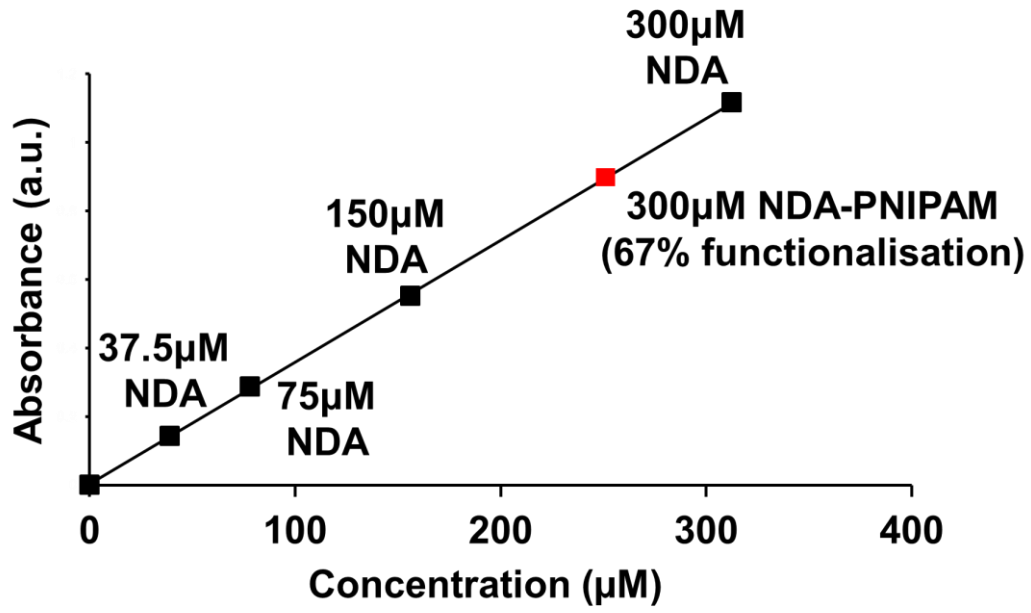

Figure 2.12. UV-vis spectroscopy of NDA-PNIPAM: Calibration curve of NDA standards from 300 – 37.5 µM to generate a linear regression where the R^2= 0.99, alongside 300µM NDA-PNIPAM. NDA-PNIPAM concentration was determined by M_w of acid-terminated PNIPAM plus the mass of a terminating molecule of NDA. Absorbance readings collected at λ_{max} (350 nm) using the formula: (absorbance-0.0027)/0.0036 to determine NDA concentration in PNIPAM. Samples were analysed in a sodium citrate buffer (1 mM, pH 5.5).

2.3.6. Preparation and characterisation of PNIPAM-coated iron oxide nanoparticles

Following the synthesis of NDA-PNIPAM, the iron oxide nanoparticle surface was coated with the polymer by sonication of both in dH_2O for 5 hours in an ice-cold bath to prevent temperature-sensitive polymer insolubility. The solution was then incubated at room temperature on a shaker overnight. During the sonication of NDA-PNIPAM with the nanoparticles, a direct ligand exchange occurs where the polymer replaces the propylene glycol coating on the nanoparticle surface through the action of the nitrocatechol-terminating group. This forms a stable, covalent bond that binds irreversibly and withstands heating to temperatures much higher than room temperature (Kurzhals et al., 2015). The literature procedure reported using sonication for 24 hours; however, I found the conditions I used were also sufficient (Kurzhals et al., 2015). PNIPAM-coated nanoparticles were subsequently purified by ultracentrifugation to remove excess polymer before analysis of the polymer coating. Magnetic separation was attempted using rare earth magnets placed under the base of the reaction vessel; however, yields were relatively poor using this approach. This is likely due to the high viscosity of the PNIPAM-nanoparticle solution limiting the migration of nanoparticles towards the magnet. After preparation, PNIPAM-coated nanoparticles were characterised for the presence of surface-bound polymer, extensiveness of coating and phase transition properties.

LCST measurements of PNIPAM-coated nanoparticles were conducted to assess whether the PNIPAM temperature-sensitive properties were retained/unchanged following nanoparticle surface coating. I could show that clear temperature-sensitive properties were displayed by PNIPAM-coated nanoparticles (**Figure 2.13**). At control temperatures, below the PNIPAM LCST at room temperature (20.6^{o}C) and 30^{o}C, PNIPAM-coated nanoparticles remained soluble as compared to uncoated control nanoparticles. Whereas upon heating the particles above the LCST to 37^{o}C or through magnetic heating for 30 min, causing a temperature rise from 30.5^{o}C to 33.8^{o}C, PNIPAM-coated nanoparticles began to precipitate as a function of the PNIPAM phase transition, uncoated nanoparticles by contrast remained soluble. This provides qualitative evidence of PNIPAM-coating, indicating that polymer-coated nanoparticles are responsive to temperature.

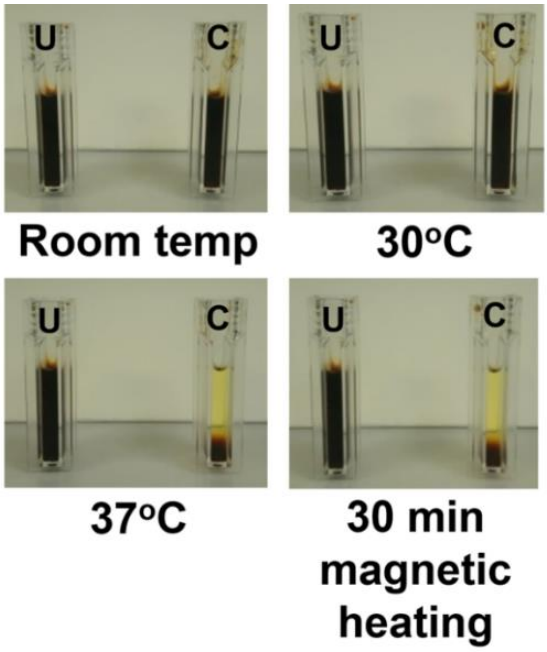

Figure 2.13. LCST measurements of PNIPAM-coated iron oxide nanoparticles: 10 mg/mL PNIPAM-coated (C) and uncoated (U) nanoparticles treated at different temperatures of 20.6°C (room temp), 30°C, 37°C and with 30 min magnetic heating (30.5°C > 33.8°C).

To further validate the presence of PNIPAM on the nanoparticle surface, XPS analysis was carried out to measure the elemental signatures present (**Figure 2.14**). Both uncoated and PNIPAM-coated nanoparticles show characteristic peaks for the presence of iron and oxygen as would be expected. However, PNIPAM-coated nanoparticles have significantly more carbon present due to the large hydrocarbon repeat structures of PNIPAM chains. Additionally, the appearance of nitrogen is evident for PNIPAM-coated nanoparticles which is an element present on repeat chains of PNIPAM. I can therefore show elemental data to support the presence of PNIPAM on the nanoparticle surface.

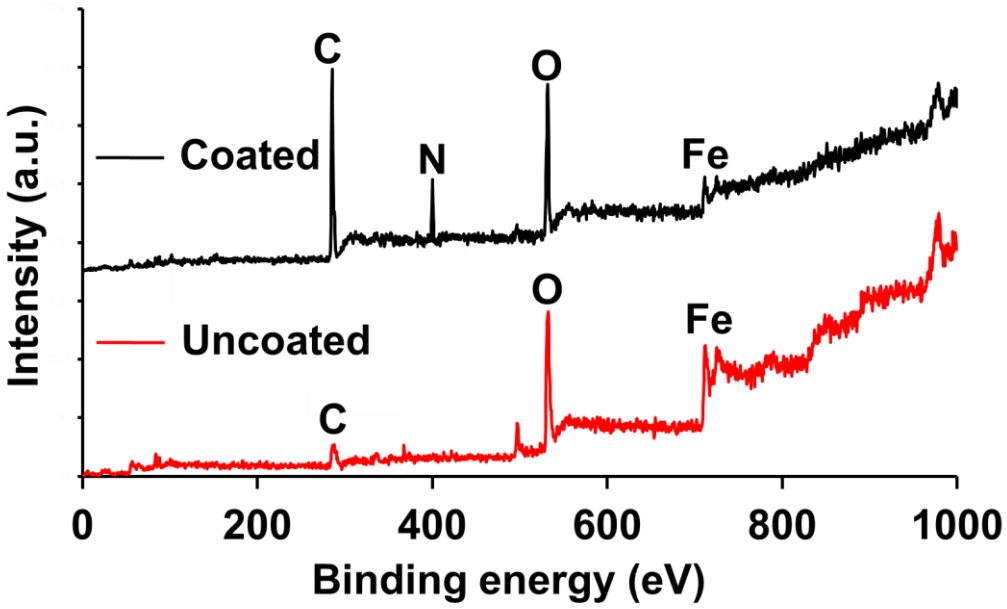

Figure 2.14. XPS of uncoated and PNIPAM-coated iron oxide nanoparticles: Peaks detected across a range between 0 – 1000 eV binding energy, elemental peaks detected at: 714.5 eV, iron (Fe); 532.6 eV, oxygen (O); 285.5 eV, carbon (C) for both uncoated and PNIPAM-coated particles, also 400.5 eV, nitrogen (N) in coated particles.

In order to ascertain the extensiveness of PNIPAM coating on the nanoparticle surface, TGA was carried out to measure the mass loss following thermal decomposition of the polymer (**Figure 2.15**). Upon heating above ~350^{o}C there was a significant mass loss of almost 50% in the PNIPAM-coated particle sample. By contrast there was little to no reduction in mass throughout the heating cycle up to 600^{o}C in the uncoated particle sample. This data suggests that around 50% of the total PNIPAM-coated nanoparticle mass is comprised of the PNIPAM shell. Additionally, upon carrying out TGA measurements on another batch of PNIPAM-coated particles, a significant mass reduction was also seen at ~350^{o}C (**Figure 2.15**).

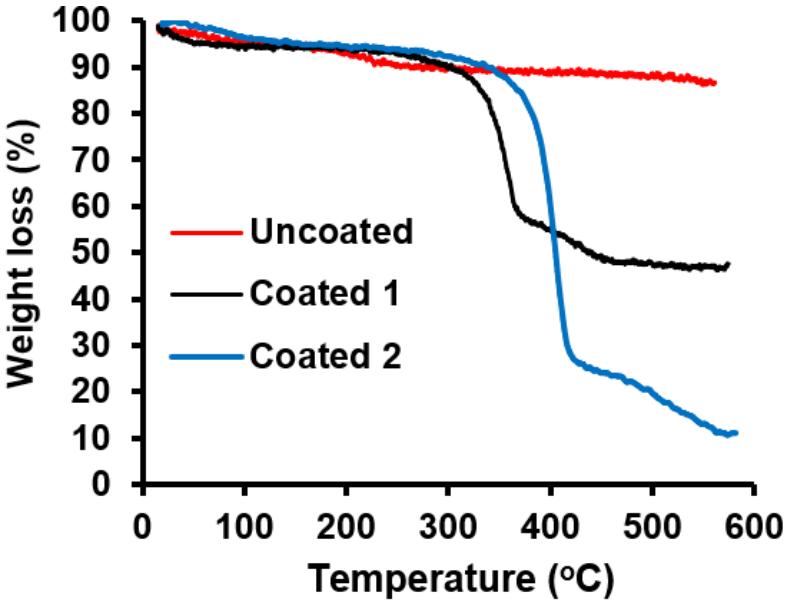

Figure 2.15. TGA analysis of uncoated and PNIPAM-coated iron oxide nanoparticles: 10 mg dry uncoated and PNIPAM-coated (coated) particle samples heated under nitrogen gas at a ramp rate of 10°C min^{-1} between 0-600°C. 'Coated 1' and 'Coated 2' represent different batches of PNIPAM-coated iron oxide nanoparticles measured.

Also, from the TGA data I could calculate the polymer grafting density on the nanoparticle surface per nm^2. This was determined by first calculating the nanoparticle volume with the equation $4/3\pi r^3$ (where r is radius) using the TEM-derived particle radius of 2.75 nm to give $87.1x10^{-21}cm^3$. From this, the mass of a single nanoparticle could be determined by multiplying the nanoparticle volume ($87.1x10^{-21}cm^3$) by the density of bulk iron oxide (5.18 g/cm) (Kurzhals et al., 2015) to give $4.51x10^{-19}g$. The mass of the nanoparticle proportion of a single PNIPAM-coated nanoparticle was derived by dividing single nanoparticle mass ($4.51x10^{-19}g$) by the inorganic fraction percentage shown by TGA (between 450 – 600°C) of 0.497 (49.7%) to give $9.07x10^{-19}g$. The polymer shell mass proportion of a PNIPAM-coated nanoparticle was determined by dividing the nanoparticle mass proportion of a PNIPAM-coated nanoparticle ($9.07x10^{-19}g$) by the organic fraction percentage shown by TGA (between 350 – 450°C) of 0.503 (50.3%) to give a value of $4.56x10^{-19}g$. To calculate how many polymer chains were present per PNIPAM-coated nanoparticle, the polymer shell mass proportion of a PNIPAM-coated nanoparticle ($4.56x10^{-19}g$) was divided by the mass of a single PNIPAM

chain ($1.745x10^{-20}$) to give ~26 polymers. The mass of a single polymer chain was determined by polymer M_w/Avagado's number ($10,512.2/6.023x10^{23}$) (polymer M_w was determined by MALDI-TOF mass spectrometry). The grafting density for polymer chains per nm^2 was calculated by dividing the number of polymer chains per PNIPAM-coated nanoparticle (26.1) by the nanoparticle surface area of 95 nm^2, determined using $4\pi r^2$ ($4\pi 2.75^2$) which gave a grafting density of ~0.3 chains/nm^2 (27.5%). A higher grafting density could possibly be achieved using shorter PNIPAM chains as longer chains will have a larger hydrodynamic diameter and may therefore partially circumvent further grafting by physically blocking binding sites once a layer has grafted onto the particle surface.

To measure the polymer-coated nanoparticle size and dispersity properties in solution, I used a DLS approach (**Table 2.3**). I could show that nanoparticles dispersed in water, both uncoated and PNIPAM-coated, were measured over 100 nm in size with large error values. Moreover, particle aggregation is indicated by zeta potential readings of almost 0 which suggests poor colloidal stability (O'Brien et al., 1990).

Previous studies have shown citrate coated iron oxide nanoparticles display good stability and dispersity properties over long periods of time with little aggregation (Saraswathy et al., 2014). To improve the nanoparticle dispersity and reduce aggregation, the particles were dispersed in sodium citrate buffer and briefly sonicated before washing away excess sodium citrate. NDA-terminated polymer was then sonicated with the particles in water to replace any bound citrate and allow for surface coating. Nanoparticles prepared with citrate showed significantly improved size and stability properties over those prepared without (**Table 2.3**). Non-polymer coated nanoparticles had a hydrodynamic diameter of 16.62 ± 4.43 nm, showing a clear reduction in size over non-citrate prepared particles. Moreover, an improved zeta potential was recorded for citrate-prepared, uncoated particles at 31.26 ± 3.02 mV, indicating good colloidal stability (O'Brien et al., 1990). PNIPAM-coated nanoparticles prepared with citrate also showed good colloidal stability with a zeta potential of 36.2 ± 1.48 mV. Interestingly these particles showed a hydrodynamic diameter of 152.5 ± 13.33 nm, the zeta potential measurements suggest this size is unlikely due to aggregation and therefore the increased size could be attributed to the expanded PNIPAM shell on the particle surface. To investigate this further the PNIPAM-coated particles were heated in the DLS machine to 37^{o}C (above the PNIPAM LCST) and the hydrodynamic

diameter was measured to observe any size reduction brought about by the collapse of the PNIPAM shell post-phase transition. However due to the temperature-induced precipitation of PNIPAM-coated particles readings could not be accurately made.

Sample	Hydrodynamic diameter (nm)	Zeta potential (mV)	PDI
Uncoated	158.8 ± 6.08	0.258 ± 0.27	0.124 ± 0.02
Coated	154.2 ± 6.71	0.31 ± 0.23	0.147 ± 0.03
Uncoated (CC)	16.62 ± 4.43	31.26 ± 3.02	0.269 ± 0.01
Coated (CC)	152.5 ± 13.33	36.2 ± 1.48	0.091 ± 0.02

Table 2.3. DLS analysis of uncoated and PNIPAM-coated iron oxide nanoparticles: Hydrodynamic diameter (nm) zeta potential (mV) and PDI measurements of nanoparticle solutions (10 mg/mL). Particles were prepared with (coated) or without (uncoated) PNIPAM-coating and measured in the presence (citrate coated) (CC) or absence of sodium citrate (1mM, pH 7.4). Sizes displayed represent mean values (± error denotes standard deviation, n=3).

Another technique that measures particle size and relates the Brownian (random) motion to size is NTA, allowing for visualisation of particles in solution (Filipe et al., 2010). Both DLS and NTA measure Brownian motion where the speed of motion is influenced by nanoparticle size. However, DLS considers particles in a sample as an ensemble rather than on an individual basis. NTA, by contrast, visualises and tracks individual particles allowing for a more accurate determination of the particle size distribution profile. The modal of the size distribution was determined as 78.3 ± 1.3 nm for PNIPAM-coated nanoparticles at room temperature (**Figure 2.16**). Additionally, nanoparticles at room temperature could be visualised at high density with clear dispersity. At 37^{o}C however, NTA showed a significant increase in particle hydrodynamic diameter with the modal of the distribution increasing to

199.7 ± 15.9 nm as a consequence of particle aggregation following PNIPAM chain collapse and transition to a hydrophobic state (**Figure 2.16**). The PNIPAM-coated particle size at room temperature in solution correlates well with that observed by DLS, both being significantly larger when compared to nanoparticle diameter seen by TEM of 6.3 ± 0.9 nm.

The polymer-coated particle sizes observed by DLS and NTA are a likely consequence of combined effects of the expanded polymer shell and solvent molecules interacting and accumulating on the particle surface (Clement et al., 2017). Both these factors will contribute to the hydrodynamic diameter in solution, whereas these will not be measured by dry samples analysed by TEM. Visualisation of the PNIPAM-shell could not be detected by TEM which is a likely consequence of contrast lacking from the carbon-dense polymer against a carbon background. Additionally, as the sample is dry during TEM analysis, the polymer shell may be collapsed in the absence of solvent.

I have used different techniques to measure particle size where each approach has its merits and drawbacks. Of the techniques I used, TEM provides the most accurate measurement of particle size since there is no influence of molecules in solution interacting with the surface and influencing the size. However, TEM does not allow for visualisation of the polymer shell on the particle surface due to the lack of contrast from the polymers against a carbon background and also, since TEM samples are imaged *in vacuo*, the polymer shell is dehydrated and therefore will not be in an expanded state. DLS and NTA allow measurements of particle size in solution which allows for the expansion/hydration of the polymer shell and therefore considers the influence of the polymer shell on particle size. However, the absolute values measured by these techniques are likely to be an overestimation since they are representative of the hydrodynamic diameter and therefore could be influenced by interactions on the particle surface with molecules in solution. NTA also allows visualisation of individual particles in solution which DLS does not, and this allowed me to observe the particle behaviour at temperatures above and below the polymer LCST.

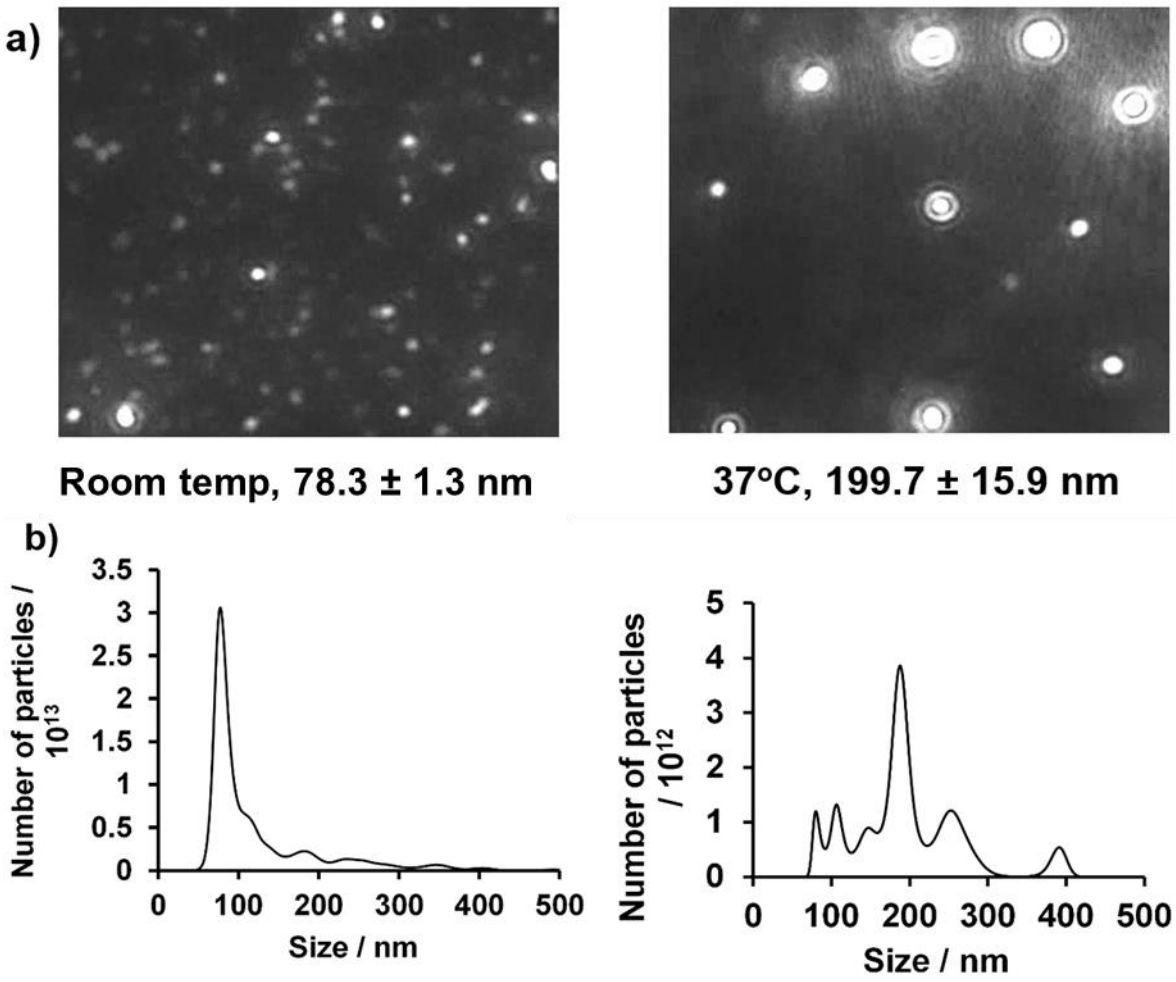

Figure 2.16. NTA of PNIPAM-coated iron oxide nanoparticles: a) NTA images at room temperature (left) and 37ºC (right) of PNIPAM-coated nanoparticles, sizes displayed represent the modal of the size distribution (± error denotes standard deviation, n=3). **b)** Size distribution profiles of PNIPAM-coated nanoparticles at room temperature (left) and 37ºC (right).

2.3.7. Synthesis and characterisation of PNIPMAM generated by NIPMAM polymerisation

As well as PNIPAM, I also worked on the synthesis of an alternative polymer termed PNIPMAM, a slight variant of PNIPAM with an additional methyl group on the monomer. It has been shown that the PNIPMAM LCST can be modulated in a M_w dependent manner (Rathfon and Tew, 2008). I began preliminary work on this polymer with a view to generating a version that displays an LCST above 37^{o}C, an ideal property for potential downstream work on developing polymer-coated nanoparticles that can release biomolecules above physiological temperature (37^{o}C) upon magnetic heating.

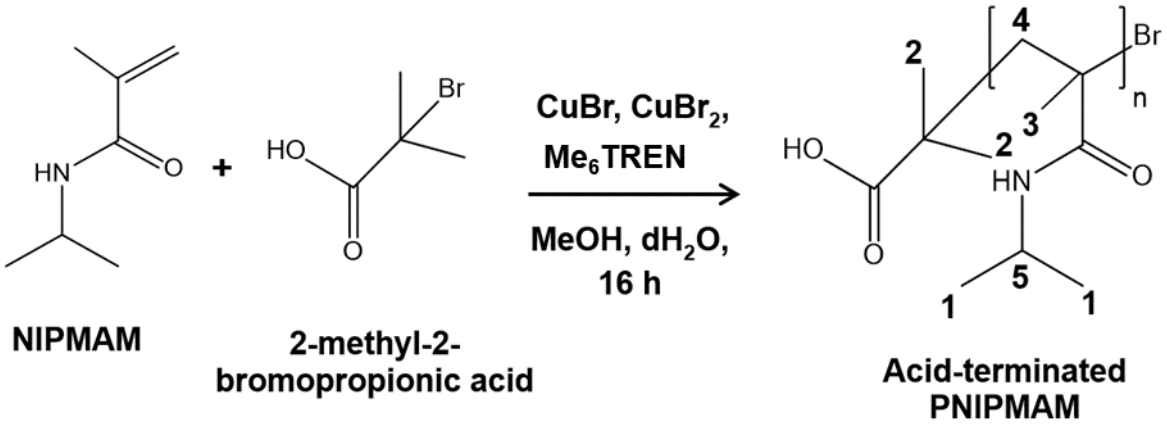

Scheme 2.9. Reaction scheme for ATRP synthesis of acid-terminated PNIPMAM, simulated PNIPMAM ^{1}H NMR: δ = 1.17 ppm (d, 3H, **1**) 1.26 ppm (s, 3H, **2**) 1.36 ppm (s, 3H, **3**) 1.78 ppm (s, 2H, **4**) 4.28 ppm (m, 1H, **5**).

Initially, I attempted to recapitulate the acid-terminated PNIPAM synthesis using the NIPMAM monomer instead of NIPAM (**Scheme 2.9**). However, following an overnight reaction I was unable to detect clear signs of polymerisation. Additionally, there was no indication of a polymer phase transition even upon heating to much higher temperatures than desired (100^{o}C). I hypothesised that possibly the rate of polymerisation using this monomer was significantly slower than that of NIPAM and therefore attempted to optimise this by lengthening the reaction under moderate heating. The reaction was repeated and left under mild heating conditions (30^{o}C) (below the anticipated polymer LCST) and small analytical aliquots (1 mL) were drawn from the reaction (under inert conditions)

after 1, 3 and 7 days. The crude products were purified in the same manner as PNIPAM but scaled down proportionally to account for the smaller volumes. I then carried out ^{1}H NMR and MALDI-TOF mass spectrometry to characterise the product at each timepoint. By ^{1}H NMR, I could see that the monomer was only present after 1 day of polymerisation, indicated by sharp peaks (**Figure 2.17**). However, after 3 and 7 days the peaks broaden, which will only be observed for the polymer, providing a qualitative indication of polymerisation. Characteristic PNIPMAM peaks can be seen after 3 and 7 days between 1 – 1.3 ppm (**1** – **3**) for CH_3 groups present on repeat monomer units and the terminating acid group. Also, at 1.5 ppm (**4**), a peak can be seen corresponding to the CH_2 of repeat monomer units and also at 4 ppm (**5**), likely representing the CH on repeat monomer units.

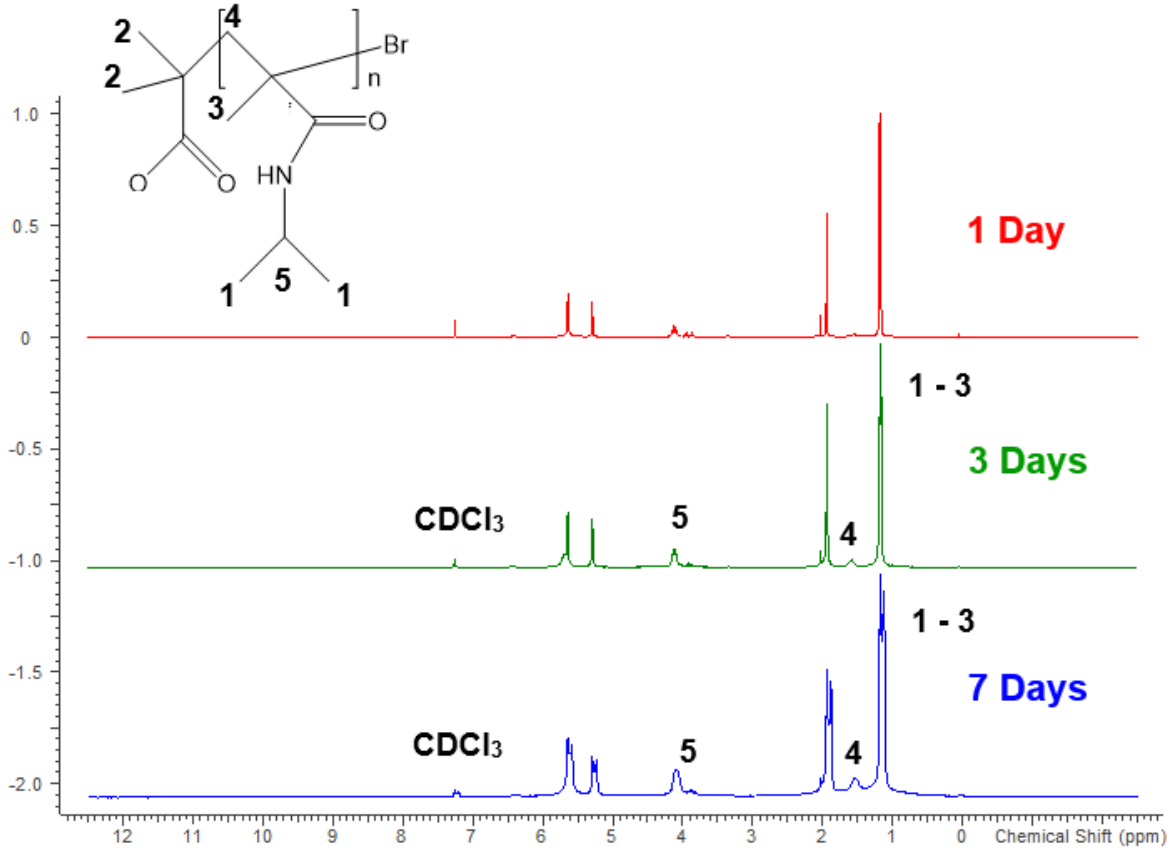

Figure 2.17. ^{1}H NMR studies of PNIPMAM synthesis over 7 days: 10 mg/mL sample dissolved in $CDCl_3$ for analysis, characteristic PNIPMAM peaks detected at: δ = 1 – 1.3 ppm (**1** – **3**) 1.5 ppm (**4**) 4 ppm (**5**). Colours indicate time during polymerisation prior to NMR analysis after 1 day (red), 3 days (green) and 7 days (blue).

By MALDI, I could detect an increase in M_w of the polymer over time between days 1 – 7, giving an indication of progressive polymer chain propagation (**Figure 2.18**). In agreement with the NMR data in **Figure 2.17**, there is no indication of polymerisation after 1 day, whereas defined polymer peaks appear by mass spectrometry after 3 and 7 days, with an increased M_w over time. After 3 days polymerisation, I could calculate 10,855 Da for the M_n and 9,568 Da for the M_w, which yielded a PDI of 0.88. After 7 days polymerisation, I calculated 12,843 Da for the M_n and 12,168 Da for the M_w with a PDI of 0.94. However, despite these observations I was still unable to detect a phase transition in response to heating to 100^{o}C. I reasoned that despite evident polymerisation occurring, initiation of insufficient polymer chains, resulting in a low polymer concentration, could be behind the lack of a bulk sample phase transition. It has been suggested in previous work that copper catalysts can be inefficient in inducing radical addition for some amide-containing monomers (Senoo et al., 1999). This approach could potentially be optimised in the future to generate a suitable polymer; however, I decided to seek alternative synthetic methods to generate the desired product.

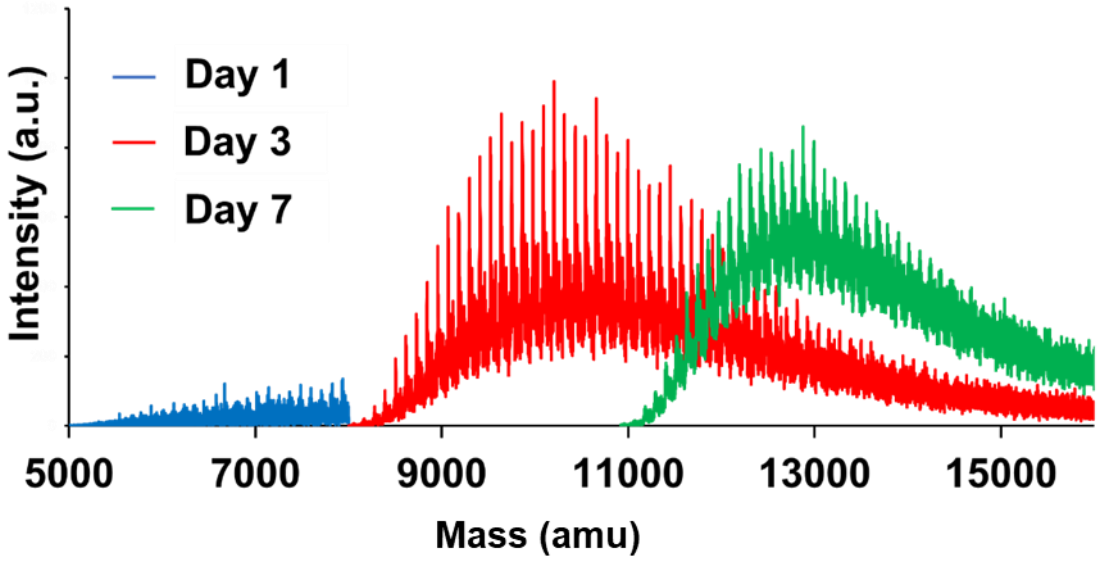

Figure 2.18. MALDI-TOF mass spectrometry of PNIPMAM synthesis over 7 days: Spectra from 1 mg/mL acid-terminated PNIPMAM acquired between mass range 5-16kDa after polymerisation for 1 (blue), 3 (red) and 7 (green) days. 3 days polymerisation: M_n = 10,855 Da, M_w = 9,568 Da, PDI = 0.88. 7 days polymerisation: M_n = 12,843 Da, M_w = 12,168 Da, PDI = 0.94.

2.3.8. Synthesis and characterisation of PMASI

Because I did not observe any phase transition when polymerising the NIPMAM monomer, an alternate synthetic approach was used. This involved following a literature procedure (Rathfon and Tew, 2008) for the synthesis of PMASI from the MASI monomer via ATRP (**Scheme 2.10**). This approach was previously shown to generate well controlled polymers for post-synthesis functionalisation (Shunmugam and Tew, 2005).

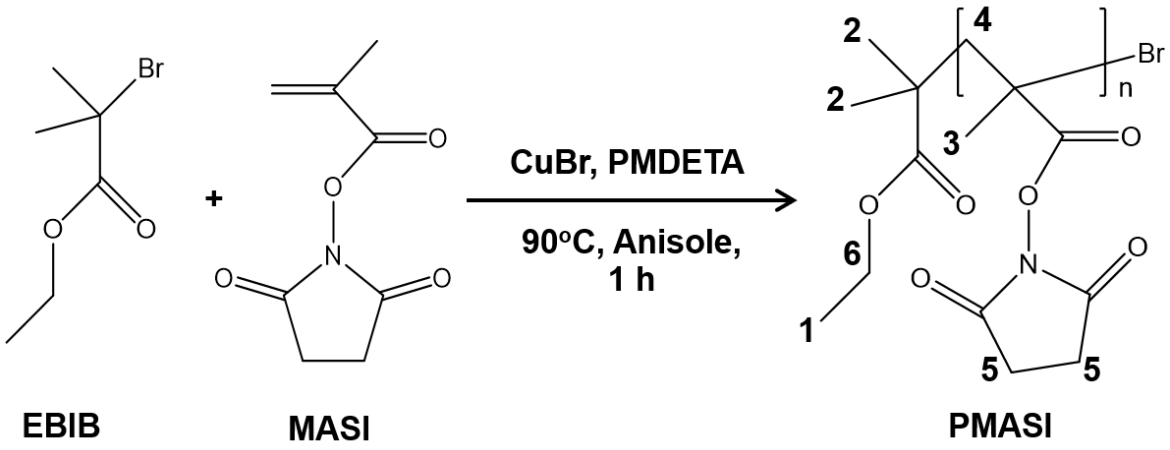

Scheme 2.10. Reaction scheme for synthesis of PMASI precursor, simulated ^{1}H NMR: δ = 1.19 ppm (t, 3H, **1**) 1.25 ppm (s, 3H, **2**) 1.44 ppm (s, 3H, **3**) 1.77 ppm (s, 2H, **4**) 2.83 ppm (m, 2H, **5**) 4.12 ppm (m, 2H, **6**).

Following the synthesis of PMASI, ^{1}H NMR was conducted to characterise the molecular properties of the product. By ^{1}H NMR, characteristic peaks were observed for PMASI indicating that the desired product had been formed (**Figure 2.19**). Proton peaks corresponding to the MASI functionality on the molecule can be seen at 2.8 ppm (**5**). Protons present along the hydrocarbon polymer backbone and terminating group likely give rise collectively to the broad peak in the region between 1 - 1.8 ppm (**1** – **4**). Also, a broad peak could be detected at 3.6 ppm (**6**) which is possibly the CH present on repeating monomer units. The abundance of several other peaks in the spectrum are probable starting materials, solvent or contaminants, therefore a more rigorous clean-up procedure will likely benefit the product purity and spectrum quality.

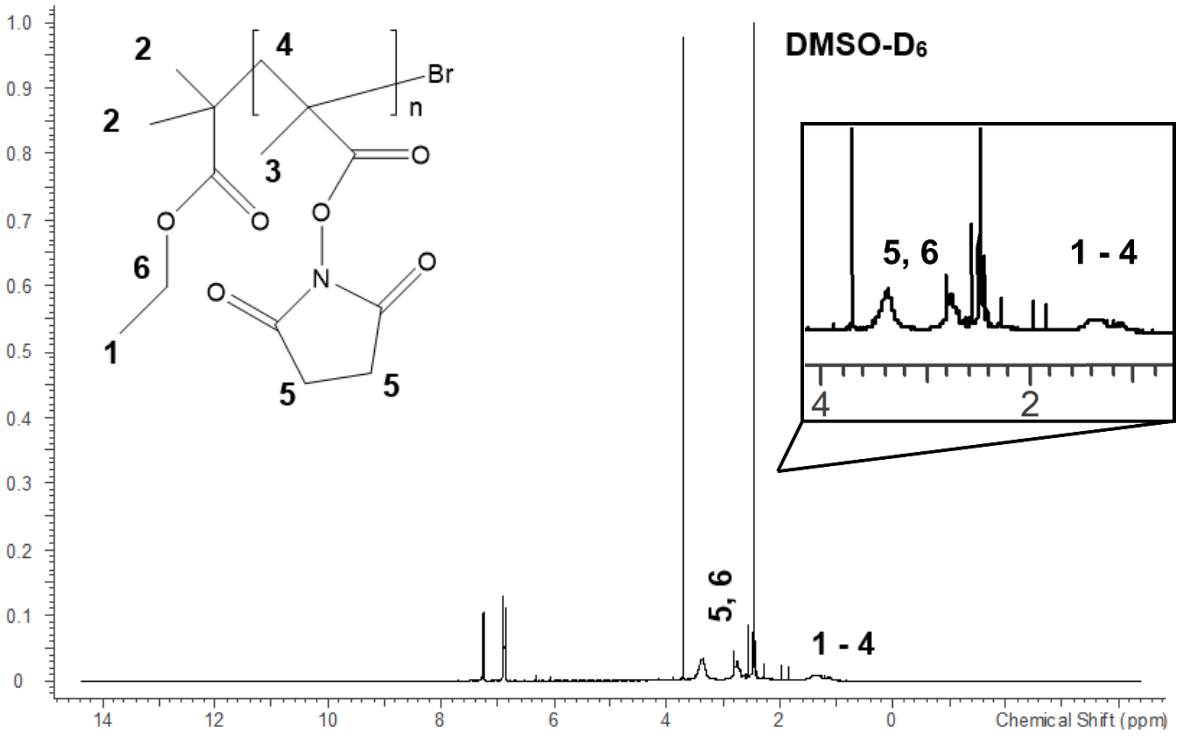

Figure 2.19. ^{1}H NMR of PMASI: 10 mg/mL sample dissolved in DMSO-D_6 for analysis, characteristic PMASI peaks detected at: δ = 1 – 1.8 ppm (**1 - 4**) 2.8 ppm (**5**) 3.6 ppm (**6**). Zoomed-in inset of important resonance peaks shown on right.

2.3.9. Synthesis and characterisation of acid-terminated PNIPMAM from PMASI

After PMASI synthesis, functionalisation with isopropylamine to generate acid-terminated PNIPMAM immediately followed (**Scheme 2.11**).

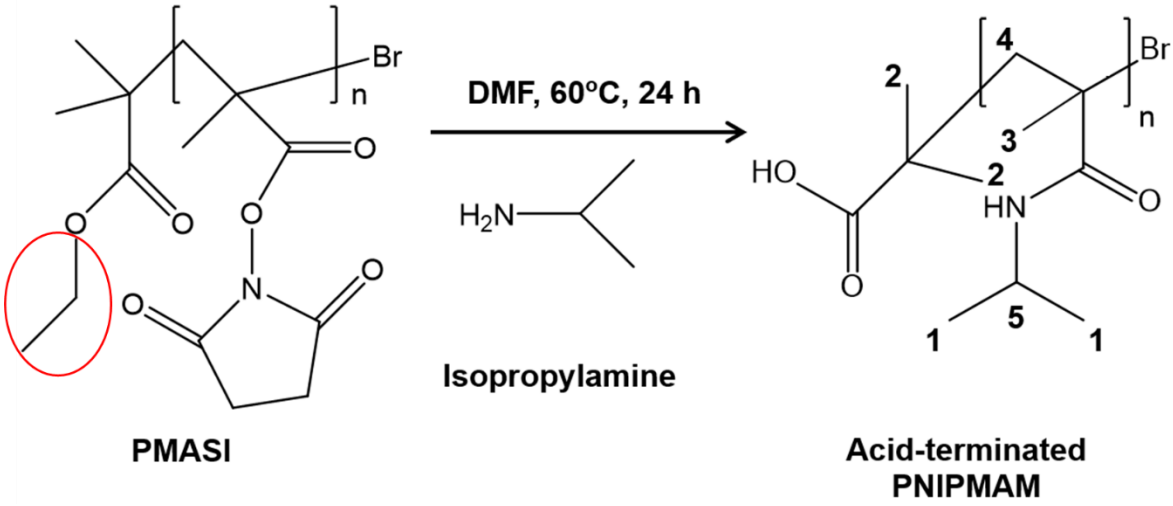

Scheme 2.11. Reaction scheme for synthesis of acid-terminated PNIPMAM, simulated ^{1}H NMR: δ = 1.17 ppm (d, 3H, **1**) 1.26 ppm (s, 3H, **2**) 1.36 ppm (s, 3H, **3**) 1.78 ppm (s, 2H, **4**) 4.28 ppm (m, 1H, **5**). Red circle highlights terminating ester group that is subsequently hydrolysed to generate acid-terminated PNIPMAM.

Characterisation of the product by ^{1}H NMR showed characteristic peaks for the polymer (**Figure 2.20**). Most notably is the appearance of a significant peak at ~1 ppm (**1**) and an enlarged peak between 3.8 – 4 ppm (**5**), corresponding to the isopropylamine functionality present on PNIPMAM. As with the PMASI ^{1}H NMR (**Figure 2.19**), the spectrum is not clear and would likely benefit from a more rigorous purification procedure.

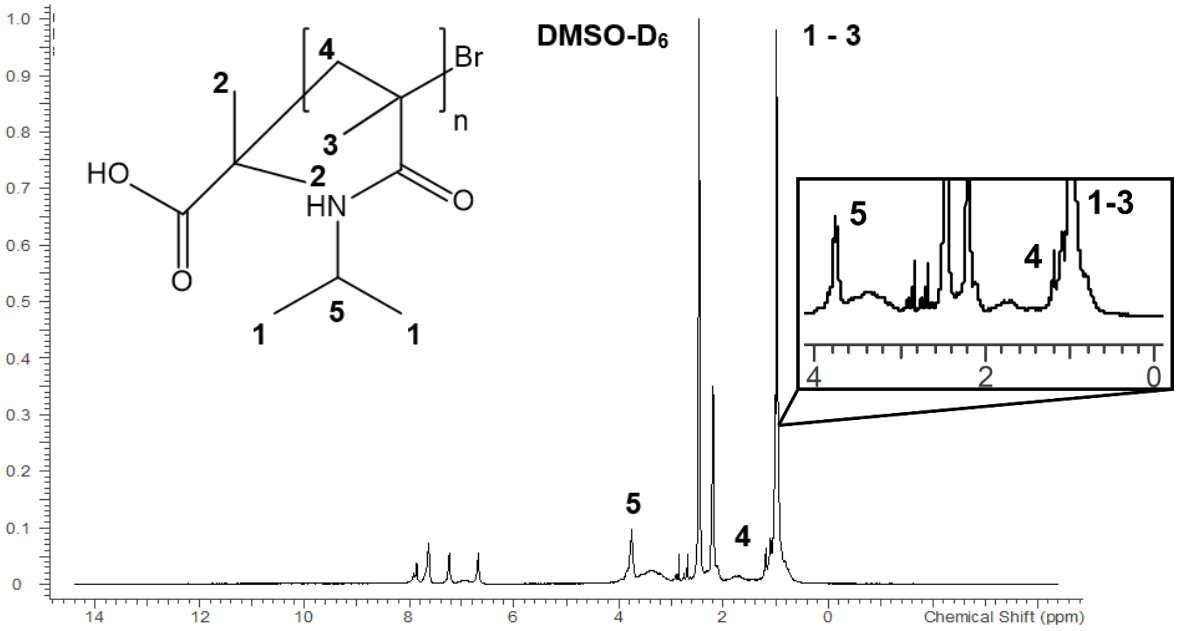

Figure 2.20. ^{1}H NMR of acid-terminated PNIPMAM: 10 mg/mL sample dissolved in DMSO-D_6 for analysis, characteristic PNIPMAM peaks detected at: δ = 1-1.4 ppm (**1** – **3**) 1.7 ppm (**4**) 3.8 – 4 ppm (**5**).

Additionally, I carried out MALDI-TOF mass spectrometry analysis on PNIPMAM to measure the M_w of the polymer. MALDI showed that the m/z distribution is consistent with polymer masses between 8.5 – 14.5 kDa yielding a calculated M_n of 11,245 Da and a M_w of 10,378 Da, with a PDI of 0.92 (**Figure 2.21**). Using NaOH, I carried out hydrolysis of the terminal ester group. This allowed for subsequent functionalisation of the polymer with NDA to permit binding to iron oxide nanoparticles. Using MALDI-TOF mass spectrometry, I could detect a mass shift of ~28 Da, which corresponds to the mass loss of the terminating ester group (**Figure 2.22**). Also, it can be seen that the peak spacings between polymer units are ~127 Da apart, correlating with the mass of monomeric units of the polymer.

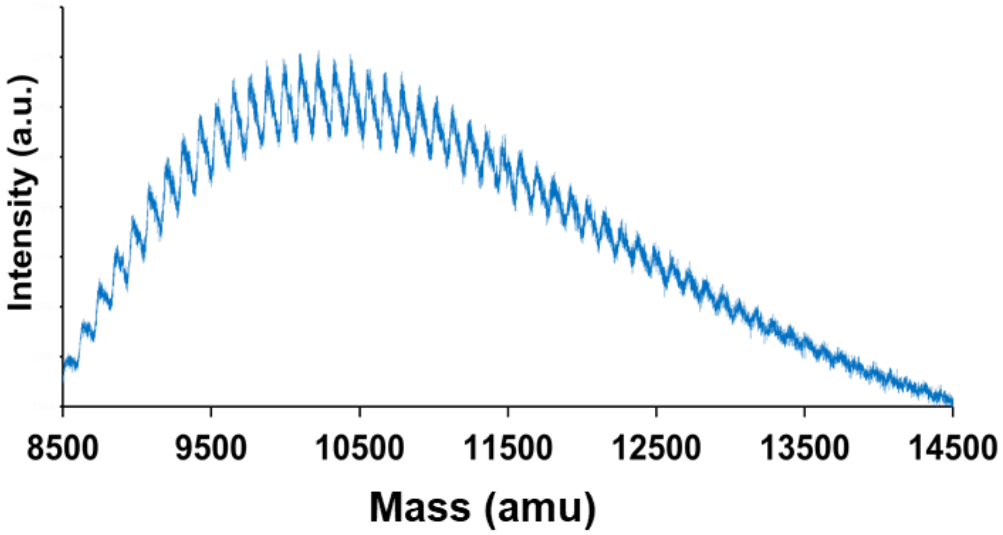

Figure 2.21. MALDI-TOF mass spectrometry of PNIPMAM: Spectra from 1 mg/mL PNIPMAM acquired for a mass range of 8.5-14.5 kDa. M_n: 11,245 Da, M_w: 10,378 Da, PDI: 0.92.

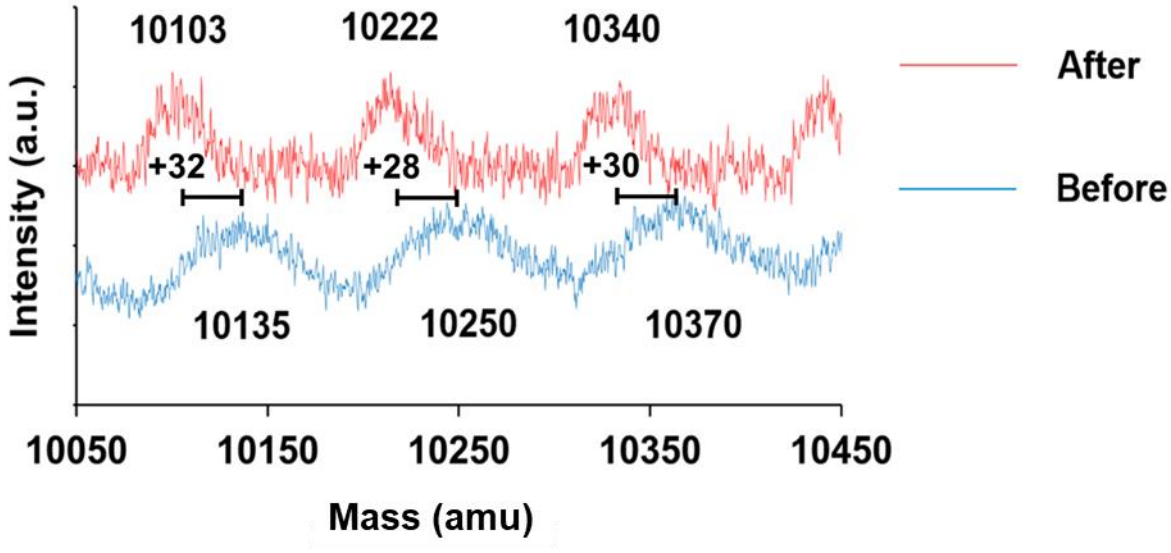

Figure 2.22. MALDI-TOF mass spectrometry of PNIPAM before and after terminating ester hydrolysis: Spectra from 1 mg/mL PNIPMAM acquired for mass range between 10050-10450 Da for PNIPMAM before (blue) and after (red) terminating ester hydrolysis. Masses for polymer chains before and after hydrolysis are indicated below (before) and above (after) peaks. Mass differences between polymer peaks before and after hydrolysis shown as '+' for corresponding mass shift.

I also assessed the phase transition properties of the polymer and was able to observe temperature-sensitive properties (**Figure 2.23**). Interestingly, I could observe a more gradual phase transition than observed for PNIPAM where the polymer solution was soluble at room temperature, turbid/cloudier from 37ºC – 41ºC, until the polymer began to precipitate at 42ºC. Despite not displaying a sharp phase transition like PNIPAM, I could observe an increased polymer LCST.

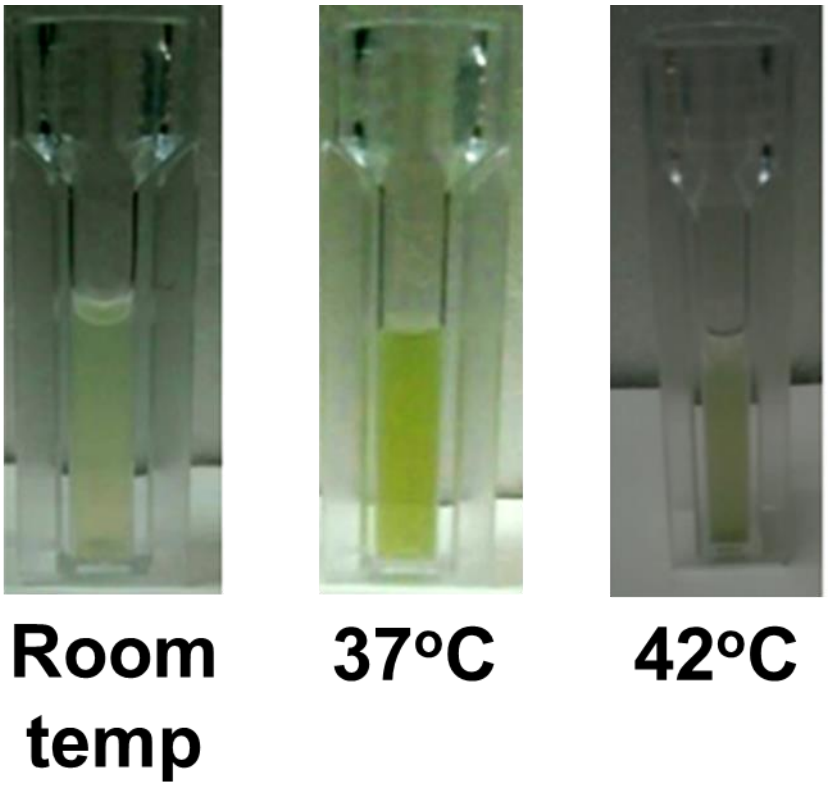

Figure 2.23 LCST measurements of acid-terminated PNIPMAM: Phase transition analysis on 10 mg/mL acid-terminated PNIPMAM following heating from at room temperature (20.3ºC, left), 37ºC (centre), and 42ºC (right).

2.3.10. Synthesis and characterisation of NDA-PNIPMAM

By exposing the carboxylic acid terminating group of the polymer, I was able to carry out functionalisation with NDA using the same approach as with acid-terminated PNIPAM (**Scheme 2.12**).

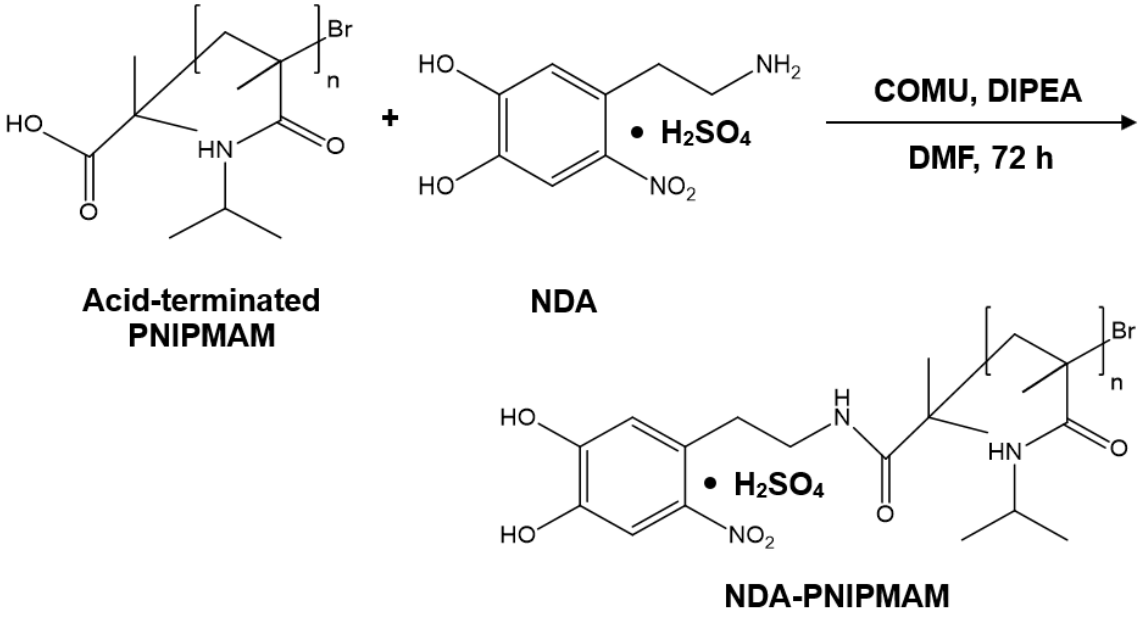

Scheme 2.12. Reaction scheme for amide coupling reaction of NDA with acid-terminated PNIPMAM to form NDA-PNIPMAM.

I characterised NDA-functionalisation of PNIPMAM using UV-vis spectroscopy where the characteristic peak at a λ_{max} of 350 nm was evident for NDA-PNIPMAM, indicating some functionalisation (**Figure 2.24**). This could be calibrated against a standard curve of NDA standards to determine that ~60% of PNIPAM units were terminally-functionalised with NDA. Additionally, there was a clear visual change following NDA functionalisation (also seen with NDA-PNIPAM) (**Figure 2.24**).

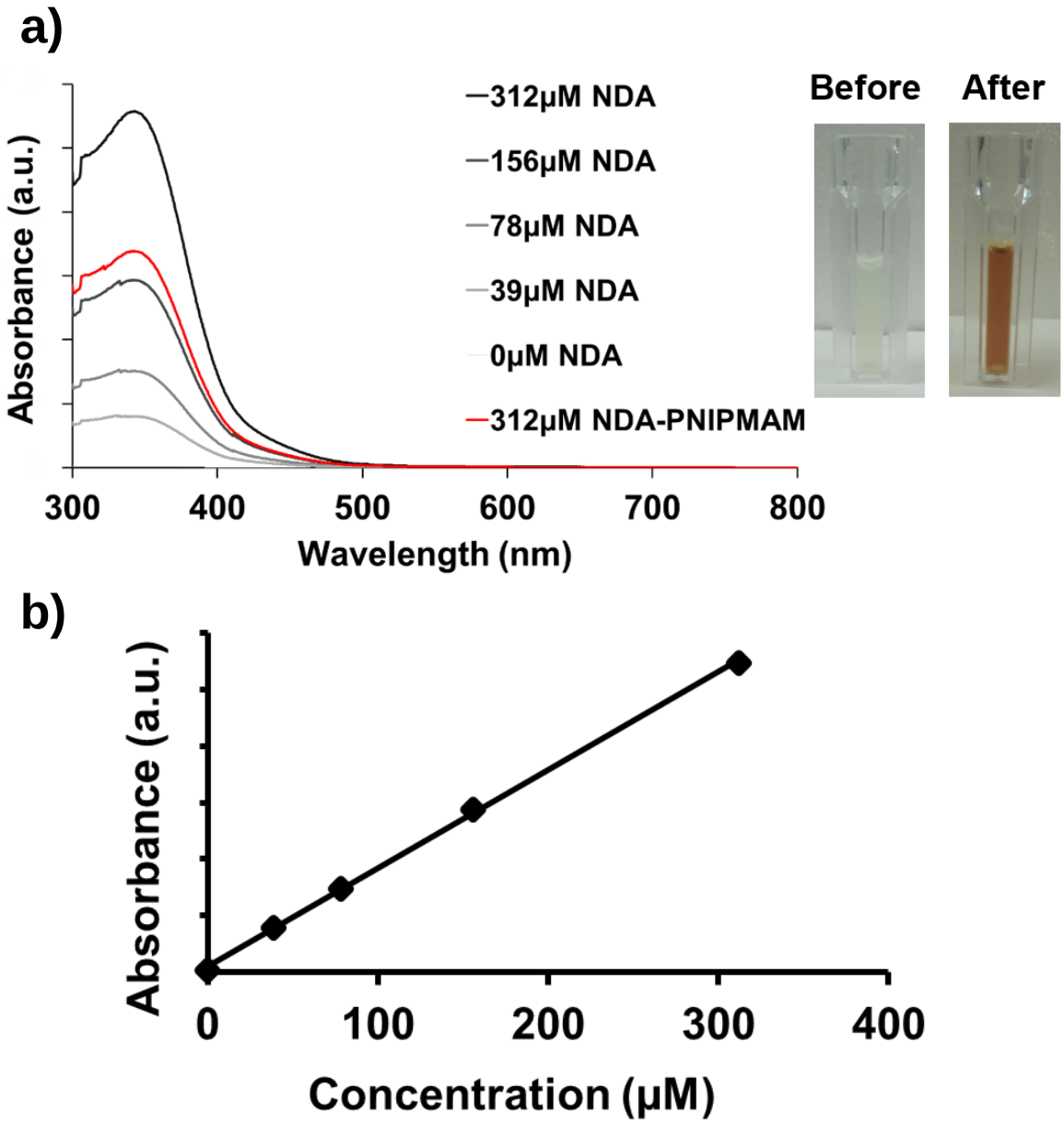

Figure 2.24. UV-vis spectroscopy of NDA-PNIPMAM: a) Spectra (left) recorded across wavelength range of 300 – 800 nm with λ_{max} of 350 detected for NDA. NDA standards were measured alongside NDA-PNIPMAM for comparison. Images of PNIPMAM (right) before (left) and after (right) NDA functionalisation. **b)** Standard curve was generated with NDA standards to generate a linear regression with an R^2 value of 0.9176. NDA concentration in NDA-PNIPMAM was determined using the formula: $(A_{350}-0.2595)/0.3532$. Samples were analysed in a sodium citrate buffer (1 mM, pH 5.5).

2.3.11. Preparation and characterisation of PNIPMAM-coated iron oxide nanoparticles

Using NDA-PNIPMAM, I conducted polymer-coating to the iron oxide nanoparticle surface using the same methodology as for PNIPAM. I could confirm PNIPMAM coating by showing clear temperature-sensitive properties are displayed by PNIPMAM-coated nanoparticles (**Figure 2.25**). Below the polymer LCST of room temperature (19.3^{o}C), PNIPMAM-coated nanoparticles remained soluble. Whereas upon heating the particles to 37^{o}C, the solution turbidity increased as seen previously for free polymer (**Figure 2.23**). PNIPMAM-coated nanoparticles began to precipitate at 42^{o}C likely indicating a complete phase transition. This provides qualitative evidence of PNIPMAM-coating, where temperature-sensitive properties are observed above physiological temperatures. This could be a more advantageous tool compared to PNIPAM-coated nanoparticles which could be developed for thermally-induced biomolecule release above physiological temperatures.

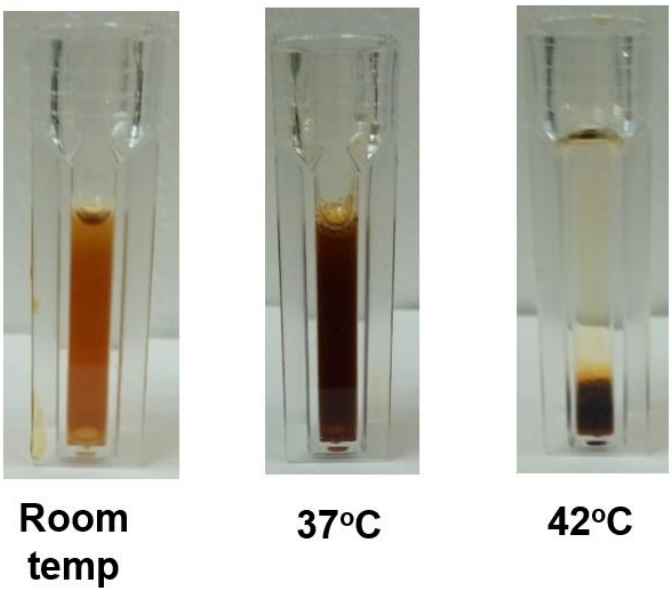

Figure 2.25. LCST measurement of PNIPMAM-coated iron oxide nanoparticles: Phase transition analysis on 10 mg/mL PNIPMAM-coated nanoparticles following heating at room temperature (19.3^{o}C, left), 37^{o}C (centre), and 42^{o}C (right).

2.4 Conclusions

In order to generate iron oxide nanoparticles that were water soluble, I followed an established procedure to generate polyol-capped particles for improved aqueous stability (Carroll et al., 2010). When particles were also surface-coated with sodium citrate, this approach yielded highly stable aqueous suspensions at a size of 6.3 ± 0.9 nm as measured in TEM images. Additionally, I showed the particles exhibited superparamagnetic properties and were able to undergo magnetic heating at a rate of 0.3^{o}C min^{-1} when exposed to an alternating magnetic field.

I selected an ATRP approach to synthesise acid-terminated PNIPAM as a well-controlled method to produce polymers with a narrow M_w distribution and defined terminal groups (Kurzhals et al., 2015, Queffelec et al., 2000). I could produce acid-terminated PNIPAM with a M_w of 13.26 kDa as confirmed by MALDI-TOF mass spectrometry, as well as characteristic broad ^{1}H NMR peaks for the polymer. Also, I could show temperature-sensitive properties for PNIPAM at an LCST of 32^{o}C.

After synthesising the nitrated catechol molecule NDA, this could be terminally-functionalised to acid-terminated PNIPAM through an amide coupling reaction (Kurzhals et al., 2015). NDA UV properties allowed characterisation of the presence and extensiveness of NDA coupling to PNIPAM, which showed a 67% reaction efficiency.

With NDA-PNIPAM, I could successfully coat the iron oxide nanoparticle surface and characterise the molecular and temperature-sensitive properties of the polymer shell. XPS analysis revealed the presence of nitrogen and increased carbon, indicative of PNIPAM presence on the particle surface. TGA analysis showed a significant mass loss when heating PNIPAM-coated particles above 350^{o}C through thermal decomposition of surface-bound polymer. I could also detect a significant increase in hydrodynamic diameter by both DLS and NTA for nanoparticles coated with PNIPAM. PNIPAM-coated nanoparticles also displayed temperature sensitivity above the polymer LCST of 32^{o}C when heated with or without magnetic heating. The phase transition of PNIPAM-coated particles could also be visualised and characterised in terms of size using NTA analysis, which revealed particle aggregation above the LCST.

Finally, following a published procedure (Rathfon and Tew, 2008), I was able to synthesise an alternative temperature-sensitive polymer PNIPMAM through the functionalisation of PMASI with isopropylamine. This generated an acid-terminated version of PNIPMAM with a M_w of 10.3 kDa, which displayed a higher LCST than PNIPAM of 42^{o}C. As with PNIPAM, I was able to functionalise acid-terminated PNIPMAM with NDA and show a similar coupling efficiency of 60%. NDA-PNIPMAM could coat the iron oxide nanoparticle surface and confer temperature-sensitive properties upon heating above 42^{o}C.

In terms of reproducibility, I was able to synthesise PNIPAM on multiple occasions that showed a narrow molecular weight distribution with an Mw of ~10 kDa and an LCST of ~32^{o}C. As for PNIPMAM, the synthesis route involving the functionalisation of PMASI was done on one occasion and would therefore benefit from further work repeating the synthesis to ascertain reproducibility. The extent of NDA functionalisation for both PNIPAM and PNIPMAM were very similar, showing similar values with ~60% of polymer chains being terminally-coupled to NDA. Different batches of PNIPAM-coated particles were prepared and showed extensive coating by TGA and temperature-sensitivity at the PNIPAM LCST. These batches were used in **Chapters 3** and **4** for experimental work involving magnetically heated release of proteins and gave similar results indicating batch-to-batch reproducibility. A single batch of PNIPMAM-coated nanoparticles was prepared and used for magnetically heated protein release experiments in **Chapter 2**, thus this work would benefit from the testing of additional batches to assess reproducibility.

In this chapter, I have been able to generate temperature-sensitive, magnetically-responsive iron oxide nanoparticles coated with two different polymers. This provided me with the tools for investigating protein encapsulation within the polymer shell of surface-functionalised nanoparticles, followed by temperature-sensitive release. Below is a schematic of how the polymer may be attached to the nanoparticle surface (**Figure 2.26**).

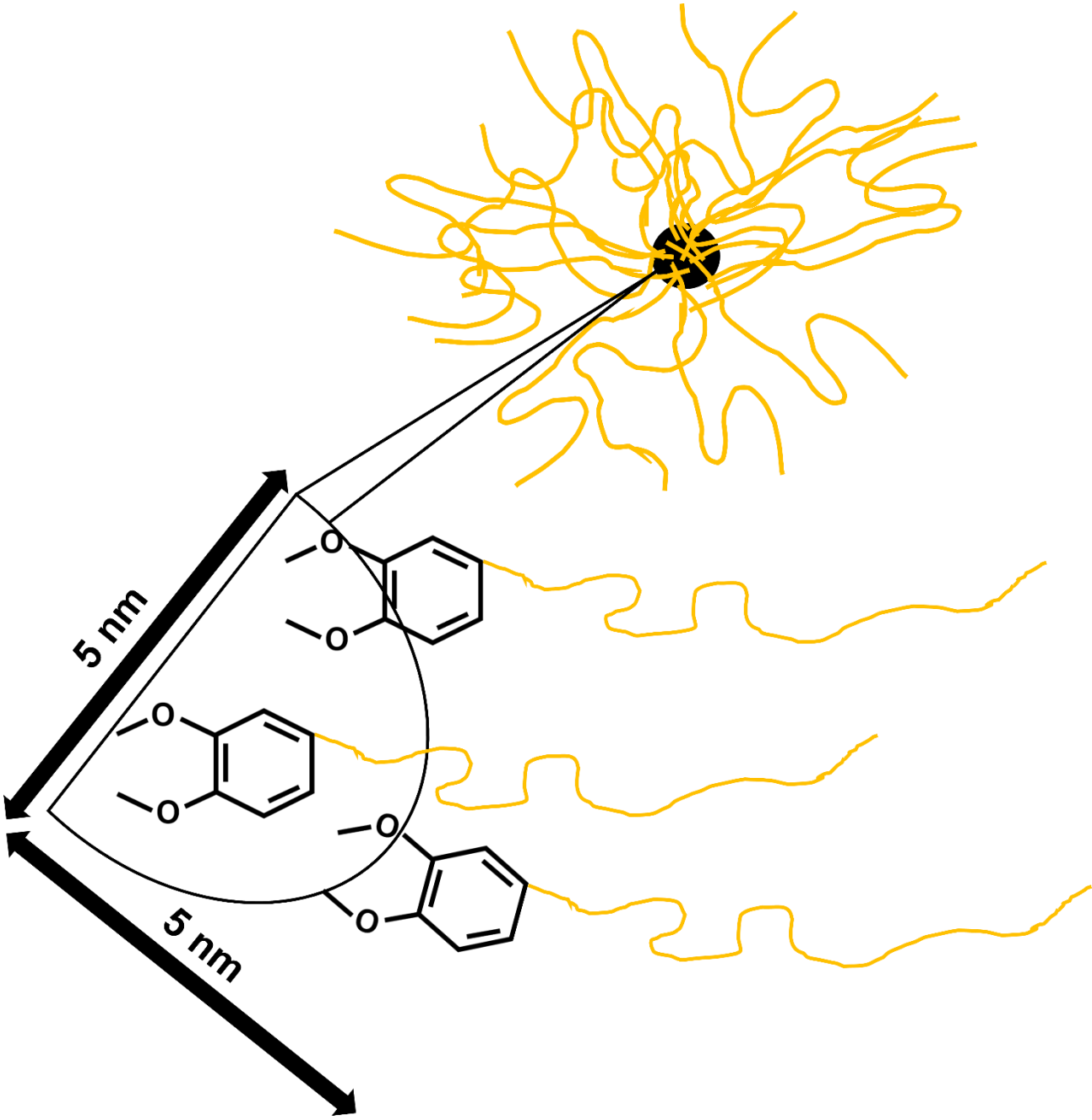

Figure 2.26. Schematic of possible PNIPAM attachment to iron oxide particle surface: Schematic based on grafting density calculations where PNIPAM-coated nanoparticle (top right) is shown with ~20 polymer chains on surface. Zoomed in inset (bottom left) represents NDA-PNIPAM attachment to particle surface with ~0.3 polymers/nm^2.

Chapter 3: Biochemical studies of protein encapsulation and release from polymer-coated nanoparticles

3.1. Rationale, aims and summary

The use of nanoparticles as a tool for biomolecule delivery is a highly attractive therapeutic application for a multitude of diseases. Small size means nanoparticles are evasive enough to reach biological niches of interest, as well as having the potential to be surface-modified with molecules like antibodies to confer targeting specificity. Also, using temperature-responsive polymer shells on the nanoparticle surface is an interesting approach for the encapsulation and release of biomolecules in response to heating. For effective nanoparticle applications as a therapeutic delivery system, it is important to characterise and understand the mechanisms by which biomolecules are encapsulated and released.

Biomolecule entrapment and release from temperature-responsive polymers has largely been studied using small molecules such as drugs and short peptides. Indeed, it has been shown previously that magnetic heating of composites using magnetic nanoparticles and temperature-sensitive polymers can be effective for the release of drug molecules Vitamin B12 (Liu et al., 2009) and DOX (Glover et al., 2013). There are some reports investigating the encapsulation and release of more complex biomolecules from temperature-responsive polymers. For example, it has been shown previously that microgels of crosslinked PNIPAM with adsorbed magnetic nanoparticles can release VEGF by magnetic heating to activate HUVECs (Dionigi et al., 2014). Whether using large microgels over nanomaterials would be suitable for biomolecule delivery and targeting specific sites *in vivo* is unclear. However, it is encouraging that there is some evidence to suggest that functional proteins can be released from temperature-responsive polymers in a magnetically-triggered manner.

In this chapter, I describe my investigations of encapsulation and release of the test protein apotransferrin from PNIPAM-coated nanoparticles generated in **Chapter 2**. I aimed to use the iron oxide nanoparticle magnetic heating properties to trigger temperature-dependent protein release from PNIPAM-coated nanoparticles. I could show that expansion of the PNIPAM shell from a collapsed state by cooling below the LCST in the presence of apotransferrin, allowed for protein encapsulation. Also, I observed that apotransferrin could be released in

both a pH- and temperature-sensitive manner. Temperature-sensitive release was markedly enhanced in the presence of additional competing protein RNaseB. Magnetic heating of PNIPAM-coated nanoparticles could trigger apotransferrin release following a continuous or pulsed application.

I wanted to use apotransferrin as a test protein since it is glycosylated, as is Wnt3a (to a lesser extent) used in subsequent cell-based experiments (**Chapter 4**), and therefore would provide useful information about the encapsulation and release mechanics of a glycosylated protein from polymer-coated nanoparticles. Moreover, apotransferrin has a molecular weight of 80 kDa which is higher than Wnt3a (39.3 kDa) which allowed comparisons to be made about any possible difference in protein encapsulation/release as a result of size differences. Additionally, apotransferrin has an isoelectric point of 5.4 giving it a negative charge at neutral pH, whereas Wnt3a has an isoelectric point of 8.5, meaning the protein has a slightly positive charge at neutral pH. The charge differences of both proteins also could be a factor in determining the extent of encapsulation/release from polymer-coated nanoparticles which makes them interesting to compare.

RNaseB, like apotransferrin, is also glycosylated (albeit to a lesser extent), and therefore is a suitable protein to act as a competitor that has similar post-translational modifications to apotransferrin. Also, RNaseB is significantly smaller than apotransferrin at 14.7 kDa and is positively charged at neutral pH (pI 9.4). These properties may be important in determining kinetics of protein release from polymer-coated nanoparticles and therefore it would be interesting to compare with proteins exhibiting different properties in future work. A comparison of these properties for apotransferrin, RNaseB and Wnt3a (used in **Chapter 4**) is provided in **Table 3.1**.

Protein	Molecular weight (kDa)	Isoelectric point (pI)	Glycosylation level
Apotransferrin	80	5.4	High - 8 *N*-glycans
RNaseB	14.7	9.3	Low - 1 *N*-glycan
Wnt3a	39.3	8.5	Low – 2 *N*-glycans

Table 3.1. Comparison of molecular weight, isoelectric point and glycosylation levels of apotransferrin, RNaseB and Wnt3a.

Additionally, I began work characterising the encapsulation and release of apotransferrin from the PNIPMAM-coated nanoparticles generated in **Chapter 2**. I could show that as with PNIPAM-coated nanoparticles, protein encapsulation was effective by incubating PNIPMAM-coated particles with test protein apotransferrin above the LCST initially, before then cooling below the LCST. Also, I observed that apotransferrin could be released from PNIPMAM-coated particles more rapidly above the polymer LCST (42^{o}C) than at a physiological temperature (37^{o}C). Through pulsed magnetic heating, I was able to detect apotransferrin release at a significantly enhanced rate than was observed at 37^{o}C. Further development of PNIPMAM-coated particles to prevent protein leakage at 37^{o}C, could be a potential tool for *in vivo* protein delivery and magnetically-triggered release.

3.2. Materials and methods

3.2.1. Preparation of protein-loaded nanoparticles

1 mg of polymer-coated nanoparticles and different amounts of apotransferrin (Sigma-Aldrich) was dissolved in 100 µL of physiological buffer (20 mM HEPES, 100 mM NaCl, pH 7.4). Solution was incubated on a shaker at 37^{o}C for 1 h to agitate and suspend nanoparticles following temperature-sensitive insolubility above the polymer LCST. Particles were then left to cool and equilibrate to room temperature for 30 min before they were re-solubilised by pipetting. Particles were then incubated on a shaker at room temperature for 1 h. Particles were then magnetically separated, and the supernatant retained as the initial wash. Then further wash steps were conducted by adding 100 µL assay-specific wash solution of either 100 µL physiological buffer or 10 mg/mL RNaseB (Sigma-Aldrich) solution in physiological buffer to the particles and incubating for 1 h at room temperature on a shaker. Particles were then magnetically separated before adding 100 µL more appropriate wash solution and incubating as before, this step was repeated multiple times (3 – 10), retaining each wash step.

3.2.2. Protein release assays

1 mg of protein-loaded PNIPAM-coated nanoparticles was prepared and subjected to different biochemical conditions or changes in temperature with or without magnetic heating. Experiments were conducted in assay-appropriate 100 µL solutions of 10 mg/mL RNaseB solution in physiological buffer (for apotransferrin temperature release experiments) or basic pH buffers (100 mM NaCl, 20 mM triethanolamine). During timepoints, samples were agitated on shakers and between timepoints nanoparticles were magnetically separated before removing 10 µL of the sample volume for analysis. For sample handling during magnetic heating experiments see **Materials and Methods, section 2.2.4.2, pg 120.**

3.2.3. Sample preparation for protein analysis

Following collection, samples were made up to 15 µL in sample buffer (5% (v/v) glycerol, 50 mM Tris-HCl pH 6.8, 50 mM DTT, 1% (w/v)SDS, 0.7 mM Bromophenol Blue) and boiled at 95^{o}C for 5 min. Proteins were separated by sodium dodecyl sulfate-polyacrylamide gel electrophoresis (SDS-PAGE) on 10% (w/v) acrylamide gels prior to coomassie staining or western blotting.

3.2.4. SDS-PAGE

SDS-PAGE gels were prepared with a separating gel composed of 10% (w/v) acrylamide, 375mM Tris pH 8.8, 0.05% (w/v) ammonium persulfate (APS) and 0.067% (w/v) N,N,N′,N′-tetramethylethylenediamine (TEMED), and a stacking gel containing 4% (w/v) acrylamide, 125mM Tris pH 6.8, 0.1% (w/v) APS, 0.1% (w/v) TEMED. Samples were loaded into wells alongside 5 µL of a pre-stained protein ladder (Precision Plus All-Blue, Bio-Rad). Gels were placed in gel tanks and immersed in running buffer (25 mM Tris, 250 mM glycine, 0.1% (w/v) SDS) before running at 120 V constant voltage for 10 min and then at 180 V constant voltage until the dye had reached the bottom of the gel.

3.2.5. Coomassie staining

Fairbanks Coomassie staining (Fairbanks et al., 1971) was carried out by boiling gels in Fairbanks solution A (25% (v/v) isopropanol, 10% (v/v) acetic acid, 0.05% (w/v) Coomassie brilliant blue) before washing with dH_2O. The process was repeated with Fairbanks solution B (10% (v/v) isopropanol, 10% (v/v) acetic acid, 0.005% (w/v) Coomassie brilliant blue), Fairbanks solution C (10% (v/v) acetic acid, 0.002% (w/v) Coomassie brilliant blue) and Fairbanks solution D (10% (v/v) acetic acid). Gels were left in solution D until distinct bands were apparent from the background. Quantification was carried out using ImageJ software.

3.2.6. Western blotting

Western blotting was conducted by semi-dry transfer of gels onto polyvinylidenefluoride (PVDF) membranes (Thermo Fisher) for 60 min at 20 V using 48 mM Tris-HCl, 39 mM glycine, 20% (v/v) MeOH and 0.0375% (w/v) SDS as the transfer buffer. Membranes were blocked using phosphate buffered saline (PBS) with 0.05% (v/v) Tween-20 (PBST) and 5% (w/v) milk for 1 h at room temperature. Membranes were then incubated with primary antibody: anti-apotransferrin (1:1000, Dako) in 5% (v/v) milk PBST solution overnight at 4°C. Following four 10 min washes at room temperature in 5% (v/v) milk PBST solution, secondary antibody goat anti rabbit-horseradish peroxidase (GAR-HRP) (1:3000, Bio-Rad) in 5% (w/v) milk PBST solution was added for 1 h at room temperature. The blot was then washed 3 times with 5% (w/v) milk PBST solution and 2 times in PBST for 10 min each at room temperature. Blots were imaged on a GeneGenius Chemi-imager (Syngene) after application of Immobilon horseradish peroxidase (HRP) substrate (Millipore). Quantification was carried out using ImageJ software.

3.3. Results

3.3.1. Apotransferrin encapsulation using PNIPAM LCST properties

In order to encapsulate proteins within the PNIPAM shell on the nanoparticle surface, I utilised the phase transition properties of the polymer. This was conducted in a protein-containing solution with PNIPAM-coated nanoparticles by increasing the temperature to 37^{o}C so that it exceeded the LCST of PNIPAM (32^{o}C), before cooling below the LCST to room temperature. This allowed for the thermally-sensitive collapse of the PNIPAM shell, followed by its reversible re-expansion. During the polymer collapse above the LCST, proteins in solution would be in close proximity to the nanoparticle surface. The subsequent drop in temperature below the PNIPAM LCST would allow for its re-expansion around the proteins in solution, resulting in encapsulation.

I could show that expansion of the PNIPAM shell from a collapsed state, by cooling below the LCST, could encapsulate the test protein apotransferrin (**Figure 3.1**). Oversaturation of the PNIPAM-coated nanoparticles with 1 mg apotransferrin was clear during the encapsulation procedure since the vast majority of protein was removed in the washing steps. However, upon quantification, I could show that a proportion of the input protein (~25 µg/2.5%) was associated with the nanoparticles.

I also attempted to release the encapsulated apotransferrin by heating the nanoparticles above the PNIPAM LCST at 37^{o}C for 1 h to trigger its collapse. However, I was unable to detect any release following 1 h heating despite protein binding to the nanoparticles (**Figure 3.1**).

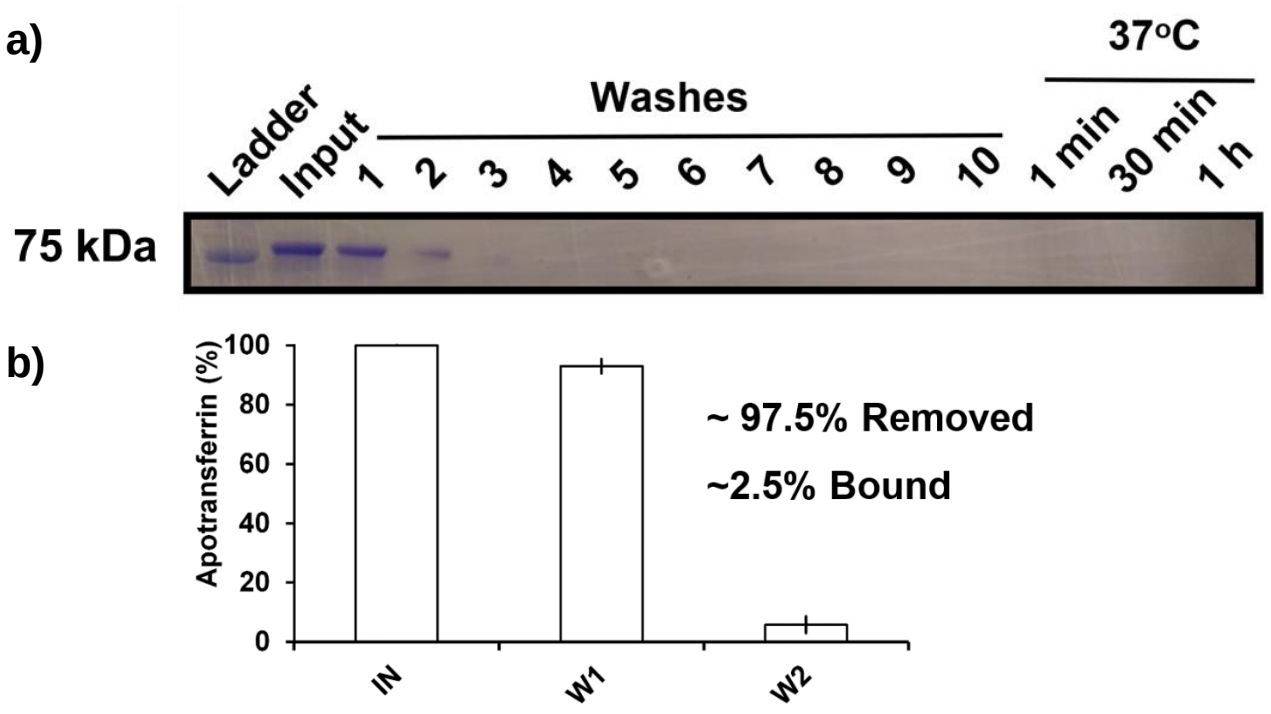

Figure 3.1. Protein encapsulation using PNIPAM LCST: a) SDS-PAGE gel following Coomassie staining following incubation of 1 mg PNIPAM-coated nanoparticles with 1 mg apotransferrin. Samples were heated at 37°C for 1 h with aliquots taken after 1 min, 30 min and 1 h. Input represents 0.1% total apotransferrin (1 µg, 1:1000 dilution), 1 µl (1% of sample volume) of washes 1-5 was diluted (1:100) and 10 µL was used for gel loading, 10 µL of washes 6-10 and 37°C treated samples was loaded (10% of sample volumes) **b)** Quantification of apotransferrin (%) detected in wash steps was carried out using ImageJ software (n=3, error bars denote standard deviation).

3.3.2. Increasing pH triggers apotransferrin release from PNIPAM-coated nanoparticles

Since I could detect that apotransferrin was associating with PNIPAM-coated nanoparticles (**Figure 3.1**), I carried out a series of biochemical treatments to try and disrupt interactions between protein molecules and the polymer shell. PNIPAM-coated nanoparticles with encapsulated apotransferrin were exposed to various solutions, including high salt (1.5 M NaCl, 20 mM HEPES, pH 7.4), acidic pH (20 mM glycine, 100 mM NaCl, pH 2.5), surfactant (2% (w/v) SDS, 100 mM NaCl. pH 7.4) and guanidine hydrochloride (6 M GuHCl, 20 mM HEPES, pH 7.4). None of these conditions could trigger any protein release as detected by coomassie staining of SDS-PAGE gels. Interestingly, when exposed to basic pH conditions (20 mM triethanolamine, 100 mM NaCl, pH 8.5 – 11.5), I was able to detect apotransferrin release from the nanoparticles in both a pH- and time-dependent manner, where protein release was calculated relative to the amount of apotransferrin still associated with the particles after washing (**Figure 3.2**). Since PNIPAM carries no charge, it is likely that hydrogen bonding is the dominant mechanism, suggesting that the nature of protein interactions with the PNIPAM shell are likely to be molecular at neutral pH, rather than through physical entrapment. Indeed, previous work has shown that BSA protein uptake and release from PNIPAM hydrogels is pH-controlled, highlighting that PNIPAM is sensitive to pH as well as temperature (Huo et al., 2006).

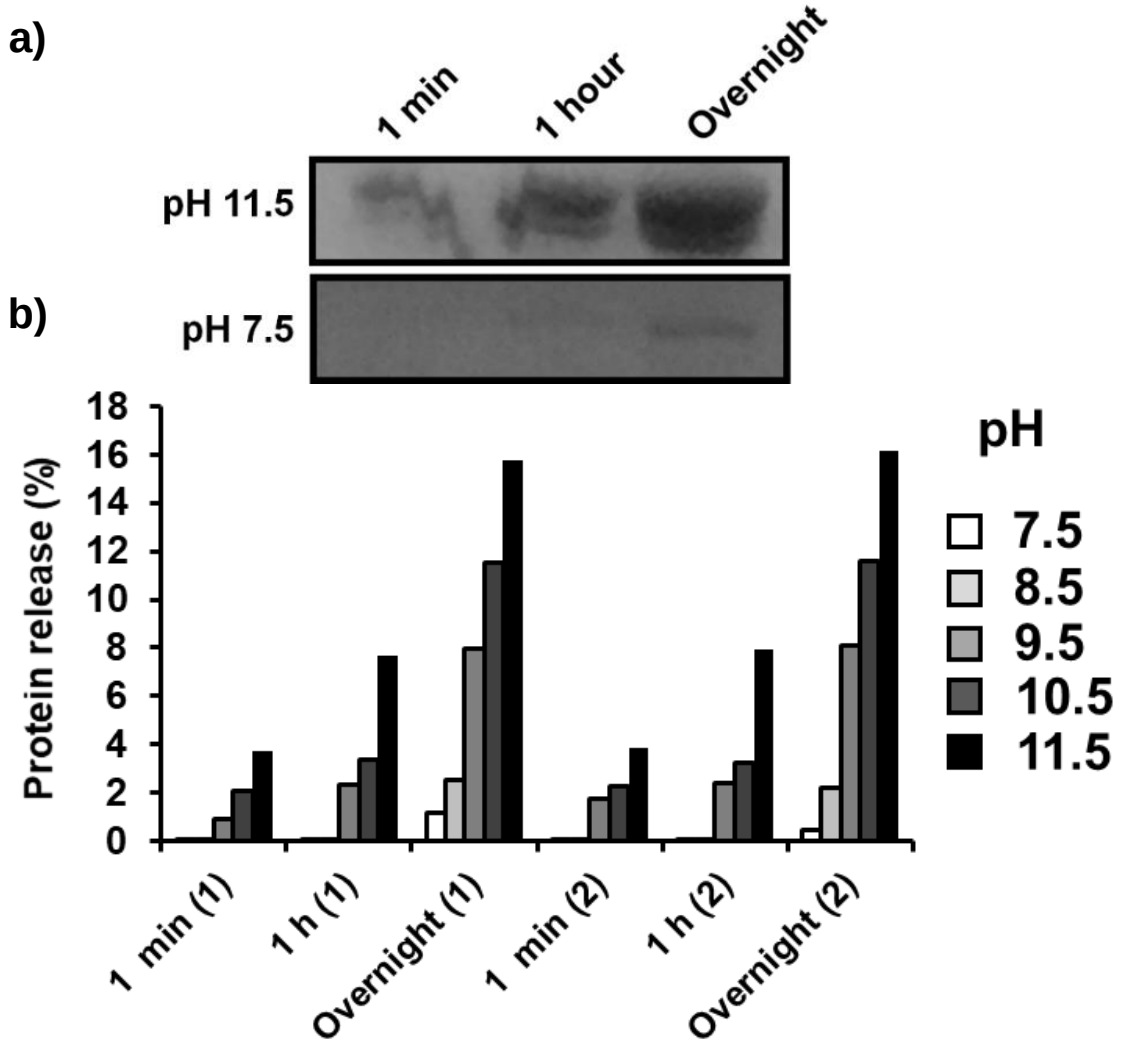

Figure 3.2. PNIPAM-coated nanoparticles release apotransferrin in a pH-sensitive manner: a) Coomassie stained SDS-PAGE gel following treatment of 1 mg PNIPAM-coated nanoparticles incubated with 1 mg apotransferrin at pH 7.5 and 11.5 for 1 min, 1 h and 16 h (Overnight) **b)** Quantification of apotransferrin released from PNIPAM-coated nanoparticles at pH range 7.5-11.5 (buffers used were in 20 mM triethanolamine, 100 mM NaCl), (1) and (2) represent replicate samples, (n=2). Protein release was calculated relative to the amount of apotransferrin still associated with the particles after washing.

3.3.3. Co-adsorption does not encapsulate apotransferrin into PNIPAM-coated nanoparticles

As I could detect apotransferrin release from PNIPAM-coated nanoparticles by increasing pH, it was clear that protein molecules were associated with the particles. Because the protein-polymer interaction was likely of a molecular nature however, this meant that increasing the temperature above the PNIPAM LCST had little to no effect on release. In an effort to encapsulate proteins within the PNIPAM shell in such a way that a change in temperature may trigger release, I performed a co-adsorption assay. This involved carrying out the nanoparticle coating experiment with free NDA-PNIPAM (**Materials and Methods, section 2.2.3.7, pg 115**) in a small volume (100 µL) of physiological buffer containing 1 mg apotransferrin. Particles were then washed as done previously (**Materials and Methods section 3.2.1, pg 165**) before analysis by Coomassie staining of SDS-PAGE gels.

Since apotransferrin was present during the attachment of PNIPAM and would be dispersed around the nanparticles, I reasoned that this may aid the entrapment of the protein more homogeneously throughout the polymer shell. Previously I was attempting to encapsulate apotransferrin using nanoparticles that already had PNIPAM grafted onto the surface, which perhaps only allowed for interactions at the periphery of the polymer shell. I rationalised that a more homogenous encapsulation of apotransferrin throughout the polymer shell may improve temperature-sensitive release following the PNIPAM collapse above its LCST.

Despite only being able to detect small amounts of apotransferrin in the wash steps, I could not see protein bands following a high pH treatment of the nanoparticles overnight (**Figure 3.3**). This suggests that apotransferrin did not associate with the PNIPAM-coated nanoparticles, and probably interacted with the excess of free polymer during NDA-PNIPAM-nanoparticle coating.

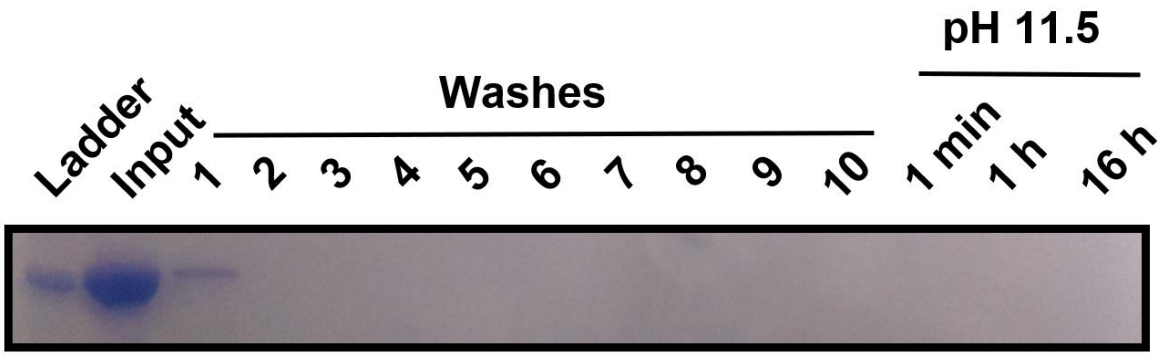

Figure 3.3. Co-adsorption does not encapsulate apotransferrin into PNIPAM-coated nanoparticles: Coomassie stained SDS-PAGE gel following incubation of 1 mg PNIPAM-coated nanoparticles with 1 mg apotransferrin in the presence of free polymer. Samples were magnetically purified before treating at pH 11.5 for 16 h with aliquots taken after 1 min, 1 h and 16 h. Input represents 0.1% total apotransferrin (1 µg, 1:1000 dilution), 1 µl (1% of sample volumes) of washes 1-5 was diluted (1:100) and 10 µL used for gel loading, 10 µL of washes 6-10 and pH 11.5 treated samples was loaded (10% of sample volumes).

3.3.4. RNaseB competition triggers apotransferrin release from PNIPAM-coated nanoparticles

Increased pH triggered apotransferrin release from PNIPAM-coated nanoparticles; however, this was not the desired protein release mechanism and certainly not an ideal approach for biological applications. Moreover, co-adsorption was not a suitable approach to encapsulate proteins, thus I continued to utilise the PNIPAM LCST encapsulation procedure (**Materials and Methods, section 3.2.1, pg 165**). As a biocompatible approach, I hypothesised that perhaps the addition of another protein may act to compete for polymer binding with the encapsulated apotransferrin, causing its release. RNaseB was selected as a competing protein to aid the release of apotransferrin since both are glycoprotains and thus have similar post-translational modifications. Since Wnt3a also is glycosylated, this provided a useful model system for comparison with Wnt3a experiments in **Chapter 4**. Additionally, the differences in isoelectric points of RNaseB (9.3) and apotransferrin (5.4) means that they have opposite charges at neutral pH, which may aid in triggering the release of apotransferrin. Also, RNaseB (14.7 kDa) is significantly smaller than apotransferrin (80 kDa) meaning for every apotransferrin molecule there are ~5 molecules of RNaseB. This allows for a significant excess of RNaseB to be present relative to apotransferrin which could help disassociate apotransferrin from the particles.

Following apotransferrin encapsulation into PNIPAM-coated nanoparticles, RNaseB was added in excess (10 mg/mL). Interestingly, I observed that with RNaseB present, apotransferrin was released from the nanoparticles. This can be seen in **Figure 3.4**, where protein release was calculated relative to the amount of apotransferrin still associated with the particles after washing. This suggests that the presence of additional proteins can act to trigger the release of protein molecules encapsulated within the polymer shell of PNIPAM-coated nanoparticles. Additionally, this is advantageous for use in biological systems in that there will be an abundance of proteins in such an environment. Also, at the 16 h timepoint there appears to be a slight reduction in RNaseB, which perhaps indicates some association with the nanoparticles in place of apotransferrin.

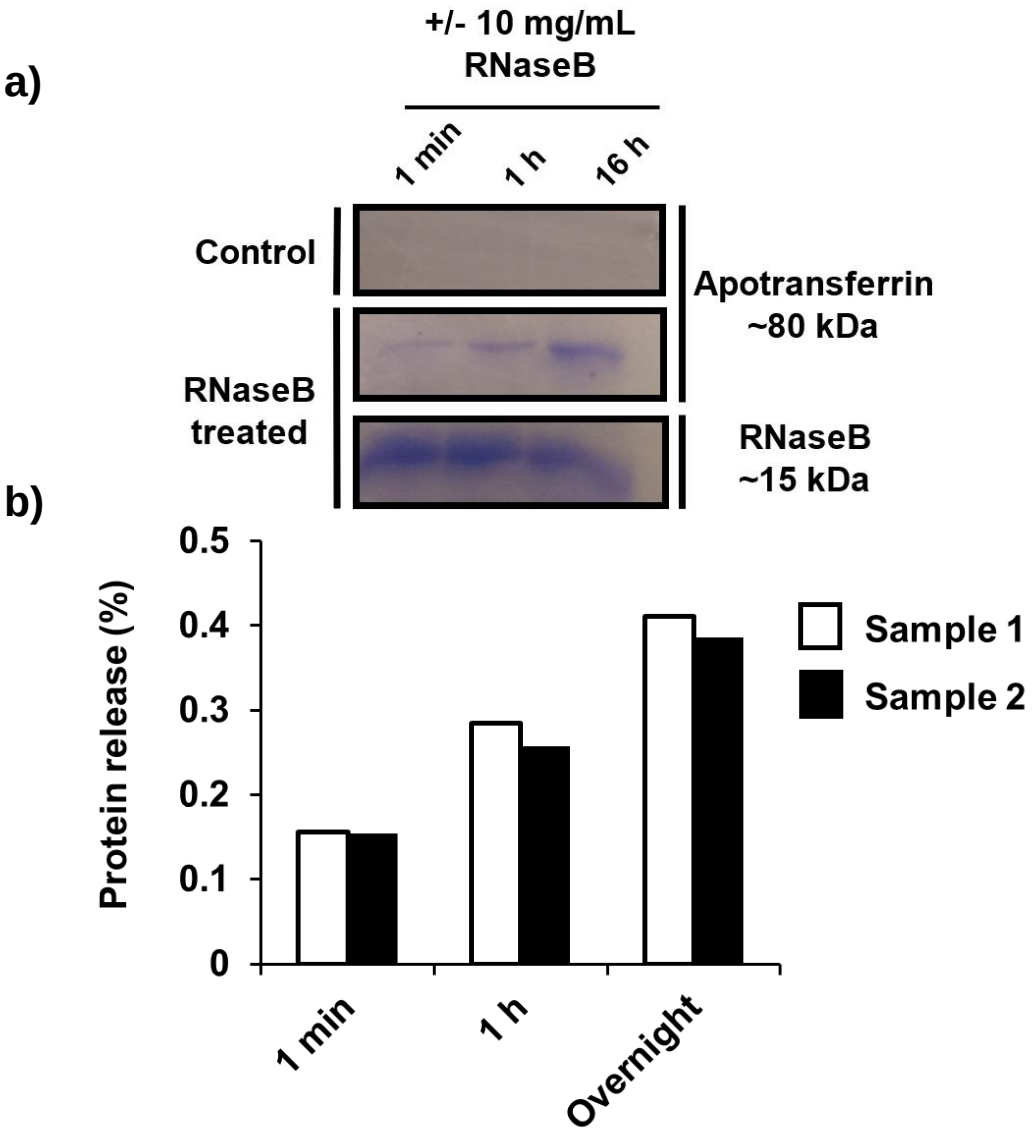

Figure 3.4. RNaseB competition triggers apotransferrin release from PNIPAM-coated nanoparticles: a) Coomassie staining of SDS-PAGE gel following incubation of 1 mg PNIPAM-coated nanoparticles with 1 mg apotransferrin. Samples were incubated without (control) or with 10 mg/mL RNaseB, and 10 µL aliquots taken after 1 min, 1 h and 16 h (overnight) for analysis by SDS-PAGE **b)** Quantification of apotransferrin released following addition of 10 mg/mL RNaseB, (n=2) Protein release was calculated relative to the amount of apotransferrin still associated with the particles after washing.

3.3.5. PNIPAM-coated nanoparticles release apotransferrin in a temperature-dependant manner

As I could observe that the addition of RNaseB can function as a competing protein to trigger the release of apotransferrin from PNIPAM-coated particles, I wanted to see whether this effect was temperature-dependent. As PNIPAM undergoes a significant morphological change above its LCST, perhaps this could impact upon the apotransferrin release in the presence of competing proteins. I also wanted to reduce the amount of input protein used for encapsulation as the 1 mg quantities used previously were in large excess. Also, the ultimate aim was to encapsulate and release the growth factor Wnt3a for cellular activation so lowering the amount encapsulated was important as Wnt3a acquisition in mg quantities was not feasible. I therefore reduced the amount of input protein during encapsulation 1000-fold to 1 µg per 1 mg PNIPAM-coated nanoparticles. I also switched from coomassie staining to western blotting for protein analysis to improve sensitivity and allow detection of lower amounts of protein. Additionally, I improved the robustness of washing steps with the addition of RNaseB prior to changing the temperature for collecting protein release samples.

I could detect the release of apotransferrin from PNIPAM-coated nanoparticles after washing, following an increase in temperature above the polymer LCST to 37ºC, where protein release was calculated relative to the amount of apotransferrin still associated with the particles after washing (**Figure 3.5**). Interestingly, despite RNaseB being present, I could not detect apotransferrin release in the control experiment (room temperature). This suggests that washing with RNaseB is important to remove bound apotransferrin that would otherwise be released at lower temperatures, before an increase above the PNIPAM LCST to allow for a clear temperature-sensitive effect.

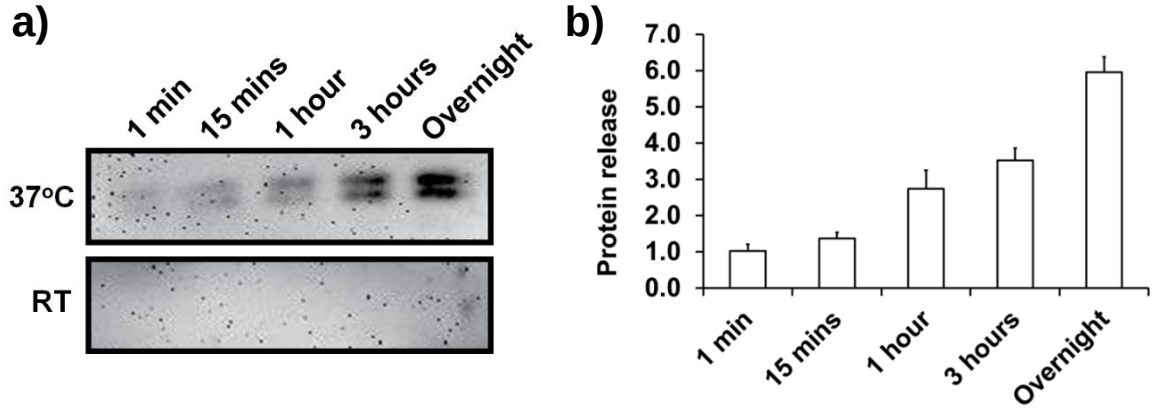

Figure 3.5. PNIPAM-coated nanoparticles release apotransferrin in a temperature-dependent manner: a) Western blot analysis following 10 mg/mL RNaseB treatment of 1 mg PNIPAM-coated nanoparticles loaded with 1 µg apotransferrin at pH 7.5 for 1 min, 15 min, 1 h, 3 h and 16 h (overnight) at 37°C or room temperature (21°C) **b)** Quantification of apotransferrin released from PNIPAM-coated nanoparticles at 37°C (n=3, error bars denote standard deviation) Protein release was calculated relative to the amount of apotransferrin still associated with the particles after washing.

3.3.6. Magnetic heating triggers apotransferrin release from PNIPAM-coated nanoparticles above 30ºC

After observing that protein release was triggered when PNIPAM-coated nanoparticles with encapsulated apotransferrin were heated above the polymer LCST, I wanted to assess whether magnetically heating the nanoparticles would have a similar affect. To investigate this, I used a temperature-controlled room at 30ºC to maintain a constant environment close to the PNIPAM LCST. As I previously had observed a magnetic heating rate of ~0.3ºC min^{-1}, it was ideal to start magnetic heating close to the phase transition temperature. The magnetic heating setup I used (**Figures 2.3** and **2.5**) allowed for measurements of the sample temperature in real-time using an infrared thermocouple probe that was immersed in the sample volume environment through an adapted plastic inlet tube. As this probe was composed of gallium arsenide, it did not contain any trace magnetic material so would not respond to the alternating magnetic field and contribute to any magnetic heating observed. Additionally, as the components of the setup around the sample area generated heat when the magnetic field was switched on, ice-cold water was pumped through the coils around the magnet to dissipate the extra heat. The control measures taken in the experimental setup ensured that any heating measurements were indicative of nanoparticle magnetic heating only.

I could show that encapsulated apotransferrin was released from PNIPAM-coated nanoparticles after magnetic heating over a 30 min period, where protein release was calculated relative to the amount of apotransferrin still associated with the particles after washing (**Figure 3.6**). Before experimentation, a control sample containing no nanoparticles was also exposed to the magnetic field over a 30 min period. It did not increase in temperature suggesting that the heat dissipation worked well. Particles loaded with apotransferrin were left in the 30ºC room throughout the timecourse and I was unable to detect any protein release for this control sample indicating that I could observe clear, temperature-dependent release. Interestingly, I could detect protein release both above and below the PNIPAM LCST (highlighted in red). I could observe faint levels of release after just 5 min magnetic heating which continued to increase as samples were collected cumulatively over the time-course. Between 15 – 30 min magnetic heating, the PNIPAM-coated nanoparticles had visibly precipitated as a function of the solution

temperature exceeding that of the polymer LCST. The temperature change, that arises as a consequence of heat generated by the nanoparticles in an alternating magnetic field, will be much higher immediate to the nanoparticle surface than further away from the surface. As heat is generated by the nanoparticles, this will dissipate throughout the surrounding environment meaning that the temperatures recorded for the sample volume are not representative of the temperatures close to the surface of the nanoparticle. Since the particle surface environment is where the polymer-protein layer is localised, I hypothesised that temperature-sensitive effects on the polymer layer, as a consequence of local heating immediate to the particle surface, could result in protein release at temperatures below the PNIPAM LCST. Additionally, combined with the particle surface heating, this release could be due to protein that is more weakly bound at the surface of the polymer.

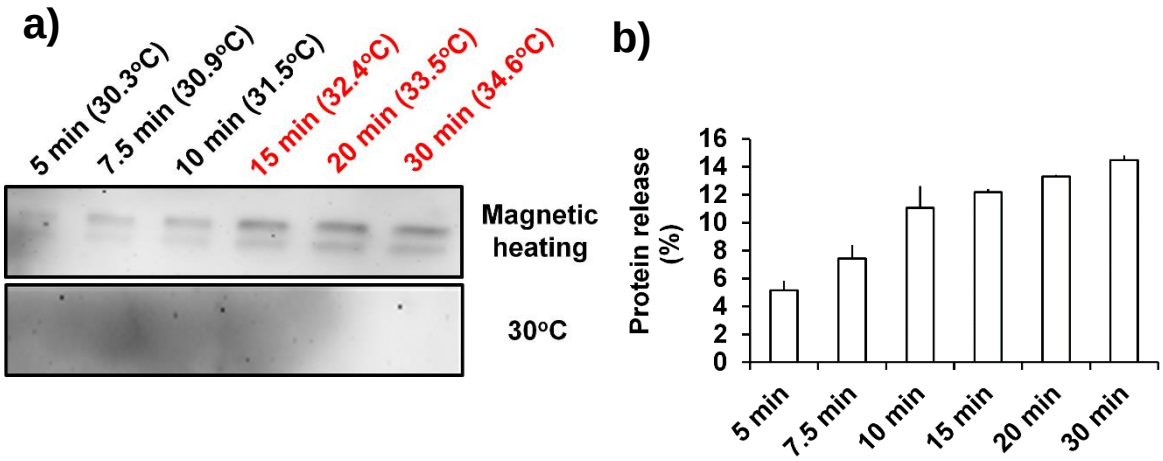

Figure 3.6. Magnetic heating triggers apotransferrin release from PNIPAM-coated nanoparticles above 30°C: a) Western blot analysis following 10 mg/mL RNaseB treatment of 1 mg PNIPAM-coated nanoparticles loaded with 1 µg apotransferrin at pH 7.5 for 5, 7.5, 10, 15, 20 and 30 min at 30°C or with magnetic heating. Temperatures during magnetic heating are provided in brackets above each timepoint and highlighted in red above the PNIPAM LCST, 30°C sample temperature was unchanged throughout timecourse **b)** Quantification of apotransferrin released from PNIPAM-coated nanoparticles with magnetic heating (n=3, error bars denote standard deviation) Protein release was calculated relative to the amount of apotransferrin still associated with the particles after washing.

3.3.7. Constant or pulsed magnetic heating triggers apotransferrin release from PNIPAM-coated nanoparticles at room temperature

After observing that PNIPAM-coated nanoparticles could release apotransferrin at temperatures below the polymer LCST (between 30 – 32^{o}C) following magnetic heating, I wanted to investigate whether this effect could also be seen at temperatures further from the LCST. To study this, I carried out magnetic heating experiments at room temperature rather than at 30^{o}C, using a laminar flow tissue culture hood as a workspace. Conducting the assays in this environment was also useful in preparation for subsequent cell-based work with magnetic heating which requires a sterile environment.

I could show that protein was released when subjecting PNIPAM-coated nanoparticles with encapsulated apotransferrin to an alternating magnetic field, where protein release was calculated relative to the amount of apotransferrin still associated with the particles after washing (**Figure 3.7**). As expected, I was unable to detect any protein release at room temperature without magnetic heating. After just a few minutes of exposure to the magnetic field released protein could be detected by western blotting. During the time-course the sample temperature did not heat up sufficiently to reach that of the PNIPAM phase transition meaning that the nanoparticles were still visibly soluble throughout. Despite this, I could detect apotransferrin release in response to magnetic heating. This supports the observations in **Figure 3.6** suggesting that the release of apotransferrin from PNIPAM-coated particles following magnetic heating is not dependent on the bulk sample temperature exceeding the LCST of PNIPAM.

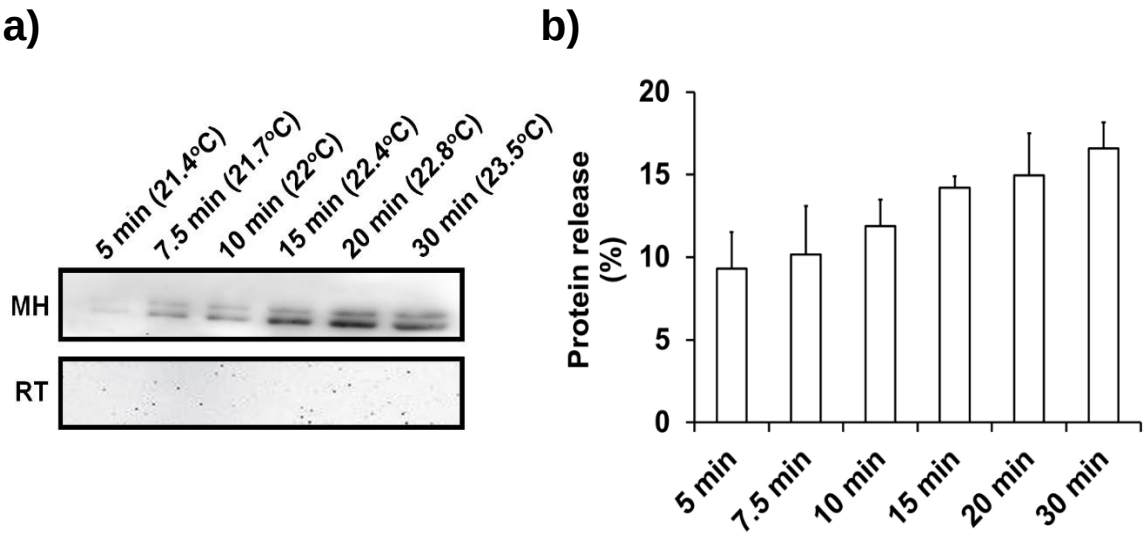

Figure 3.7. Constant magnetic heating triggers apotransferrin release from PNIPAM-coated nanoparticles at room temperature: a) Western blot analysis following 10 mg/mL RNaseB treatment of 1 mg PNIPAM-coated nanoparticles incubated with 1 µg apotransferrin at pH 7.5 for 5, 7.5, 10, 15, 20 and 30 min at room temperature (RT) (21.3°C) or with magnetic heating (MH). Temperatures during magnetic heating are provided in brackets above each timepoint. **b)** Quantification of apotransferrin release from PNIPAM-coated nanoparticles with magnetic heating (n=3, error bars denote standard deviation), Protein release was calculated relative to the amount of apotransferrin still associated with the particles after washing.

To further assess the magnetic heating effect on protein release, I conducted an assay that would allow me to specifically probe the environment at the nanoparticle surface. This was achieved by magnetically heating the apotransferrin-loaded particles in pulses, switching the field on and off in 10 sec cycles throughout the time-course. This maintained a relatively consistent bulk solution temperature whilst applying bursts of magnetic heating to the nanoparticle surface. Interestingly, I observed that in response to pulses of magnetic heating from 10 min onwards (highlighted in green), apotransferrin was still released at a rate comparable to that seen in **Figure 3.7** during constant magnetic field application, where protein release was calculated relative to the amount of apotransferrin still associated with the particles after washing (**Figure 3.8**). This

suggests that magnetic heating immediate at the particle surface is likely sufficient to trigger apotransferrin release.

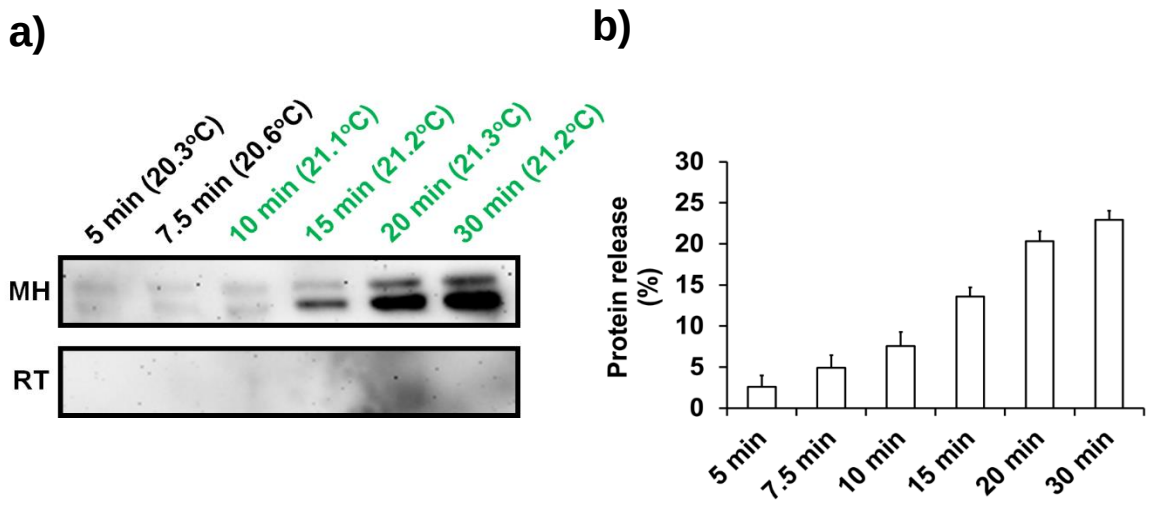

Figure 3.8. Pulsed magnetic heating triggers apotransferrin release from PNIPAM-coated nanoparticles at room temperature: a) Western blot analysis following 10 mg/mL RNaseB treatment of 1 mg PNIPAM-coated nanoparticles incubated with 1 µg apotransferrin at pH 7.5 for 5, 7.5, 10, 15, 20 and 30 min at room temperature (RT) (20.8°C) or with pulsed magnetic heating (MH). Timepoints during pulsed magnetic heating (10 sec on/off) are highlighted in green. Temperatures during magnetic heating are provided in brackets above each timepoint. **b)** Quantification of apotransferrin release from PNIPAM-coated nanoparticles with magnetic heating (n=3, error bars denote standard deviation), Protein release was calculated relative to the amount of apotransferrin still associated with the particles after washing.

Additionally, I wanted to determine whether any polymer conformational changes brought about by magnetic heating would irreversibly continue to permit the release of apotransferrin. To measure this, apotransferrin-loaded particles were exposed to the field briefly to release a proportion of protein, before switching off the field and monitoring any further release with time. I could observe that once the field was switched off after 10 min (highlighted in red), levels of apotransferrin released began to plateau and remain constant, where protein release was calculated relative to the amount of apotransferrin still associated with the particles after washing (**Figure 3.9**).

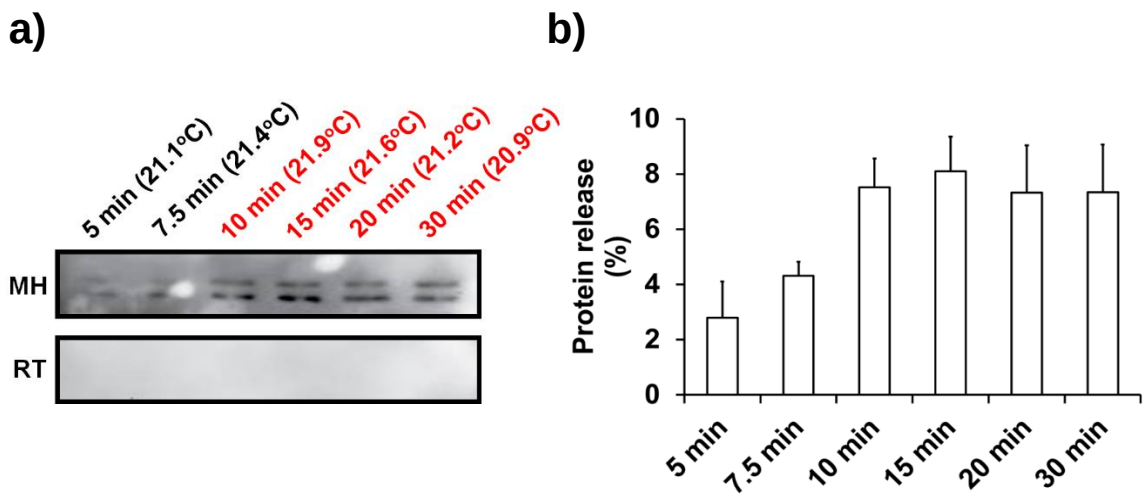

Figure 3.9. Switching off pulsed magnetic field during heating stops apotransferrin release from PNIPAM-coated nanoparticles: a) Western blot analysis following 10 mg/mL RNaseB treatment of 1 mg PNIPAM-coated nanoparticles incubated with 1 µg apotransferrin at pH 7.5 for 5, 7.5, 10, 15, 20 and 30 min at room temperature (RT) (21.1°C) or with pulsed magnetic heating (MH). Timepoints where magnetic field was switched off are highlighted in red, and temperatures during magnetic heating are provided in brackets above each timepoint. **b)** Quantification of apotransferrin released from PNIPAM-coated nanoparticles with pulsed magnetic heating (n=3, error bars denote standard deviation), Protein release was calculated relative to the amount of apotransferrin still associated with the particles after washing.

3.3.8. PNIPMAM-coated nanoparticles release apotransferrin more rapidly at 42ºC than 37ºC

As well as generating PNIPAM-coated nanoparticles, I also was able to synthesise an alternative polymer, PNIPMAM, which exhibited a higher LCST than PNIPAM of 42ºC (**Figure 2.23**). Interestingly, the phase transition appeared more gradual than that of PNIPAM, where I could observe increased solution turbidity with free PNIPMAM from 37ºC to 42ºC before precipitation occurred (**Figure 2.23**). The phase transition in **Figure 2.23** is somewhat difficult to see and would likely benefit from conducting the experiment using higher polymer concentrations to more clearly observe temperature-sensitive changes. As with PNIPAM, I could terminally functionalise PNIPMAM with NDA and coat the nanoparticle surface, which conferred the same temperature-sensitive properties to the coated particles as seen with free polymer (**Figure 2.25**). I wanted to load the polymer shell of PNIPMAM-coated nanoparticles with apotransferrin and study the protein release when heated above the polymer LCST. Apotransferrin encapsulation was carried out using the same approach as for PNIPAM-coated nanoparticles (**Materials and Methods, section 3.2.1, pg 165**), but adapted for the increase in LCST by a 1 h incubation at 42ºC rather than 37ºC.

By incubating apotransferrin-encapsulated PNIPMAM-coated nanoparticles at 42ºC, I could detect protein release as compared to a room temperature control where no protein release was detected; protein release was calculated relative to the amount of apotransferrin still associated with the particles after washing (**Figure 3.10**). I also carried out an incubation at 37ºC which interestingly also showed protein release, but to a lesser degree than the sample at 42ºC. This may suggest that a partial phase transition occurs between 37ºC and 42ºC that is incomplete and requires heating over 42ºC for completion. Structural alterations to PNIPMAM during the partial phase transition may permit slower release of encapsulated apotransferrin, whereas heating to induce a complete phase transition allows protein release to occur more rapidly. Being able to release proteins from PNIPMAM-coated nanoparticles more rapidly at 42ºC than 37ºC is potentially promising for developing a biomolecule release tool above physiological temperature. However, for use in a biological system, further optimisation would be required to prevent protein loss during nanoparticle delivery.

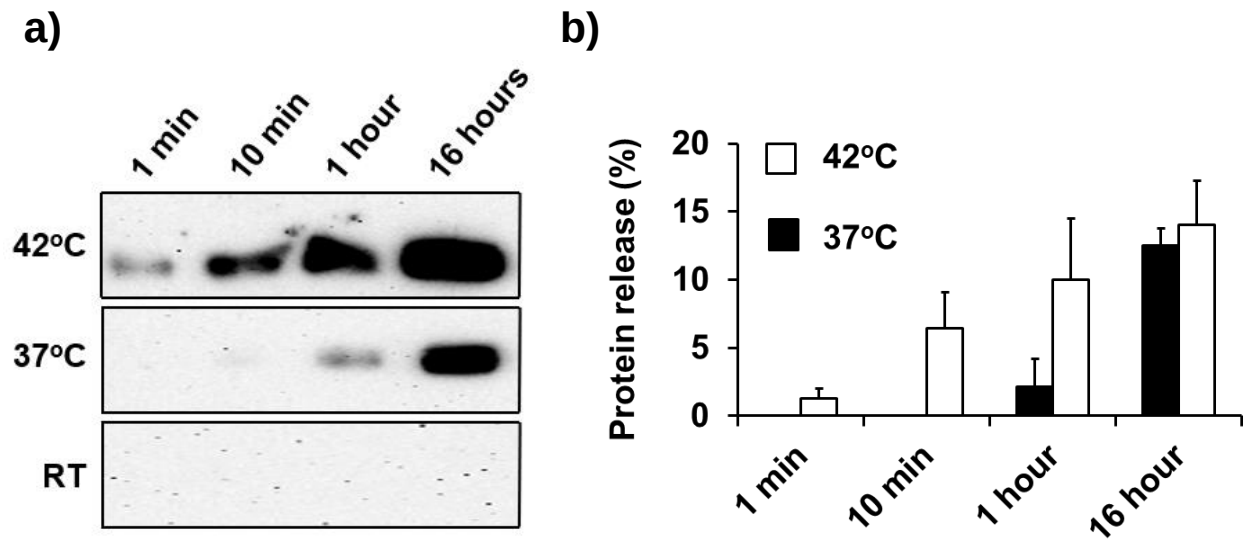

Figure 3.10. PNIPMAM-coated nanoparticles release apotransferrin more rapidly at 42°C as compared to 37°C: a) Western blot analysis following 10 mg/mL RNaseB treatment of 1 mg PNIPMAM-coated nanoparticles incubated with 1 µg apotransferrin at pH 7.5 for 1 min, 10 min, 1 h or 16 h at room temperature (RT) (21.3^{0}C), 37°C or 42°C. **b)** Quantification of apotransferrin released from PNIPMAM-coated nanoparticles at 42°C and 37°C (n=3, error bars denote standard deviation), Protein release was calculated relative to the amount of apotransferrin still associated with the particles after washing.

3.3.9. Pulsed magnetic heating triggers apotransferrin release from PNIPMAM-coated nanoparticles above physiological temperature

After observing that PNIPMAM-coated nanoparticles could release encapsulated apotransferrin more rapidly at 42ºC than at 37ºC, I wanted to trigger release of protein that would otherwise remain encapsulated at physiological temperature using magnetic heating. I could see that within the initial 10 min period of heating no detectable protein was released at 37ºC, but was at 42ºC (**Figure 3.10**). After 1 h, I could detect protein release for both temperature treatments, albeit in larger amounts at 42ºC. I conducted an assay using pulsed magnetic heating, as done for PNIPAM-coated nanoparticles (**Figure 3.8**), over a 30 min period at 37ºC. I anticipated that magnetic heating over this time course might be sufficient to trigger apotransferrin release before it was detectable in the 37ºC control.

I could show that with a pulsed magnetic heating application, apotransferrin was released from PNIPMAM-coated nanoparticles without detection of protein release in the 37ºC control over a 20 min period, where protein release was calculated relative to the amount of apotransferrin still associated with the particles after washing (**Figure 3.11**). At the 30 min timepoint, there was some apotransferrin release for the 37ºC control. This suggests protein was released at a consistent low rate before becoming detectable at the 30 min timepoint. I could show that the sample volume temperature remained largely unchanged throughout the pulsed heating treatment.

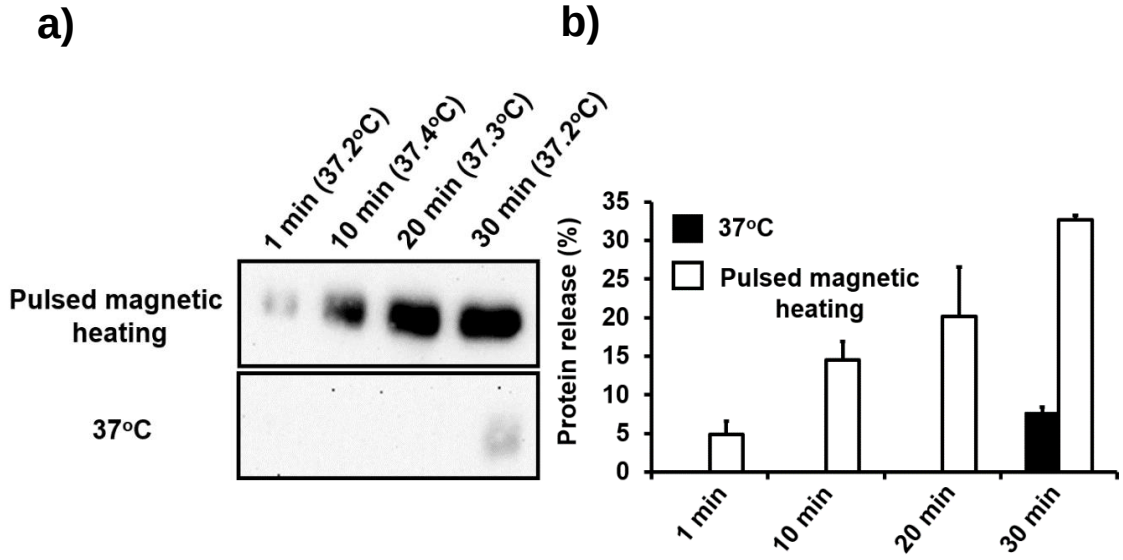

Figure 3.11. Pulsed magnetic heating triggers apotransferrin release from PNIPMAM-coated nanoparticles above physiological temperature: a) Western blot analysis following 10 mg/mL RNaseB treatment of 1 mg PNIPMAM-coated nanoparticles incubated with 1 µg apotransferrin at pH 7.5 for 1, 10, 20 or 30 min at 37°C or 37°C with pulsed magnetic heating. **b)** Quantification of apotransferrin released from PNIPMAM-coated nanoparticles with pulsed magnetic heating (n=3, error bars denote standard deviation), Protein release was calculated relative to the amount of apotransferrin still associated with the particles after washing.

I could show with this preliminary work on PNIPMAM-coated nanoparticles that with further optimisation there may be potential for their development as a means to deliver and release proteins above physiological temperature. Despite being able to release apotransferrin through heating above the polymer LCST the leakage of protein at physiological temperature is an issue that would need to be addressed during further development.

3.4. Conclusions

Using the polymer-coated nanoparticles generated in **Chapter 2**, I have been able to develop a system for protein encapsulation and release in a temperature-dependent manner.

I could show that effective protein encapsulation could be achieved through incubation of PNIPAM-coated nanoparticles with the test protein apotransferrin above the polymer LCST and then cooling below this temperature. The collapse and subsequent re-expansion of the polymer shell allowed for encapsulation of apotransferrin.

Also, I could characterise the conditions that trigger protein release of apotransferrin encapsulated into PNIPAM-coated nanoparticles. This was shown to be pH-dependent where increasing pH caused encapsulated apotransferrin to be released from the nanoparticles. As pH disruptions trigger protein release, this could be due to chemical alterations of the polymer shell which subsequently disrupts hydrogen bonding between apotransferrin and the polymer. Moreover, I could show that apotransferrin could be released in a temperature-dependent manner through the addition of competing protein RNaseB.

As well as with ambient heating, I could trigger the release of encapsulated apotransferrin from PNIPAM-coated nanoparticles using magnetic heating of the nanoparticle. Through a continuous pulsed magnetic field application, I could detect protein release that otherwise remained associated with the nanoparticles without magnetic heating. I observed that triggering a phase transition through heating of the entire sample volume above the polymer LCST was not required for protein release. After probing the nanoparticle surface environment through a pulsed magnetic heating application, I could also detect apotransferrin release. During magnetic heating, the temperatures of the sample volume were well below the polymer LCST, but this heating still caused apotransferrin release. This possibly suggests that the temperature-dependent effects that govern protein release from the protein-polymer network are largely influenced by the local, nanoparticle surface environment during magnetic heating. Higher temperatures immediate to the nanoparticle surface than are recorded for the bulk volume could be responsible for structural changes to PNIPAM, thus permitting apotransferrin release.

A comparison of time-dependant release from **Figures 3.6, 3.7, 3.8** and **3.9** can be seen below in **Figure 3.12**. The rates of apotransferrin release from PNIPAM-coated nanoparticles following a constant magnetic heating application were quite similar when carried out at both room temperature and 30^{o}C, with slightly elevated levels seen at room temperature. Interestingly, following a pulsed magnetic heating application after 10 min, the rate of release was more rapid than the other conditions and had the highest proportion of release after the 30 min period. This could perhaps be more rapid as a function of the PNIPAM shell expanding and contracting during the heating-cooling that occurs when the pulses of magnetic heating are switched on and off. Also, it is clear that the release of apotransferrin is halted when the magnetic field is switched off after 10 min, showing protein release is dependent on applying either pulsed, or constant magnetic heating.

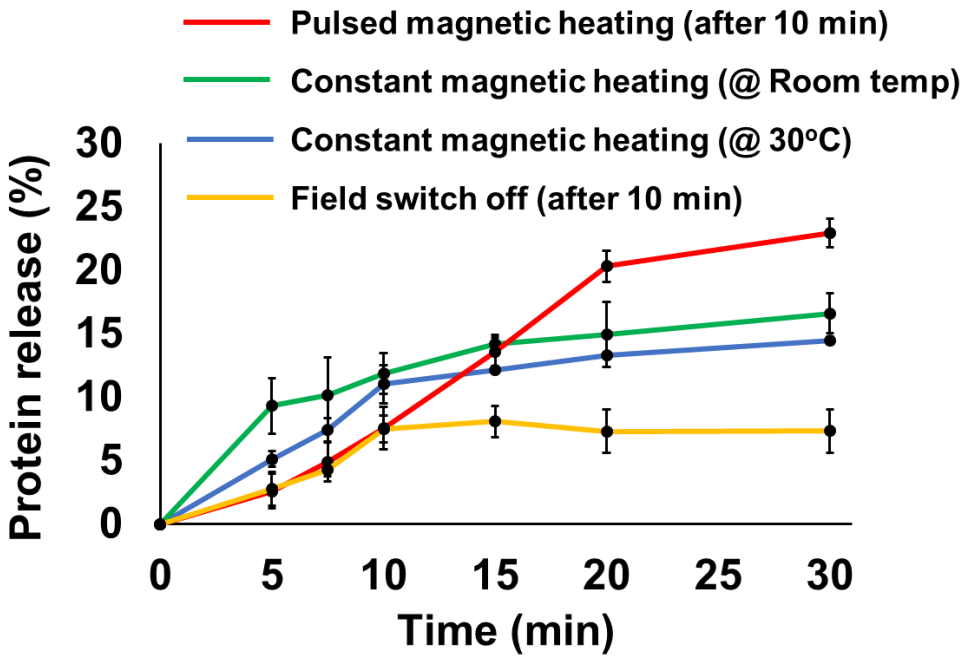

Figure 3.12. Comparison of rates of apotransferrin release from PNIPAM-coated nanoparticles following different applications of magnetic heating: Data taken from **Figures 3.6, 3.7, 3.8** and **3.9**.

Finally, I could show that PNIPMAM-coated nanoparticles can release apotransferrin above physiological temperature by heating to 42^{o}C or with pulsed magnetic heating. Prevention of protein leakage at 37^{o}C through further development may improve their use as a tool in biological systems for protein delivery and release above physiological temperature.

Chapter 4: Activation of MSCs using magnetically-triggered Wnt3a release from PNIPAM-coated SPIONs

4.1. Rationale, aims and summary

MSCs are a heterogeneous population of cells which are bone marrow derived, but also have origins in other tissues such as adipose (Bunnell et al., 2008). Populations of MSCs contain stem cells that are capable of tissue differentiation into osteoblasts, chondrocytes and adipocytes (Dominici et al., 2006). Due to their multipotent capacity to form cell types that are integral components of important tissues, MSCs have great potential in regenerative medicine. Research into cell-based treatments for joint disease is particularly appealing, where the most effective current therapies are tissue replacements through surgical intervention, which have drawbacks such as improper joint function and susceptibility to infection post-surgery.

MSC function and fate is controlled by cell signalling, where specific pathways have been implicated in regulating important events. The Wnt/β-catenin pathway has been associated with many key cellular processes, including tissue regeneration of adult bone marrow, skin and intestine (Goessling et al., 2009). The delivery of Wnt ligands is an appealing method to stimulate MSCs through the initiation of signalling events. Wnt3a is an example of a growth factor and natural ligand of the Wnt/β-catenin pathway that can stimulate MSCs by enhancing proliferation, as well as inhibit osteogenic differentiation (Shang et al., 2007, Boland et al., 2004) Additionally, a Wnt-responsive MSC reporter line has previously been generated that produces eGFP in response to canonical Wnt signalling activation (Saleh et al., 2016). Using cellular response as a readout of signalling activation is useful for determining the functional activity of biomolecules to ascertain their suitability for therapeutic applications.

Regenerating tissue at a damaged site by directly administering MSCs though intravenous injection *in vivo* is challenging as the cells have been shown to accumulate in the lungs after circulation (Nenasheva et al., 2017). Due to this observation, methods of targeting tissue regeneration in a localised fashion is an appealing application for joint repair. The use of biomaterials for regenerative medicine has great potential as a tool for local cellular activation. A variety of biomaterials have been manufactured using a plethora of fabrication methods in

an attempt to regenerate tissues, such as bone and cartilage in joints. Work in this field has largely involved producing biocompatible scaffolds to be implanted at damaged sites, which are often highly porous and designed to sequester and release biomolecules, such as growth factors, to activate MSCs. However, despite scaffolds showing promise as a template for tissue formation, there are several challenges during development such as requirements for biodegradability, cell adherence and immune response evasion.

Nanoparticles offer an alternative biomaterial for tissue regeneration applications due to their small size and propensity for surface-functionalisation. These properties improve the effectiveness of delivery during targeting and also coating with biocompatible polymer shells can act as a layer for biomolecule entrapment and release. Moreover, nanoparticles can be functionalised with targeting molecules such as antibodies or ligands to recognise cell/tissue-specific markers which aids homing to niches of interest and prevents off-target effects. Nanoparticle properties also offer significant advantages over the use of larger, implanted scaffolds. In terms of immune evasion, it has been shown that the size threshold for clearance by phagocytosis is generally below 200 nm (van Rijt et al., 2014). Nanoparticles can be generated at sizes significantly below this threshold; thus, they are an ideal candidate for bypassing premature clearance during delivery. Additionally, it has been shown that nanocarrier size below 150 nm is essential for entry into and exit from capillary circulation. Particles between 20-100 nm are able to distribute to tissues such as bone marrow (Blasi et al., 2007). The small size of nanoparticles therefore increases their potential to circulate through small blood vessels and reach sites of tissue damage. Also, small nanoparticle size means they will not accumulate for prolonged periods after targeting and have been shown to be excreted effectively, particularly at smaller sizes of 20 nm (Choi et al., 2012). Additionally, as nanoparticles are used to deliver molecules that activate cells already at target sites, there is no requirement to adhere cells to the biomaterial as is the case for scaffolds.

Biomaterial applications with MSCs have been extensively studied, where nanoparticles have largely been used as a tool for cell tracking, particularly using SPIONs as an MRI contrast agent (Moraes et al., 2012). Some studies have investigated using the magnetic properties of SPIONs for cell homing to an injury site, for example, using MSCs with internalised nanoparticles (Yun et al., 2018). Applications using polymer biomaterials have often been PNIPAM-based with a

focus on its use as a hydrogel surface. Generally, this has involved studying cellular interactions with the substrate and subsequent effects on functional events such as differentiation (Dai et al., 2016). Despite a large amount of research activity concerning SPION and PNIPAM applications with MSCs, the use of SPION-PNIPAM nanomaterials as a tool for biomolecule delivery to activate MSCs is relatively unexplored. This is a potentially interesting application, particularly considering the temperature-sensitivity of PNIPAM and magnetic heating properties of SPIONs.

In this chapter, I loaded PNIPAM-coated nanoparticles with Wnt3a to assess MSC activation following magnetically-activated protein release. I could show activation of a Wnt-responsive MSC reporter line following magnetically-triggered Wnt3a release from PNIPAM-coated nanoparticles. Also, using immortalised and primary MSCs, I observed significantly enhanced proliferation following Wnt3a release from magnetically heated PNIPAM-coated nanoparticles. This data provides evidence to suggest PNIPAM-coated nanoparticles can be used as a tool to activate MSCs following delivery and magnetically-triggered protein release.

4.2. Materials and Methods

4.2.1. Cell culture

Cell culture components were purchased from Invitrogen and plasticware from Sigma-Aldrich. Custom-made cell tubes for magnetic heating experiments were designed in-house. Cells were cultured in media composed of Dulbecco's Modified Eagle's Medium (DMEM) (high glucose, pyruvate, glutamine) supplemented with 10% (v/v) FBS and 1% (w/v) penicillin/streptomycin (P/S).

4.2.2. Cell lines and primary cells

Cell lines used were Y201 hTERT immortalised MSCs generated and characterised prior to this research (James et al., 2015). The MSC Wnt reporter line was generated from Y201 cells and characterised in previous work (Saleh et al., 2016).

Primary MSCs were isolated from femoral heads of female arthritis patients with similar age and body mass index (BMI) details following knee replacement surgery (Clifton Park Hospital, York). These samples were donated with the individuals consent and all ethical considerations were accounted for.

4.2.3. Cell vessels for magnetic heating

Cell tubes were engineered and designed in-house with dimensions of 35 mm x 20 mm x 8 mm (length x depth x width) (**Figure 4.1**). The 20 mm depth corresponds to the proportion of the vessel where a volume can be added within the glass-sided, transparent region. Base and lids are composed of polyether ether ketone (PEEK) with a smoothed base secured to glass sides (flame polished) with a silicon o-ring.

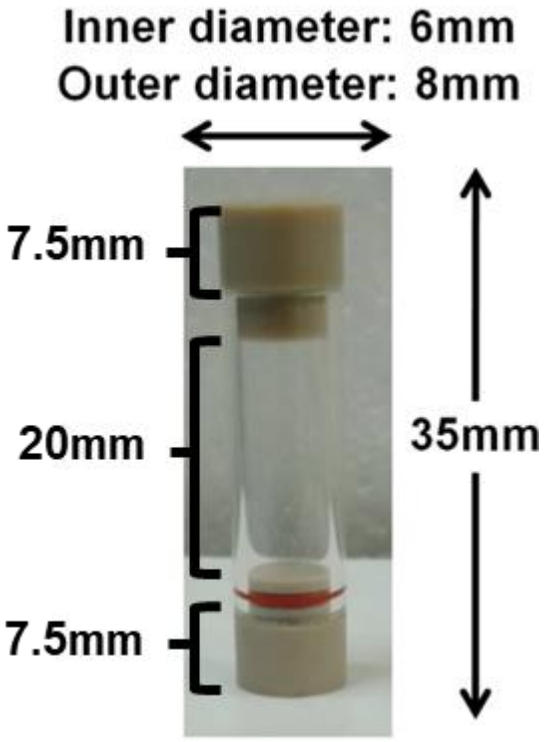

Figure 4.1: Image of custom-made vessel for MSC magnetic heating experiments with annotated dimensions.

4.2.4. 3-(4,5-dimethylthiazol-2-yl)-2,5-diphenyltetrazolium (MTT) assay

Y201 MSCs were seeded at a density of 1200 cells in a 96 well culture plate or custom-made tubes. After 1, 2, 4 and 7 days, culture media (200 µL) was replaced with fresh media containing 25 µL MTT solution (5 mg/mL in PBS). Plates were then incubated for 3 h at 37^{o}C. MTT-containing media was removed from the wells and 100 µL of 0.04 M HCl in isopropanol was added to each well. Plates were left to shake at room temperature for 10 min to allow for complete solubilisation. Absorbance was then read at 570 nm using a plate reader (Thermo Scientific, MuiltiSkan Go). MTT assay is measuring the absorption (at wavelength of 570 nm) of the purple dye formazan which forms following the enzymatic reduction of MTT by cellular NAD(P)H-dependent oxidoreductase.

4.2.5. Fluorescence-activated cell sorting (FACS)

Samples were analysed using a flow cytometer (DakoCytoautimation, Beckman Coulter) at a high flow rate of ~100 events per sec before ending each measurement after ~8000 events were recorded. During each measurement lasers (405 nm, 488 nm and 633 nm) were operated throughout. Lasers used were required for the excitation of the GFP fluorophore which occurs at a major peak of 395 nm and also a minor peak at 475 nm to give an emission wavelength of 509 nm. Analysis was carried out using Summit 4.3 version software by gating on eGFP-positive, live cells using a PE-Texas Red vs. FITC plot, where green fluorescent-positive cells were represented as a percentage of total live cells.

4.2.6. Wnt reporter assays

Wnt reporter MSCs were seeded overnight at 50% confluency in either custom-made vessels (5000 cells) or wells in a 24 well plate (100,000 cells). Wnt3a-loaded PNIPAM-coated nanoparticles (1 µg Wnt3a per 1 mg nanoparticle) were prepared (**Materials and Methods, section 3.2.1, pg 165**) in a sterile environment using a laminar flow hood where DMEM was used during the wash steps. Wnt3a-loaded nanoparticles were added to the cells before subjecting to magnetic heating in 200 µL of DMEM. An infrared thermocouple probe was immersed in the volume though a plastic inlet (see **Figure 2.5**) to measure the sample temperature. Cells treated with Wnt3a standards overnight at concentrations ranging between 0-100 ng/mL were used as a calibration curve. Cells were incubated overnight at 30^{o}C or 37^{o}C with Wnt3a standards, nanoparticles, or Wnt3a released from nanoparticles. Removal of nanoparticles was conducted by magnetic separation. Prior to analysis, cells were washed 3 times with 200 µL of PBS. Cells were then detached with 200 µL of trypsin/EDTA (0.25% (v/v) stock) at 37^{o}C and then made up to 1 mL in DMEM before analysis by flow cytometry.

4.2.7. MSC proliferation and viability assays

For proliferation assays, Y201 or primary MSCs were seeded overnight at 10% confluency (1000 cells) in custom-made tubes or in a 96 well plate. Wnt3a-loaded PNIPAM-coated nanoparticles (1 µg Wnt3a per 1 mg nanoparticle) were prepared (**Materials and Methods, section 3.2.1, pg 165**) in a sterile environment using a laminar flow hood where DMEM was used during the wash steps. Wnt3a-loaded nanoparticles were added to the cells before subjecting to magnetic heating for 30 min in 200 µL of DMEM. Nanoparticles were then magnetically removed and cells were incubated overnight at 37^{o}C. Fresh media was added and cells were cultured for 5 (Y201s) or 10 days (primary MCSs). As a calibration curve, in parallel, Y201 and primary MSCs were treated overnight with Wnt3a standards at final concentrations of 0-100 ng/mL, before changing media and culturing for 5 or 10 days. The optimal duration of the cell culture was based on the time taken for each cell type to reach confluency in the custom-made tubes.

For viability assays, Y201 or primary MSCs were seeded overnight at 10% confluency (1000 cells) in custom made tubes. Cells were then treated with varying concentrations of PNIPAM-coated nanoparticles from 0-20 mg/mL in DMEM containing 10% (v/v) FBS and cultured for 7 days at 37^{o}C.

For both proliferation and viability assays, cultured cells were washed once with carbonate buffer (0.133 M Na_2CO_3, 0.066 M $NaHCO_3$), then 150 µL 0.1% (v/v) Triton-X in carbonate buffer was added to each well. Cells were then freeze/thawed between 37^{o}C and -80^{o}C three times. Manual agitation was done throughout to ensure complete lysis. 50 µL of lysate was transferred into a black opaque 96 well plate (Greiner 96 well microplate black, SLS) for the PicoGreen DNA assay. Salmon sperm DNA standards (8 - 0.25 µg/mL) were used to calibrate the assay of DNA content. 50 µL of the PicoGreen reagent (Quant-iT PicoGreen dsDNA Reagent, Invitrogen) diluted 1:50 in 100 mM Tris, 1 mM EDTA, pH 7.5 was added to each sample well. Plates were covered with foil and left to shake for 5 min. Plates were then analysed using excitation and emission wavelengths of 485 nm and 538 nm, respectively using a fluorescence plate reader (Clariostar, BMG Labtech).

4.2.8. Nanoparticle cell uptake microscopy

Y201 MSCs were seeded in a 96 well plate at a density of 1200 cells per well in media with or without 5 mg/mL PNIPAM-coated nanoparticles added. Cells were grown for 7 days at 37^{o}C before washing 3 times with PBS. Brightfield images were subsequently taken of the cells using a Leica DM IRB microscope (Leica DC 500 camera, 10X objective, IM50 processing software).

4.2.9. Statistics

Statistical analysis of data was carried out using SigmaPlot 12.3 software. A normality test (Shapiro-Wilk) was conducted prior to statistical analysis and a test of equal variance was also performed. Tests for multiple groups were done using one-way ANOVA tests followed by Holm Sidak post-hoc tests if required. If the data failed the normality or variance tests, equivalent non-parametric tests were applied instead using a Kruskal-Wallis One-Way Analysis of Variance on Ranks followed by Dunn's post-hoc tests. Throughout the results presented, * = $p<0.05$, ** = $p<0.01$ and any data sets without an Asterix are not significantly different.

4.3. Results

4.3.1. Custom-made cell vessel characterisation

Before conducting magnetic heating assays with MSCs, I generated custom-made cell vessels that were of dimensions compatible with the sample area in the magnetic heating setup (**Figure 2.5**). The width of the area where the alternating magnetic field was concentrated was 10 mm which meant that vessels needed to be smaller than this to easily fit in the device. Also, the dimensions of the vessels allowed for similar seeding densities to that of a 96 well so that ~10,000 MSCs could occupy the area at confluency. Seeding densities for experimental work were at 10% confluency (~1000 cells) which were suitable numbers for downstream analysis. A diagrammatical representation within the magnetic heating setup using MSCs seeded on the surface of the vessels can be seen in **Figure 4.2**. The vessels were designed to be inert using glass sides and PEEK for the lid and base for cell attachment and growth. PEEK has previously been shown to be biocompatible with MSCs (Roskies et al., 2016). After design of the tubes, I assessed their suitability for MSC experiments by analysing cell viability.

Using an MTT assay I could detect no significant difference between the viability of Y201 MSCs when cultured in the custom-made vessels, or standard tissue culture plasticware for 7 days (**Figure 4.3**). This suggests that the in-house designed vessels would be suitable for MSC experimental work involving prolonged growth periods.

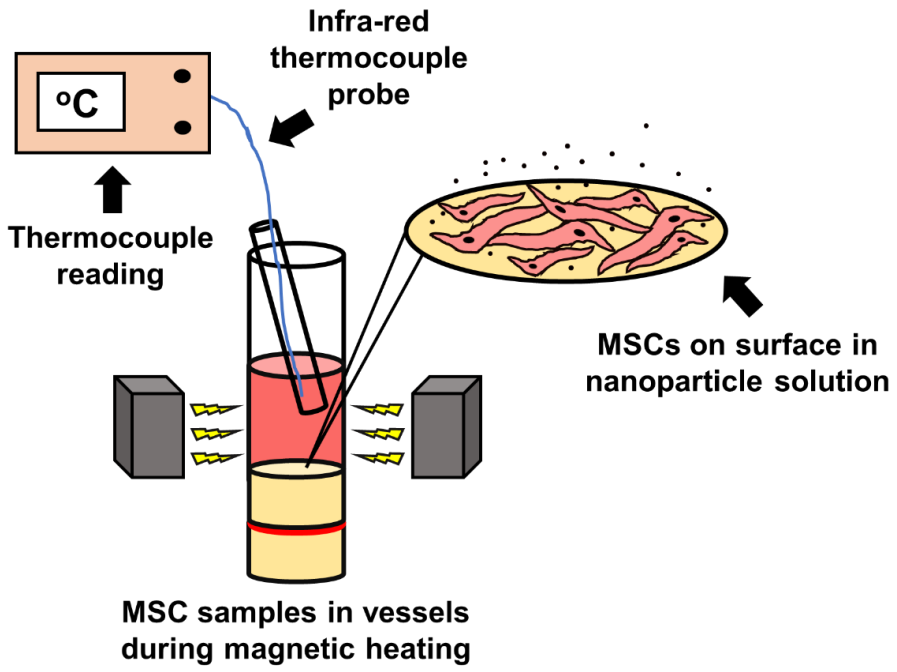

Figure 4.2. MSCs attached to surface within custom-made vessels during magnetic heating experiments: Schematic shows cells attached to surface at bottom of custom-made vessels in a 200 µL media volume with thermocouple probe in medium recording the temperature in real-time during magnetic heating.

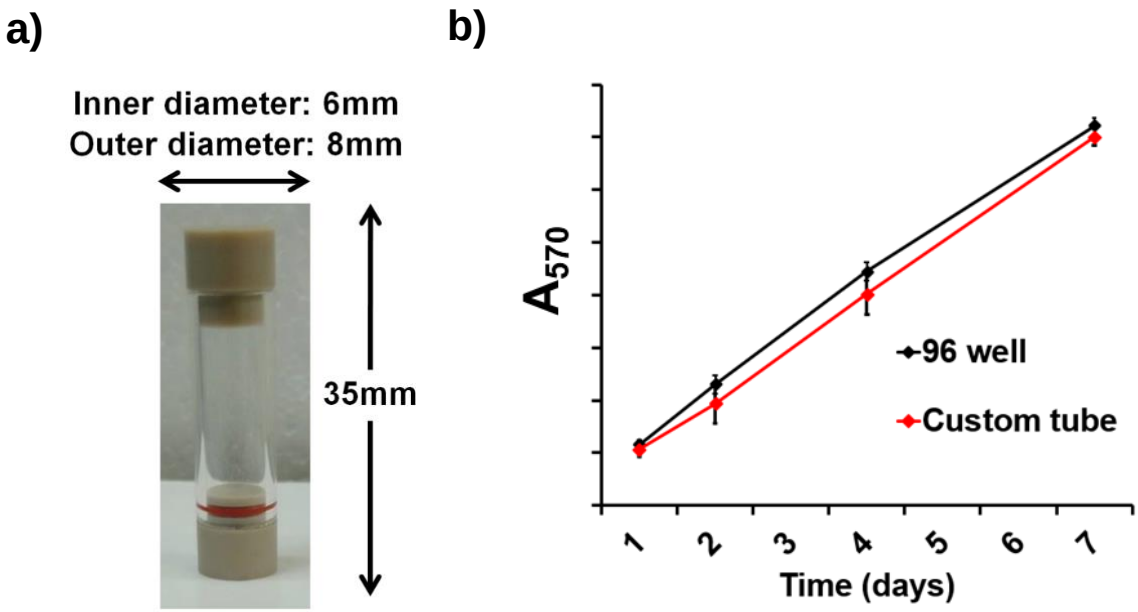

Figure 4.3. Characterisation of custom-made vessels for cell magnetic heating experiments: a) Image of custom-made vessel and its dimensions **b)** MTT assay on Y201 MSCs seeded in either custom made tube or a96 well plate at 10% confluency and cultured over 7 days (n=3, error bars denote standard deviation).

4.3.2. Wnt reporter MSC dose-dependent response to exogenous Wnt3a at 37ºC

In order to ascertain the detection limit of the eGFP response in Wnt reporter MSCs to the addition of exogenous Wnt3a, I generated a dose-response curve following an overnight incubation of Wnt reporter MSCs with Wnt3a (0 – 200 ng/mL) at 37ºC. This would provide an indication of how much Wnt3a would need to be released from nanoparticles to allow detection above background while avoiding signal oversaturation.

I could detect a clear eGFP response above background autofluorescence using the lowest concentration of the series at 12.5 ng/mL (**Figure 4.4**). A linear relationship between Wnt3a concentration and eGFP response was observed up to 50 ng/mL, where the signal appeared to saturate with no further change in cell response at 100 or 200 ng/mL Using the values between 0 – 50 ng/mL, I could plot a linear regression with a good r^2 value of 0.98. This concentration range was selected as suitable for calibration curves in subsequent analyses.

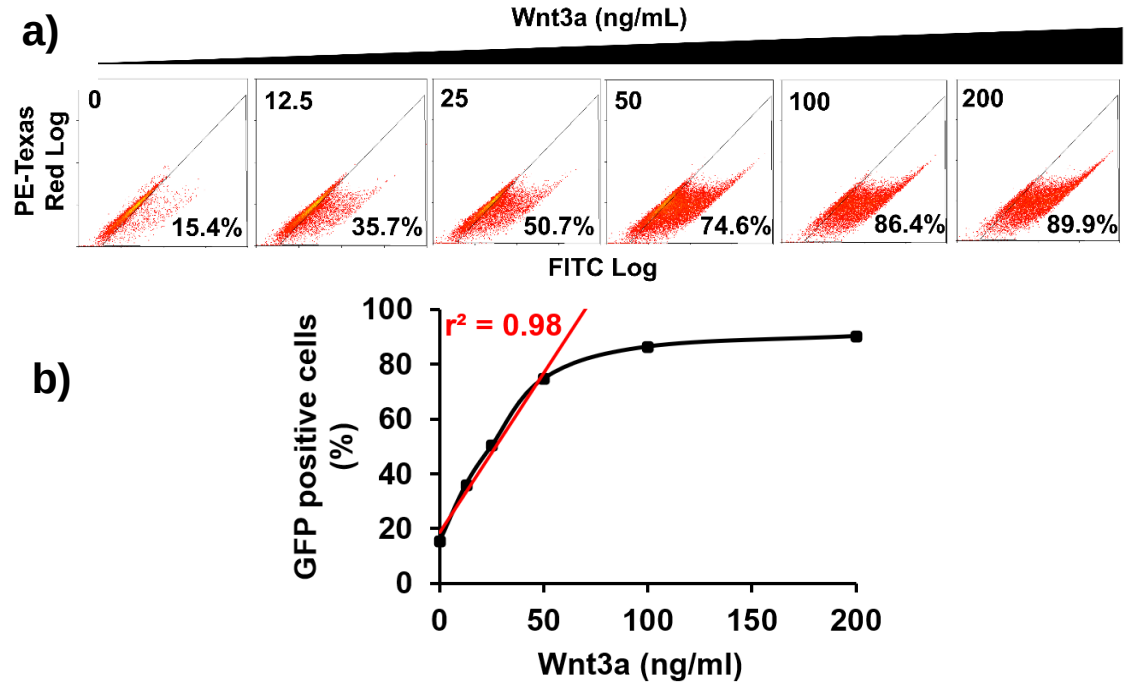

Figure 4.4. Wnt reporter MSC dose-dependent response to exogenous Wnt3a at 37ºC: a) FACS plots of eGFP-positive Wnt reporter MSCs following dose-dependent treatment with Wnt3a (0 – 200 ng/mL) overnight at 37ºC. Percentages denote populations of eGFP-positive cells. **b)** eGFP-positive cells vs. Wnt3a concentration regime (black) between 0 – 200 ng/mL with linear regression fit for 0 – 50 ng/mL concentrations (red) (r^2=0.98).

4.3.3. Wnt3a shows temperature-sensitive activity loss over 37ºC

An important consideration for magnetic heating assays using Wnt3a encapsulated nanoparticles was how sensitive Wnt3a would be to increased temperature above physiological conditions. As observed previously in **Chapter 3**, the nanoparticle surface environment immediate to the polymer-protein network is important for protein release during magnetic heating. The temperatures in this environment are not known and difficult to model, therefore high temperatures in this region could be detrimental to protein function because of thermally-induced protein denaturation.

By establishing the dose response of Wnt reporter MSCs upon addition of exogenous Wnt3a (**Figure 4.4**), this allowed me to determine an appropriate concentration at which to observe activity loss. I selected 100 ng/mL as a suitable concentration since beyond this the cellular response appeared to saturate and it also provided me with a broad window in which to observe potential activity loss. A Wnt reporter MSC overnight response assay was conducted at 37ºC after pre-incubation in 100 ng/mL Wnt3a at 37ºC, 40ºC, 45ºC and 50ºC for 10 min. There are no previous studies investigating the thermal stability of Wnt3a and therefore this provides a novel insight into the sensitivity of the protein.

I could observe a temperature-sensitive loss in Wnt3a activity following pre-incubation above 37ºC (**Figure 4.5**). Some activity was retained in samples treated at 40ºC and 45ºC; however, complete loss of function was observed for the 50ºC sample. This data suggests that in order to retain Wnt3a function care must be exercised during heating assays to ensure that temperatures do not significantly exceed physiological levels.

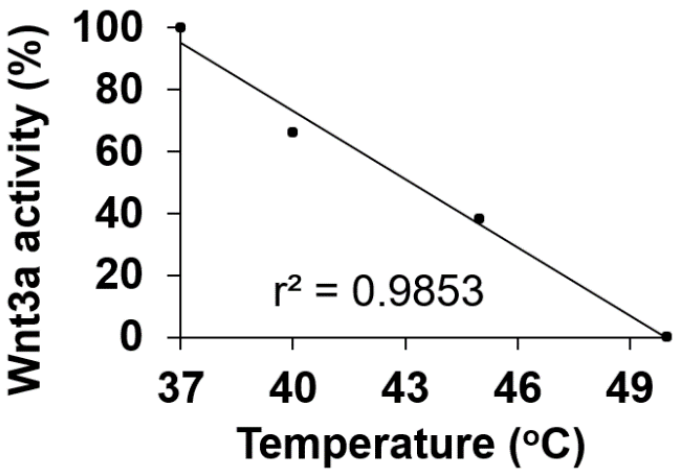

Figure 4.5. Wnt3a shows temperature-sensitive activity loss above 37°C: Wnt3a activity plotted as a function of temperature with a linear regression (r^2=0.9853). Wnt3a activity calculated using eGFP-positive Wnt reporter MSC response relative to control sample at 37°C.

4.3.4. Magnetically-activated nanoparticles release Wnt3a and trigger a bioactive response from Wnt reporter MSCs

I prepared 1 mg PNIPAM-coated nanoparticles incubated with 1 µg Wnt3a using the same procedure followed in **Chapter 3** (**Materials and Methods, section 3.2.1, pg 165**). Since the Wnt3a I used was recombinant from *E.coli* there was no lipidation like the Wnt produced in mammalian cells, so the use of detergent was not needed for solubilisation. Rather than RNaseB, I used serum-containing media (10% (v/v) FBS-containing DMEM) as a plentiful source of competing proteins during washing steps of the encapsulation procedure. The magnetic heating assay was conducted in a tissue culture, laminar flow hood to maintain a sterile environment. Also, this environment was at a temperature significantly below the PNIPAM LCST which prevented a phase transition as the result of an increase in the bulk solution temperature.

I was able to show a bioactive response from the Wnt reporter MSCs following 30 min magnetic heating of Wnt3a-loaded nanoparticles with the cells (**Figure 4.6**). This was shown over a time course, where I could correlate prolonged magnetic heating with increased eGFP response from the cells. FACS plots showed an increase in eGFP-positive cells correlated with increased exposure to the magnetic field, indicating progressive release of bioactive Wnt3a over time. Using Wnt3a standards as a calibration curve, I was able to calculate the Wnt3a release based on the proportion of eGFP-positive MSCs. After 30 min of magnetic heating, I could observe ~40 ng/mL Wnt3a had been released, which corresponds to ~200 ng (~20%) total Wnt3a released in the sample volume. Also, bioactive Wnt3a release was at recorded temperatures below the PNIPAM LCST, which provides further evidence to suggest effects at the particle surface during magnetic heating can release proteins. Moreover, I did not observe a significant response from the cells when treated with Wnt3a-loaded nanoparticles that did not undergo magnetic heating, indicating temperature-sensitive protein release.

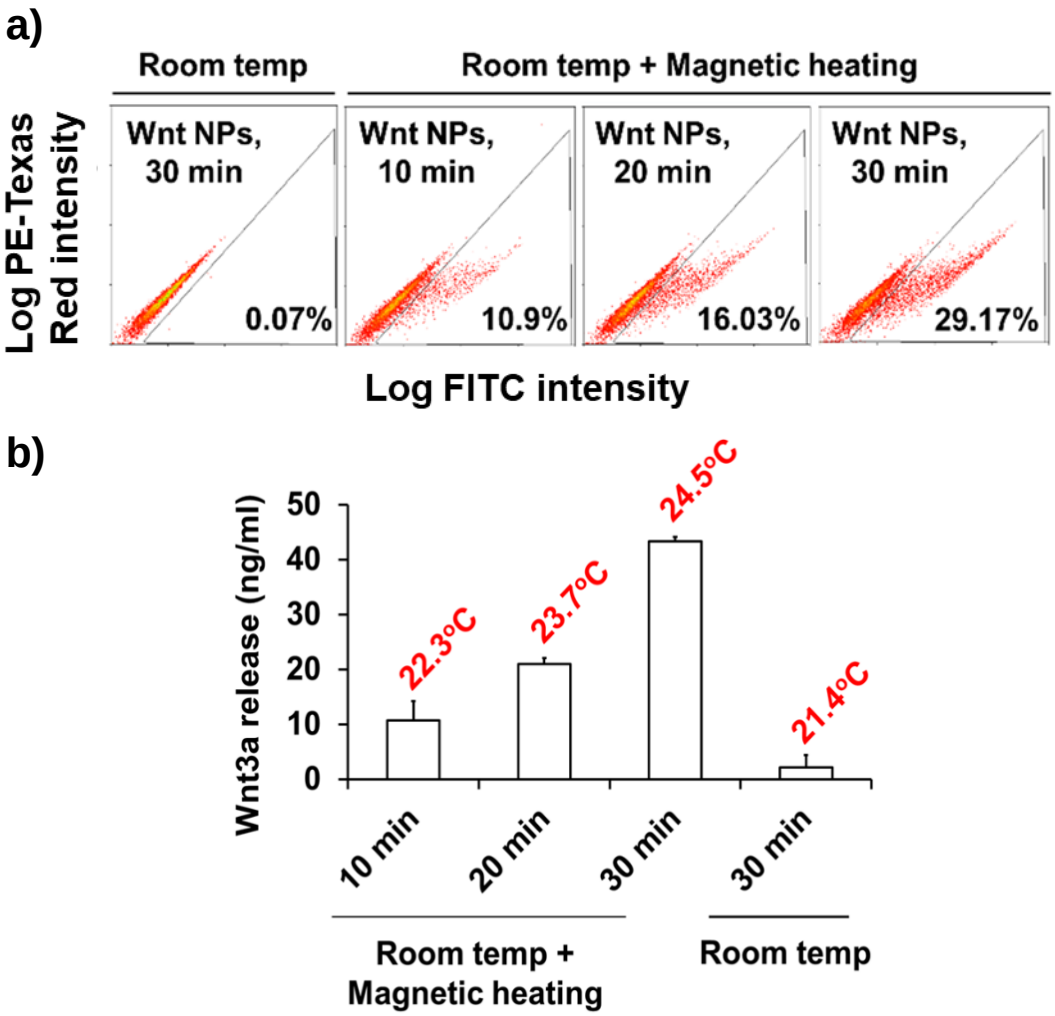

Figure 4.6. Magnetically-activated nanoparticles release Wnt3a and trigger a bioactive response from Wnt reporter MSCs: a) FACS plots of eGFP-positive Wnt reporter MSCs with/without magnetic heating treatment using Wnt3a-loaded nanoparticles. Percentages denote populations of eGFP-positive cells. **b)** Quantification of Wnt3a release from PNIPAM-coated nanoparticles following Wnt reporter MSC response after magnetic heating of Wnt3a-loaded nanoparticles for 10, 20 and 30 min, or 30 min at room temperature (21.4°C). Wnt3a release is deduced from calibration curves based on cellular response to a range of Wnt3a concentrations between 0-100 ng/mL. Nanoparticles were removed before incubation of the cells at 37°C overnight. 1 mg PNIPAM-coated nanoparticles were loaded with 1 µg Wnt3a for each sample (n=3, error bars denote standard deviation).

4.3.5. Wnt reporter MSC dose-dependent response to exogenous Wnt3a at 37ºC

It was clear that bioactive Wnt3a could be released from PNIPAM-coated nanoparticles using magnetic heating (**Figure 4.6**). However, it was still unclear whether encapsulated Wnt3a could also trigger reporter activity. To test this, I first needed to culture cells below the LCST overnight and assess their response to exogenous Wnt3a in a dose dependent manner as done previously at 37ºC (**Figure 4.4**). I selected 30ºC as an appropriate temperature for this assay as it is below the PNIPAM LCST and also makes short term MSC culture feasible.

I was able to detect a dose-dependent response to Wnt3a from Wnt reporter MSCs following overnight incubation at 30ºC (**Figure 4.7**). As a positive control for comparison, I also conducted a Wnt reporter response overnight at 37ºC. I could observe a strong linear correlation for both the 30ºC and 37ºC samples with a slightly reduced response at 30ºC which is likely to be expected as a consequence of slower cell activity rates. However, the response at 30ºC is more than sufficient to detect Wnt3a release from PNIPAM-coated nanoparticles based on the magnetic heating quantification for Wnt3a release carried out previously (**Figure 4.6**)

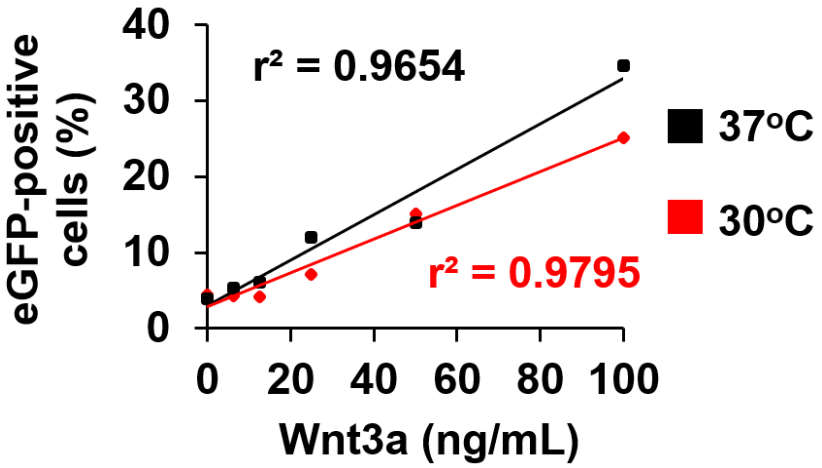

Figure 4.7. Wnt reporter MSC dose-dependent response to exogenous Wnt3a at 37ºC: Quantification of eGFP-positive Wnt reporter MSCs following dose-dependent treatment with Wnt3a (0 – 100 ng/mL) overnight at 37ºC (black) or 30ºC (red). Linear regression was done for each dataset (r^2 value displayed).

4.3.6. Wnt reporter MSCs only respond to magnetically-released Wnt3a from PNIPAM-coated particles

It was unclear whether the released Wnt3a was solely contributing to the cellular response, or whether Wnt3a still associated with the nanoparticles was also acting upon the MSCs. To assess this, I conducted a Wnt reporter response assay at 30^{o}C, a temperature below the phase transition of the polymer. This allowed MSC culture with Wnt-loaded nanoparticles that would be incapable of releasing entrapped Wnt3a, thereby showing any effects brought about by protein loosely associated with the nanoparticles.

I showed that Wnt reporter MSCs did not respond to PNIPAM-coated particles alone, or Wnt-loaded nanoparticles incubated with the cells at 30^{o}C without magnetic heating (**Figure 4.8**). In contrast, I observed that Wnt reporter MSCs gave a significant response to Wnt-loaded nanoparticles that were magnetically heated for 30 min, and either removed or left exposed to the cells. The response from both treatments was very similar, indicating that the Wnt3a released from the nanoparticles following magnetic heating is contributing to the cellular response, rather than protein loosely associated with the nanoparticles.

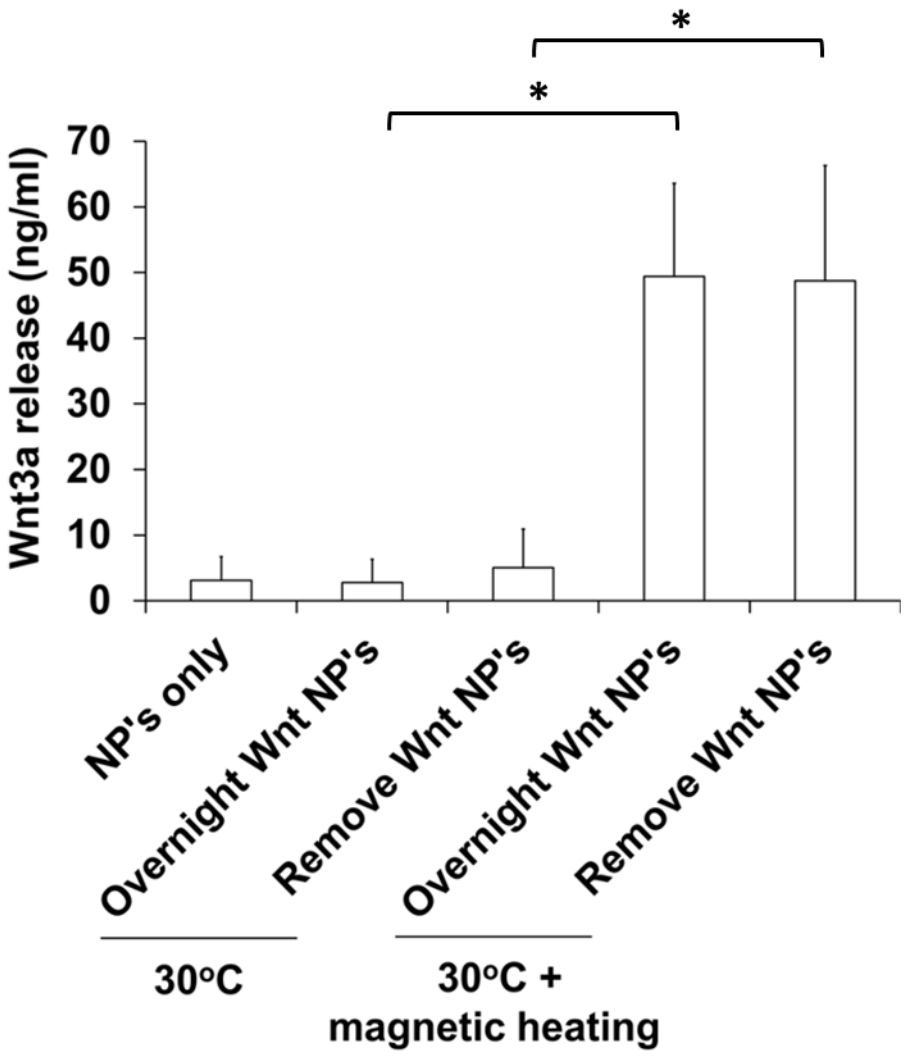

Figure 4.8. Wnt reporter MSCs only respond to magnetically-released Wnt3a from PNIPAM-coated particles: Quantification of Wnt3a release from PNIPAM-coated nanoparticles by following Wnt reporter MSC response after magnetic heating of Wnt3a-loaded nanoparticles for 30 min. Cells incubated at 30°C with protein-free particles overnight (NP's only), Wnt3a-loaded particles overnight (Overnight Wnt NP's) with/without magnetic heating, or Wnt3a-loaded particles that were removed after 30 min (Remove Wnt NP's) with/without magnetic heating. (magnetically heated samples underwent a temperature change from 21°C - 24.5°C). The amount of Wnt3a release is estimated from calibration curves of Wnt reporter MSC response to a range of Wnt3a concentrations between 0-100 ng/mL. 1 mg PNIPAM-coated nanoparticles were incubated with 1 µg Wnt3a for each sample, (n=3, error bars denote standard deviation). *=$p<0.05$ as compared with 'Overnight Wnt-NPs at 30°C.

4.3.7. PNIPAM-coated nanoparticles have no adverse effects on Y201 MSC viability over 7 days

Using DNA content as a readout, I assessed the cell viability of Y201 MSCs when incubated with PNIPAM-coated nanoparticles over 7 days. As previously I had only incubated cells with the nanoparticles previously for a maximum duration of 16 h, it was important to characterise the effect on cells over a longer period of time.

I could show that there was no significant effect on the DNA content of cultured Y201 MSCs at nanoparticle concentrations ranging between 0-20 mg/mL (**Figure 4.9**). A nanoparticle concentration of 5 mg/mL has been highlighted as this concentration was used for viability assays. This data suggests that at the nanoparticle concentrations used in experimental work, prolonged incubations would likely have had no detrimental effect on cell viability. The biocompatibility of PNIPAM-coated nanoparticles is promising for future development and their potential use in a more complex, biological environment.

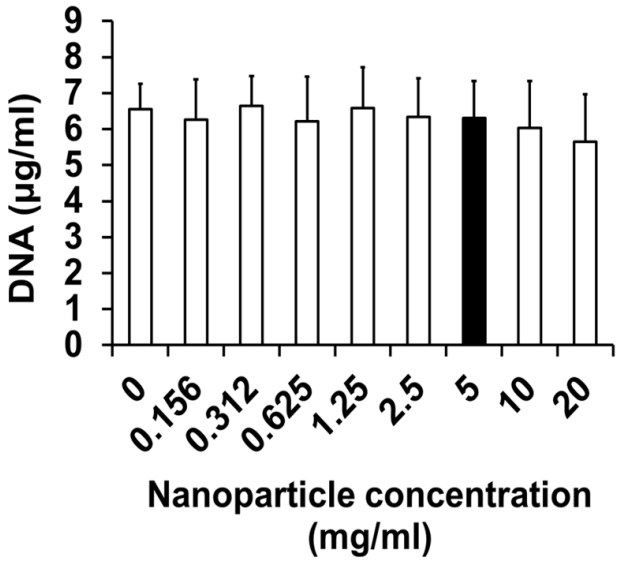

Figure 4.9. PNIPAM-coated nanoparticles have no adverse effects on Y201 MSC viability over 7 days: PicoGreen DNA quantification in Y201 MSCs treated with PNIPAM-coated nanoparticle concentrations between 0 - 20 mg/mL for 7 days. A nanoparticle concentration of 5 mg/mL was used in viability assays (highlighted in black). DNA quantification was done using a calibration curve prepared with salmon sperm DNA standards (0 – 8 µg/mL), (n=3, error bars denote standard deviation).

4.3.8. PNIPAM-coated nanoparticles are associated with Y201 MSCs after 7 days

After conducting cell viability assays over 7 days with Y201 MSCs (**Figure 4.9**), I wanted to observe whether the nanoparticles were internalised or associated with the cells.

Using brightfield microscopy, I could see that the particles appeared to be either internalised or surface associated with the MSCs (**Figure 4.10**). Prior to imaging, the cells were washed multiple times with PBS which would remove any particles loosely associated with the cells. This indicates that these images are representative of truly adsorbed nanoparticles, rather than any in the surrounding volume. The cells were cultured at 37ºC, which is above the PNIPAM LCST, thus the particles will collapse and aggregate as observed in the NTA data (**Figure 2.16**). This likely explains why the particles in **Figure 4.10** appear as large clusters.

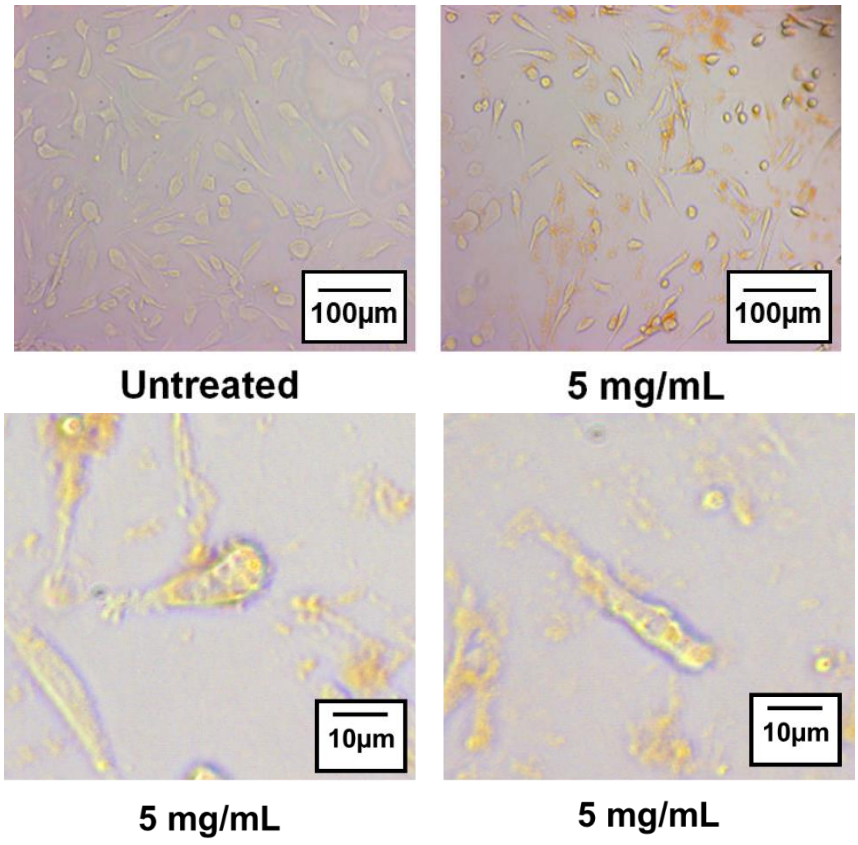

Figure 4.10. PNIPAM-coated nanoparticles are associated with Y201 MSCs after 7 days: Brightfield microscopy images of untreated Y201 MSCs and MSCs exposed to 5 mg/mL PNIPAM-coated nanoparticles at 37ºC for 7 days.

4.3.9. Determining the amount of exogenous Wnt3a required to significantly enhance proliferation of Y201 MSCs

The observed Wnt reporter MSC activation by magnetically-triggered Wnt3a release provided a functional readout of bioactive Wnt3a release from PNIPAM-coated nanoparticles. To further assess the functional release of Wnt3a, I sought to use MSC proliferation as a readout of cellular stimulation. Indeed, it has previously been shown that Wnt3a is a potent enhancer of proliferation when MSCs were exposed to conditioned media from cells overexpressing Wnt3a (Boland et al., 2004). However, the amount and conditions required for a significant enhancement of proliferation using purified Wnt3a was not known. Therefore, I conducted an assay to investigate the required Wnt3a concentration and culture conditions necessary to induce a significant increase in proliferation of Y201 MSCs.

Y201s were seeded in 96 wells at 10% confluency to allow for a large period in which to observe differences in growth between treatments. Wnt3a treatments were removed following an overnight exposure as it was assumed that, like the Wnt reporters, this would be sufficient time to stimulate the MSCs. The cells were cultured for 7 days following the treatment with samples analysed after 1, 3, 5 and 7 days. 7 days was selected as an appropriate time course since Y201 MSCs have a doubling time of roughly 48 h and would likely be approaching confluency after this period of time.

It was observed after 1 day that there were no significant differences across the different samples, likely because insufficient time had been allowed for proliferation to occur (**Figure 4.11**). However, after 3 days, I began to observe significant differences for the higher Wnt3a doses of 50 and 100 ng/mL. This was also apparent after 5 and 7 days where I could see significant differences for the 25 ng/mL treatment as well. This data provided useful information regarding how much Wnt3a release would be required from nanoparticles to significantly stimulate Y201 MSC proliferation.

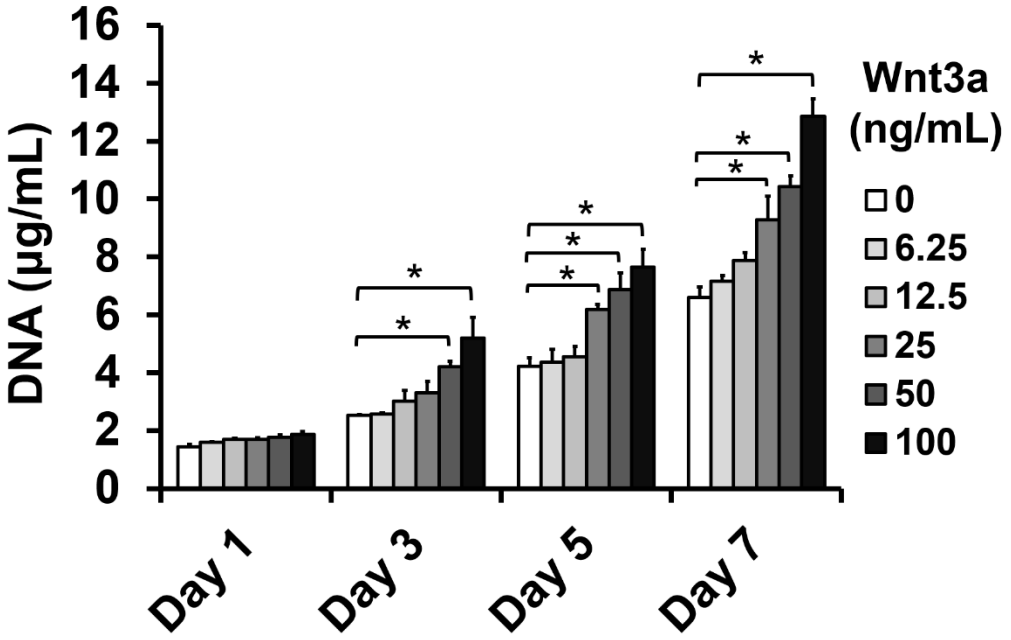

Figure 4.11. Determination of exogenous Wnt3a required to significantly enhance proliferation of Y201 MSCs: Quantification of Y201 MSC DNA content (µg/mL) following lysis after overnight treatment with exogenous Wnt3a (0 – 100 ng/mL) and incubation at 37ºC for 1, 3, 5 and 7 days. DNA quantification was done using a PicoGreen calibration curve prepared with salmon sperm DNA standards (0 – 8 µg/mL) (n=3, error bars denote standard deviation, * = $p < 0.05$).

4.3.10. Magnetically-activated nanoparticles release Wnt3a to stimulate enhanced proliferation of Y201 MSCs

Using the Wnt reporter activation data in **Figure 4.6** and Wnt3a dose-response data for Y201 MSCs in **Figure 4.11**, I could estimate how long Wnt3a-encapsulated nanoparticles would need to undergo magnetic heating to release sufficient protein to enhance cell proliferation. I chose to magnetically heat for 30 min and allow MSC growth for 5 days which should theoretically release ~40 ng/mL Wnt3a and lead to significant stimulation of Y201 MSCs over this period of time.

I showed that when Wnt3a-loaded nanoparticles were magnetically heated for 30 min in the presence of Y201 MSCs, significantly enhanced proliferation was observed after 5 days of culture (**Figure 4.12**). I could detect roughly a two-fold increase in DNA content as compared to Wnt-loaded particles without magnetic heating and nanoparticles alone. Also, I was unable to detect a cellular response from Wnt3a-encapsulated particles without magnetic heating, highlighting a clear temperature-sensitive effect.

Here I could provide further evidence of bioactive Wnt3a release following magnetically-triggered release from PNIPAM-coated nanoparticles.

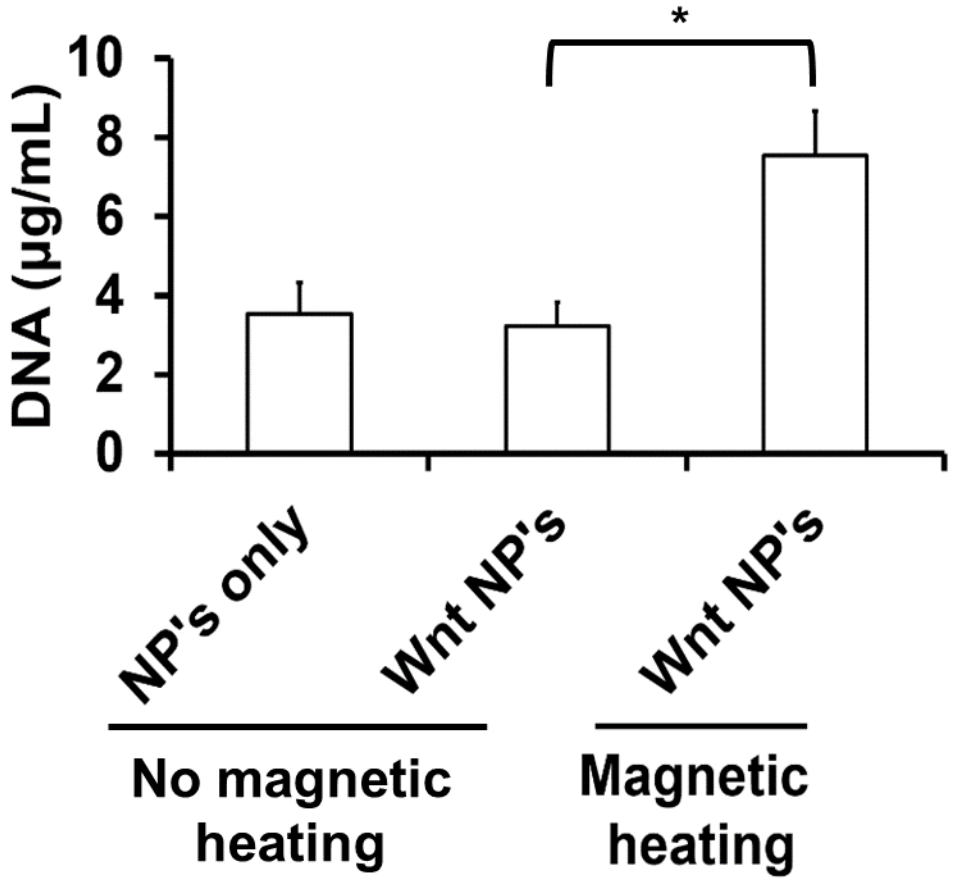

Figure 4.12. Magnetically-activated nanoparticles release Wnt3a to stimulate enhanced proliferation of Y201 MSCs: PicoGreen DNA quantification for Y201 MSCs treated for 30 min with Wnt3a-loaded nanoparticles (Wnt NP's) with/without magnetic heating (magnetic heating caused a temperature change from 20.9^{o}C to 24.1^{o}C) or protein-free nanoparticles (NP's only) before magnetic removal. DNA quantification was done using a calibration curve prepared with salmon sperm DNA standards (0 – 8 µg/mL). Cells were incubated overnight at 37^{o}C before changing the media and culturing for 5 days. Wnt-loaded nanoparticles were prepared by incubating1 mg PNIPAM-coated nanoparticles with 1 µg Wnt3a (n=3, error bars denote standard deviation, * = $p < 0.05$).

4.3.11. PNIPAM-coated nanoparticles have no adverse effects on primary MSC viability over 7 days

As with Y201 MSCs, I wanted to measure the cell viability of primary cells using DNA content as a readout. This allowed me to assess the biocompatibility of PNIPAM-coated nanoparticles with cells that are a better representation of those found in a tissue environment.

I was able to observe that a 7-day incubation with PNIPAM-coated particles had no effect on cell viability (**Figure 4.13**). I tested a range of nanoparticle concentrations from 0 – 20 mg/mL with 5 mg/mL being highlighted as the concentration used other in experimental work.

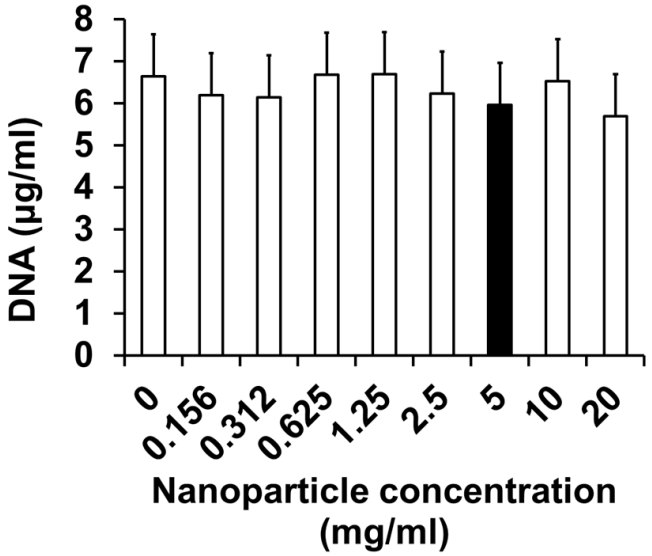

Figure 4.13. PNIPAM-coated nanoparticles have no adverse effects on primary MSC viability over 7 days: PicoGreen DNA quantification in primary MSCs derived from 3 different donors treated with PNIPAM-coated nanoparticle concentrations between 0 - 20 mg/mL for 7 days. A nanoparticle concentration of 5 mg/mL was used in viability assays (highlighted in black). DNA quantification was done using a calibration curve prepared with salmon sperm DNA standards (0 – 8 µg/mL) (n=3, error bars denote standard deviation).

4.3.12. Determination of exogenous Wnt3a required to significantly enhance proliferation of primary MSCs

As a more rigorous readout of cellular activity, I also assessed Wnt3a response using primary MSCs derived from patient femoral heads (Clifton Park Hospital, York). Primary MSCs are known to vary between donors, which coupled with the heterogeneous nature of MSCs, means there is no guarantee donor-derived cells will behave similarly. Therefore, conducting reproducible experiments with primary MSCs is a robust measure of cellular activation.

Primary MSCs have a doubling time roughly twice as long as the immortalised Y201 cells used in previous work so I conducted a dose-dependent Wnt3a response assay over a 10-day period. I showed a significant enhancement in proliferation was detectable after 7- and 10-day growth periods following 50 and 100 ng/mL Wnt3a treatments (**Figure 4.14**). The amount of error with primary MSCs was noticeably larger than that observed with Y201s (**Figure 4.11**), which is likely a consequence of the donor variability factor.

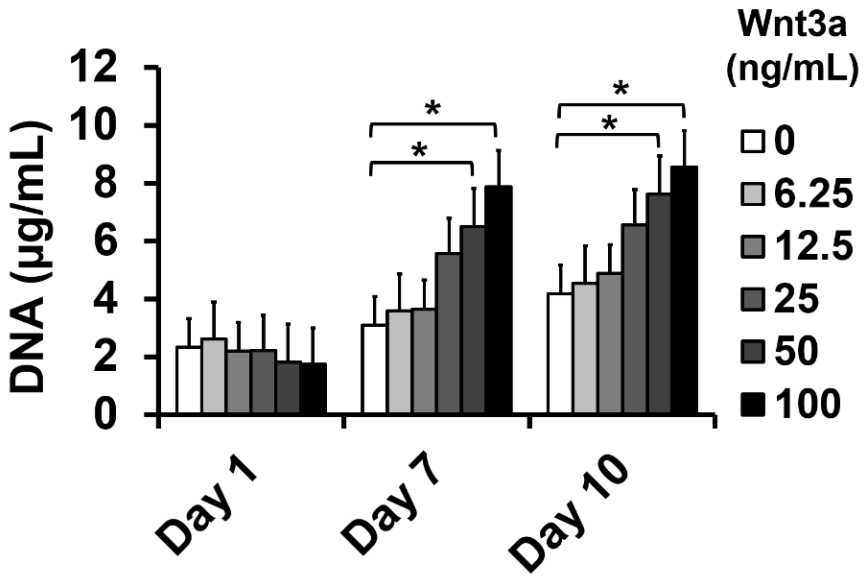

Figure 4.14. Determination of exogenous Wnt3a concentration required to significantly enhance proliferation of primary MSCs: Quantification of primary MSC DNA content (µg/mL) following lysis after overnight treatment with exogenous Wnt3a (0 – 100 ng/mL) and incubation at 37ºC for 1, 7 and 10 days. DNA quantification was done using a PicoGreen calibration curve prepared with salmon sperm DNA standards (0 – 8 µg/mL). Cells used were derived from 3 separate donors, (n=3, error bars denote standard deviation, * = $p < 0.05$).

4.3.13. Magnetically-activated nanoparticles release Wnt3a to stimulate enhanced proliferation of primary MSCs

A significant enhancement in Y201 proliferation was observed following Wnt3a release from magnetic nanoparticles after 30 min of heating, thus I chose to reproduce this for primary MSCs. However, following nanoparticle removal after magnetic heating and an overnight incubation with the released Wnt3a, the cells were left to grow for 10 days rather than 5 days. This was to account for the slower rate of primary cell growth as compared with immortalised cells, and allow for any effects on proliferation (**Figure 4.14**) to be observed.

As with the Y201 MSCs, I detected a significant increase in DNA content following release of Wnt3a from nanoparticles by magnetic heating, indicating bioactive protein release (**Figure 4.15**). As with the Y201 cells, I was unable to detect a response using Wnt3a-encapsulated nanoparticles that had not undergone magnetic heating.

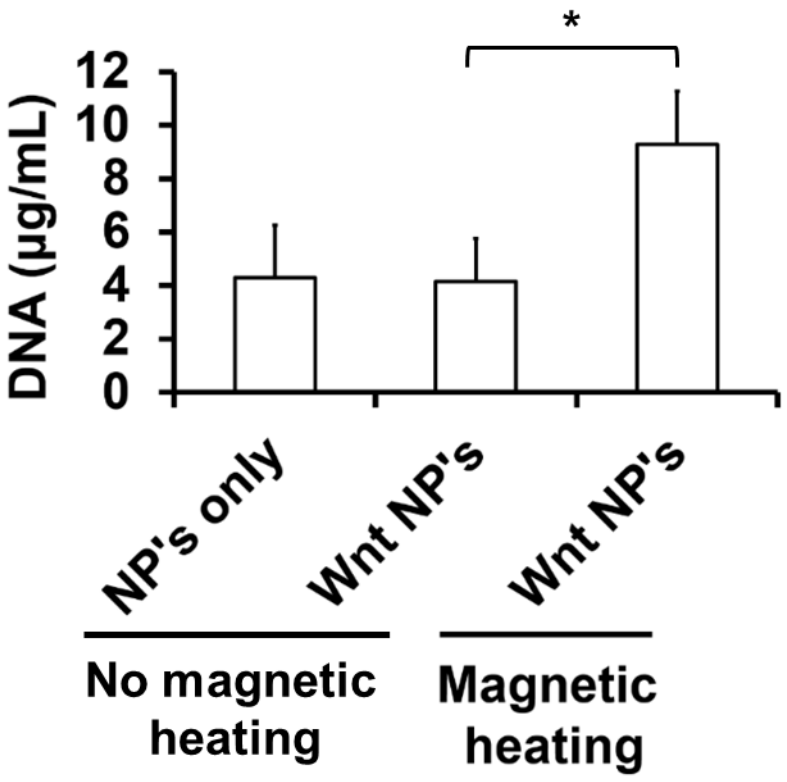

Figure 4.15. Magnetically-activated nanoparticles release Wnt3a to stimulate enhanced proliferation of primary MSCs: PicoGreen DNA quantification for primary MSCs isolated from 3 different donors, treated for 30 min with Wnt3a-loaded nanoparticles (Wnt NP's) with/without magnetic heating (magnetic heating caused a temperature change from 20.5^{o}C to 23.4^{o}C) or protein-free nanoparticles (NP's only) before magnetic removal. DNA quantification was done using a calibration curve prepared with salmon sperm DNA standards (0 – 8 µg/mL). Cells were incubated overnight at 37^{o}C before changing the media and culturing for 10 days. Wnt-loaded nanoparticles were prepared by incubating1 mg PNIPAM-coated nanoparticles with 1 µg Wnt3a, (n=3, error bars denote standard deviation, * = $p < 0.05$).

4.4. Conclusions

Using the PNIPAM-coated nanoparticles generated in **Chapter 2** and building on the protein release studies of **Chapter 3**, I have been able to show that bioactive Wnt3a can be released from PNIPAM-coated nanoparticles upon magnetic heating to functionally stimulate MSCs.

I was able to design custom-made vessels in-house that were compatible with both the magnetic heating setup, as well as biocompatible with cultured cells. Cell viability of Y201 MSCs seeded in the custom vessels was initially confirmed via an MTT assay, before continuing with their use in magnetic heating, cell-based work.

I could also characterise the Wnt reporter MSC response to exogenous Wnt3a in a dose-dependent manner at both 37^{o}C and 30^{o}C. Using FACS as a readout of eGFP response from Wnt reporter MSCs, I detected activation at concentrations as low as 12.5 ng/mL. This concentration is significantly lower used previously fluorescence microscopy experiments at Wnt3a concentrations of 200 ng/mL or higher (Saleh et al., 2016). This level of sensitivity was crucial for detection of Wnt3a release from PNIPAM-coated particles in subsequent experiments. I used the dose-response of Wnt reporter MCSs to exogenous Wnt3a as a calibration curve for nanoparticle experiments to determine the amounts of Wnt3a released.

Using magnetic heating, I could show that bioactive Wnt3a was released from PNIPAM-coated nanoparticles at concentrations sufficient to trigger a Wnt reporter MSC eGFP response that was significantly above background levels. I also showed that Wnt3a is functionally sensitive to temperatures slightly above physiological levels. The Wnt3a release from nanoparticles suggest that magnetic heating is not detrimental to protein function since at least a proportion of the protein is bioactive. For future work, it would be interesting to quantify the total amount of Wnt3a released relative to the cellular response as a measure of bioactive vs. inactive Wnt3a released. As a control experiment, I showed that magnetically heated release of encapsulated Wnt3a was required to activate MSCs, and that Wnt reporter cell incubation with Wnt3a-encapsulated nanoparticles below the PNIPAM LCST did not trigger a response. This suggests that any Wnt3a loosely associated with the particle surface is insufficient to elicit a significant response from the cells, and that the majority of encapsulated Wnt3a has to be released through magnetic heating to observe cellular activation.

As another readout of Wnt3a-triggered cellular activation, I conducted proliferation assays with both Y201 and primary MSCs. I determined the concentration of endogenous Wnt3a and culture conditions required to stimulate enhanced proliferation for both the immortalised and primary MSCs. After establishing this, I showed that magnetically-triggered Wnt3a release from PNIPAM-coated nanoparticles could activate both Y201 and primary cells leading to enhanced proliferation.

I also assessed the cell viability of both Y201 and primary MSCs using DNA content as a readout after incubating the cells for 7 days with a range of PNIPAM-coated nanoparticle concentrations. I was unable to detect any adverse effects for either of the MSC samples tested, highlighting their biocompatibility. After a 7-day cell viability assay, I showed by microscopy that the nanoparticles were associated with Y201 MSCs. It appears that the nanoparticles have been largely internalised by MSCs over time which is explained by the fact that during culture at 37^{o}C the PNIPAM shell will be collapsed which will significantly decrease the hydrodynamic diameter of the polymer shell. This will generate a nanoparticle size more compatible with clathrin-mediated endocytosis, thus permitting nanoparticle entry into the MSCs via this mechanism. Additionally, some particles that are more aggregated and too large for uptake by clathrin-mediated endocytosis may be associated with the cell surface of MSCs. This could occur through passive adsorption or interactions between the polymer shell and cell surface molecules. A diagram illustrating how the nanoparticles may associate with the MSCs can be seen below in **Figure 4.16**.

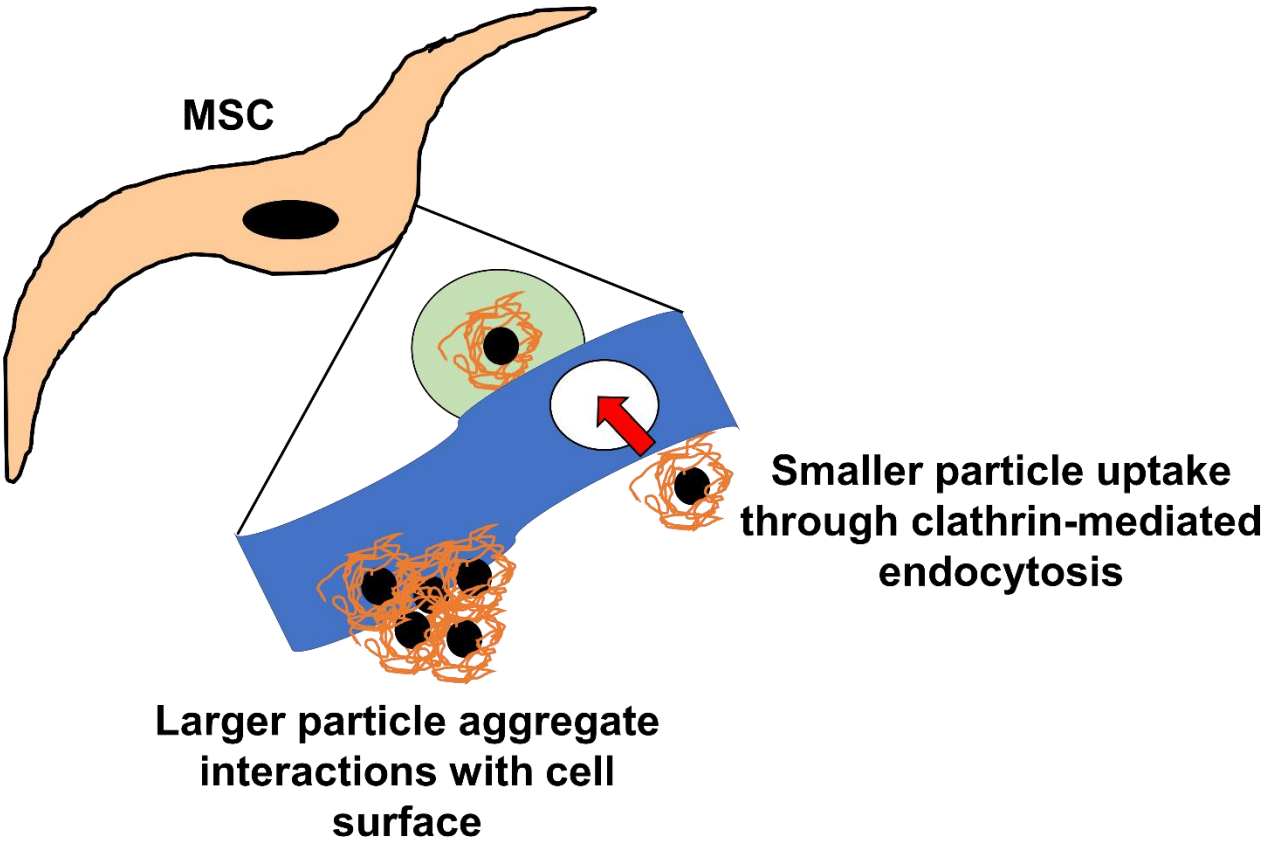

Figure 4.16. Diagram to show possible mechanisms of nanoparticle association with MSCs.

Chapter 5: Discussion

The differentiation potential of MSCs is advantageous in regenerative medicine and makes them an attractive target for the delivery of molecules *in situ* to stimulate their cellular activation. Delivery of MSCs to sites of tissue damage is often an inefficient process leading to a requirement for alternatives to activate MSCs endogenous to the damaged tissue. The development of effective biomaterials to deliver and release biomolecules that will stimulate MSCs is an appealing application. Nanoparticles offer a tool for the targeted delivery of biological cargo to MSCs which can be released in a triggered manner from stimuli-responsive polymers. PNIPAM is a temperature-sensitive polymer that can be coated onto nanoparticle surfaces as a layer for biomolecule entrapment. In tissue engineering this polymer has largely been used as a hydrogel scaffold to act as a surface substrate for cell attachment with its potential as tool for biomolecule release being relatively unexplored. Also, SPIONs have been used predominantly in tissue engineering as a contrast agent for MRI-based imaging to track MSCs through tissue. It is known that appropriately sized SPIONs can undergo magnetic heating in the presence of an alternating magnetic field which is a property seldom used in regenerative medicine. Here, I have generated PNIPAM-coated SPIONs and assessed their potential as a magnetically- and temperature-responsive delivery system of biomolecules to activate MSCs. I also began work characterising an additional temperature-responsive polymer, PNIPMAM, which displays an LCST above physiological temperature. This is significant for developing a system that can release bioactive molecules upon magnetic heating in a physiological setting. I could generate PNIPMAM-coated SPIONs and assess their potential as a tool for magnetically-triggered, temperature-sensitive biomolecule release above physiological temperature.

5.1. Synthesis and characterisation of temperature-sensitive, magnetically-responsive nanoparticles

In **Chapter 2** I described the synthesis of PNIPAM-coated SPIONs and characterised their size, magnetic, molecular and temperature-sensitive properties. The generated nanoparticles were measured at a size suitable for cellular delivery *in vivo*, the largest being measured at 152.5 ± 13.33 nm by DLS, being below the threshold for clearance by phagocytosis (<200 nm) (van Rijt et al., 2014). Additionally, it has been shown that nanocarrier size <150 nm is essential for entry and exit from capillary circulation with particles between 20-100 nm possibly able to distribute to tissues such as bone marrow (Blasi et al., 2007). When soluble, the PNIPAM-coated particles I have generated are likely to be between 83 – 152 nm based on NTA and DLS analysis of hydrodynamic diameter in solution, meaning it is probable that their size would be appropriate for permitting access to/from circulation and distribution to areas such as bone marrow. Also, the nanoparticle size observations by TEM (6.3 ± 0.9 nm) are smaller than those produced by the literature procedure followed which were 15 ± 2.5 nm (Carroll et al., 2010). Exact replication of nanoparticle synthesis can be challenging; however, factors such as the rate of nanoparticle seed nucleation, growth and termination are all influenced by multiple factors during the synthetic procedure. Nanoparticle size and uniformity can vary based on variables such as rate of stirring, which maintains sample homogeneity during seed nucleation by metal salt reduction (Rahmawati et al., 2017). The nanoparticles generated also show relatively high polydispersity, where their composition is uncertain. The particles generated in the literature procedure followed report a core-shell contrast that contains a mixture of iron and iron oxide (Carroll et al., 2010). However, by TEM it appears that the nanoparticles I have synthesised are fully oxidised, as there is no evident contrast.

In terms of magnetic properties, the nanoparticles I have generated display clear superparamagnetism, indicated by no remanent magnetisation in the absence of an applied field shown by no hysteresis. This data corresponds well to the magnetisation observed for the literature prepared particles, which also showed clear superparamagnetic properties by VSM (Carroll et al., 2010). Superparamagnetic nanoparticles are favourable for magnetic heating applications as they have a single magnetic moment which responds well to an alternating

magnetic field. Ferromagnetic particles will display even stronger magnetic heating properties; however, their larger size generally makes them unsuitable for biological applications. Moreover, the prepared nanoparticles appear stable over long periods of time with very little magnetic susceptibility loss over a 3-month period which also corresponds with high stability reports from the literature procedure followed (Carroll et al., 2010). High stability in aqueous solution is favourable as this allows for large scale production of particles capable of being stored over time and used when required with little consequent effects on magnetisation. I could also show that 5 mg/mL SPIONs displayed a heating rate of 0.3^{o}C/min in the presence of an alternating magnetic field with a 0.67 T field strength at an operating frequency of 108 kHz. From these measurements, I could ascertain an SAR value of 65.27 W/g Fe. Previous work investigating size dependence on magnetic nanoparticle heating has shown that particles between 15-40 nm have significantly higher SAR values than those between 6-11 nm (Tong et al., 2017). This study also showed that magnetic heating of SPIONs for 1 hr through tumour tissue was ineffective for 6 nm SPIONs, but showed significant heating at 19 nm and 40 nm (Tong et al., 2017). Larger SPIONs with a higher SAR could help magnetically-triggered release of bioactive molecules *in vivo* and may be necessary for the release I have seen with apotransferrin and Wnt3a. More accurate reproducibility of the conditions used in the literature (Carroll et al., 2010) may produce larger nanoparticles that undergo magnetic heating effectively. However, there is no guarantee of producing highly monodisperse particles using an aqueous synthetic approach. Studies using particles in the 15-40 nm size range generally produce nanoparticles using an organic synthetic route though the thermal decomposition of iron carbonyl complexes (Tong et al., 2015, Hufschmid et al., 2015). Organic synthesis approaches are generally based on slower reactions where the conditions used cause significantly slower growth than nucleation which results in the production of monodisperse particles. Whereas aqueous syntheses are based on extremely fast hydrolysis where the nanoparticle growth phase is generally short leading to high polydispersity. While size modulation using an organic synthetic approach allowed for better size tunability, it will not generate nanoparticles suitable for biological applications due to their aqueous insolubility. To address this, ligand exchange steps will be required, which can be challenging and require significant optimisation. As well as individual nanoparticle size being an important factor for magnetic heating, it has been

suggested that clustering of nanoparticles is an important factor in optimising magnetic heating efficiency, which could be a consideration for future development (Pearce et al., 2013). When using alternating magnetic fields with magnetic nanoparticles to effectively heat tissues, the local nature of the field means that the clustering and spatial distribution of nanoparticles is very important. The local heat transfer between clusters of nanoparticles has been modelled and shown to be significantly more effective at magnetic heating than dispersed individual nanoparticles in tissue (Pearce et al., 2013).

The importance of surface coating was not only necessary to generate the temperature-sensitive particle desired, but also to improve biocompatibility for cellular studies. Indeed, previous work has highlighted iron oxide nanoparticles without coating can have adverse cytotoxic effects on human mesothelium and murine fibroblast cells (Brunner et al., 2006). PNIPAM-based hydrogels have been used in previous studies with MSCs, showing little to no adverse effects on cell viability, making it an ideal candidate for coating SPIONs and use in cellular assays with MSCs (Chen et al., 2015). Another study conducted an extensive assessment on the cytotoxicity of PNIPAM and found no such effects following direct contact tests with endothelial cells, epithelial cells, smooth muscle cells and fibroblasts (Cooperstein and Canavan, 2013). I generated PNIPAM with a M_w of 13.26 kDa that was functionalised with NDA at a coupling efficiency of 67% and could also show that the polymer displayed an LCST at 32^{o}C which was unchanged following NDA functionalisation. The characterisation of NDA-PNIPAM agreed well with that of the literature procedure followed for the synthesis (Kurzhals et al., 2015). A polymer grafting density to the particle surface of 0.275 chains/nm^2 was calculated, a value which has been suggested in previous studies to be within a range indicating good colloidal stability of superparamagnetic nanoparticles in complex media and when undergoing magnetic heating (Amstad et al., 2011, Zirbs et al., 2015, Amstad et al., 2009). Additionally, I could calculate that there were 26.1 PNIPAM chains per particle, which has been shown previously to be important for generating stable solutions, where gold nanoparticles without PEG coating showed aggregation and could be readily dispersed following PEG grafting of 50 chains per particle (Liu et al., 2007). Also, from the grafting density, I could calculate a 27.5% coverage of the SPION surface, which has previously been shown to impact on nanoparticle biodistribution, where PEG-PLA nanocapsules were shown to have longer blood

circulation times and reduced clearance by the liver, spleen, and kidneys with 30% coverage, as compared to materials with 20% less (Mosqueira et al., 2001).

I also carried out work on the synthesis and characterisation of an additional polymer, PNIPMAM, which has been reported to exhibit a higher LCST than PNIPAM that can be influenced by the polymer molecular weight and concentration (Djokpé and Vogt 2001, Rathfon and Tew, 2008). Since PNIPAM has an LCST below physiological temperature, encapsulated molecules within a PNIPAM shell would likely be released when exposed to the body environment, which would decrease its effectiveness as a tool for drug delivery. It is therefore important to consider developing alternative polymers for temperature-sensitive biomolecule delivery that could function to trigger release above physiological temperature. It has been shown previously that PNIPMAM can release DOX in a temperature-sensitive manner, where significantly higher amounts of DOX were released at 48^{o}C than at 37^{o}C (Peters et al., 2018). I reasoned that PNIPMAM-coated SPIONs could be a temperature-responsive tool for future development that could release biomolecules to MSCs above physiological temperature with magnetic heating.

My initial attempt at PNIPMAM synthesis was carried out using the same approach as with PNIPAM but using the monomer for PNIPMAM instead. However, despite observing signs of polymerisation over time by an increase in molecular weight and NMR peak broadening, I was still unable to detect a phase transition in response to heating as high as 100^{o}C. I reasoned that despite evident polymerisation occurring, initiation of insufficient polymer chains, resulting in a low polymer concentration, could be behind the lack of a bulk sample phase transition. Indeed, it has been suggested in previous work copper catalysts can be inefficient in inducing radical addition for some amide-containing monomers (Senoo et al., 1999). Using an alternative approach (Rathfon and Tew, 2008), I could generate an acid-terminated version of PNIPMAM by the functionalisation of PMASI with isopropylamine. The generated polymer exhibited an LCST at 42^{o}C which is 10^{o}C higher than that observed for PNIPAM. Interestingly, the phase transition for PNIPMAM appeared more gradual than the sharp collapse of PNIPAM at its LCST, where I could observe an increase in solution turbidity between 37^{o}C-42^{o}C. In previous work assessing the cloud point of PNIPMAM, transmittance at 500 nm was measured using a UV-vis spectrophotometer with temperature increased at a rate of 1^{o}C/min in 5^{o}C increments, where the LCST was determined based on the

temperature at 50% transmittance (Rathfon and Tew, 2008). This study also showed that increasing molecular weight correlated with increasing LCST. This work determined a higher LCST of ~58^{o}C for PNIPMAM with a similar molecular weight (9.1 kDa) to the PNIPMAM I synthesised at ~10 kDa which displayed an LCST of 42^{o}C. This difference in observations could be attributable to the different methodology used in each study. A gradual phase transition has also been seen previously with other polymers in response to temperature change, such as polystyrene in the solvent cyclohexanol (Schultz and Flory, 1952). After PNIPMAM functionalisation with NDA and SPION coating, I could observe that, as well as the free polymer, PNIPMAM-coated SPIONs showed a gradual phase transition in response to heating from 37^{o}C to 42^{o}C.

5.2. Biochemical studies of protein encapsulation and release from polymer-coated nanoparticles

In **Chapter 3,** I demonstrated that the PNIPAM-coated nanoparticles generated in **Chapter 2** could be loaded with the model test protein apotransferrin. Apotransferrin could be released in both a pH- and temperature-sensitive manner with/without magnetic heating. Temperature-sensitive release of proteins from PNIPAM using magnetic SPION heating has seldom been done in previous work and is therefore an area of novelty in the project. Protein encapsulation within the polymer shell was effective by allowing the polymer to expand around protein molecules in solution, following a heating/cooling transition of PNIPAM-coated particles above and below the PNIPAM LCST. The observed effect of increasing pH on apotransferrin release from PNIPAM-coated SPIONs likely suggests a molecular interaction. Since PNIPAM has no charge properties, it is likely that the nature of the interaction involves hydrogen bonding between protein molecules and polymer chains. Indeed, a previous study found that binding of BSA to PNIPAM microparticles was caused by hydrogen bonding between carboxyl groups of BSA and amide groups of the polymer (Huo et al., 2006). This study also showed that BSA binding to PNIPAM micrgels was optimum between pH 5-6 and by increasing the pH above this point, BSA could be released indicating that PNIPAM is sensitive to pH as well as temperature (Huo et al., 2006). By increasing the pH this will also give apotransferrin a more negative charge since these conditions are further away from its isoelectric point (5.4). As a consequence of this, the interactions between apotrasnferrin and the polymer shell may be disrupted leading to its release. I found that, presumably due to molecular interactions, incubating PNIPAM-coated nanoparticles loaded with apotransferrin above the PNIPAM LCST was insufficient to release the encapsulated protein. With the addition of a competing protein RNaseB, I could show a temperature-sensitive release of apotransferrin from PNIPAM-coated nanoparticles above the polymer LCST. This is perhaps explained by the temperature-sensitive phase transition of PNIPAM, where the structural collapse of the polymer could expose encapsulated apotransferrin to binding competition from RNaseB which triggers its release. In the expanded PNIPAM form below the LCST, since apotransferrin remains associated with PNIPAM-coated SPIONs, this release mechanism is likely not permitted. Also, at neutral pH, RNaseB carries a positive charge since its isoelectric point is 9.3, which opposes that of apotransferrin. This could be

responsible for some attraction between the negatively charged apotransferrin and positively charged RNaseB that contributes somewhat to apotransferrin release, coupled with competition for hydrogen bonding to the polymer due to the higher concentration of the competing protein. A diagram depicting apotransferrin pH-sensitive release and competitive release driven by RNaseB can be seen below in **Figure 5.1**.

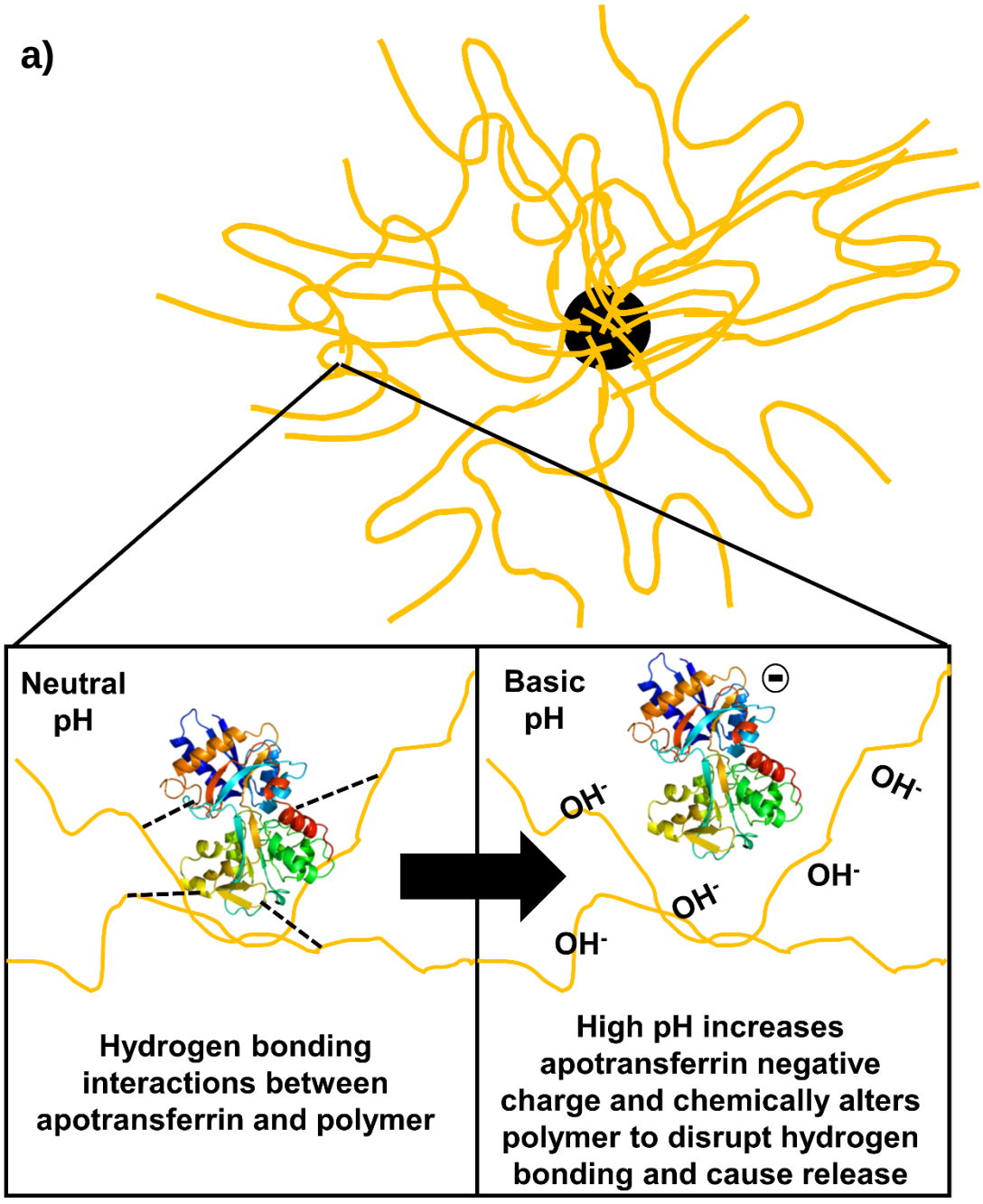

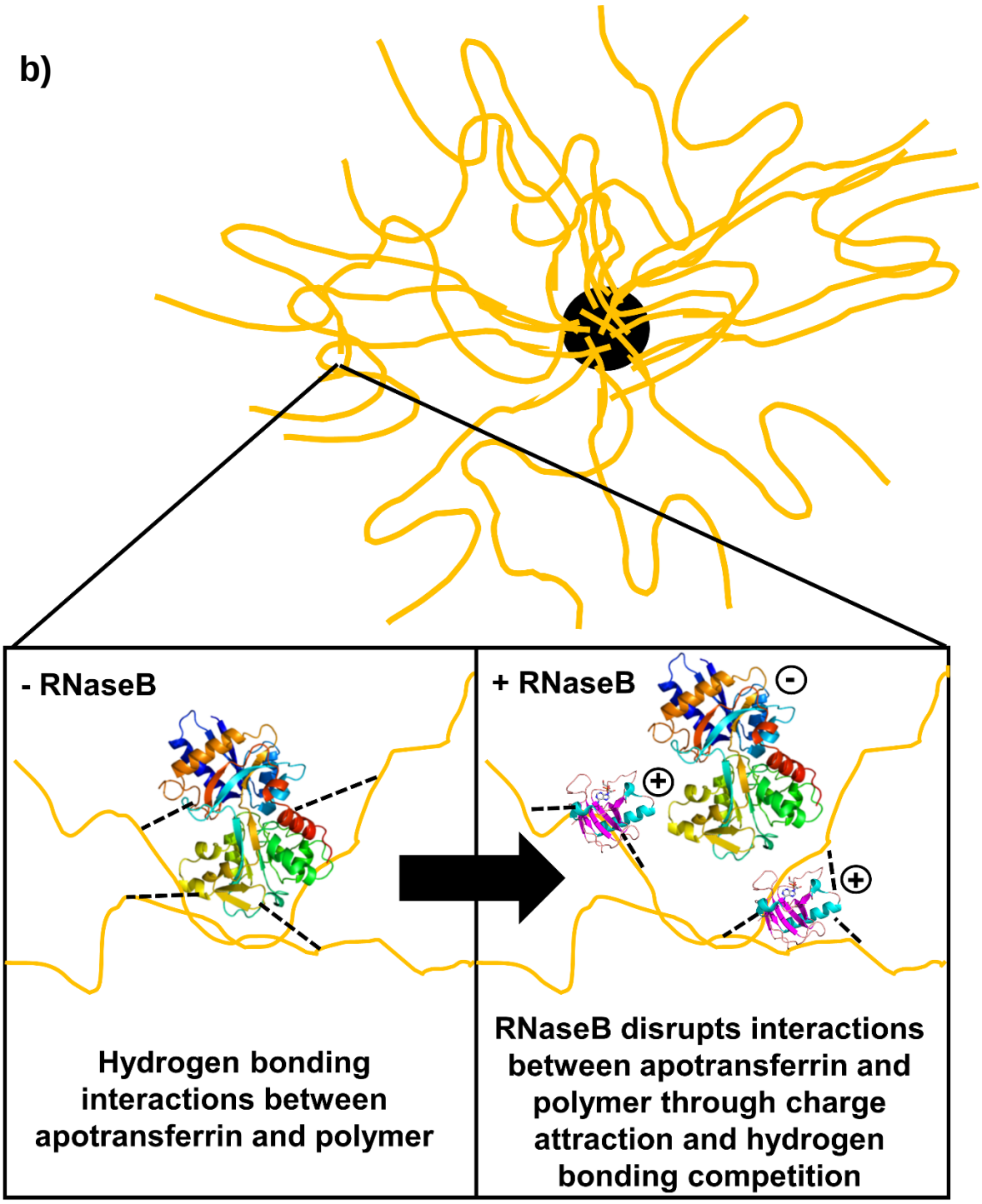

Figure 5.1. Diagrammatic models to depict possible release mechanisms of apotransferrin from polymer-coated nanoparticles as a function of pH and competitive protein binding: a) Zoomed-in diagram of apotransferrin interactions with polymer at either neutral or basic pH (with hydroxyl ions shown as OH^-). **b)** Zoomed-in diagram of apotransferrin interactions with polymer in the absence/presence of RNaseB at neutral pH.

Through magnetically heating PNIPAM-coated nanoparticles, I could also show temperature-sensitive release, interestingly at temperatures below the polymer LCST, an effect which was dependant on alternating magnetic field application either through constant or pulsed heating. The pulsed magnetic heating results allowed maintenance of a relatively constant sample volume temperature, through heating/cooling cycles, and is therefore a useful readout of heating effects on protein release within the nanoparticle surface environment. The data suggests that the nanoscale environment immediate to the nanoparticle surface is sufficient during magnetic heating to trigger protein release through temperature-induced structural alterations of PNIPAM. It is likely that a phase transition is occurring to cause protein release, despite the bulk volume temperature not exceeding the PNIPAM LCST, since encapsulated Wnt3a is hidden when added to Wnt reporter MSCs slightly below the LCST and only triggers a cellular response following magnetically-triggered release. The particle surface-localised magnetic heating effect on protein release could be an advantageous property in future clinical applications, in that it should be unnecessary to magnetically heat whole tissue environments to trigger biomolecule release when a subtler heating approach is sufficient. Modelling the temperature immediate to the nanoparticle surface during magnetic heating may help to elucidate the observed release by understanding the polymer/protein environment better. Studies on drug release using magnetic heating and PNIPAM-based polymers are better characterised than that of proteins. Indeed, a previous study investigating mitoxantrone drug release from iron oxide nanoparticle-PNIPAM composite microgels also showed magnetically heated temperature-sensitive release below the PNIPAM LCST (Regmi et al., 2010). The temperature on the particle surface was not modelled in this study, therefore it is unclear what temperature the encapsulated drug was exposed to during magnetic heating and whether any PNIPAM structural alterations occurred as a consequence of heating. It may be possible to model the surface heating of nanoparticles by considering the heat capacity of a particular solvent during magnetic heating measurements relative to the heating rate of nanoparticles. Understanding the heat dissipation into the environment at the particle surface, relative to the bulk volume temperature, could help highlight the differences between the two during magnetic heating. This could provide information about the environment that proteins encapsulated in the polymer shell are exposed to, thus

leading to a better understanding of the structural changes that the temperature-sensitive polymer shell may undergo to cause protein release.

Using the PNIPMAM-coated SPIONs generated in **Chapter 2,** I characterised their ability to encapsulate and release apotransferrin in a temperature-sensitive manner in **Chapter 3**. I had previously observed that PNIPMAM displayed a more gradual phase transition than PNIPAM between 37ºC-42ºC, at which point complete collapse from solution was seen. Interestingly, after incubating apotransferrin-loaded PNIPAM-coated SPIONs at both 37ºC and 42ºC, I saw an enhanced rate of release at 42ºC compared to 37ºC. As with PNIPAM-coated particles, I could not observe any apotransferrin release at room temperature, where no signs of a phase transition were evident. The protein release observed at 37ºC may be a consequence of a partial PNIPMAM phase transition that is markedly enhanced upon complete collapse of the polymer shell. I could also show that pulses of magnetic heating were sufficient to trigger apotransferrin release from PNIPMAM-coated SPIONs at 37ºC significantly faster than without magnetic heating. Here I have generated a tool that can release proteins at an enhanced rate above physiological temperatures. Further PNIPMAM development may optimise its retention of encapsulated proteins at physiological temperature and allow for triggered, magnetically-dependant release above such temperatures. This could perhaps be achieved by generating a version of PNIPMAM with slightly increased LCST at 42ºC, which can be achieved through increasing the polymer molecular weight (Rathfon and Tew, 2008). If protein leaking occurs during the gradual phase transition of PNIPMAM, increasing the phase transition temperature slightly, so the polymer is still soluble at physiological temperature, may aid retention of the encapsulated protein content.

5.3. Activation of MSCs using magnetically-triggered Wnt3a release from PNIPAM-coated particles

As well as apotransferrin, I was also able show in **Chapter 4** that I could encapsulate Wnt3a into PNIPAM-coated nanoparticles. Wnt3a is a growth factor and natural ligand of the Wnt/β-catenin pathway which has been shown to enhance MSC proliferation (Boland et al., 2004). I used an MSC Wnt reporter line that produces eGFP upon Wnt3a activation as a readout of Wnt3a release and functional activity. Also, using Wnt reporter MSCs, I could characterise the temperature sensitivity of Wnt3a itself as I reasoned that magnetic heating could be detrimental to the protein function. I treated Wnt3a at temperatures ranging from 37^{o}C – 50^{o}C before ascertaining protein function by its exposure to Wnt reporter cells. I observed losses in Wnt3a activity following pre-treatment at temperatures above 37^{o}C with almost no cellular response following a 50^{o}C treatment. This indicates that any heating above physiological temperatures would be detrimental to Wnt3a activity. For magnetic heating assays with MSCs, custom-made vessels were designed for compatibility with the setup. PEEK was chosen for the design as a material suitable for cell work based on previous work highlighting its relatively inert properties and compatibility with MSCs (Roskies et al., 2016). I could show that the designed vessels were suitable for MSC work after conducting an MTT cell viability assay. I was able to detect a Wnt reporter cell response above background autofluorescence using Wnt3a concentrations as low as 6.25 ng/mL, which is much lower than the lowest amounts used in the literature (Saleh et al., 2016). The sensitivity of FACS for eGFP positive cell detection was advantageous for measuring low levels of Wnt3a release from PNIPAM-coated nanoparticles. As with apotransferrin, I could detect Wnt3a release from PNIPAM-coated nanoparticles following magnetic heating which did not exceed temperatures above the polymer LCST. Triggering an eGFP response from the Wnt reporter cells shows that at least a proportion of the magnetically-released Wnt3a is bioactive and suggests that the magnetic heating does not completely deteriorate the protein function, despite Wnt3a showing temperature sensitivity. By analysing the Wnt3a and apotransferrin released after 30 min magnetic heating, I could calculate almost a 4-fold increase in apotransferrin release by comparison which perhaps indicates a proportion of the released Wnt3a is not bioactive. However, this assumes that Wnt3a is being released at the same rate as apotransferrin, which is perhaps naïve since Wnt3a has very

different molecular properties that could impact release, being significantly smaller than apotransferrin with a higher isoelectric point. Recombinant Wnt3a is not phosphorylated which likely contributes to its instability. Therefore, it would be interesting, if possible, to engineer a more thermally-stable version of Wnt3a. This could perhaps be more resistant to any detrimental effects of magnetic heating during its release from temperature-responsive nanoparticles and may lead to an improved bioactive response from cells.

It was encouraging to see that Wnt3a-loaded nanoparticles do not trigger a cellular response when exposed to Wnt reporter MSCs overnight below the polymer LCST (30^{o}C). This suggests that magnetic heating is essential to release the encapsulated, bioactive protein as a consequence of triggering a PNIPAM phase transition. Additionally, this result provides an insight into the nature of the Wnt3a encapsulation within the PNIPAM shell, suggesting that the protein is associated deeper within the polymer matrix, rather than being bound to the surface. Surface-bound Wnt3a would likely be able to interact with Fz receptors on the surface of Wnt reporter MSCs and trigger a response, whereas entrapped protein would not.

Prior to proliferation assays, it was necessary to ascertain the exogenous Wnt3a concentration required to significantly enhance proliferation by conducting a Wnt3a dose response with MSCs. In previous work investigating Wnt3a influence on MSC proliferation, Wnt3a was added in the form of conditioned media rather than purified protein, therefore the amount of Wnt3a required to enhance proliferation was unknown (Boland et al., 2004). I could determine that an overnight exposure of MSCs to Wnt3a followed by either a 5- or 10-day growth period, for immortalised or primary cell respectively, was sufficient to trigger a significant enhancement in proliferation at certain concentrations. This data was used to calibrate Wnt3a release from the nanoparticles where I could show bioactive Wnt3a was released following magnetic heating in concentrations sufficient to significantly stimulate MSC proliferation. As with the protein, it may have also been possible to titrate the amount of nanoparticles used in the experiments and quantify how much was present. This could perhaps have been achieved using a dye for iron, such as Prussian blue, to stain for oxidation of ferrous ferrocyanide salts relative to standard amounts of iron oxide nanoparticles (Dunbar & Heintz, 1997). Perhaps this could then help to accurately correlate the cellular response with the exact amount of iron-containing nanoparticles added. Also, cell viability appeared largely unaffected following a prolonged 7-day exposure to PNIPAM-

coated particles, highlighting their bio-suitability. Indeed, it has been shown previously that the cytotoxicity was unaffected for both HeLa and HEK293 cells exposed to composite nanogels using iron oxide nanoparticles and PNIPAM (Deptuła et al., 2015). Also, I could show that exposure to PNIPAM-coated nanoparticles for 7 days resulted in cell uptake. It has been shown previously that there is nanoparticle size dependence on clathrin-mediated endocytosis with 20-30 nm being optimal for uptake (Banerjee et al., 2013). Given that MSCs were cultured at 37^{o}C for 7 days the PNIPAM shell of the nanoparticles would have been collapsed, significantly reducing the diameter, which likely permitted cellular uptake via clathrin-mediated endocytosis. Larger particles between sizes of 0.5 – 5 µm are taken up more commonly through macropinocytosis or circular dorsal ruffles where cells simply envelop materials into the cytoplasm. By contrast, for smaller particles between 20 – 500 nm the slower, more regulated mechanism for uptake is clathrin-mediated endocytosis. Scavenger, mannose and Toll-like receptors are known recognition and induction mechanisms for the process, involving formation of clathrin pits in the cell membrane that wrap and pull their cargo into the cell (Gustafson et al., 2015).

In previous tissue engineering work, scaffolds have largely been used for the incorporation and delivery of growth factors. For example, polycaprolactone (PCL)/PLGA scaffolds could release BMP-2 in an initial burst, before sustained release over 28 days that could enhance osteoblast activity *in vitro* and also bone formation *in vivo* (Kim et al., 2014). The release of BMP-2 in this study was ~13 ng/mL during the first day, followed by a gradual increase over 28 days to ~20 ng/mL (Kim et al., 2014). This release rate is significantly slower than that observed for Wnt3a release from PNIPAM-coated SPIONs, where over 40 ng/mL was released after just 30 min magnetic heating. Another study showed that HA hydrogel scaffolds could release growth and differentiation factor 5 (GDF-5) to enhance osteogenic differentiation, which as shown by Kim et al., (2014), showed an initial burst, followed by gradual sustained release over 28 days (Bae et al., 2014). Increased rates of release were found to correlate with higher amounts of initial GDF-5 loading, where after 7 hrs, 2.18, 15.05, and 152.09 ng/mL of the growth factor was released from hydrogels loaded with 10, 100 or 1000 ng/mL GDF-5 respectively (Bae et al., 2014). A drawback from the approaches highlighted above could be the lack of a specific trigger to release the growth

factor content at a desired point, which could result in a proportion of protein loss during delivery of the scaffold to the site of interest.

Nanoparticles offer advantages over scaffold-based approaches for growth factor delivery and release with their vastly higher surface area to volume ratio which contributes to much more efficient biomolecule encapsulation efficiency. The small size of nanoparticles and their capacity for surface functionalisation also add to their potential as a growth factor delivery system that show effective biodistribution and can be modified to target specific cells/tissues of interest. Nanoparticles that have been used in previous work for growth factor delivery have largely been used in Alzheimer's research. These nanoparticles are generally composed of natural polymers such as chitosan or synthetic polymers like PLA or PLGA. A study showed that for growth factor biodistribution in brain tissues, an intranasal spray administration of chitosan nanoparticles loaded with bFGF was much more effective than intravenous injection of bFGF, showing over two-fold more effective uptake in the olfactory bulb, cerebrum, cerebellum and hippocampus (Feng et al., 2012). The biodistribution of the bFGF-containing chitosan nanoparticles varied between tissues, where the majority of the cargo was released in an initial burst for each, notably in the olfactory bulb at ~19 ng/g after 5 min (Feng et al., 2012). Although this approach shows effective biodistribution and growth factor release throughout brain tissue, this may not be suitable for other applications where growth factor release is desired at a specific site using a trigger to prevent losses during delivery. Another intranasal approach could deliver synthetic polymer-based nanoparticles of PEG-PLGA that facilitated the transport of bFGF across the blood brain barrier (Zhang et al., 2014). These particles could release the growth factor in a more gradual manner than that observed for the aforementioned chitosan particle studies over a 24-hr period, where roughly 3 µg (10% of the input protein) was released within the initial hour and reached around 60% after 24 hr (Zhang et al., 2014). Losses of about 40% could be detected in the nasal wash, indicating a large proportion of the growth factor was released during delivery.

The magnetically-responsive, temperature-sensitive particles I have generated could be a useful tool for growth factor delivery and triggered release that will maximise the efficiency and effectiveness of this approach in tissue engineering.

5.4. Future work

Potential future directions for this work could involve further optimisation of the PNIPMAM-coated particles to prevent protein release at physiological temperatures. This could generate a temperature-sensitive polymer that only releases proteins above 37^{o}C which could be triggered by magnetic nanoparticle heating. Prevention of protein leakage during transit when particles are being delivered to cells is important to allow for magnetically-activated release at the desired site only. The preliminary work I have carried out using this polymer showed that the rate of protein release is elevated at temperatures above physiological levels and there could be scope to further develop this delivery system. However, when considering magnetically-triggered release at temperatures above 37^{o}C, it will be important to consider the thermal stability of proteins being used. As I have already seen, Wnt3a becomes increasingly unstable after heating to levels only slightly above physiological temperatures and therefore selecting the most suitable biomolecules to use for this work will be important to ensure optimum bioactivity following heating.

It would also be interesting to functionalise the surface of the polymer shell with an antibody that recognises a specific cell surface marker of MSCs, such as CD44 (Corradetti et al., 2017). This could confer specific targeting to MSCs *in vivo* which would make the developed particles much more suitable as a biomolecule delivery application.

Additionally, it would be important to assess the temperature-responsive release of proteins *in vivo* to assess how effective magnetic nanoparticle heating is through tissue. In order to optimise the SPION magnetic heating properties, it would be useful to improve the SPION dispersity and size. Whether magnetically-triggered protein release will be effective in a more complex biological environment remains to be seen, but certainly should be addressed. For example, the delivery and magnetically-triggered release of a growth factor that stimulates MSCs to drive bone regeneration *in vivo*, would be a highly robust measure of the system effectiveness. The penetration of an alternating magnetic field through tissue to activate magnetic nanoparticles will certainly be more difficult to achieve than in a controlled, cell culture environment. Moreover, the parameters of the alternating magnetic field could be modified to improve the magnetic heating efficiency in a more complex biological environment. This can be achieved by increasing the

frequency of the field oscillation, thus leading to an increase in the rate at which the magnetic moment of the nanoparticles flips. Optimising both the nanoparticle and magnetic heating properties could be interesting for the development of a system that can effectively trigger the release of bioactive molecules in biological tissue as a result of magnetically heating thermally-sensitive nanoparticles.

5.5. Conclusions

I have generated PNIPAM surface-functionalised iron oxide nanoparticles that are both magnetically-responsive and temperature-sensitive. I could encapsulate the model test protein apotransferrin within the PNIPAM shell and trigger protein release upon changes in temperature with/without magnetic heating. Using these tools and mechanisms, I was able to engineer conditions where Wnt3a could be released from PNIPAM-coated nanoparticles upon magnetic heating. I found that the release occurred at bulk solution temperatures that were below that of the PNIPAM LCST. Activity of released Wnt3a was shown both by a Wnt reporter MSC line response and enhanced proliferation of both immortalised and primary MSCs. I could show nanoparticle stability over long periods as well as biocompatibility with MSCs. This study provides evidence to support the use of temperature-sensitive nanoparticles to deliver and release complex biomolecules upon magnetic heating to bioactive MSCs in cell culture.

Abbreviations

5-FU = 5-fuorouracil

ALP = Alkaline phosphatase

APC = Adenomatosis polyposis coil

APS = Ammonium persulfate

ATRP = Atom transfer radical polymerisation

BCL9 = B-cell CLL/lymphoma 9 protein

bFGF = Basic fibroblast growth factor

BMI = Body mass index

BMP = Bone morphogenetic protein

BSA = Bovine serum albumin

$CDCl_3$ = Deuterated chloroform

CK1α = Casein kinase 1α

Col2a1 = Collagen type 2 alpha 1

COMU = 1-cyano-2-ethoxy-2-oxoethylidenaminooxy)dimethylamino-morpholino-carbenium hexafluorophosphate

dH_2O = Deionised water

DIPEA = *N*, *N*-diisopropylethylamine

DLS = Dynamic light scattering

DMEM = Dulbecco's Modified Eagle's Medium

DMF = Dimethylformamide

DMSO-D_6 = Deuterated dimethyl sulfoxide

DOX = Doxorubicin

Dsh = Dishevelled

EBIB = Ethyl 2-bromoisobutyrate

EBs = Embryonic bodies

eGFP = Enhanced green fluorescent protein

emu = Electromagnetic units/magnetic moment

FACS = Fluorescence-activated cell sorting

FOXO3A = Forkhead box O3A

FRP = Free radical polymerisation

Fz = Frizzled

GAR-HRP = Goat anti rabbit-horseradish peroxidase

GDF-5 = Growth and differentiation factor 5

GSK3 = Glycogen synthase 3

HA = Hyaluronic acid

HABA = 2-(4-hydroxyphenylazo)benzoic acid

hESCs = Human embryonic stem cells

Hh = Hedgehog

HPA = $H_3PW_{12}O_{40}$

HRP = Horseradish peroxidase

HSCs = Haematopoietic stem cells

HSP70 = Heat shock protein 70

hTERT = Human telomerase reverse transcriptase

HUVECs = Human umbilical vein endothelial cells

IHh = Indian hedgehog

int1 = integration 1

LCST = Lower critical solution temperature

LEF = Lymphoid enhancer factor

LRP5/6 = Low-density lipoprotein receptor-related protein 5/6

m/z = Mass-to-charge ratio

MALDI-TOF = Matrix-assisted laser desorption/ionisation-time of flight

MASI = *N*-succinimidyl methacrylate

Me_6TREN = Tris[2-(dimethylamino)ethyl]amine

M_n = Number average molar mass

MRI = Magnetic resonance imaging

MSCs = Mesenchymal stem/stromal cells

MTT = 3-(4,5-dimethylthiazol-2-yl)-2,5-diphenyltetrazolium

M_w = Mass average molar mass

NDA = 6-Nitrodopamine hydrogensulfate

NDA-PNIPAM = 6-Nitrodopamine hydrogensulfate-terminated poly(*N*-isopropylacrylamide)

NDA-PNIPMAM = 6-Nitrodopamine hydrogensulfate-terminated poly(*N*-isopropylmethacrylamide)

NIPAM = *N*-isopropylacrylamide

NIPMAM = *N*-isopropylmethacrylamide

NIR = Near infrared

NMP = Nitroxide-mediated polymerisation

NMR = Nuclear magnetic resonance

NTA = Nanoparticle tracking analysis

P/S = Penicillin/streptomycin

PBS = Phosphate buffered saline

PBST = Phosphate buffered saline tween-20

PCL = Polycaprolactone

PDA = Polydopamine

PDI = Polydispersity index

PEEK = Polyether ether ketone

PEG = Polyethylene glycol

PLA = Poly(lactic acid)

PLGA = Poly(lactic-co-glycolic acid)

PMASI = Poly(*N*-succinimidyl methacrylate)

PMDETA = *N, N, N', N", N"*- pentamethyldiethylenetriamine

PNB = Poly(4,5-dimethoxy-2-nitrobenzyl methacrylate)

PNIPAM = Poly(*N*-isopropylacrylamide)

PNIPMAM = Poly(*N*-isopropylmethacrylamide)

POEG = Poly(methoxy polyethylene glycol monomethacrylate)

PP2A = Protein phosphatase 2A

PVDF = Polyvinylidenefluoride

R6G = Rhodamine 6G

RA = Retinoic acid

RAFT = Reversible addition-fragmentation chain transfer

RDRP = Reversible-deactivation radical polymerisation

RGD = Arginine-glycine-aspartic acid

Runx2 = Runt-related transcription factor 2

SAR = Specific absorption rate

SDF-1α = Stromal-derived factor 1α

SDS = Sodium dodecyl sulfate

SDS-PAGE = Sodium dodecyl sulfate-polyacrylamide gel electrophoresis

Sox9 = SRY-related high mobility group-box gene 9

SPINUS = Structure-based Predictions in Nuclear Magnetic Resonance Spectroscopy

SPIONs = Superparamagnetic iron oxide nanoparticles

TCF = T-cell factor

TEM = Transmission electron microscopy

TEMED = N,N,N′,N′-tetramethylethylenediamine

TGA = Thermal gravimetric analysis

TGF-β = Transforming growth factor β

THF = Tetrahydrofuran

UCST = Upper critical solution temperature

VEGF = Vascular endothelial growth factor

VSM = Vibrating sample magnometry

Wg = Wingless

XPS = X-ray photoelectron spectroscopy

ZNF145 = Zinc-finger protein 145

References

1. Abbey, T., Christine, F., Paula, F., Paul, H., Ian, B., Chris, S. and Christine, L. (2016). Osteogenic differentiation of human mesenchymal stem cells in hydroxyapatite loaded thermally triggered, injectable hydrogel scaffolds to promote repair and regeneration of bone defects. *Frontiers in Bioengineering and Biotechnology*, 4.
2. Adibfar, A., Amoabediny, G., Baghaban Eslaminejad, M., Mohamadi, J., Bagheri, F. and Zandieh Doulabi, B. (2018). VEGF delivery by smart polymeric PNIPAM nanoparticles affects both osteogenic and angiogenic capacities of human bone marrow stem cells. *Materials Science and Engineering: C*, 93, pp.790-799.
3. Afroze, F., Nies, E. and Berghmans, H. (2000). Phase transitions in the system poly(N-isopropylacrylamide)/water and swelling behaviour of the corresponding networks. *Journal of Molecular Structure*, 554(1), pp.55-68.
4. Al-Ahmady, Z., Scudamore, C. and Kostarelos, K. (2015). Triggered doxorubicin release in solid tumors from thermosensitive liposome-peptide hybrids: Critical parameters and therapeutic efficacy. *International Journal of Cancer*, 137(3), pp.731-743.
5. Amstad, E., Gillich, T., Bilecka, I., Textor, M. and Reimhult, E. (2009). Ultrastable Iron Oxide Nanoparticle Colloidal Suspensions Using Dispersants with Catechol-Derived Anchor Groups. *Nano Letters*, 9(12), pp.4042-4048.
6. Amstad, E., Textor, M. and Reimhult, E. (2011). Stabilization and functionalization of iron oxide nanoparticles for biomedical applications. *Nanoscale*, 3(7), p.2819.
7. Atkinson, W., Brezovich, I. and Chakraborty, D. (1984). Usable Frequencies in Hyperthermia with Thermal Seeds. *IEEE Transactions on Biomedical Engineering*, BME-31(1), pp.70-75.
8. Auffan, M., Rose, J., Bottero, J., Lowry, G., Jolivet, J. and Wiesner, M. (2009). Towards a definition of inorganic nanoparticles from an environmental, health and safety perspective. *Nature Nanotechnology*, 4(10), pp.634-641.
9. Augello, A. and De Bari, C. (2010). The Regulation of Differentiation in Mesenchymal Stem Cells. *Human Gene Therapy*, 21(10), pp.1226-1238.
10. Ayano, E. and Kanazawa, H. (2006). Aqueous chromatography system using temperature-responsive polymer-modified stationary phases. *Journal of Separation Science*, 29(6), pp.738-749.

11. Bae, M., Ohe, J., Lee, J., Heo, D., Byun, W., Bae, H., Kwon, Y. and Kwon, I. (2014). Photo-cured hyaluronic acid-based hydrogels containing growth and differentiation factor 5 (GDF-5) for bone tissue regeneration. *Bone*, 59, pp.189-198.

12. Banerjee, A., Berezhkovskii, A. and Nossal, R. (2013). On the Size Dependence of Cellular Uptake of Nanoparticle via Clathrin-Mediated Endocytosis. *Biophysical Journal*, 104(2), p.622a.

13. Bartholomew, A., Sturgeon, C., Siatskas, M., Ferrer, K., McIntosh, K., Patil, S., Hardy, W., Devine, S., Ucker, D., Deans, R., Moseley, A. and Hoffman, R. (2002). Mesenchymal stem cells suppress lymphocyte proliferation in vitro and prolong skin graft survival in vivo. *Experimental Hematology*, 30(1), pp.42-48.

14. Batista, C., Larson, R., Kotov, N., (2015) Nonadditivity of nanoparticle interactions, *Science*, 350(6257), pp. 1242477

15. Behrens, J., von Kries, J., Kühl, M., Bruhn, L., Wedlich, D., Grosschedl, R. and Birchmeier, W. (1996). Functional interaction of β-catenin with the transcription factor LEF-1. *Nature*, 382(6592), pp.638-642.

16. Belloni, J., Mostafavi, M., Remita, H., Marignier, J. and Delcourt, a. (1998). Radiation-induced synthesis of mono- and multi-metallic clusters and nanocolloids. *New Journal of Chemistry*, 22(11), pp.1239-1255.

17. Benoit, D., Zhu, H., Lilierose, M., Verm, R., Ali, N., Morrison, A., Fortner, J., Avendano, C. and Colvin, V. (2012). Measuring the Grafting Density of Nanoparticles in Solution by Analytical Ultracentrifugation and Total Organic Carbon Analysis. *Analytical Chemistry*, 84(21), pp.9238-9245.

18. Betzer, O., Shilo, M., Opochinsky, R., Barnoy, E., Motiei, M., Okun, E., Yadid, G. and Popovtzer, R. (2017). The effect of nanoparticle size on the ability to cross the blood–brain barrier: an in vivo study. *Nanomedicine*, 12(13), pp.1533-1546.

19. Blasi, P., Giovagnoli, S., Schoubben, A., Ricci, M. and Rossi, C. (2007). Solid Lipid Nanoparticles for Targeted Brain Drug Delivery. *ChemInform*, 38(48).

20. Boland, G., Perkins, G., Hall, D. and Tuan, R. (2004). Wnt 3a promotes proliferation and suppresses osteogenic differentiation of adult human mesenchymal stem cells. *Journal of Cellular Biochemistry*, 93(6), pp.1210-1230.

21. Borden, B., Yockman, J. and Kim, S. (2010). Thermoresponsive Hydrogel as a Delivery Scaffold for Transfected Rat Mesenchymal Stem Cells. *Molecular Pharmaceutics*, 7(4), pp.963-968.

22. Bridgewater, L., Lefebvre, V. and de Crombrugghe, B. (1998). Chondrocyte-specific Enhancer Elements in the Col11a2 Gene Resemble the Col2a1 Tissue-specific Enhancer. *Journal of Biological Chemistry*, 273(24), pp.14998-15006.

23. Brunner, T., Wick, P., Manser, P., Spohn, P., Grass, R., Limbach, L., Bruinink, A. and Stark, W. (2006). In Vitro Cytotoxicity of Oxide Nanoparticles: Comparison to Asbestos, Silica, and the Effect of Particle Solubility†. *Environmental Science & Technology*, 40(14), pp.4374-4381.

24. Bulte, J. and Kraitchman, D. (2004). Iron oxide MR contrast agents for molecular and cellular imaging. *NMR in Biomedicine*, 17(7), pp.484-499.

25. Bunnell, B., Flaat, M., Gagliardi, C., Patel, B. and Ripoll, C. (2008). Adipose-derived stem cells: Isolation, expansion and differentiation. *Methods*, 45(2), pp.115-120.

26. Burmistrova, A., Richter, M., Eisele, M., Üzüm, C. and von Klitzing, R. (2011). The Effect of Co-Monomer Content on the Swelling/Shrinking and Mechanical Behaviour of Individually Adsorbed PNIPAM Microgel Particles. *Polymers*, 3(4), pp.1575-1590.

27. Carrey, J., Mehdaoui, B. and Respaud, M. (2011). Simple models for dynamic hysteresis loop calculations of magnetic single-domain nanoparticles: Application to magnetic hyperthermia optimization. *Journal of Applied Physics*, 109(8), p.083921.

28. Carroll, K., Shultz, M., Fatouros, P. and Carpenter, E. (2010). High magnetization aqueous ferrofluid: A simple one-pot synthesis. *Journal of Applied Physics*, 107(9), pp.107.

29. Cencer, M., Murley, M., Liu, Y. and Lee, B. (2014). Effect of Nitro-Functionalization on the Cross-Linking and Bioadhesion of Biomimetic Adhesive Moiety. *Biomacromolecules*, 16(1), pp.404-410.

30. Chen, J. (1990). Polymer-protein conjugatesII. Affinity precipitation separation of human immunogammaglobulin by a poly(N-isopropylacrylamide)-protein A conjugate. *Biomaterials*, 11(9), pp.631-634.

31. Chen, S., Shi, J., Zhang, M., Chen, Y., Wang, X., Zhang, L., Tian, Z., Yan, Y., Li, Q., Zhong, W., Xing, M., Zhang, L. and Zhang, L. (2015). Mesenchymal

stem cell-laden anti-inflammatory hydrogel enhances diabetic wound healing. *Scientific Reports*, 5(1).

32. Cheng, M., Prabakaran, P., Kumar, R., Sridhar, S. and Ebong, E. (2018). Synthesis of Functionalized 10-nm Polymer-coated Gold Particles for Endothelium Targeting and Drug Delivery. *Journal of Visualized Experiments*, (131).

33. Chiefari, J., Chong, Y., Ercole, F., Krstina, J., Jeffery, J., Le, T., Mayadunne, R., Meijs, G., Moad, C., Moad, G., Rizzardo, E. and Thang, S. (1998). Living Free-Radical Polymerization by Reversible Addition−Fragmentation Chain Transfer: The RAFT Process. *Macromolecules*, 31(16), pp.5559-5562.

34. Choi, S., Baek, M., Chung, H., Yu, J., Lee, J., Kim, T., Oh, J., Lee, W., Paek, S., Lee, J., Jeong, J. and Choy, J. (2012). Pharmacokinetics, tissue distribution, and excretion of zinc oxide nanoparticles. *International Journal of Nanomedicine*, p.3081.

35. Chung, T., Hsu, S., Wu, S., Hsiao, J., Lin, C., Yao, M. and Huang, D. (2018). Dextran-coated iron oxide nanoparticle-improved therapeutic effects of human mesenchymal stem cells in a mouse model of Parkinson's disease. *Nanoscale*, 10(6), pp.2998-3007.

36. Clement, S., Gardner, B., Razali, W., Coleman, V., Jämting, Å., Catchpoole, H., Goldys, E., Herrmann, J. and Zvyagin, A. (2017). Quantification of nanoparticle concentration in colloidal suspensions by a non-destructive optical method. *Nanotechnology*, 28(47), p.475702.

37. Cooperstein, M. and Canavan, H. (2013). Assessment of cytotoxicity of (N-isopropyl acrylamide) and Poly(N-isopropyl acrylamide)-coated surfaces. *Biointerphases*, 8(1), p.19.

38. Corradetti, B., Taraballi, F., Martinez, J., Minardi, S., Basu, N., Bauza, G., Evangelopoulos, M., Powell, S., Corbo, C. and Tasciotti, E. (2017). Hyaluronic acid coatings as a simple and efficient approach to improve MSC homing toward the site of inflammation. *Scientific Reports*, 7(1).

39. da Silva Meirelles, L. (2006). Mesenchymal stem cells reside in virtually all post-natal organs and tissues. *Journal of Cell Science*, 119(11), pp.2204-2213.

40. Dai, Z., Shu, Y., Wan, C. and Wu, C. (2016). Effects of Culture Substrate Made of Poly(N-isopropylacrylamide-co-acrylic acid) Microgels on Osteogenic Differentiation of Mesenchymal Stem Cells. *Molecules*, 21(9), p.1192.

41. Day, T., Guo, X., Garrett-Beal, L. and Yang, Y. (2005). Wnt/β-Catenin Signaling in Mesenchymal Progenitors Controls Osteoblast and Chondrocyte Differentiation during Vertebrate Skeletogenesis. *Developmental Cell*, 8(5), pp.739-750.

42. Deptuła, T., Warowicka, A., Woźniak, A., Grzeszkowiak, M., Jarzębski, M., Bednarowicz, M., Patkowski, A. and Słomski, R. (2015). Cytotoxicity of thermo-responsive polymeric nanoparticles based on N-isopropylacrylamide for potential application as a bioscaffold. *Acta Biochimica Polonica*, 62(2), pp.311-316.

43. Dinarvand, R. and D'Emanuele, A. (1995). The use of thermoresponsive hydrogels for on-off release of molecules. *Journal of Controlled Release*, 36(3), pp.221-227.

44. Dionigi, C., Lungaro, L., Goranov, V., Riminucci, A., Piñeiro-Redondo, Y., Bañobre-López, M., Rivas, J. and Dediu, V. (2014). Smart magnetic poly(N-isopropylacrylamide) to control the release of bio-active molecules. *Journal of Materials Science: Materials in Medicine*, 25(10), pp.2365-2371.

45. Djokpé, E. and Vogt, W. (2001). N-Isopropylacrylamide and N-Isopropylmethacryl-amide: Cloud Points of Mixtures and Copolymers. *Macromolecular Chemistry and Physics*, 202(5), pp.750-757.

46. Dominici, M., Le Blanc, K., Mueller, I., Slaper-Cortenbach, I., Marini, F., Krause, D., Deans, R., Keating, A., Prockop, D. and Horwitz, E. (2006). Minimal criteria for defining multipotent mesenchymal stromal cells. The International Society for Cellular Therapy position statement. *Cytotherapy*, 8(4), pp.315-317.

47. Ducy, P., Zhang, R., Geoffroy, V., Ridall, A. and Karsenty, G. (1997). Osf2/Cbfa1: A Transcriptional Activator of Osteoblast Differentiation. *Cell*, 89(5), pp.747-754.

48. Dunbar, K. R. & Heintz, R. A. (1997). *Chemistry of Transition Metal Cyanide Compounds: Modern Perspectives*. Progress in Inorganic Chemistry. **45**. pp. 283–391.

49. Duprez, D., de H. Bell, E., Richardson, M., Archer, C., Wolpert, L., Brickell, P. and Francis-West, P. (1996). Overexpression of BMP-2 and BMP-4 alters the size and shape of developing skeletal elements in the chick limb. *Mechanisms of Development*, 57(2), pp.145-157.

50. Etheridge, S., Spencer, G., Heath, D. and Genever, P. (2004). Expression Profiling and Functional Analysis of Wnt Signaling Mechanisms in Mesenchymal Stem Cells. *Stem Cells*, 22(5), pp.849-860.

51. Fairbanks, G., Steck, T. and Wallach, D. (1971). Electrophoretic analysis of the major polypeptides of the human erythrocyte membrane. *Biochemistry*, 10(13), pp.2606-2617.

52. Faraday, M. (1857). The Bakerian Lecture: Experimental Relations of Gold (and Other Metals) to Light. *Philosophical Transactions of the Royal Society of London*, 147(0), pp.145-181.

53. Fedoryshin, L., Tavares, A., Petryayeva, E., Doughan, S. and Krull, U. (2014). Near-Infrared-Triggered Anticancer Drug Release from Upconverting Nanoparticles. *ACS Applied Materials & Interfaces*, 6(16), pp.13600-13606.

54. Feng, C., Zhang, C., Shao, X., Liu, Q., Qian, Y., Feng, L., Chen, J., Zha, Y., Zhang, Q. and Jiang, X. (2012). Enhancement of nose-to-brain delivery of basic fibroblast growth factor for improving rat memory impairments induced by co-injection of β-amyloid and ibotenic acid into the bilateral hippocampus. *International Journal of Pharmaceutics*, 423(2), pp.226-234.

55. Ferreira, R., Fonseca, M., Santos, T., Sargento-Freitas, J., Tjeng, R., Paiva, F., Castelo-Branco, M., Ferreira, L. and Bernardino, L. (2016). Retinoic acid-loaded polymeric nanoparticles enhance vascular regulation of neural stem cell survival and differentiation after ischaemia. *Nanoscale*, 8(15), pp.8126-8137.

56. Fiedler, M., Mendoza-Topaz, C., Rutherford, T., Mieszczanek, J. and Bienz, M. (2011). Dishevelled interacts with the DIX domain polymerization interface of Axin to interfere with its function in down-regulating β-catenin. *Proceedings of the National Academy of Sciences*, 108(5), pp.1937-1942.

57. Filipe, V., Hawe, A. and Jiskoot, W. (2010). Critical Evaluation of Nanoparticle Tracking Analysis (NTA) by NanoSight for the Measurement of Nanoparticles and Protein Aggregates. *Pharmaceutical Research*, 27(5), pp.796-810.

58. Flory, P. J. (1937), “The mechanism of vinyl polymerizations,” *Journal of the American Chemical Society*, 59(2), pp. 241–253

59. Fortin, J., Wilhelm, C., Servais, J., Ménager, C., Bacri, J. and Gazeau, F. (2007). Size-Sorted Anionic Iron Oxide Nanomagnets as Colloidal Mediators for Magnetic Hyperthermia. *Journal of the American Chemical Society*, 129(9), pp.2628-2635.

60. Francis, D., Mielewczik, M., Zargaran, D. and Cole, G. (2013). Autologous bone marrow-derived stem cell therapy in heart disease: Discrepancies and contradictions. *International Journal of Cardiology*, 168(4), pp.3381-3403.

61. Frith, J. and Genever, P. (2008). Transcriptional Control of Mesenchymal Stem Cell Differentiation. *Transfusion Medicine and Hemotherapy*, 35(3), pp.216-227.

62. Fujishige, S., Kubota, K. and Ando, I. (1989). Phase transition of aqueous solutions of poly(N-isopropylacrylamide) and poly(N-isopropylmethacrylamide). *The Journal of Physical Chemistry*, 93(8), pp.3311-3313.

63. Gao, C., Seuntjens, J., Kaufman, G., Tran-Khanh, N., Butler, A., Li, A., Wang, H., Buschmann, M., Harvey, E. and Henderson, J. (2012). Mesenchymal stem cell transplantation to promote bone healing. *Journal of Orthopaedic Research*, 30(8), pp.1183-1189.

64. Gaur, T., Lengner, C., Hovhannisyan, H., Bhat, R., Bodine, P., Komm, B., Javed, A., van Wijnen, A., Stein, J., Stein, G. and Lian, J. (2005). Canonical WNT Signaling Promotes Osteogenesis by Directly Stimulating Runx2 Gene Expression. *Journal of Biological Chemistry*, 280(39), pp.33132-33140.

65. Georges, M., Veregin, R., Kazmaier, P. and Hamer, G. (1993). Narrow molecular weight resins by a free-radical polymerization process. *Macromolecules*, 26(11), pp.2987-2988.

66. Georgiou, T., Vamvakaki, M., Patrickios, C., Yamasaki, E. and Phylactou, L. (2004). Nanoscopic Cationic Methacrylate Star Homopolymers: Synthesis by Group Transfer Polymerization, Characterization and Evaluation as Transfection Reagents. *Biomacromolecules*, 5(6), pp.2221-2229.

67. Gersh, B. (2010). A Randomized, Double-Blind, Placebo-Controlled, Dose-Escalation Study of Intravenous Adult Human Mesenchymal Stem Cells (Prochymal) After Acute Myocardial Infarction. *Yearbook of Cardiology*, 2010, pp.389-391.

68. Glover, A., Bennett, J., Pritchett, J., Nikles, S., Nikles, D., Nikles, J. and Brazel, C. (2013). Magnetic Heating of Iron Oxide Nanoparticles and Magnetic Micelles for Cancer Therapy. *IEEE Transactions on Magnetics*, 49(1), pp.231-235.

69. Goessling, W., North, T., Loewer, S., Lord, A., Lee, S., Stoick-Cooper, C., Weidinger, G., Puder, M., Daley, G., Moon, R. and Zon, L. (2009). Genetic Interaction of PGE2 and Wnt Signaling Regulates Developmental Specification of Stem Cells and Regeneration. *Cell*, 136(6), pp.1136-1147.

70. Guérit, D., Brondello, J., Chuchana, P., Philipot, D., Toupet, K., Bony, C., Jorgensen, C. and Noël, D. (2014). FOXO3A Regulation by miRNA-29a Controls Chondrogenic Differentiation of Mesenchymal Stem Cells and Cartilage Formation. *Stem Cells and Development*, 23(11), pp.1195-1205.

71. Guo, X., Li, W., Luo, L., Wang, Z., Li, Q., Kong, F., Zhang, H., Yang, J., Zhu, C., Du, Y. and You, J. (2017). External Magnetic Field-Enhanced Chemo-Photothermal Combination Tumor Therapy via Iron Oxide Nanoparticles. *ACS Applied Materials & Interfaces*, 9(19), pp.16581-16593.

72. Guo, X., Mak, K., Taketo, M. and Yang, Y. (2009). The Wnt/β-Catenin Pathway Interacts Differentially with PTHrP Signaling to Control Chondrocyte Hypertrophy and Final Maturation. *PLoS ONE*, 4(6), p.e6067.

73. Gustafson, H., Holt-Casper, D., Grainger, D. and Ghandehari, H. (2015). Nanoparticle uptake: The phagocyte problem. *Nano Today*, 10(4), pp.487-510.

74. Gyöngyösi, M., Wojakowski, W., Lemarchand, P., Lunde, K., Tendera, M., Bartunek, J., Marban, E., Assmus, B., Henry, T., Traverse, J., Moyé, L., Sürder, D., Corti, R., Huikuri, H., Miettinen, J., Wöhrle, J., Obradovic, S., Roncalli, J., Malliaras, K., Pokushalov, E., Romanov, A., Kastrup, J., Bergmann, M., Atsma, D., Diederichsen, A., Edes, I., Benedek, I., Benedek, T., Pejkov, H., Nyolczas, N., Pavo, N., Bergler-Klein, J., Pavo, I., Sylven, C., Berti, S., Navarese, E. and Maurer, G. (2015). Meta-Analysis of Cell-based CaRdiac stUdiEs (ACCRUE) in Patients With Acute Myocardial Infarction Based on Individual Patient Data. *Circulation Research*, 116(8), pp.1346-1360.

75. Hamidian, H. and Tavakoli, T. (2016). Preparation of a new Fe 3 O 4 /starch- g -polyester nanocomposite hydrogel and a study on swelling and drug delivery properties. *Carbohydrate Polymers*, 144, pp.140-148.

76. Han, D. and Hubbell, J. (1996). Lactide-Based Poly(ethylene glycol) Polymer Networks for Scaffolds in Tissue Engineering. *Macromolecules*, 29(15), pp.5233-5235.

77. Hayashi, C. (1997). Ultra-Fine Particles and Coatings. *SHINKU*, 40(9), pp.709-716.

78. Hergt, R., Dutz, S. and Röder, M. (2008). Effects of size distribution on hysteresis losses of magnetic nanoparticles for hyperthermia. *Journal of Physics: Condensed Matter*, 20(38), p.385214.

79. Heskins, M. and Guillet, J. (1968). Solution Properties of Poly(N-isopropylacrylamide). *Journal of Macromolecular Science: Part A - Chemistry*, 2(8), pp.1441-1455.

80. Heydari, M., Javidi, M., Attar, M., Karimi, A., Navidbackhsh, M., Haghpanai, M. and Amanpour, S. (2015). Magnetic Fluid Hyperthermia in a Cylindrical Gel Contains Water Flow. *Journal of Mechanics in Medicine and Biology*, 15(05), p.1550088.

81. Hjørringgaard, C., Brust, A. and Alewood, P. (2012). Evaluation of COMU as a coupling reagent for in situ neutralization Boc solid phase peptide synthesis. *Journal of Peptide Science*, 18(3), pp.199-207.

82. Hu, H. (2004). Sequential roles of Hedgehog and Wnt signaling in osteoblast development. *Development*, 132(1), pp.49-60.

83. Huang, G., Gao, J., Hu, Z., St. John, J., Ponder, B. and Moro, D. (2004). Controlled drug release from hydrogel nanoparticle networks. *Journal of Controlled Release*, 94(2-3), pp.303-311.

84. Huang, Y. and Liu, T. (2012). Mobilization of mesenchymal stem cells by stromal cell-derived factor-1 released from chitosan/tripolyphosphate/fucoidan nanoparticles. *Acta Biomaterialia*, 8(3), pp.1048-1056.

85. Huang, Y., Lu, Y. and Chen, J. (2017). Magnetic graphene oxide as a carrier for targeted delivery of chemotherapy drugs in cancer therapy. *Journal of Magnetism and Magnetic Materials*, 427, pp.34-40.

86. Huang, Y., Mao, K., Zhang, B. and Zhao, Y. (2017). Superparamagnetic iron oxide nanoparticles conjugated with folic acid for dual target-specific drug delivery and MRI in cancer theranostics. *Materials Science and Engineering: C*, 70, pp.763-771.

87. Huber, O., Korn, R., McLaughlin, J., Ohsugi, M., Herrmann, B. and Kemler, R. (1996). Nuclear localization of β-catenin by interaction with transcription factor LEF-1. *Mechanisms of Development*, 59(1), pp.3-10.

88. Huffman, A., Afrassiabi, A. and Dong, L. (1986). Thermally reversible hydrogels: II. Delivery and selective removal of substances from aqueous solutions. *Journal of Controlled Release*, 4(3), pp.213-222.

89. Hufschmid, R., Arami, H., Ferguson, R., Gonzales, M., Teeman, E., Brush, L., Browning, N. and Krishnan, K. (2015). Synthesis of phase-pure and monodisperse iron oxide nanoparticles by thermal decomposition. *Nanoscale*, 7(25), pp.11142-11154.

90. Huo, D., Li, Y. and Kobayashi, T. (2006). Temperature-pH Controlled Uptake and Release of Bovine Serum Albumin Protein in Environmental Sensitive Microgel Based on Crosslinked Poly(N-isopropylacrylamide-co-acrylic acid). *Advanced Materials Research*, 11-12, pp.299-302.

91. Hwang, Y., Chung, B., Ortmann, D., Hattori, N., Moeller, H. and Khademhosseini, A. (2009). Microwell-mediated control of embryoid body size regulates embryonic stem cell fate via differential expression of WNT5a and WNT11. *Proceedings of the National Academy of Sciences*, 106(40), pp.16978-16983.

92. James, S., Fox, J., Afsari, F., Lee, J., Clough, S., Knight, C., Ashmore, J., Ashton, P., Preham, O., Hoogduijn, M., Ponzoni, R., Hancock, Y., Coles, M. and Genever, P. (2015). Multiparameter Analysis of Human Bone Marrow Stromal Cells Identifies Distinct Immunomodulatory and Differentiation-Competent Subtypes. *Stem Cell Reports*, 4(6), pp.1004-1015.

93. Jang, K., Lee, K., Yang, S. and Jeun, S. (2010). In vivoTracking of Transplanted Bone Marrow-Derived Mesenchymal Stem Cells in a Murine Model of Stroke by Bioluminescence Imaging. *Journal of Korean Neurosurgical Society*, 48(5), p.391.

94. Javidi, M., Heydari, M., Attar, M., Haghpanahi, M., Karimi, A., Navidbakhsh, M. and Amanpour, S. (2014). Cylindrical agar gel with fluid flow subjected to an alternating magnetic field during hyperthermia. *International Journal of Hyperthermia*, 31(1), pp.33-39.

95. Jenkins, A., Jones, R. and Moad, G. (2009). Terminology for reversible-deactivation radical polymerization previously called "controlled" radical or "living" radical polymerization (IUPAC Recommendations 2010). *Pure and Applied Chemistry*, 82(2), pp.483-491.

96. Jenkins, A., Kratochvíl, P., Stepto, R. and Suter, U. (1996). Glossary of basic terms in polymer science (IUPAC Recommendations 1996). *Pure and Applied Chemistry*, 68(12), pp.2287-2311.

97. Jiang, R., Han, Z., Zhuo, G., Qu, X., Li, X., Wang, X., Shao, Y., Yang, S. and Han, Z. (2011). Transplantation of placenta-derived mesenchymal stem cells in type 2 diabetes: a pilot study. *Frontiers of Medicine*, 5(1), pp.94-100.

98. Kaamyabi, S., Habibi, D. and Amini, M. (2016). Preparation and characterization of the pH and thermosensitive magnetic molecular imprinted

nanoparticle polymer for the cancer drug delivery. *Bioorganic & Medicinal Chemistry Letters*, 26(9), pp.2349-2354.

99. Karanes, C., Nelson, G., Chitphakdithai, P., Agura, E., Ballen, K., Bolan, C., Porter, D., Uberti, J., King, R. and Confer, D. (2008). Twenty Years of Unrelated Donor Hematopoietic Cell Transplantation for Adult Recipients Facilitated by the National Marrow Donor Program. *Biology of Blood and Marrow Transplantation*, 14(9), pp.8-15.

100. Kato, M., Kamigaito, M., Sawamoto, M. and Higashimura, T. (1995). Polymerization of Methyl Methacrylate with the Carbon Tetrachloride/Dichlorotris- (triphenylphosphine)ruthenium(II)/Methylaluminum Bis(2,6-di-tert-butylphenoxide) Initiating System: Possibility of Living Radical Polymerization. *Macromolecules*, 28(5), pp.1721-1723.

101. Kebriaei, P., Isola, L., Bahceci, E., Holland, K., Rowley, S., McGuirk, J., Devetten, M., Jansen, J., Herzig, R., Schuster, M., Monroy, R. and Uberti, J. (2009). Adult Human Mesenchymal Stem Cells Added to Corticosteroid Therapy for the Treatment of Acute Graft-versus-Host Disease. *Biology of Blood and Marrow Transplantation*, 15(7), pp.804-811.

102. Khan, F. (2012). *Biotechnology fundamentals*. 1st ed. Boca Raton: CRC Press/Taylor & Francis Group, pp.328.

103. Kim, T., Yun, Y., Park, Y., Lee, S., Yong, W., Kundu, J., Jung, J., Shim, J., Cho, D., Kim, S. and Song, H. (2014). In vitro and in vivo evaluation of bone formation using solid freeform fabrication-based bone morphogenic protein-2 releasing PCL/PLGA scaffolds. *Biomedical Materials*, 9(2), p.025008.

104. Komori, T., Yagi, H., Nomura, S., Yamaguchi, A., Sasaki, K., Deguchi, K., Shimizu, Y., Bronson, R., Gao, Y., Inada, M., Sato, M., Okamoto, R., Kitamura, Y., Yoshiki, S. and Kishimoto, T. (1997). Targeted Disruption of Cbfa1 Results in a Complete Lack of Bone Formation owing to Maturational Arrest of Osteoblasts. *Cell*, 89(5), pp.755-764.

105. Kon, E., Muraglia, A., Corsi, A., Bianco, P., Marcacci, M., Martin, I., Boyde, A., Ruspantini, I., Chistolini, P., Rocca, M., Giardino, R., Cancedda, R. and Quarto, R. (2000). Autologous bone marrow stromal cells loaded onto porous hydroxyapatite ceramic accelerate bone repair in critical-size defects of sheep long bones. *Journal of Biomedical Materials Research*, 49(3), pp.328-337.

106. Kramps, T., Peter, O., Brunner, E., Nellen, D., Froesch, B., Chatterjee, S., Murone, M., Züllig, S. and Basler, K. (2002). Wnt/Wingless Signaling Requires

BCL9/Legless-Mediated Recruitment of Pygopus to the Nuclear β-Catenin-TCF Complex. *Cell*, 109(1), pp.47-60.

107. Kubota, K., Hamano, K., Kuwahara, N., Fujishige, S. and Ando, I. (1990). Characterization of Poly(N-isopropylmethacrylamide) in Water. *Polymer Journal*, 22(12), pp.1051-1057.

108. Kulkarni, N., Onyia, J., Zeng, Q., Tian, X., Liu, M., Halladay, D., Frolik, C., Engler, T., Wei, T., Kriauciunas, A., Martin, T., Sato, M., Bryant, H. and Ma, Y. (2006). Orally Bioavailable GSK-3α/β Dual Inhibitor Increases Markers of Cellular Differentiation In Vitro and Bone Mass In Vivo. *Journal of Bone and Mineral Research*, 21(6), pp.910-920.

109. Kumar, R., Korideck, H., Ngwa, W., Berbeco, RI., Makrigiorgos, GM., Sridhar, S,. (2013), Third generation gold nanoplatform optimized for radiation therapy *Transl Cancer Res.* 2(4), pp. 1–18.

110. Kurayoshi, M., Yamamoto, H., Izumi, S. and Kikuchi, A. (2007). Post-translational palmitoylation and glycosylation of Wnt-5a are necessary for its signalling. *Biochemical Journal*, 402(3), pp.515-523.

111. Kurzhals, S., Zirbs, R. and Reimhult, E. (2015). Synthesis and Magneto-Thermal Actuation of Iron Oxide Core–PNIPAM Shell Nanoparticles. *ACS Applied Materials & Interfaces*, 7(34), pp.19342-19352.

112. Laughlin, R. (1976). An expedient technique for determining solubility phase boundaries in surfactant—water systems. *Journal of Colloid and Interface Science*, 55(1), pp.239-241.

113. Lechner, S. and Huss, R. (2006). Bone Engineering: Combining Smart Biomaterials and the Application of Stem Cells. *Artificial Organs*, 30(10), pp.770-774.

114. Lee, E. and von Recum, H. (2010). Cell culture platform with mechanical conditioning and nondamaging cellular detachment. *Journal of Biomedical Materials Research Part A*, 93(2), pp. 411-418.

115. Lee, K., Hui, J., Song, I., Ardany, L. and Lee, E. (2007). Injectable Mesenchymal Stem Cell Therapy for Large Cartilage Defects-A Porcine Model. *Stem Cells*, 25(11), pp.2964-2971.

116. Lee, K., Kim, H., Li, Q., Chi, X., Ueta, C., Komori, T., Wozney, J., Kim, E., Choi, J., Ryoo, H. and Bae, S. (2000). Runx2 Is a Common Target of Transforming Growth Factor beta 1 and Bone Morphogenetic Protein 2, and Cooperation between Runx2 and Smad5 Induces Osteoblast-Specific Gene

Expression in the Pluripotent Mesenchymal Precursor Cell Line C2C12. *Molecular and Cellular Biology*, 20(23), pp.8783-8792.

117. Lee, M., Kwon, T., Park, H., Wozney, J. and Ryoo, H. (2003). BMP-2-induced Osterix expression is mediated by Dlx5 but is independent of Runx2. *Biochemical and Biophysical Research Communications*, 309(3), pp.689-694.

118. Li, C., Wang, L., Yang, Z., Kim, G., Chen, H. and Ge, Z. (2012). A Viscoelastic Chitosan-Modified Three-Dimensional Porous Poly(L-Lactide-co-ε-Caprolactone) Scaffold for Cartilage Tissue Engineering. *Journal of Biomaterials Science, Polymer Edition*, 23(1-4), pp.405-424.

119. Li, Q., Kartikowati, C., Horie, S., Ogi, T., Iwaki, T. and Okuyama, K. (2017). Correlation between particle size/domain structure and magnetic properties of highly crystalline Fe3O4 nanoparticles. *Scientific Reports*, 7(1).

120. Liao, J., Hu, N., Zhou, N., Lin, L., Zhao, C., Yi, S., Fan, T., Bao, W., Liang, X., Chen, H., Xu, W., Chen, C., Cheng, Q., Zeng, Y., Si, W., Yang, Z. and Huang, W. (2014). Sox9 Potentiates BMP2-Induced Chondrogenic Differentiation and Inhibits BMP2-Induced Osteogenic Differentiation. *PLoS ONE*, 9(2), p.e89025.

121. Liu, K., Pan, P. and Bao, Y. (2015). Synthesis, micellization, and thermally-induced macroscopic micelle aggregation of poly(vinyl chloride)-g-poly(N-isopropylacrylamide) amphiphilic copolymer. *RSC Advances*, 5(115), pp.94582-94590.

122. Liu, S., Zhang, E., Yang, M. and Lu, L. (2014). Overexpression of Wnt11 promotes chondrogenic differentiation of bone marrow-derived mesenchymal stem cells in synergism with TGF-β. *Molecular and Cellular Biochemistry*, 390(1-2), pp.123-131.

123. Liu, T., Guo, X., Tan, H., Hui, J., Lim, B. and Lee, E. (2011). Zinc-finger protein 145, acting as an upstream regulator of SOX9, improves the differentiation potential of human mesenchymal stem cells for cartilage regeneration and repair. *Arthritis & Rheumatism*, 63(9), pp.2711-2720.

124. Liu, T., Liu, K., Liu, D., Chen, S. and Chen, I. (2009). Temperature-Sensitive Nanocapsules for Controlled Drug Release Caused by Magnetically Triggered Structural Disruption. *Advanced Functional Materials*, 19(4), pp.616-623.

125. Liu, Y., Shipton, M., Ryan, J., Kaufman, E., Franzen, S. and Feldheim, D. (2007). Synthesis, Stability, and Cellular Internalization of Gold Nanoparticles

Containing Mixed Peptide−Poly(ethylene glycol) Monolayers. *Analytical Chemistry*, 79(6), pp.2221-2229.

126. Lu, Z., Duan, C., Tian, Y., You, X. and Huang, X. (1996). Synthesis, Characterization, and Crystal Structure of a Novel Copper(II) Complex with an Asymmetric Coordinated 2,2‘-Bipyridine Derivative: A Model for the Associative Complex in the Ligand-Substitution Reactions of [Cu(tren)L]2+?. *Inorganic Chemistry*, 35(8), pp.2253-2258.

127. Malard, F. and Mohty, M. (2014). New Insight for the Diagnosis of Gastrointestinal Acute Graft-versus-Host Disease. *Mediators of Inflammation*, 2014, pp.1-9.

128. Mannaris, C., Efthymiou, E., Escoffre, J., Bouakaz, A., Khokhlova, V., Ilyin, S. and Averkiou, M. (2011). Use of high intensity focused ultrasound for localized activation of thermosensitive liposomes for drug delivery. *The Journal of the Acoustical Society of America*, 129(4), pp.2577-2577.

129. Marcacci, M., Kon, E., Quarto, R., Kutepov, S., Mukhachev, V., Lavroukov, A. and Cancedda, R. (2000). Repair of Large Bone Defects by Autologous Human Bone Marrow Stromal Cells. *Key Engineering Materials*, 192-195, pp.1053-0.

130. Matyjaszewski, K. and Tsarevsky, N. (2009). Nanostructured functional materials prepared by atom transfer radical polymerization. *Nature Chemistry*, 1(4), pp.276-288.

131. Moad, G. and Rizzardo, E. (1995). Alkoxyamine-Initiated Living Radical Polymerization: Factors Affecting Alkoxyamine Homolysis Rates. *Macromolecules*, 28(26), pp.8722-8728.

132. Mohapatra, J., Zeng, F., Elkins, K., Xing, M., Ghimire, M., Yoon, S., Mishra, S. and Liu, J. (2018). Size-dependent magnetic and inductive heating properties of Fe3O4 nanoparticles: scaling laws across the superparamagnetic size. *Physical Chemistry Chemical Physics*, 20(18), pp.12879-12887.

133. Moraes, L., Vasconcelos-dos-Santos, A., Santana, F., Godoy, M., Rosado-de-Castro, P., Jasmin, Azevedo-Pereira, R., Cintra, W., Gasparetto, E., Santiago, M. and Mendez-Otero, R. (2012). Neuroprotective effects and magnetic resonance imaging of mesenchymal stem cells labeled with SPION in a rat model of Huntington's disease. *Stem Cell Research*, 9(2), pp.143-155.

134. Mosimann, C., Hausmann, G. and Basler, K. (2006). Parafibromin/Hyrax Activates Wnt/Wg Target Gene Transcription by Direct Association with β-catenin/Armadillo. *Cell*, 125(2), pp.327-341.

135. Mosqueira, V., Legrand, P., Gulik, A., Bourdon, O., Gref, R., Labarre, D. and Barratt, G. (2001). Relationship between complement activation, cellular uptake and surface physicochemical aspects of novel PEG-modified nanocapsules. *Biomaterials*, 22(22), pp.2967-2979.

136. Nakamura, T., Hamada, F., Ishidate, T., Anai, K., Kawahara, K., Toyoshima, K. and Akiyama, T. (1998). Axin, an inhibitor of the Wnt signalling pathway, interacts with beta-catenin, GSK-3 beta and APC and reduces the beta-catenin level. *Genes to Cells*, 3(6), pp.395-403.

137. Nakashima, K., Zhou, X., Kunkel, G., Zhang, Z., Deng, J., Behringer, R. and de Crombrugghe, B. (2002). The Novel Zinc Finger-Containing Transcription Factor Osterix Is Required for Osteoblast Differentiation and Bone Formation. *Cell*, 108(1), pp.17-29.

138. Napolitano, A., d'Ischia, M., Costantini, C. and Prota, G. (1992). A new oxidation pathway of the neurotoxin 6-aminodopamine. Isolation and characterisation of a dimer with a tetrahydro[3,4]aiminoethanophenoxazine ring system. *Tetrahedron*, 48(39), pp.8515-8522.

139. Naseroleslami, M., Aboutaleb, N. and Parivar, K. (2018). The effects of superparamagnetic iron oxide nanoparticles-labeled mesenchymal stem cells in the presence of a magnetic field on attenuation of injury after heart failure. *Drug Delivery and Translational Research*, 8(5), pp.1214-1225.

140. Néel, N. (1949). Theorie du Trainage Magnetique des Ferromagnetiques en Grains Fins avec Applications aux Terres Cuites. *Ann. Geophys,* 5, pp. 99-136

141. Nenasheva, T., Nikolaev, A., Diykanov, D., Sukhanova, A., Tcyganov, E., Panteleev, A., Bocharova, I., Serdyuk, Y., Nezlin, L., Radaeva, T., Adrianov, N., Rubtsov, Y. and Lyadova, I. (2017). The introduction of mesenchymal stromal cells induces different immunological responses in the lungs of healthy and M. tuberculosis infected mice. *PLOS ONE*, 12(6), p.e0178983.

142. Novotna, B., Herynek, V., Rossner, P., Turnovcova, K. and Jendelova, P. (2017). The effects of grafted mesenchymal stem cells labeled with iron oxide or cobalt-zinc-iron nanoparticles on the biological macromolecules of rat brain tissue extracts. *International Journal of Nanomedicine*, Volume 12, pp.4519-4526.

143. Nowbar, A., Mielewczik, M., Karavassilis, M., Dehbi, H., Shun-Shin, M., Jones, S., Howard, J., Cole, G. and Francis, D. (2014). Discrepancies in autologous bone marrow stem cell trials and enhancement of ejection fraction (DAMASCENE): weighted regression and meta-analysis. *BMJ*, 348(apr28 1), pp.g2688-g2688.

144. Nugraha, B., Hong, X., Mo, X., Tan, L., Zhang, W., Chan, P., Kang, C., Wang, Y., Beng, L., Sun, W., Choudhury, D., Robens, J., McMillian, M., Silva, J., Dallas, S., Tan, C., Yue, Z. and Yu, H. (2011). Galactosylated cellulosic sponge for multi-well drug safety testing. *Biomaterials*, 32(29), pp.6982-6994.

145. Nurchi, V., Pivetta, T., Lachowicz, J. and Crisponi, G. (2009). Effect of substituents on complex stability aimed at designing new iron(III) and aluminum(III) chelators. *Journal of Inorganic Biochemistry*, 103(2), pp.227-236.

146. Nusse, R., van Ooyen, A., Cox, D., Fung, Y. and Varmus, H. (1984). Mode of proviral activation of a putative mammary oncogene (int-1) on mouse chromosome 15. *Nature*, 307(5947), pp.131-136.

147. Nuttelman, C., Tripodi, M. and Anseth, K. (2005). Synthetic hydrogel niches that promote hMSC viability. *Matrix Biology*, 24(3), pp.208-218.

148. O'Brien, R., Midmore, B., Lamb, A. and Hunter, R. (1990). Electroacoustic studies of moderately concentrated colloidal suspensions. *Faraday Discussions of the Chemical Society*, 90, p.301.

149. Pankhurst, Q., Connolly, J., Jones, S. and Dobson, J. (2003). Applications of magnetic nanoparticles in biomedicine. *Journal of Physics D: Applied Physics*, 36(13), pp.R167-R181.

150. Paris, J., Torre, P., Manzano, M., Cabañas, M., Flores, A. and Vallet-Regí, M. (2016). Decidua-derived mesenchymal stem cells as carriers of mesoporous silica nanoparticles. In vitro and in vivo evaluation on mammary tumors. *Acta Biomaterialia*, 33, pp.275-282.

151. Patten, T. and Matyjaszewski, K. (1998). Atom Transfer Radical Polymerization and the Synthesis of Polymeric Materials. *Advanced Materials*, 10(12), pp.901-915.

152. Pearce, J., Giustini, A., Stigliano, R. and Jack Hoopes, P. (2013). Magnetic Heating of Nanoparticles: The Importance of Particle Clustering to Achieve Therapeutic Temperatures. *Journal of Nanotechnology in Engineering and Medicine*, 4(1), p.011005.

153. Penczek, S. and Moad, G. (2008). Glossary of terms related to kinetics, thermodynamics, and mechanisms of polymerization (IUPAC Recommendations 2008). *Pure and Applied Chemistry*, 80(10), pp.2163-2193.

154. Peters, J., Hutchinson, S., Lizana, N., Verma, I. and Peppas, N. (2018). Synthesis and characterization of poly(N-isopropyl methacrylamide) core/shell nanogels for controlled release of chemotherapeutics. *Chemical Engineering Journal*, 340, pp.58-65.

155. Pittenger, M. (1999). Multilineage Potential of Adult Human Mesenchymal Stem Cells. *Science*, 284(5411), pp.143-147.

156. Purushotham, S., Chang, P., Rumpel, H., Kee, I., Ng, R., Chow, P., Tan, C. and Ramanujan, R. (2009). Thermoresponsive core–shell magnetic nanoparticles for combined modalities of cancer therapy. *Nanotechnology*, 20(30), p.305101.

157. Quarto, N., Behr, B. and Longaker, M. (2010). Opposite Spectrum of Activity of Canonical Wnt Signaling in the Osteogenic Context of Undifferentiated and Differentiated Mesenchymal Cells: Implications for Tissue Engineering. *Tissue Engineering Part A*, 16(10), pp.3185-3197.

158. Queffelec, J., Gaynor, S. and Matyjaszewski, K. (2000). Optimization of Atom Transfer Radical Polymerization Using Cu(I)/Tris(2-(dimethylamino)ethyl)amine as a Catalyst. *Macromolecules*, 33(23), pp.8629-8639.

159. Rahmawati, R., Permana, M., Harison, B., Nugraha, Yuliarto, B., Suyatman and Kurniadi, D. (2017). Optimization of Frequency and Stirring Rate for Synthesis of Magnetite (Fe_3O_4) Nanoparticles by Using Coprecipitation-Ultrasonic Irradiation Methods. *Procedia Engineering*, 170, pp.55-59.

160. Rathfon, J. and Tew, G. (2008). Synthesis of thermoresponsive poly(N-isopropylmethacrylamide) and poly(acrylic acid) block copolymers via post-functionalization of poly(N-methacryloxysuccinimide). *Polymer*, 49(7), pp.1761-1769.

161. Regmi, R., Bhattarai, S., Sudakar, C., Wani, A., Cunningham, R., Vaishnava, P., Naik, R., Oupicky, D. and Lawes, G. (2010). Hyperthermia controlled rapid drug release from thermosensitive magnetic microgels. *Journal of Materials Chemistry*, 20(29), p.6158.

162. Reinhold, M., Kapadia, R., Liao, Z. and Naski, M. (2005). The Wnt-inducible Transcription Factor Twist1 Inhibits Chondrogenesis. *Journal of Biological Chemistry*, 281(3), pp.1381-1388.

163. Ren, G., Chen, X., Dong, F., Li, W., Ren, X., Zhang, Y. and Shi, Y. (2011). Concise Review: Mesenchymal Stem Cells and Translational Medicine: Emerging Issues. *STEM CELLS Translational Medicine*, 1(1), pp.51-58.

164. Reya, T. and Clevers, H. (2005). Wnt signalling in stem cells and cancer. *Nature*, 434(7035), pp.843-850.

165. Rimann, M. and Graf-Hausner, U. (2012). Synthetic 3D multicellular systems for drug development. *Current Opinion in Biotechnology*, 23(5), pp.803-809.

166. Ringden, O. and Keating, A. (2011). Mesenchymal stromal cells as treatment for chronic GVHD. *Bone Marrow Transplantation*, 46(2), pp.163-164.

167. Rizlan, Z. and Mamat, O. (2014). Process Parameters Optimization of Silica Sand Nanoparticles Production Using Low Speed Ball Milling Method. *Chinese Journal of Engineering*, 2014, pp.1-4.

168. Roger, M., Clavreul, A., Venier-Julienne, M., Passirani, C., Sindji, L., Schiller, P., Montero-Menei, C. and Menei, P. (2010). Mesenchymal stem cells as cellular vehicles for delivery of nanoparticles to brain tumors. *Biomaterials*, 31(32), pp.8393-8401.

169. Roskies, M., Jordan, J., Fang, D., Abdallah, M., Hier, M., Mlynarek, A., Tamimi, F. and Tran, S. (2016). Improving PEEK bioactivity for craniofacial reconstruction using a 3D printed scaffold embedded with mesenchymal stem cells. *Journal of Biomaterials Applications*, 31(1), pp.132-139.

170. Saitoh, T., Hirai, M. and Katoh, M. (2001). Molecular Cloning and Characterization of WNT3A and WNT14 Clustered in Human Chromosome 1q42 Region. *Biochemical and Biophysical Research Communications*, 284(5), pp.1168-1175.

171. Saleh, F., Carstairs, A., Etheridge, S. and Genever, P. (2016). Real-Time Analysis of Endogenous Wnt Signalling in 3D Mesenchymal Stromal Cells. *Stem Cells International*, 2016, pp.1-9.

172. Samiee, L., Dehghani Mobarake, M., Karami, R., Ayazi, M. (2012). Developing of Ethylene Glycol as a New Reducing Agent for Preparation of Pd-Ag/PSS Composite Membrane for Hydrogen Separation, *Journal of Petroleum Science and Technology*, 2(2), pp. 25-32.

173. Saraswathy, A., Nazeer, S., Jeevan, M., Nimi, N., Arumugam, S., Harikrishnan, V., Varma, P. and Jayasree, R. (2014). Citrate coated iron oxide nanoparticles with enhanced relaxivity for in vivo magnetic resonance imaging of liver fibrosis. *Colloids and Surfaces B: Biointerfaces*, 117, pp.216-224.

174. Schild, H. (1992). Poly(N-isopropylacrylamide): experiment, theory and application. *Progress in Polymer Science*, 17(2), pp.163-249.

175. Schultz, A. Flory, P. (1952) *Phase Equilibria in Polymer-Solvent Systems*, Journal of the American Chemical Society, 74, pp. 4760–4767.

176. Schulz, G. V. (1935) “On the relationship between the rate of reaction and composition of the reaction products in macro polymerisation processes,” *Zeitschrift für Physikalische Chemie,* 30, p. 379.

177. Senoo, M., Kotani, Y., Kamigaito, M. and Sawamoto, M. (1999). Living Radical Polymerization ofN,N-Dimethylacrylamide with RuCl2(PPh3)3-Based Initiating Systems1. *Macromolecules*, 32(24), pp.8005-8009.

178. Seuring, J. and Agarwal, S. (2012). Polymers with Upper Critical Solution Temperature in Aqueous Solution. *Macromolecular Rapid Communications*, 33(22), pp.1898-1920.

179. Shang, Y., Wang, S., Xiong, F., Zhao, C., Peng, F., Feng, S., Li, M., Li, Y. and Zhang, C. (2007). Wnt3a signaling promotes proliferation, myogenic differentiation, and migration of rat bone marrow mesenchymal stem cells. *Acta Pharmacologica Sinica*, 28(11), pp.1761-1774.

180. Shen, B., Ma, Y., Yu, S. and Ji, C. (2016). Smart Multifunctional Magnetic Nanoparticle-Based Drug Delivery System for Cancer Thermo-Chemotherapy and Intracellular Imaging. *ACS Applied Materials & Interfaces*, 8(37), pp.24502-24508.

181. Shigeta, M. and Murphy, A. (2011). Thermal plasmas for nanofabrication. *Journal of Physics D: Applied Physics*, 44(17), p.174025.

182. Shinkai, M., Ueda, K., Ohtsu, S., Honda, H., Kohri, K. and Kobayashi, T. (1999). Effect of Functional Magnetic Particles on Radiofrequency Capacitive Heating. *Japanese Journal of Cancer Research*, 90(6), pp.699-704.

183. Shinkai, M., Ueda, K., Ohtsu, S., Honda, H., Kohri, K. and Kobayashi, T. (2002). Effect of Functional Magnetic Particles on Radiofrequency Capacitive Heating: An *in vivo* Study. *Japanese Journal of Cancer Research*, 93(1), pp.103-108.

184. Shipp, D. (2011). Reversible-Deactivation Radical Polymerizations. *Polymer Reviews*, 51(2), pp.99-103.

185. Shunmugam, R. and Tew, G. (2005). Unique Emission from Polymer Based Lanthanide Alloys. *Journal of the American Chemical Society*, 127(39), pp.13567-13572.

186. Simmons, D. and Sanchez, I. (2008). A Model for a Thermally Induced Polymer Coil-to-Globule Transition. *Macromolecules*, 41(15), pp.5885-5889.

187. Soenen, SJ., De Cuyper, M., De Smedt, SC., Braeckmans, K. (2012) Investigating the toxic effects of iron oxide nanoparticles, *Methods Enzymol,* 509, pp. 195-224

188. Šolc, K., Dušek, K., Koningsveld, R. and Berghmans, H. (1995). "Zero" and "Off-Zero" Critical Concentrations in Solutions of Polydisperse Polymers with Very High Molar Masses. *Collection of Czechoslovak Chemical Communications*, 60(10), pp.1661-1688.

189. Somasundaran, P. (2006). *Encyclopedia of surface and colloid science*. New York: Taylor & Francis. p. 3471.

190. Staudinger, H. (1920) “Über Polymerisation,” *Berichte der Deutschen Chemischen Gesellschaft*, 53(6), pp. 1073–1085

191. Staudinger, H. (1926) “Die Chemie der hochmolekularen organischen Stoffe im Sinne der Kekuléschen Strukturlehre,” *Berichte der Deutschen Chemischen Gesellschaft*, 59, pp. 3019–3043

192. St-Jacques, B., Hammerschmidt, M. and McMahon, A. (1999). Indian hedgehog signaling regulates proliferation and differentiation of chondrocytes and is essential for bone formation. *Genes & Development*, 13(16), pp.2072-2086.

193. Suedee, R., Seechamnanturakit, V., Canyuk, B., Ovatlarnporn, C. and Martin, G. (2006). Temperature sensitive dopamine-imprinted (N,N-methylene-bis-acrylamide cross-linked) polymer and its potential application to the selective extraction of adrenergic drugs from urine. *Journal of Chromatography A*, 1114(2), pp.239-249.

194. Sugimoto, T. and Matijević, E. (1980). Formation of uniform spherical magnetite particles by crystallization from ferrous hydroxide gels. *Journal of Colloid and Interface Science*, 74(1), pp.227-243.

195. Sung Lee, J., Myung Cha, J., Young Yoon, H., Lee, J. and Keun Kim, Y. (2015). Magnetic multi-granule nanoclusters: A model system that exhibits universal size effect of magnetic coercivity. *Scientific Reports*, 5(1).

196. Tamai, K., Semenov, M., Kato, Y., Spokony, R., Liu, C., Katsuyama, Y., Hess, F., Saint-Jeannet, J. and He, X. (2000). LDL-receptor-related proteins in Wnt signal transduction. *Nature*, 407(6803), pp.530-535.

197. Taniguchi, I., Fukuda, N. and Konarova, M. (2008). Synthesis of spherical LiMn2O4 microparticles by a combination of spray pyrolysis and drying method. *Powder Technology*, 181(3), pp.228-236.

198. Teja, A. and Koh, P. (2010). ChemInform Abstract: Synthesis, Properties, and Applications of Magnetic Iron Oxide Nanoparticles. *ChemInform*, 55(1-2), pp. 22-45

199. Temtem, M., Barroso, T., Casimiro, T., Mano, J. and Aguiar-Ricardo, A. (2012). Dual stimuli responsive poly(N-isopropylacrylamide) coated chitosan scaffolds for controlled release prepared from a non residue technology. *The Journal of Supercritical Fluids*, 66, pp.398-404.

200. Tong, S., Quinto, C., Zhang, L., Mohindra, P. and Bao, G. (2017). Size-Dependent Heating of Magnetic Iron Oxide Nanoparticles. *ACS Nano*, 11(7), pp.6808-6816.

201. Ulrich, S., Laguecir, A. and Stoll, S. (2005). Titration of hydrophobic polyelectrolytes using Monte Carlo simulations. *The Journal of Chemical Physics*, 122(9), p.094911.

202. Vallejo-Fernandez, G., Whear, O., Roca, A., Hussain, S., Timmis, J., Patel, V. and O'Grady, K. (2013). Mechanisms of hyperthermia in magnetic nanoparticles. *Journal of Physics D: Applied Physics*, 46(31), p.312001.

203. van Rijt, S., Bein, T. and Meiners, S. (2014). Medical nanoparticles for next generation drug delivery to the lungs. *European Respiratory Journal*, 44(3), pp.765-774.

204. Villani, S., Adami, R., Reverchon, E., Ferretti, A., Ponti, A., Lepretti, M., Caputo, I. and Izzo, L. (2017). pH-sensitive polymersomes: controlling swelling via copolymer structure and chemical composition. *Journal of Drug Targeting*, 25(9-10), pp.899-909.

205. von Bahr, L., Sundberg, B., Lönnies, L., Sander, B., Karbach, H., Hägglund, H., Ljungman, P., Gustafsson, B., Karlsson, H., Le Blanc, K. and Ringdén, O. (2012). Long-Term Complications, Immunologic Effects, and Role of Passage

for Outcome in Mesenchymal Stromal Cell Therapy. *Biology of Blood and Marrow Transplantation*, 18(4), pp.557-564.

206. Wang, J. and Matyjaszewski, K. (1995). "Living"/Controlled Radical Polymerization. Transition-Metal-Catalyzed Atom Transfer Radical Polymerization in the Presence of a Conventional Radical Initiator. *Macromolecules*, 28(22), pp.7572-7573.

207. Wang, Z., Li, X., He, X., Wu, B., Xu, M., Chang, H., Zhang, X., Xing, Z., Jing, X., Kong, D., Kou, X. and Yang, Y. (2014). Delivery of the Sox9 gene promotes chondrogenic differentiation of human umbilical cord blood-derived mesenchymal stem cells in an in vitro model. *Brazilian Journal of Medical and Biological Research*, 47(4), pp.279-286.

208. Ward, M. and Georgiou, T. (2010). Thermoresponsive terpolymers based on methacrylate monomers: Effect of architecture and composition. *Journal of Polymer Science Part A: Polymer Chemistry*, 48(4), pp.775-783.

209. Wei, H., Bruns, O., Kaul, M., Hansen, E., Barch, M., Wiśniowska, A., Chen, O., Chen, Y., Li, N., Okada, S., Cordero, J., Heine, M., Farrar, C., Montana, D., Adam, G., Ittrich, H., Jasanoff, A., Nielsen, P. and Bawendi, M. (2017). Exceedingly small iron oxide nanoparticles as positive MRI contrast agents. *Proceedings of the National Academy of Sciences*, 114(9), pp.2325-2330.

210. Wilkinson, D., Bailes, J. and McMahon, A. (1987). Expression of the proto-oncogene int-1 is restricted to specific neural cells in the developing mouse embryo. *Cell*, 50(1), pp.79-88.

211. Willert, K., Shibamoto, S. and Nusse, R. (1999). Wnt-induced dephosphorylation of Axin releases beta -catenin from the Axin complex. *Genes & Development*, 13(14), pp.1768-1773.

212. Wu, C. and Wang, X. (1998). Globule-to-Coil Transition of a Single Homopolymer Chain in Solution. *Physical Review Letters*, 80(18), pp.4092-4094.

213. Xiang, J., Tong, X., Shi, F., Yan, Q., Yu, B. and Zhao, Y. (2018). Near-infrared light-triggered drug release from UV-responsive diblock copolymer-coated upconversion nanoparticles with high monodispersity. *Journal of Materials Chemistry B*, 6(21), pp.3531-3540.

214. Yang, B., Guo, H., Zhang, Y., Chen, L., Ying, D. and Dong, S. (2011). MicroRNA-145 Regulates Chondrogenic Differentiation of Mesenchymal Stem Cells by Targeting Sox9. *PLoS ONE*, 6(7), p.e21679.

215. Yang, Y. (2003). Wnt5a and Wnt5b exhibit distinct activities in coordinating chondrocyte proliferation and differentiation. *Development*, 130(5), pp.1003-1015.

216. Yoon, B., Ovchinnikov, D., Yoshii, I., Mishina, Y., Behringer, R. and Lyons, K. (2005). Bmpr1a and Bmpr1b have overlapping functions and are essential for chondrogenesis in vivo. *Proceedings of the National Academy of Sciences*, 102(14), pp.5062-5067.

217. Yoon, B., Pogue, R., Ovchinnikov, D., Yoshii, I., Mishina, Y., Behringer, R. and Lyons, K. (2006). BMPs regulate multiple aspects of growth-plate chondrogenesis through opposing actions on FGF pathways. *Development*, 133(23), pp.4667-4678.

218. Yun, W., Choi, J., Ju, H., Kim, M., Choi, S., Oh, E., Seo, Y. and Key, J. (2018). Enhanced Homing Technique of Mesenchymal Stem Cells Using Iron Oxide Nanoparticles by Magnetic Attraction in Olfactory-Injured Mouse Models. *International Journal of Molecular Sciences*, 19(5), p.1376.

219. Zhang, C., Chen, J., Feng, C., Shao, X., Liu, Q., Zhang, Q., Pang, Z. and Jiang, X. (2014). Intranasal nanoparticles of basic fibroblast growth factor for brain delivery to treat Alzheimer's disease. *International Journal of Pharmaceutics*, 461(1-2), pp.192-202.

220. Zhang, X., Pint, C., Lee, M., Schubert, B., Jamshidi, A., Takei, K., Ko, H., Gillies, A., Bardhan, R., Urban, J., Wu, M., Fearing, R. and Javey, A. (2011). Optically- and Thermally-Responsive Programmable Materials Based on Carbon Nanotube-Hydrogel Polymer Composites. *Nano Letters*, 11(8), pp.3239-3244.

221. Zhao, Y., Tang, S., Guo, J., Alahdal, M., Cao, S., Yang, Z., Zhang, F., Shen, Y., Sun, M., Mo, R., Zong, L. and Jin, L. (2017). Targeted delivery of doxorubicin by nano-loaded mesenchymal stem cells for lung melanoma metastases therapy. *Scientific Reports*, 7(1).

222. Zheng, H., Guo, Z., Ma, Q., Jia, H. and Dang, G. (2004). Cbfa1/osf2 Transduced Bone Marrow Stromal Cells Facilitate Bone Formation In Vitro and In Vivo. *Calcified Tissue International*, 74(2), pp.194-203.

223. Zhernenkov, M., Ashkar, R., Feng, H., Akintewe, O., Gallant, N., Toomey, R., Ankner, J. and Pynn, R. (2015). Thermoresponsive PNIPAM Coatings on Nanostructured Gratings for Cell Alignment and Release. *ACS Applied Materials & Interfaces*, 7(22), pp.11857 -11862.

224. Zhou, Z., Zhu, S. and Zhang, D. (2007). Grafting of thermo-responsive polymer inside mesoporous silica with large pore size using ATRP and investigation of its use in drug release. *Journal of Materials Chemistry*, 17(23), p.2428.

225. Zirbs, R., Lassenberger, A., Vonderhaid, I., Kurzhals, S. and Reimhult, E. (2015). Melt-grafting for the synthesis of core–shell nanoparticles with ultra-high dispersant density. *Nanoscale*, 7(25), pp.11216-11225.